نبذة عن الطاقة التقليدية ومشاكلها

ما هو الوقود الأحفوري؟

أعتمدت البشرية لعدة عقود على الوقود الأحفوري الذي يتميز بخصائص، منها سهولة نقله وتخزينه، لكنه تسبب في تغيرات مناخية حادة لكوكب الأرض.

الوقود الأحفوري هو وقود يتم استعماله لإنتاج الطاقة الأحفورية. ويستخرج الوقود الأحفوري من المواد الأحفورية كالفحم الحجري ،الفحم النفطي الأسود، الغاز الطبيعي، ومن البترول.

و تستخرج هذه المواد بدورها من باطن الأرض وتحترق في الهواء مع الأكسجين لإنتاج حرارة تستخدم في كافة الميادين.

التعريف

بعد أن دفنت بقايا الكائنات الحية (نباتات وحيوانات) تحت طبقات القشرة الأرضية تعرضت لدرجات حرارة وضغط مرتفعة جدا، وهو ما أدى إلى تركيز مادة الكربون فيها وتحويلها بالتالي إلى وقود أحفوري يستخدم لإنتاج الطاقة الأحفورية.

ويعتمد تركيب الوقود الأحفوري على دورة الكربون في الطبيعة، ويستخرج من المواد الأحفورية كالفحم الحجري، والفحم النفطي الأسود، والغاز الطبيعي، ومن البترول.

وقد قامت الثورة الصناعية في القرنين الـ18 والـ19 تزامنا مع استعمال الطاقة الأحفورية في المجال التقني، خاصة الفحم الحجري في ذاك الوقت، ولاحقا أصبح النفط الخام يلعب الدور الأكبر في تلبية احتياجات الطاقة نظرا لسهولة استخراجه ومعالجته ونقله، مما يجعله أزهد ثمنا.

الخصائص

يتميز الوقود الأحفوري بامتلاكه كثافة طاقة عالية وبسهولة نقله وتخزينه، كما أنه بمعالجته بتروكيميائيا يمكن الحصول على أنواع مختلفة منه، خاصة من الوقود الأحفوري السائل والغازي، حيث يتم استخراج وقود منه، وذلك للاستعمالات المختلفة في المحركات والطائرات والسفن بعد المعالجة البتروكيميائية اللازمة، بالإضافة إلى توليد الطاقة الكهربائية.

المشاكل

أولاً: التلوث الهوائي:

تعتبر الصناعات التي تعتمد على الوقود الحفري [الفحم . النفط . الغاز الطبيعي] كمصدر أساسي للطاقة من أكبر مصادر الملوثات الهوائية، إذ ينطلق منها عند احتراقها كميات كبيرة جداً من الغازات والجسيمات التي تعمل من خلال تراكمها في الغلاف الجوي على تغيير [إفساد] تركيبة الهواء، مما يؤدي إلى حدوث خلل في نظامه الأيكولوجي، يصبح معه الهواء مصدراً لكثير من المخاطر والأضرار التي باتت تهدد كافة صور الحياة على الأرض، وذلك نتيجه لتعدد أنواع الغازات والشوائب التي تتصاعد إلى الهواء نتيجة إحراق الوقود في المصانع، ومحطات القوي، وفي محركات السيارات. مما يجعل الهواء ملوثاً بالآتي.

1. تلوث الهواء بثاني أكسيد الكربون.
2. تلوث الهواء بثاني أكسد الكبريت، وأكاسيد النيتروجين، وأول أكسيد الكربون.
3. تلوث الهواء بعادم السيارات والرصاص.

وذلك على التفصيل.

ثانياً: الأضرار الناجمة عن تلوث الهواء:

وتتمثل في الأمطار الحمضية والإخلال بطبقة الأوزون.

1. الأمطار الحمضية:

لقد ثبت أن السبب الرئيسي في تكوين الأمطار الحمضية هو محطات القوي والمراكز الصناعية الضخمة التي تنتشر في كثير من الدول. وتحرق كميات ضخمة من الوقود وتدفع إلى الهواء يومياً بكميات هائلة من الغازات الحمضية (مثل ثاني أكسيد الكبريت، كبريتيد الهيدروجين وأكاسيد النيتروجين...)، وتحمل الرياح هذه الغازات من مكان لآخر. وبذلك يمتد تأثيرها وفعلها أحياناً لمسافات بعيدة كل البعد عن المصدر الذي خرجت منه.

وتلك الأمطار تتعدد آثارها السلبية فهي عندما تسقط على سطح الأرض تتفاعل مع بعض مكونات التربة القلوية وتعادلها، وتساعد على تفتيت كثير من الصخور، وتذيب عناصر الكالسيوم الموجودة في التربة وتحملها معها لمياه الأنهار. وتؤدي هذه العملية لحدوث عدة أضرار وهي:.

نحر في التربة، ذوبان بعض الفلزات الهامة في مياه الأمطار الحمضية يبعدها عن جذور النباتات. كما تؤدي تلك الأمطار للإضرار بكثير من المجاري المائية المكشوفة والبحيرات المغلقة بصفة خاصة، وترتفع بذلك حموضة مياه هذه البحيرات، فيؤدي ذلك للقضاء على ما فيها من كائنات (كالأسماك وخلافه)، كما تؤثر تلك الأمطار على مياه الشرب لتجعلها غير صالحه لاستخدام الكائنات الحية لها دون أن تضر بصحتها.

2الإضرار بطبقة الأوزون:

سبق الإشارة إلى أن من أهم الأضرار الناشئة عن الأكاسيد الناتجة عن احتراق الوقود هو ثقب طبقة الأوزون، ونتج عن ثقب تلك الطبقة الكثير من الإضرار بالحياة على الأرض، سواء كانت بالنسبة للإنسان والحيوان والنباتات.

فبالنسبة للإنسان يؤدي وصول الأشعة الناتجة عن ثقب طبقة الأوزون إلى انتشار مرض سرطان الجلد، والتأثير الوراثى (حدوث تلف في الحمض النووي D.N.A)، حدوث المياه البيضاء (الكتاركت) في العيون، حدوث أمراض متعددة بالجهاز التنفسي والأزمات الصدرية، النزلات الشعبية، ضعف الجهاز المناعي، وأمراض القلب والسرطان.

أما بالنسبة للحيوان يؤدي ثقب طبقة الأوزون إلى إصابة الثروة الحيوانية بالأمراض، حيث يمتد التلوث للأعشاب والزراعات التي تتغذى عليها الحيوانات، مما يلحق الضرر بالثروة الحيوانية أيضاً، فانتشار المجاعات لن يقتصر على غذاء الإنسان فقط بل أيضاً الحيوان.

كما يؤثر على الثروة السمكية، ويسبب هلاك يرقات الأسماك التي تعيش قريباً من سطح ماء المحيطات والأنهار.

كما يؤثر ثقب الأوزون على النباتات: حيث يؤدي لنقص المحاصيل الزراعية من النباتات الحساسة للأشعة كالقطن، وبعض النباتات التي ثبت توقفها عن عمليات بناء الأنسجة في ثلثي النباتات محل التجربة. وهذا يعني أن تسرب الأشعة فوق البنفسجية سيضر بالمحاصيل، وسيقلل غلتها وإنتاجها، ويلحق الضرر بكثير منها.

مما سبق نجد أن مخاطر تلوث الهوائي تمتد لتشمل كافة جوانب الحياة على سطح الأرض.

ثالثاً: التلوث المائي:

يساهم النفط بصورة كبيرة في حدوث التلوث المائي فهناك العديد من الأضرار الناتجة عن تلوث الماء بزيت البترول. ومنها ظهور آثار سامة في منطقة الحادث نتيجة بعض العناصر الثقيلة (كالزئبق، والرصاص، الكادميوم)،وقيام الرياح وحركة الأمواج بدفع أجزاء من بقعة الزيت نحو الشواطئ المقابلة لمنطقة الحادث فتلوث رمالها وتحيلها لمنطقة عديمة النفع والفائدة. كما تعتبر أيضاً النفايات والمخلفات البترولية التي تلقيها ناقلات البترول في البحار أثناء سيرها فيها من أهم أسباب تلوث المياه بزيت البترول، ذلك الأخير الذي يؤدي للعديد من الأضرار البيئية.

Renewable Energy Types:

1-Solar energy

2-Wind energy

3-Biomass & Biofuels

4-Geothermal energy

5-Tidal energy

6-Fuel cell

7-Ocean energy conversion

8-Hydro-power energy

9-Hydrogen energy

Solar Energy

Solar Radiation

The sun's structure and characteristics determine the nature of the energy it radiates into space. The first major topic concerns the characteristics of this energy outside the earth's atmosphere, its intensity, and its spectral distribution. We will be concerned primarily with radiation in a wavelength range of 0.25 to 3.0 μm, the portion of the electromagnetic radiation that includes most of the energy radiated by the sun. The second major topic is solar geometry, that is, the position of the sun in the sky, the direction in which beam radiation is incident on surfaces of various orientations, and shading. The third topic is extraterrestrial radiation on a horizontal surface, which represents the theoretical upper limit of solar radiation available at the earth's surface.

THE SUN

The sun is a sphere of intensely hot gaseous matter with a diameter of 1.39×10^9 m and is, on the average, 1.5×10^{11} m from the earth. As seen from the earth, the sun rotates on its axis about once every 4 weeks.

The sun has an effective blackbody temperature of 5777 K. The temperature in the central interior regions is variously estimated at 8×10^6 to 40×10^6 K and the density is estimated to be about 100 times that of water. The sun is, in effect, a continuous fusion reactor with its constituent gases as the ‘‘containing vessel’’ retained by gravitational forces. Several fusion reactions have been suggested to supply the energy radiated by the sun. The one considered the most important is a process in which hydrogen (i.e., four protons) combines to form helium (i.e., one helium nucleus); the mass of the helium nucleus is less than that of the four protons, mass having been lost in the reaction and converted to energy.

A schematic structure of the sun is shown in Figure 1. It is estimated that 90% of the energy is generated in the region of 0 to 0.23*R* (where *R* is the radius of the sun), which contains 40% of the mass of the sun. At a distance 0.7*R* from the center, the temperature has dropped to about 130,000 K; here convection processes begin to become important, and the zone from 0.7 to 1.0 *R* is known as the **convective zone**. Within this zone the temperature drops to about 5000 K.

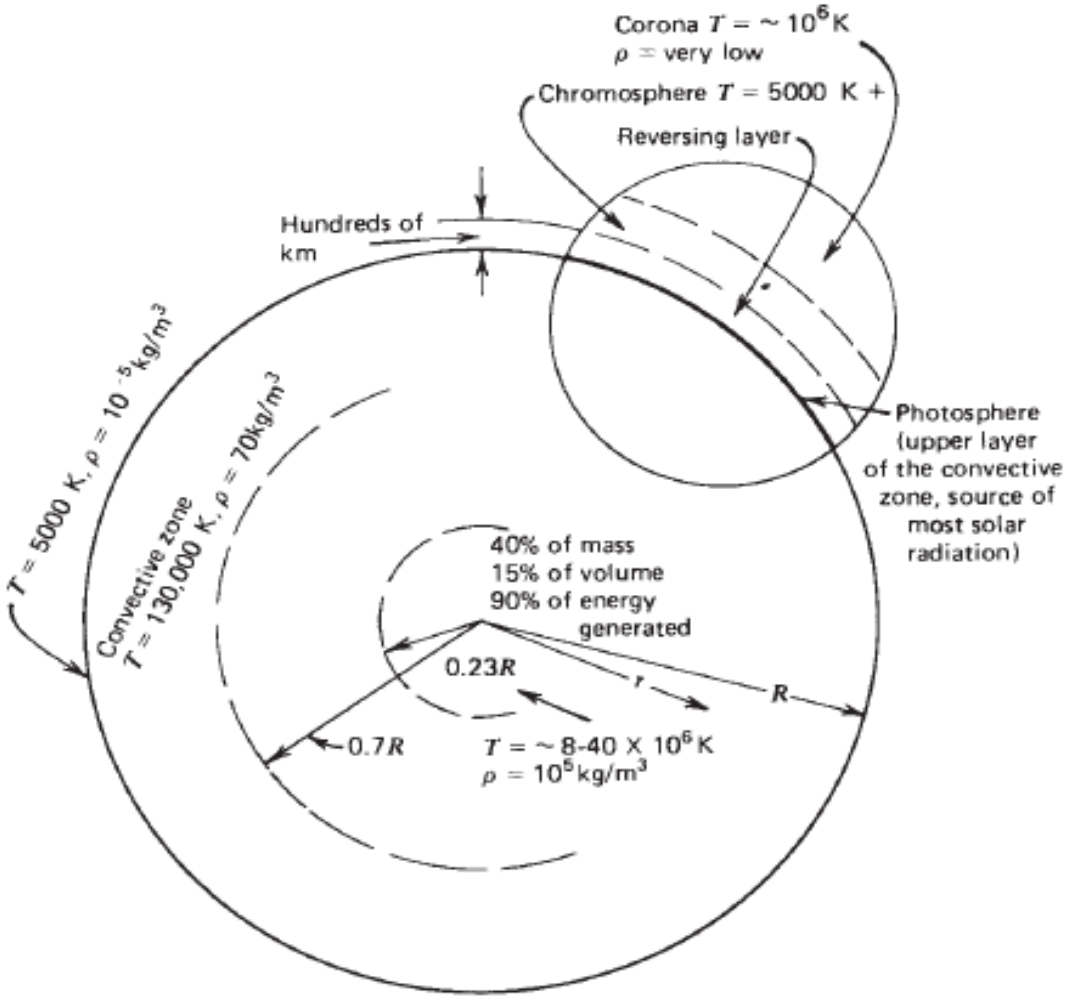

Fig. (1) structure of the sun

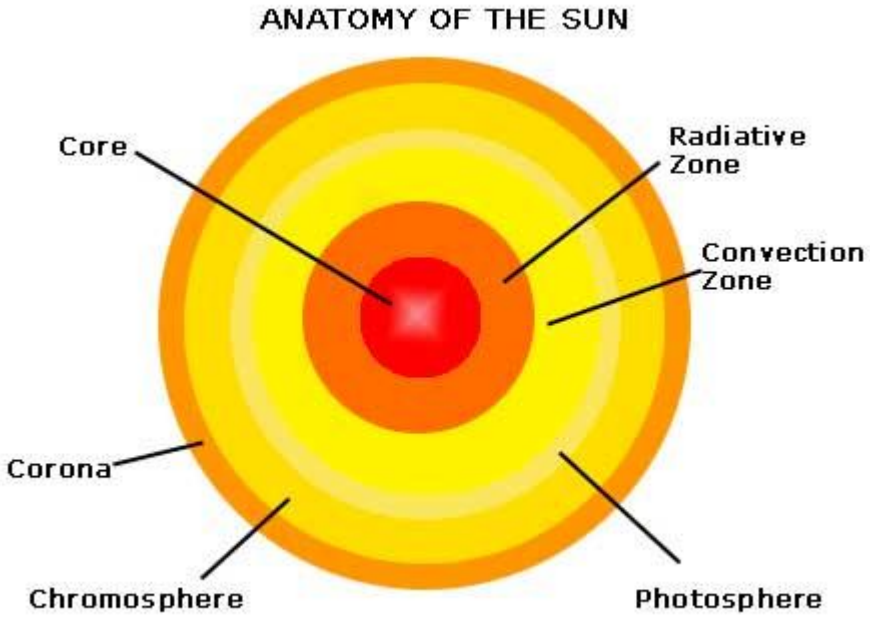

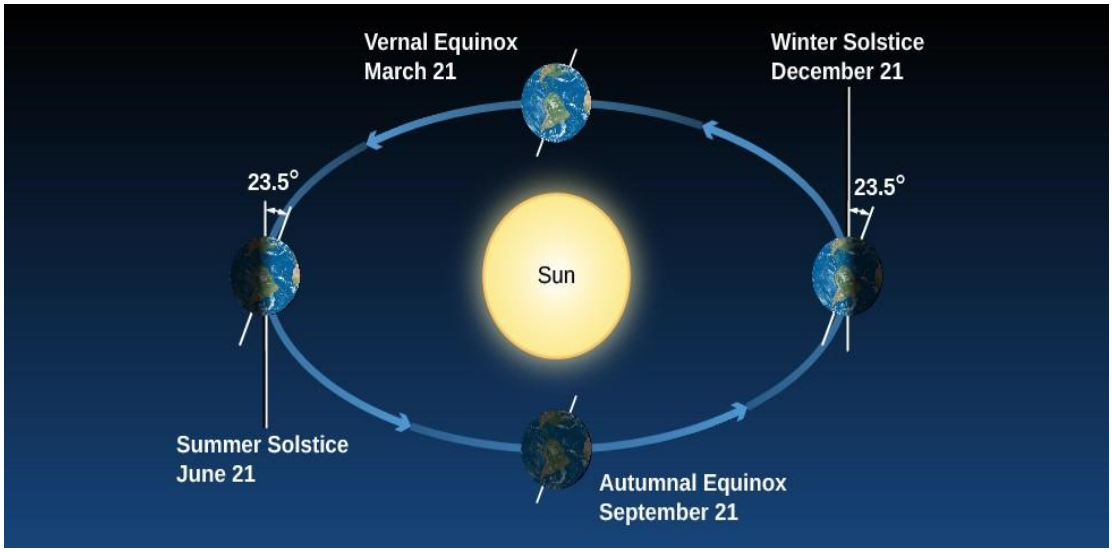

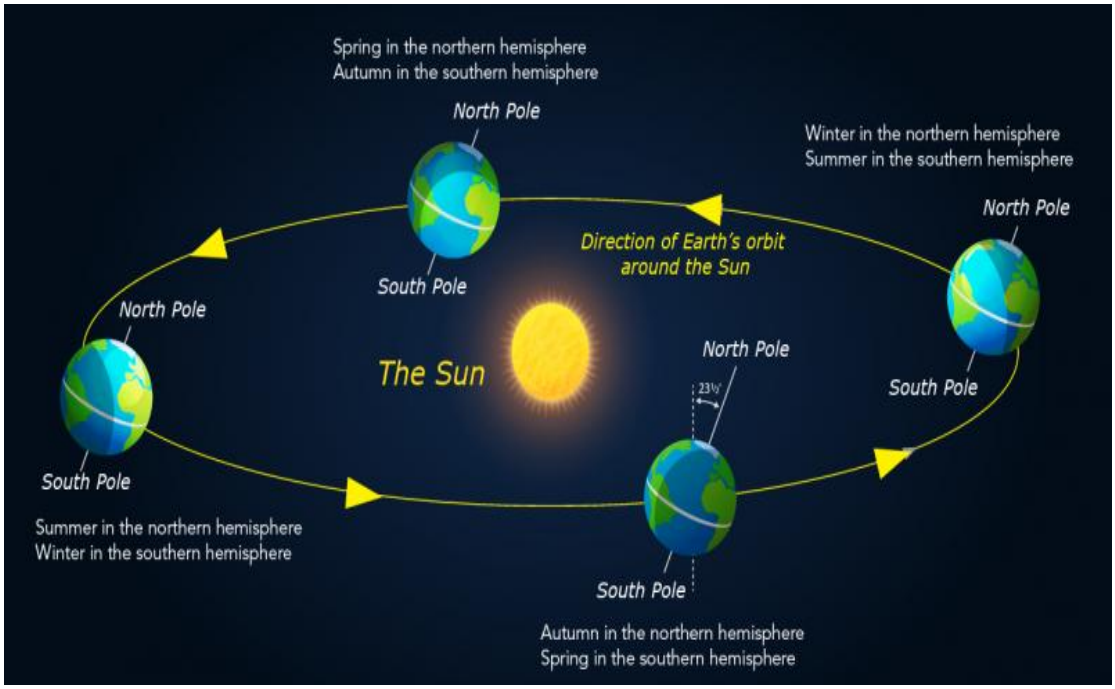

Sun-Earth Distance:

A good approximation to calculating the distance from the sun is to use Kepler's first law.

The Earth's orbit is elliptical and the distance r of the Earth from the Sun can be calculated as:

$$r = \frac{a\left(1 - e^2\right)}{1 - e\cos\theta}$$

Where a=149,600,000km is the semi-major axis distance, e=0.0167 is the eccentricity of the Earth's orbit and θ is the angle from perihelion.

$$\theta = \frac{2\pi n}{365.256}$$

Where n is the number of days from perihelion which is 3rd January.

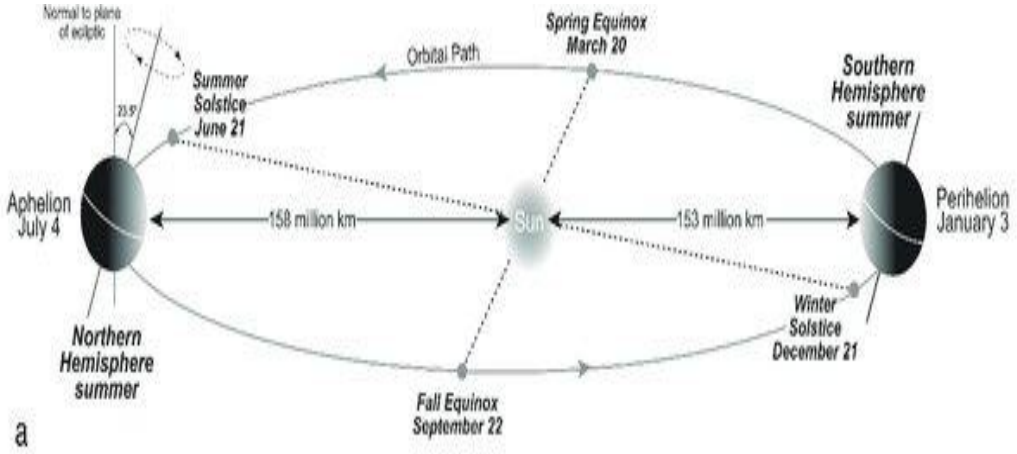

The Solar Constant

Figure 2 shows schematically the geometry of the sun-earth relationships. The eccentricity of the earth's orbit is such that the distance between the sun and the earth varies by 1.7%. At a distance of one astronomical unit, 1.495×10^{11} m, the mean earth-sun distance, the sun subtends an angle of 32`. The radiation emitted by the sun and its spatial relationship to the earth result in a nearly fixed intensity of solar radiation outside of the earth's atmosphere. The **solar constant** G_{sc} is the energy from the sun per unit time received on a unit area of surface perpendicular to the direction of propagation of the radiation at mean earth-sun distance outside the atmosphere. A value of G_{sc} of 1367 W/m^2 is used in this book.

Estimation of Solar Constant:

Sun Power density=$\boldsymbol{\sigma}\times T^4=(5.67\times10^{-8})\times(5777)^4=6.31\times10^7$Watt/m^2

Sun Power=Sun power density×Sun surface area=$6.31\times10^7\times4\boldsymbol{\pi}(1.39\times\mathbf{10^9}/2)^2$

Sun Power=3.85×10^{24} Watt

Power (sun-Earth)=Sun power/Sun-earth surface area

=$3.85\times10^{24}/4\boldsymbol{\pi}(1.49\times\mathbf{10^{11}})^2$=1367 Watt/m^2

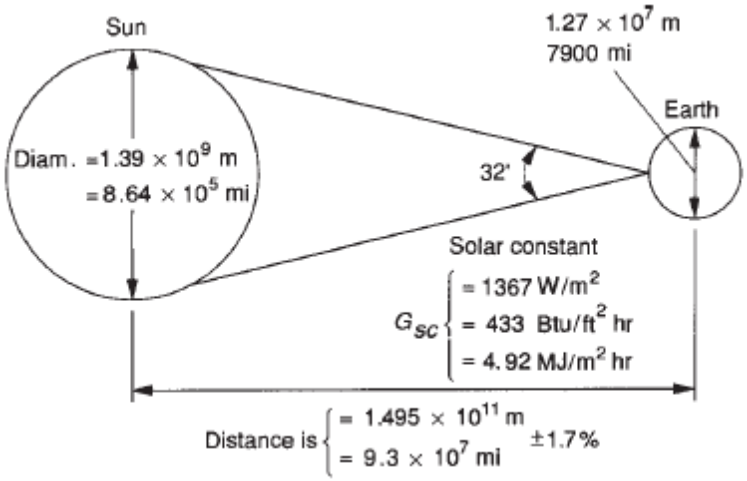

Fig. (2) Sun-Earth relationship

SPECTRAL DISTRIBUTION OF EXTRATERRESTRIAL RADIATION

In addition to the total energy in the solar spectrum (i.e., the solar constant), it is useful to know the spectral distribution of the extra-terrestrial radiation, that is, the radiation that would be received in the absence of the atmosphere. A standard spectral irradiance curve has been compiled based on high-altitude and space measurements. The WRC standard is shown in Figure 3. Table 1. provides the same information on the WRC spectrum in numerical form. The average energy $G_{sc,\lambda}$ (in W/m^2 μm) over small bandwidths centered at wavelength λ is given in the second column. The fraction $f_{0-\lambda}$ of the total energy in the spectrum that is between wavelengths zero and λ is given in the third column. The table is in two parts, the first at regular intervals of wavelength and the second at even fractions $f_{0-\lambda}$.

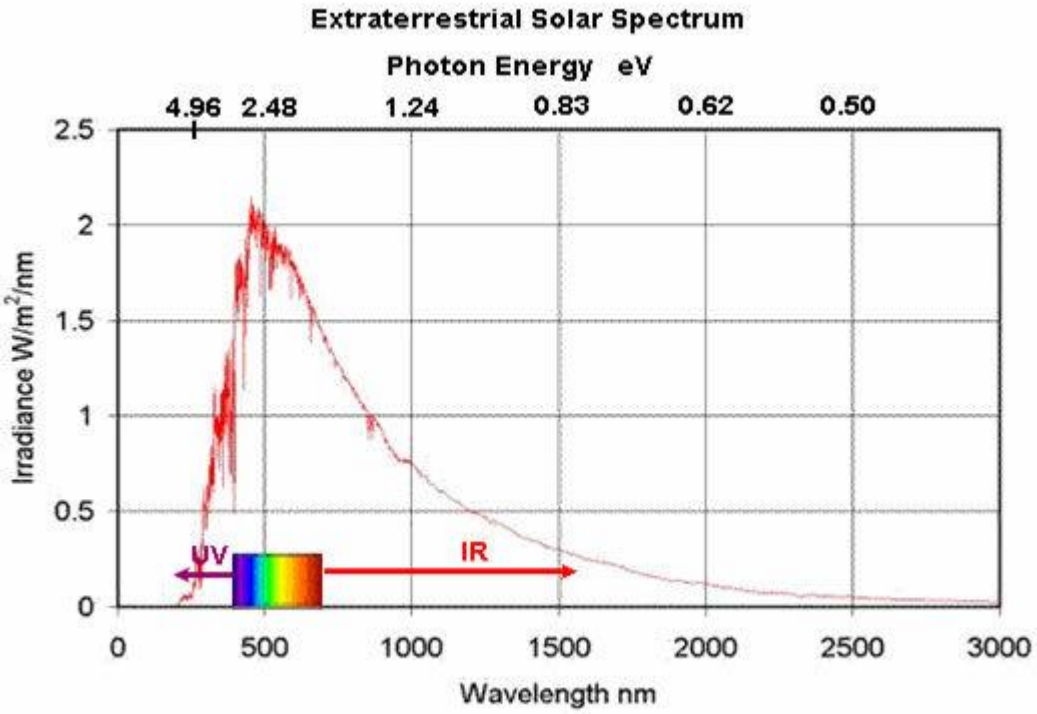

Fig. (3) Solar Spectral distribution

Table 1.3.1a Extraterrestrial Solar Irradiance (WRC Spectrum) in Increments of Wavelength[a]

λ (μm)	$G_{sc,\lambda}$ (W/m^2 μm)	$f_{0-\lambda}$ (–)	λ (μm)	$G_{sc,\lambda}$ (W/m^2 μm)	$f_{0-\lambda}$ (–)	λ (μm)	$G_{sc,\lambda}$ (W/m^2 μm)	$f_{0-\lambda}$ (–)
0.250	81.2	0.001	0.520	1849.7	0.243	0.880	955.0	0.622
0.275	265.0	0.004	0.530	1882.8	0.257	0.900	908.9	0.636
0.300	499.4	0.011	0.540	1877.8	0.271	0.920	847.5	0.648
0.325	760.2	0.023	0.550	1860.0	0.284	0.940	799.8	0.660
0.340	955.5	0.033	0.560	1847.5	0.298	0.960	771.1	0.672
0.350	955.6	0.040	0.570	1842.5	0.312	0.980	799.1	0.683
0.360	1053.1	0.047	0.580	1826.9	0.325	1.000	753.2	0.695
0.370	1116.2	0.056	0.590	1797.5	0.338	1.050	672.4	0.721
0.380	1051.6	0.064	0.600	1748.8	0.351	1.100	574.9	0.744
0.390	1077.5	0.071	0.620	1738.8	0.377	1.200	507.5	0.785
0.400	1422.8	0.080	0.640	1658.7	0.402	1.300	427.5	0.819
0.410	1710.0	0.092	0.660	1550.0	0.425	1.400	355.0	0.847
0.420	1687.2	0.105	0.680	1490.2	0.448	1.500	297.8	0.871
0.430	1667.5	0.116	0.700	1413.8	0.469	1.600	231.7	0.891
0.440	1825.0	0.129	0.720	1348.6	0.489	1.800	173.8	0.921
0.450	1992.8	0.143	0.740	1292.7	0.508	2.000	91.6	0.942
0.460	2022.8	0.158	0.760	1235.0	0.527	2.500	54.3	0.968
0.470	2015.0	0.173	0.780	1182.3	0.544	3.000	26.5	0.981
0.480	1975.6	0.188	0.800	1133.6	0.561	3.500	15.0	0.988
0.490	1940.6	0.202	0.820	1085.0	0.578	4.000	7.7	0.992
0.500	1932.2	0.216	0.840	1027.7	0.593	5.000	2.5	0.996
0.510	1869.1	0.230	0.860	980.0	0.608	8.000	1.0	0.999

Example 1.3.1

Calculate the fraction of the extraterrestrial solar radiation and the amount of that radiation in the ultraviolet ($\lambda < 0.38$ μm), the visible (0.38 μm $< \lambda <$ 0.78 μm), and the infrared ($\lambda > 0.78$ μm) portions of the spectrum.

Solution

From Table 1.3.1a, the fractions of $f_{0-\lambda}$ corresponding to wavelengths of 0.38 and 0.78 μm are 0.064 and 0.544. Thus, the fraction in the ultraviolet is 0.064, the fraction in the visible range is 0.544 – 0.064 = 0.480, and the fraction in the infrared is 1.0 – 0.544 = 0.456. Applying these fractions to a solar constant of 1367 W/m^2 and tabulating the results, we have:

Wavelength range (μm)	0–0.38	0.38–0.78	0.78–∞
Fraction in range	0.064	0.480	0.456
Energy in range (W/m^2)	87	656	623

■

VARIATION OF EXTRATERRESTRIAL RADIATION:

Two sources of variation in extraterrestrial radiation must be considered. The first is the variation in the radiation emitted by the sun. There are conflicting reports in the literature on periodic variations of intrinsic solar radiation. It has been suggested that there are small variations (less than ±1.5%) with different periodicities and variation related to sunspot activities.

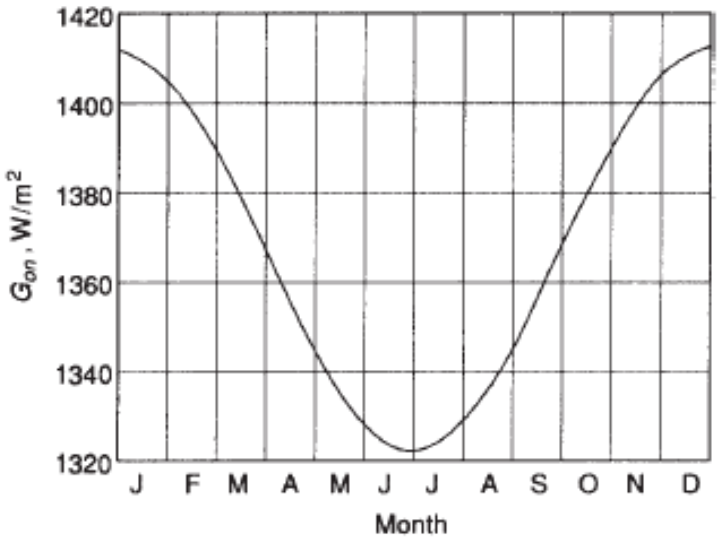

Fig. (4) Variation of extraterrestrial Solar radiation with time of year

The second is the variation of the earth-sun distance, however, does lead to variation of extraterrestrial radiation flux in the range of 3.3%. The dependence of extraterrestrial radiation on time of year is shown in Figure 4. A simple equation with accuracy adequate for most engineering calculations is

$$G_{on} = \begin{cases} G_{sc}\left(1 + 0.033 \cos \dfrac{360n}{365}\right) & (1.4.1a) \\ G_{sc}(1.000110 + 0.034221 \cos B + 0.001280 \sin B \\ \quad +0.000719 \cos 2B + 0.000077 \sin 2B) & (1.4.1b) \end{cases}$$

where G_{on} is the extraterrestrial radiation incident on the plane normal to the radiation on the nth day of the year and B is given by

$$B = (n-1)\frac{360}{365} \qquad (1.4.2)$$

DEFINITIONS

Air Mass m The ratio of the mass of atmosphere through which beam radiation passes to the mass it would pass through if the sun were at the zenith (i.e., directly overhead). Thus at sea level m = 1 when the sun is at the zenith and m = 2 for a zenith angle θz of 60◦. For zenith angles from 0◦ to 70◦ at sea level, to a close approximation:

$$m = \frac{1}{\cos \theta_z} \qquad (1.5.1)$$

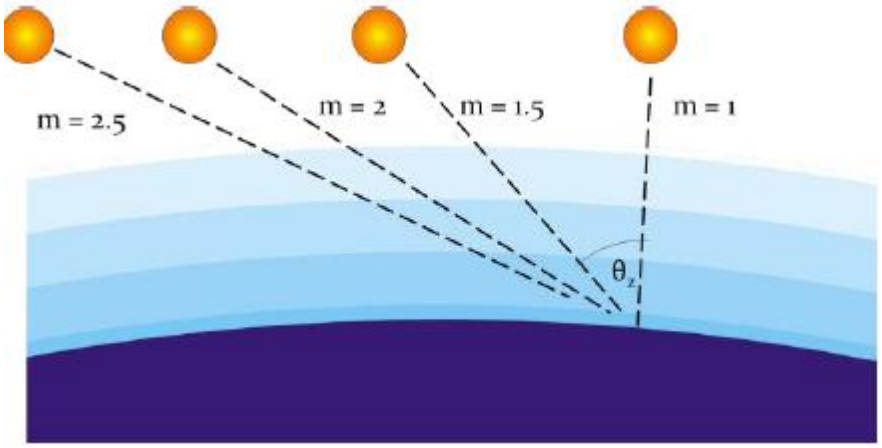

Beam Radiation The solar radiation received from the sun without having been scattered by the atmosphere. (Beam radiation is often referred to as direct solar radiation; to avoid confusion between subscripts for direct and diffuse, we use the term beam radiation.)

Diffuse Radiation The solar radiation received from the sun after its direction has been changed by scattering by the atmosphere. (Diffuse radiation is referred to in some meteorological literature as sky radiation or solar sky radiation; the definition used here will distinguish the diffuse solar radiation from infrared radiation emitted by the atmosphere.)

Total Solar Radiation The sum of the beam and the diffuse solar radiation on a surface. (The most common measurements of solar radiation are total radiation on a horizontal surface, often referred to as **global radiation** on the surface.)

Irradiance, W/m^2 The rate at which radiant energy is incident on a surface per unit area of surface. The symbol *G* is used for solar irradiance, with appropriate subscripts for beam, diffuse, or spectral radiation.

Solar Time Time based on the apparent angular motion of the sun across the sky with **solar noon** the time the sun crosses the meridian of the observer.
Solar time is the time used in all of the sun-angle relationships; it does not coincide with local clock time. It is necessary to convert **standard time** to **solar time** by applying **two corrections**. First, there is a constant correction for the difference in longitude between the observer's meridian (longitude) and the meridian on which the local standard time is based. The sun takes 4 min to transverse 1° of longitude. The second correction is from the **equation of time**, which takes into account the perturbations in the earth's rate of rotation

which affect the time the sun crosses the observer's meridian. The difference in minutes between solar time and standard time is:

$$\text{Solar time} - \text{standard time} = 4(L_{st} - L_{loc}) + E \tag{1.5.2}$$

where L_{st} is the standard meridian for the local time zone, L_{loc} is the longitude of the location in question, and longitudes are in degrees west, that is, $0^\circ < L < 360^\circ$. The parameter E is the equation of time (in minutes) from Figure 1.5.1 or Equation 1.5.3[6] [from Spencer (1971), as cited by Iqbal (1983)]:

$$E = 229.2(0.000075 + 0.001868 \cos B - 0.032077 \sin B - 0.014615 \cos 2B - 0.04089 \sin 2B) \tag{1.5.3}$$

where B is found from Equation 1.4.2 and n is the day of the year. Thus $1 \leq n \leq 365$.

Example 1.5.1

At Madison, Wisconsin, what is the solar time corresponding to 10:30 AM central time on February 3?

Solution

In Madison, where the longitude is 89.4° and the standard meridian is 90°, Equation 1.5.2 gives

$$\text{Solar time} = \text{standard time} + 4(90 - 89.4) + E$$
$$= \text{standard time} + 2.4 + E$$

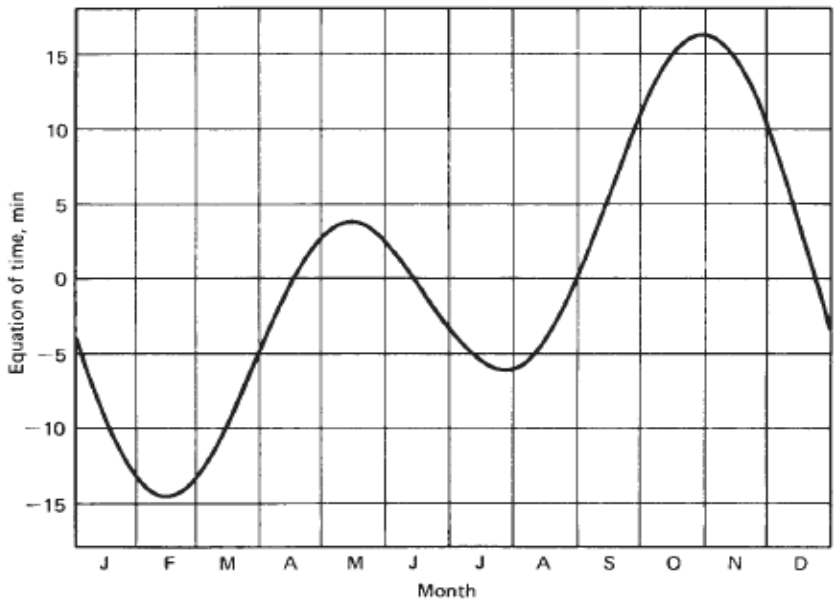

Figure 1.5.1 The equation of time E in minutes as a function of time of year.

On February 3, $n = 34$, and from Equation 1.5.3 or Figure 1.5.1, $E = -13.5$ min, so the correction to standard time is −11 min. Thus 10:30 AM Central Standard Time is 10:19 AM solar time. ■

DIRECTION OF BEAM RADIATION

The geometric relationships between a plane of any particular orientation relative to the earth at any time (whether that plane is fixed or moving relative to the earth) and the incoming beam solar radiation, that is, the position of the sun relative to that plane, can be described in terms of several angles. Some of the angles are indicated in Figure 1.6. The angles and a set of consistent sign conventions are as follows:

ϕ **Latitude**, the angular location north or south of the equator, north positive; $-90^\circ \leq \phi \leq 90^\circ$.

δ **Declination**, the angular position of the sun at solar noon (i.e., when the sun is on the local meridian) with respect to the plane of the equator, north positive; $-23.45^\circ \leq \delta \leq 23.45^\circ$.

β **Slope**, the angle between the plane of the surface in question and the horizontal; $0^\circ \leq \beta \leq 180^\circ$. ($\beta > 90^\circ$ means that the surface has a downward-facing component.)

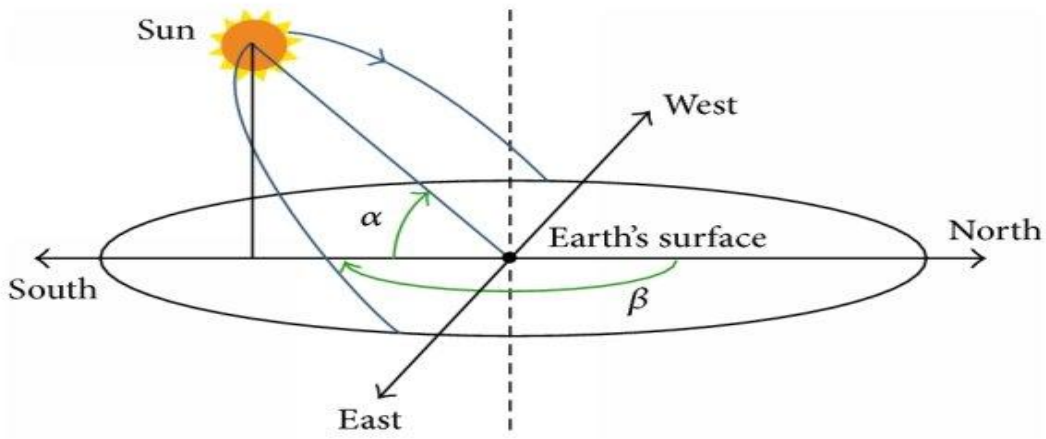

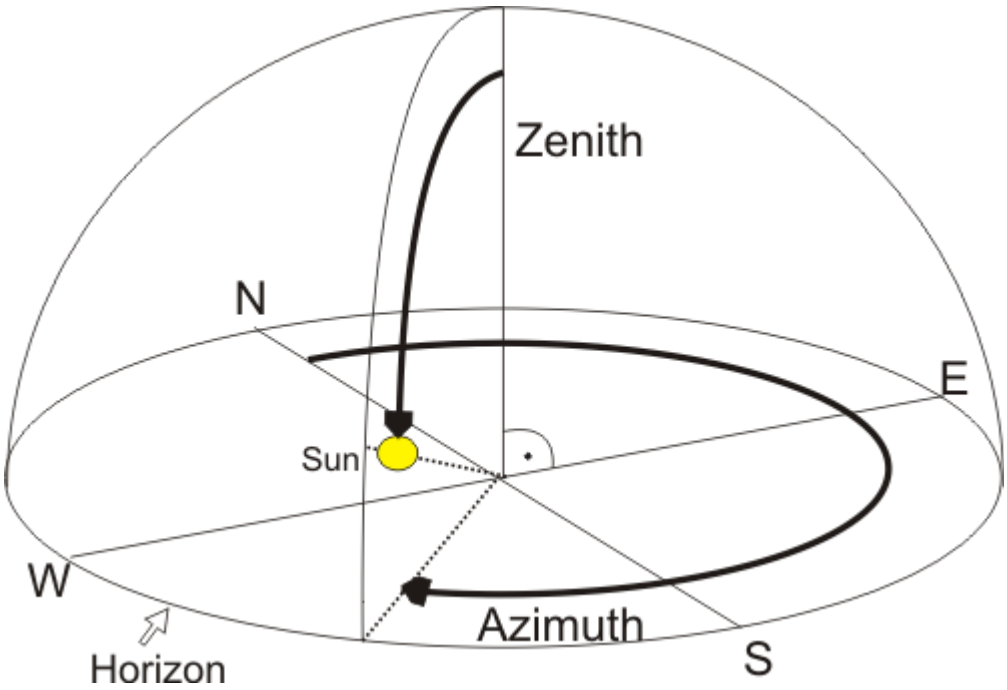

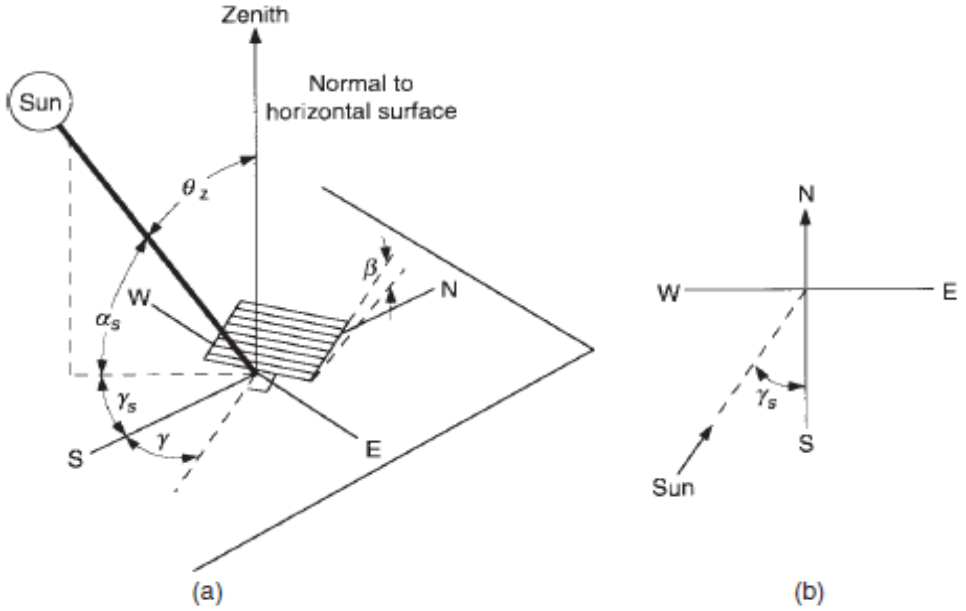

Figure 1.6.1 (a) Zenith angle, slope, surface azimuth angle, and solar azimuth angle for a tilted surface. (b) Plan view showing solar azimuth angle.

γ **Surface azimuth angle**, the deviation of the projection on a horizontal plane of the normal to the surface from the local meridian, with zero due south, east negative, and west positive; $-180^\circ \leq \gamma \leq 180^\circ$.

ω **Hour angle**, the angular displacement of the sun east or west of the local meridian due to rotation of the earth on its axis at 15° per hour; morning negative, afternoon positive.

θ **Angle of incidence**, the angle between the beam radiation on a surface and the normal to that surface.

Additional angles are defined that describe the position of the sun in the sky:

θ_z **Zenith angle**, the angle between the vertical and the line to the sun, that is, the angle of incidence of beam radiation on a horizontal surface.

α_s **Solar altitude angle**, the angle between the horizontal and the line to the sun, that is, the complement of the zenith angle.

γ_s **Solar azimuth angle**, the angular displacement from south of the projection of beam radiation on the horizontal plane, shown in Figure 1.6.1. Displacements east of south are negative and west of south are positive.

The declination δ can be found from the approximate equation of Cooper (1969),

$$\delta = 23.45 \sin\left(360 \frac{284 + n}{365}\right) \qquad (1.6.1a)$$

Hour angle=15 (solar time -12:00)

Table 1.6.1 Recommended Average Days for Months and Values of n by Months[a]

Month	n for ith Day of Month	For Average Day of Month		
		Date	n	δ
January	i	17	17	−20.9
February	$31 + i$	16	47	−13.0
March	$59 + i$	16	75	−2.4
April	$90 + i$	15	105	9.4
May	$120 + i$	15	135	18.8
June	$151 + i$	11	162	23.1
July	$181 + i$	17	198	21.2
August	$212 + i$	16	228	13.5
September	$243 + i$	15	258	2.2
October	$273 + i$	15	288	−9.6
November	$304 + i$	14	318	−18.9
December	$334 + i$	10	344	−23.0

[a]From Klein (1977). Do not use for $|\phi| > 66.5°$.

or from the more accurate equation (error $< 0.035°$) [from Spencer (1971), as cited by Iqbal (1983)]

$$\begin{aligned}\delta = (180/\pi)(&0.006918 - 0.399912\cos B + 0.070257\sin B \\ &- 0.006758\cos 2B + 0.000907\sin 2B \\ &- 0.002697\cos 3B + 0.00148\sin 3B)\end{aligned} \tag{1.6.1b}$$

where B is from Equation 1.4.2 and the day of the year n can be conveniently obtained with the help of Table 1.6.1.

There is a set of useful relationships among these angles. Equations relating the angle of incidence of beam radiation on a surface, θ, to the other angles are

$$\begin{aligned}\cos\theta = &\sin\delta\sin\phi\cos\beta - \sin\delta\cos\phi\sin\beta\cos\gamma \\ &+ \cos\delta\cos\phi\cos\beta\cos\omega + \cos\delta\sin\phi\sin\beta\cos\gamma\cos\omega \\ &+ \cos\delta\sin\beta\sin\gamma\sin\omega\end{aligned} \tag{1.6.2}$$

and

$$\cos\theta = \cos\theta_z\cos\beta + \sin\theta_z\sin\beta\cos(\gamma_s - \gamma) \tag{1.6.3}$$

The angle θ may exceed $90°$, which means that the sun is behind the surface. Also, when using Equation 1.6.2, it is necessary to ensure that the earth is not blocking the sun (i.e., that the hour angle is between sunrise and sunset).

Example 1.6.1

Calculate the angle of incidence of beam radiation on a surface located at Madison, Wisconsin, at 10:30 (solar time) on February 13 if the surface is tilted 45° from the horizontal and pointed 15° west of south.

Solution

Under these conditions, $n = 44$, the declination δ from Equation 1.6.1 is $-14°$, the hour angle $\omega = -22.5°$ (15° per hour times 1.5 h before noon), and the surface azimuth angle $\gamma = 15°$. Using a slope $\beta = 45°$ and the latitude ϕ of Madison of 43° N, Equation 1.6.2 is

$$\begin{aligned}\cos\theta &= \sin(-14)\sin 43\cos 45 - \sin(-14)\cos 43\sin 45\cos 15\\ &\quad + \cos(-14)\cos 43\cos 45\cos(-22.5)\\ &\quad + \cos(-14)\sin 43\sin 45\cos 15\cos(-22.5)\\ &\quad + \cos(-14)\sin 45\sin 15\sin(-22.5)\\ \cos\theta &= -0.117 + 0.121 + 0.464 + 0.418 - 0.068 = 0.817\\ \theta &= 35°\end{aligned}$$

■

There are several commonly occurring cases for which Equation 1.6.2 is simplified. For fixed surfaces sloped toward the south or north, that is, with a surface azimuth angle γ of 0° or 180° (a very common situation for fixed flat-plate collectors), the last term drops out.

For vertical surfaces, $\beta = 90°$ and the equation becomes

$$\cos\theta = -\sin\delta\cos\phi\cos\gamma + \cos\delta\sin\phi\cos\gamma\cos\omega + \cos\delta\sin\gamma\sin\omega \qquad (1.6.4)$$

For horizontal surfaces, the angle of incidence is the zenith angle of the sun, θ_z. Its value must be between 0° and 90° when the sun is above the horizon. For this situation, $\beta = 0$, and Equation 1.6.2 becomes

$$\cos\theta_z = \cos\phi\cos\delta\cos\omega + \sin\phi\sin\delta \qquad (1.6.5)$$

The solar azimuth angle γ_s can have values in the range of 180° to −180°. For north or south latitudes between 23.45° and 66.45°, γ_s will be between 90° and −90° for days less than 12 h long; for days with more than 12 h between sunrise and sunset, γ_s will be greater than 90° or less than −90° early and late in the day when the sun is north of the east-west line in the northern hemisphere or south of the east-west line in the southern hemisphere. For tropical latitudes, γ_s can have any value when $\delta - \phi$ is positive in the northern hemisphere or negative in the southern, for example, just before noon at $\phi = 10°$ and $\delta = 20°$, $\gamma_s = -180°$, and just after noon $\gamma_s = +180°$. Thus γ_s is negative when the hour angle is negative and positive when the hour angle is positive. The sign function in Equations 1.6.6 is equal to +1 if ω is positive and is equal to −1 if ω is negative:

$$\gamma_S = \text{sign}(\omega)\left|\cos^{-1}\left(\frac{\cos\theta_z\sin\phi - \sin\delta}{\sin\theta_z\cos\phi}\right)\right| \qquad (1.6.6)$$

Example 1.6.2

Calculate the zenith and solar azimuth angles for $\phi = 43^\circ$ at a 9:30 AM on February 13 and **b** 6:30 PM on July 1.

Solution

a On February 13 at 9:30, $\delta = -14^\circ$ and $\omega = -37.5^\circ$. From Equation 1.6.5,

$$\cos\theta_z = \cos 43 \cos(-14) \cos(-37.5) + \sin 43 \sin(-14) = 0.398$$

$$\theta_z = 66.5^\circ$$

From Equation 1.6.6

$$\gamma_s = -1 \left| \cos^{-1} \left(\frac{\cos 66.5 \sin 43 - \sin(-14)}{\sin 66.5 \cos 43} \right) \right| = -40.0^\circ$$

b On July 1 at 6:30 PM, $n = 182$, $\delta = 23.1^\circ$, and $\omega = 97.5^\circ$. From Equation 1.6.5,

$$\cos\theta_z = \cos 43 \cos 23.1 \cos 97.5 + \sin 43 \sin 23.1$$

$$\theta_z = 79.6^\circ$$

$$\gamma_s = +1 \left| \cos^{-1} \left(\frac{\cos 79.6 \sin 43 - \sin 23.1}{\sin 79.6 \cos 43} \right) \right| = 112.0^\circ$$

■

Useful relationships for the angle of incidence of surfaces sloped due north or due south can be derived from the fact that surfaces with slope β to the north or south have the same angular relationship to beam radiation as a horizontal surface at an artificial latitude of $\phi - \beta$. The relationship is shown in Figure 1.6.2 for the northern hemisphere. Modifying Equation 1.6.5 yields

$$\cos\theta = \cos(\phi - \beta) \cos\delta \cos\omega + \sin(\phi - \beta) \sin\delta \qquad (1.6.7a)$$

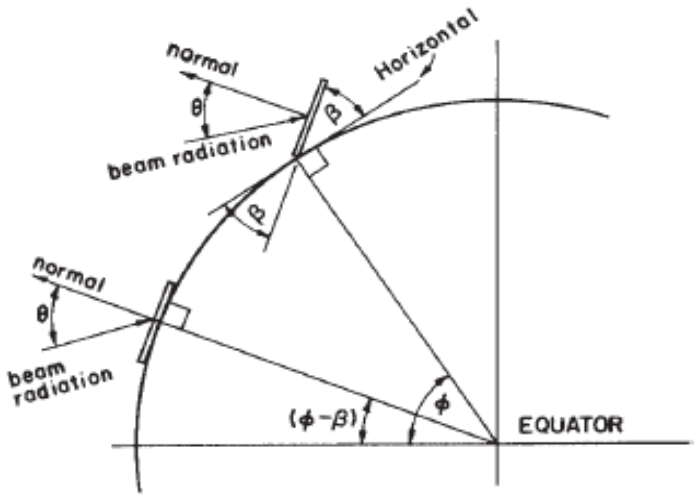

Figure 1.6.2 Section of earth showing β, θ, ϕ, and $\phi - \beta$ for a south-facing surface.

For the southern hemisphere modify the equation by replacing $\phi - \beta$ by $\phi + \beta$, consistent with the sign conventions on ϕ and δ:

$$\cos\theta = \cos(\phi + \beta)\cos\delta\cos\omega + \sin(\phi + \beta)\sin\delta \tag{1.6.7b}$$

For the special case of solar noon, for the south-facing sloped surface in the northern hemisphere,

$$\theta_{\text{noon}} = |\phi - \delta - \beta| \tag{1.6.8a}$$

and in the southern hemisphere

$$\theta_{\text{noon}} = |-\phi + \delta - \beta| \tag{1.6.8b}$$

where $\beta = 0$, the angle of incidence is the zenith angle, which for the northern hemisphere is

$$\theta_{z,\text{noon}} = |\phi - \delta| \tag{1.6.9a}$$

and for the southern hemisphere

$$\theta_{z,\text{noon}} = |-\phi + \delta| \tag{1.6.9b}$$

Equation 1.6.5 can be solved for the **sunset hour angle** ω_s, when $\theta_z = 90^\circ$:

$$\cos\omega_s = -\frac{\sin\phi\sin\delta}{\cos\phi\cos\delta} = -\tan\phi\tan\delta \tag{1.6.10}$$

The sunrise hour angle is the negative of the sunset hour angle. It also follows that the number of daylight hours is given by

$$N = \frac{2}{15}\cos^{-1}(-\tan\phi\tan\delta) \tag{1.6.11}$$

Figure 1.6.4. The plane *adef* includes the sun. Note that the solar altitude and profile angle are the same when the sun is in a plane perpendicular to the surface R (e.g., at solar noon for a surface with a surface azimuth angle of 0° or 180°). The profile angle is useful in calculating shading by overhangs and can be determined from

$$\tan\alpha_p = \frac{\tan\alpha_s}{\cos(\gamma_s - \gamma)} \tag{1.6.12}$$

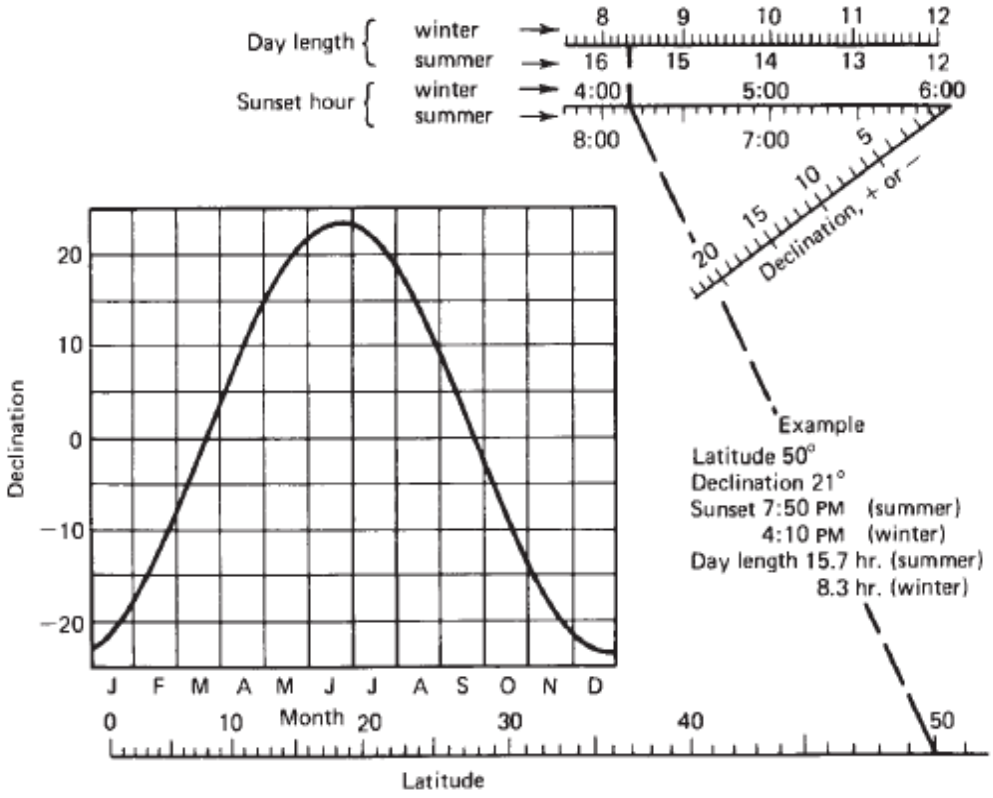

Figure 1.6.3 Nomogram to determine time of sunset and day length. Adapted from Whillier (1965).

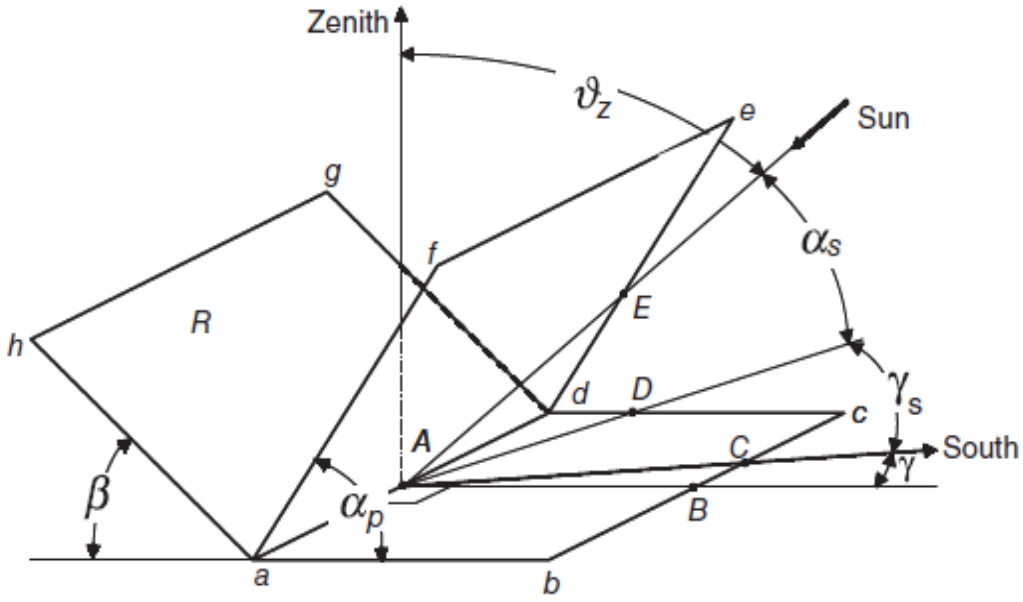

Figure 1.6.4 The solar altitude angle α_s ($\angle EAD$) and the profile angle α_p ($\angle fab$) for surface R.

Example 1.6.3

Calculate the time of sunrise, solar altitude, zenith, solar azimuth, and profile angles for a 60° sloped surface facing 25° west of south at 4:00 PM solar time on March 16 at a latitude of 43°. Also calculate the time of sunrise and sunset on the surface.

Solution

The hour angle at sunset is determined using Equation 1.6.10. For March 16, from Equation 1.6.1 (or Table 1.6.1), $\delta = -2.4°$:

$$\omega_s = \cos^{-1}[-\tan 43 \tan(-2.4)] = 87.8°$$

The sunrise hour angle is therefore −87.8°. With the earth's rotation of 15° per hour, sunrise (and sunset) occurs 5.85 h (5 h and 51 min) from noon so sunrise is at 6:09 AM (and sunset is at 5:51 PM).

The solar altitude angle α_s is a function only of time of day and declination. At 4:00 PM, $\omega = 60°$. From Equation 1.6.5, recognizing that $\cos\theta_z = \sin(90 - \theta_z) = \sin\alpha_s$,

$$\sin\alpha_s = \cos 43 \cos(-2.4) \cos 60 + \sin 43 \sin(-2.4) = 0.337$$
$$\alpha_s = 19.7° \quad \text{and} \quad \theta_z = 90 - \alpha_s = 70.3°$$

The solar azimuth angle for this time can be calculated with Equation 1.6.6:

$$\gamma_s = \text{sign}(60)\left[\cos^{-1}\left(\frac{\cos 70.3 \sin 43 - \sin(-2.4)}{\sin 70.3 \cos 43}\right)\right] = 66.8°$$

The profile angle for the surface with $\gamma = 25°$ is calculated with Equation 1.6.12:

$$\alpha_p = \tan^{-1}\left(\frac{\tan 19.7}{\cos(66.8 - 25)}\right) = 25.7°$$

The hour angles at which sunrise and sunset occur on the surface are calculated from Equation 1.6.2 with $\theta = 90°$ ($\cos\theta = 0$):

$$0 = \sin(-2.4) \sin 43 \cos 60 - \sin(-2.4) \cos 43 \sin 60 \cos 25$$
$$+ [\cos(-2.4) \cos 43 \cos 60 + \cos(-2.4) \sin 43 \sin 60 \cos 25] \cos\omega$$
$$+ [\cos(-2.4) \sin 60 \sin 25] \sin\omega$$

or

$$0 = 0.008499 + 0.9077 \cos\omega + 0.3657 \sin\omega$$

which, using $\sin^2\omega + \cos^2\omega = 1$, has two solutions: $\omega = -68.6°$ and $\omega = 112.4°$. Sunrise on the surface is therefore 68.6/15 = 4.57 h before noon, or 7:26 AM. The time of sunset on the collector is the actual sunset since 112.4° is greater than 87.8° (i.e., when $\theta = 90°$ the sun has already set). ■

RATIO OF BEAM RADIATION ON TILTED SURFACE TO THAT ON HORIZONTAL SURFACE

For purposes of solar process design and performance calculations, it is often necessary to calculate the hourly radiation on a tilted surface of a collector from measurements or estimates of solar radiation on a horizontal surface. The most commonly available data are total radiation for hours or days on the horizontal surface, whereas the need is for beam and diffuse radiation on the plane of a collector. The geometric factor *Rb*, the ratio of beam radiation on the tilted surface to that on a horizontal surface at any time, can be calculated exactly by appropriate:-

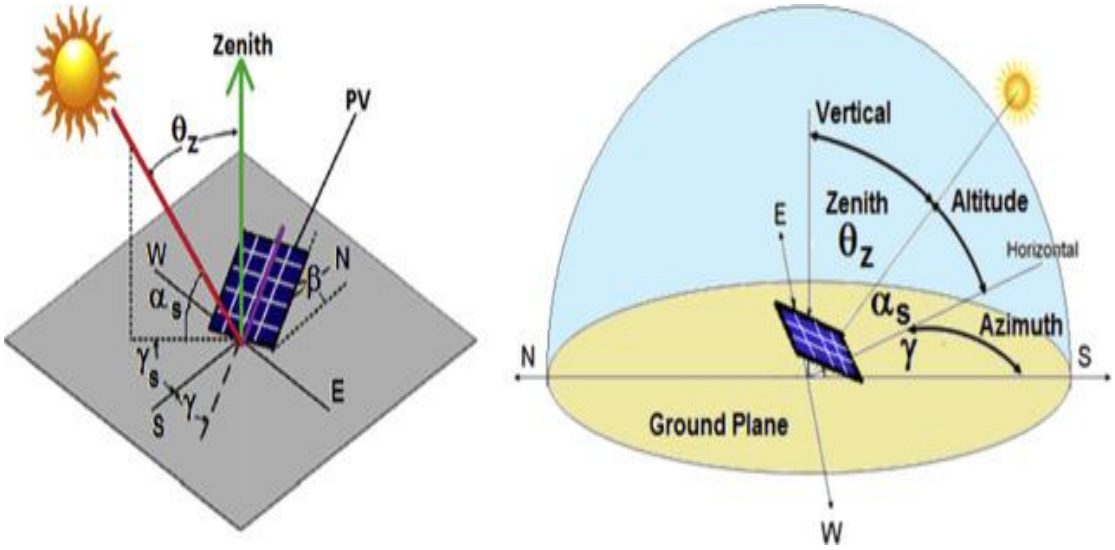

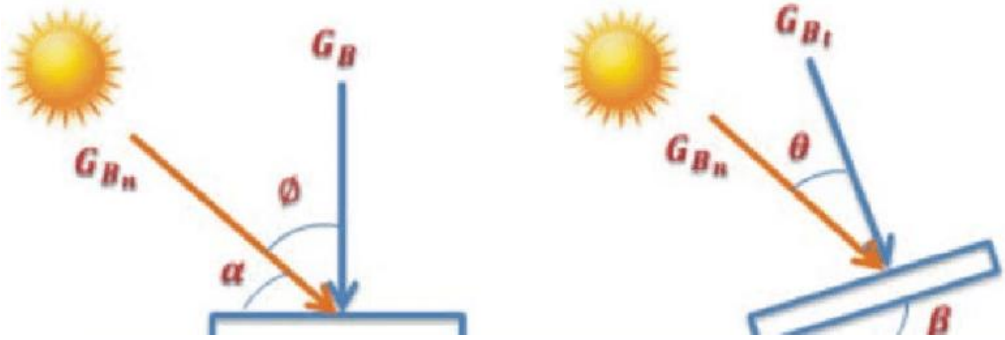

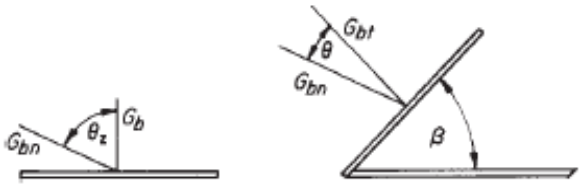

Figure 1.8.1 Beam radiation on horizontal and tilted surfaces.

Equation 1.6.2. Figure 1.8.1 indicates the angle of incidence of beam radiation on the horizontal and tilted surfaces. The ratio $G_{b,T}/G_b$ is given by[7]

$$R_b = \frac{G_{b,T}}{G_b} = \frac{G_{b,n}\cos\theta}{G_{b,n}\cos\theta_z} = \frac{\cos\theta}{\cos\theta_z} \tag{1.8.1}$$

and $\cos\theta$ and $\cos\theta_z$ are both determined from Equation 1.6.2 (or from equations derived from Equation 1.6.2).

Example 1.8.1

What is the ratio of beam radiation to that on a horizontal surface for the surface and time specified in Example 1.6.1?

Solution

Example 1.6.1 shows the calculation for $\cos\theta$. For the horizontal surface, from Equation 1.6.5,

$$\cos\theta_z = \sin(-14)\sin 43 + \cos(-14)\cos 43\cos(-22.5) = 0.491$$

And from Equation 1.8.1

$$R_b = \frac{\cos\theta}{\cos\theta_z} = \frac{0.818}{0.491} = 1.67$$

■

The optimum azimuth angle for flat-plate cssollectors is usually 0° in the northern hemisphere (or 180° in the southern hemisphere). Thus it is a common situation that $\gamma = 0°$ (or 180°). In this case, Equations 1.6.5 and 1.6.7 can be used to determine $\cos\theta_z$ and $\cos\theta$, respectively, leading in the northern hemisphere, for $\gamma = 0°$, to

$$R_b = \frac{\cos(\phi-\beta)\cos\delta\cos\omega + \sin(\phi-\beta)\sin\delta}{\cos\phi\cos\delta\cos\omega + \sin\phi\sin\delta} \tag{1.8.2}$$

In the southern hemisphere, $\gamma = 180°$ and the equation is

$$R_b = \frac{\cos(\phi+\beta)\cos\delta\cos\omega + \sin(\phi+\beta)\sin\delta}{\cos\phi\cos\delta\cos\omega + \sin\phi\sin\delta} \tag{1.8.3}$$

Example 1.8.2

Calculate R_b for a surface at latitude 40° N at a tilt 30° toward the south for the hour 9 to 10 solar time on February 16.

Solution

Use Figure 1.8.2(c) for the hour ±2.5 h from noon as representative of the hour from 9 to 10. To find cos θ_z, enter at a latitude of 40° for the north latitude date of February 16. Here cos $\theta_z = 0.45$. To find cos θ, enter at a latitude of $\phi - \beta = 10°$ for the same date. Here cos $\theta = 0.73$. Then

$$R_b = \frac{\cos\theta}{\cos\theta_z} = \frac{0.73}{0.45} = 1.62$$

The ratio can also be calculated using Equation 1.8.2. The declination on February 16 is −13°:

$$R_b = \frac{\cos 10\cos(-13)\cos(-37.5) + \sin 10\sin(-13)}{\cos 40\cos(-13)\cos(-37.5) + \sin 40\sin(-13)} = \frac{0.722}{0.448} = 1.61$$ ■

Example 1.8.3

Calculate R_b for a latitude 40° N at a tilt of 50° toward the south for the hour 9 to 10 solar time on February 16.

Solution

As found in the previous example, cos $\theta_z = 0.45$. To find cos θ, enter at an abscissa of +10°, using the curve for February 16 for south latitudes. The value of cos θ from the curve is 0.80. Thus $R_b = 0.80/0.45 = 1.78$. Equation 1.8.2 can also be used:

$$R_b = \frac{\cos 10\cos(-13)\cos(-37.5) + \sin(-10)\sin(-13)}{\cos 40\cos(-13)\cos(-37.5) + \sin 40\sin(-13)} = \frac{0.800}{0.448} = 1.79$$ ■

EXTRATERRESTRIAL RADIATION ON A HORIZONTAL SURFACE

Several types of radiation calculations are most conveniently done using normalized radiation levels, that is, the ratio of radiation level to the theoretically possible radiation that would be available if there were no atmosphere. For these calculations, we need a method of calculating the extraterrestrial radiation. At any point in time, the solar radiation incident on a horizontal plane outside of the atmosphere is the normal incident solar radiation as given by:

$$G_o = G_{sc}\left(1 + 0.033\cos\frac{360n}{365}\right)\cos\theta_z \tag{1.10.1}$$

where G_{sc} is the solar constant and n is the day of the year. Combining Equation 1.6.5 for $\cos\theta_z$ with Equation 1.10.1 gives G_o for a horizontal surface at any time between sunrise and sunset:

$$G_o = G_{sc}\left(1 + 0.033\cos\frac{360n}{365}\right)(\cos\phi\cos\delta\cos\omega + \sin\phi\sin\delta) \tag{1.10.2}$$

It is often necessary for calculation of daily solar radiation to have the integrated daily extraterrestrial radiation on a horizontal surface, H_o. This is obtained by integrating Equation 1.10.2 over the period from sunrise to sunset. If G_{sc} is in watts per square meter, H_o in daily joules per square meter per day is

$$H_o = \frac{24 \times 3600 G_{sc}}{\pi}\left(1 + 0.033\cos\frac{360n}{365}\right) \times \left(\cos\phi\cos\delta\sin\omega_s + \frac{\pi\omega_s}{180}\sin\phi\sin\delta\right) \tag{1.10.3}$$

where ω_s is the sunset hour angle, in degrees, from Equation 1.6.10.

The monthly mean[11] daily extraterrestrial radiation $\overline{H}_o$ is a useful quantity. For latitudes in the range +60 to −60 it can be calculated with Equation 1.10.3 using n and δ for the mean day of the month[12] from Table 1.6.1. Mean radiation H_o is plotted as a function of latitude for the northern and southern hemispheres in Figure 1.10.1. The curves are for dates that give the mean radiation for the month and thus show $\overline{H}_o$. Values of H_o

Example 1.10.1

What is H_o, the day's solar radiation on a horizontal surface in the absence of the atmosphere, at latitude 43° N on April 15?

Table 1.10.1 Monthly Average Daily Extraterrestrial Radiation, MJ/m^2

ϕ	Jan	Feb	Mar	Apr	May	Jun	Jul	Aug	Sep	Oct	Nov	Dec
90	0.0	0.0	1.2	19.3	37.2	44.8	41.2	26.5	5.4	0.0	0.0	0.0
85	0.0	0.0	2.2	19.2	37.0	44.7	41.0	26.4	6.4	0.0	0.0	0.0
80	0.0	0.0	4.7	19.6	36.6	44.2	40.5	26.1	9.0	0.6	0.0	0.0
75	0.0	0.7	7.8	21.0	35.9	43.3	39.8	26.3	11.9	2.2	0.0	0.0
70	0.1	2.7	10.9	23.1	35.3	42.1	38.7	27.5	14.8	4.9	0.3	0.0
65	1.2	5.4	13.9	25.4	35.7	41.0	38.3	29.2	17.7	7.8	2.0	0.4
60	3.5	8.3	16.9	27.6	36.6	41.0	38.8	30.9	20.5	10.8	4.5	2.3
55	6.2	11.3	19.8	29.6	37.6	41.3	39.4	32.6	23.1	13.8	7.3	4.8
50	9.1	14.4	22.5	31.5	38.5	41.5	40.0	34.1	25.5	16.7	10.3	7.7
45	12.2	17.4	25.1	33.2	39.2	41.7	40.4	35.3	27.8	19.6	13.3	10.7
40	15.3	20.3	27.4	34.6	39.7	41.7	40.6	36.4	29.8	22.4	16.4	13.7
35	18.3	23.1	29.6	35.8	40.0	41.5	40.6	37.3	31.7	25.0	19.3	16.8
30	21.3	25.7	31.5	36.8	40.0	41.1	40.4	37.8	33.2	27.4	22.2	19.9
25	24.2	28.2	33.2	37.5	39.8	40.4	40.0	38.2	34.6	29.6	25.0	22.9
20	27.0	30.5	34.7	37.9	39.3	39.5	39.3	38.2	35.6	31.6	27.7	25.8
15	29.6	32.6	35.9	38.0	38.5	38.4	38.3	38.0	36.4	33.4	30.1	28.5
10	32.0	34.4	36.8	37.9	37.5	37.0	37.1	37.5	37.0	35.0	32.4	31.1
5	34.2	36.0	37.5	37.4	36.3	35.3	35.6	36.7	37.2	36.3	34.5	33.5
0	36.2	37.4	37.8	36.7	34.8	33.5	34.0	35.7	37.2	37.3	36.3	35.7
−5	38.0	38.5	37.9	35.8	33.0	31.4	32.1	34.4	36.9	38.0	37.9	37.6
−10	39.5	39.3	37.7	34.5	31.1	29.2	29.9	32.9	36.3	38.5	39.3	39.4
−15	40.8	39.8	37.2	33.0	28.9	26.8	27.6	31.1	35.4	38.7	40.4	40.9
−20	41.8	40.0	36.4	31.3	26.6	24.2	25.2	29.1	34.3	38.6	41.2	42.1
−25	42.5	40.0	35.4	29.3	24.1	21.5	22.6	27.0	32.9	38.2	41.7	43.1
−30	43.0	39.7	34.0	27.2	21.4	18.7	19.9	24.6	31.2	37.6	42.0	43.8
−35	43.2	39.1	32.5	24.8	18.6	15.8	17.0	22.1	29.3	36.6	42.0	44.2
−40	43.1	38.2	30.6	22.3	15.8	12.9	14.2	19.4	27.2	35.5	41.7	44.5
−45	42.8	37.1	28.6	19.6	12.9	10.0	11.3	16.6	24.9	34.0	41.2	44.5
−50	42.3	35.7	26.3	16.8	10.0	7.2	8.4	13.8	22.4	32.4	40.5	44.3
−55	41.7	34.1	23.9	13.9	7.2	4.5	5.7	10.9	19.8	30.5	39.6	44.0
−60	41.0	32.4	21.2	10.9	4.5	2.2	3.1	8.0	17.0	28.4	38.7	43.7
−65	40.5	30.6	18.5	7.9	2.1	0.3	1.0	5.2	14.1	26.2	37.8	43.7
−70	40.8	28.8	15.6	5.0	0.4	0.0	0.0	2.6	11.1	24.0	37.4	44.9
−75	41.9	27.6	12.6	2.4	0.0	0.0	0.0	0.8	8.0	21.9	38.1	46.2
−80	42.7	27.4	9.7	0.6	0.0	0.0	0.0	0.0	5.0	20.6	38.8	47.1
−85	43.2	27.7	7.2	0.0	0.0	0.0	0.0	0.0	2.4	20.3	39.3	47.6
−90	43.3	27.8	6.2	0.0	0.0	0.0	0.0	0.0	1.4	20.4	39.4	47.8

Solution

For these circumstances, $n = 105$ (from Table 1.6.1), $\delta = 9.4^\circ$ (from Equation 1.6.1), and $\phi = 43^\circ$. From Equation 1.6.10

$$\cos \omega_s = -\tan 43 \tan 9.4 \text{ and } \omega_s = 98.9^\circ$$

Then from Equation 1.10.3, with $G_{sc} = 1367 \text{ W/m}^2$,

$$H_o = \frac{24 \times 3600 \times 1367}{\pi}\left(1 + 0.033 \cos \frac{360 \times 105}{365}\right)$$
$$\times \left(\cos 43 \cos 9.4 \sin 98.9 + \frac{\pi \times 98.9}{180} \sin 43 \sin 9.4\right)$$
$$= 33.8 \text{ MJ/m}^2$$

From Figure 1.10.1(a), for the curve for April, we read $H_o = 34.0 \text{ MJ/m}^2$, and from Table 1.10.1 we obtain $H_o = 33.8 \text{ MJ/m}^2$ by interpolation. ■

It is also of interest to calculate the extraterrestrial radiation on a horizontal surface for an hour period. Integrating Equation 1.10.2 for a period between hour angles ω_1 and ω_2 which define an hour (where ω_2 is the larger),

$$I_o = \frac{12 \times 3600}{\pi} G_{sc}\left(1 + 0.033 \cos \frac{360n}{365}\right)$$
$$\times \left[\cos \phi \cos \delta \left(\sin \omega_2 - \sin \omega_1\right) + \frac{\pi(\omega_2 - \omega_1)}{180} \sin \phi \sin \delta\right] \qquad (1.10.4)$$

(The limits ω_1 and ω_2 may define a time other than an hour.)

Example 1.10.2

What is the solar radiation on a horizontal surface in the absence of the atmosphere at latitude 43° N on April 15 between the hours of 10 and 11?

Solution

The declination is 9.4° (from the previous example). For April 15, $n = 105$. Using Equation 1.10.4 with $\omega_1 = -30^\circ$ and $\omega_2 = -15^\circ$,

$$I_o = \frac{12 \times 3600 \times 1367}{\pi}\left(1 + 0.033 \cos \frac{360 \times 105}{365}\right)$$
$$\times \left(\cos 43 \cos 9.4 [\sin(-15) - \sin(-30)] + \frac{\pi[-15 - (-30)]}{180} \sin 43 \sin 9.4\right)$$
$$= 3.79 \text{ MJ/m}^2$$ ■

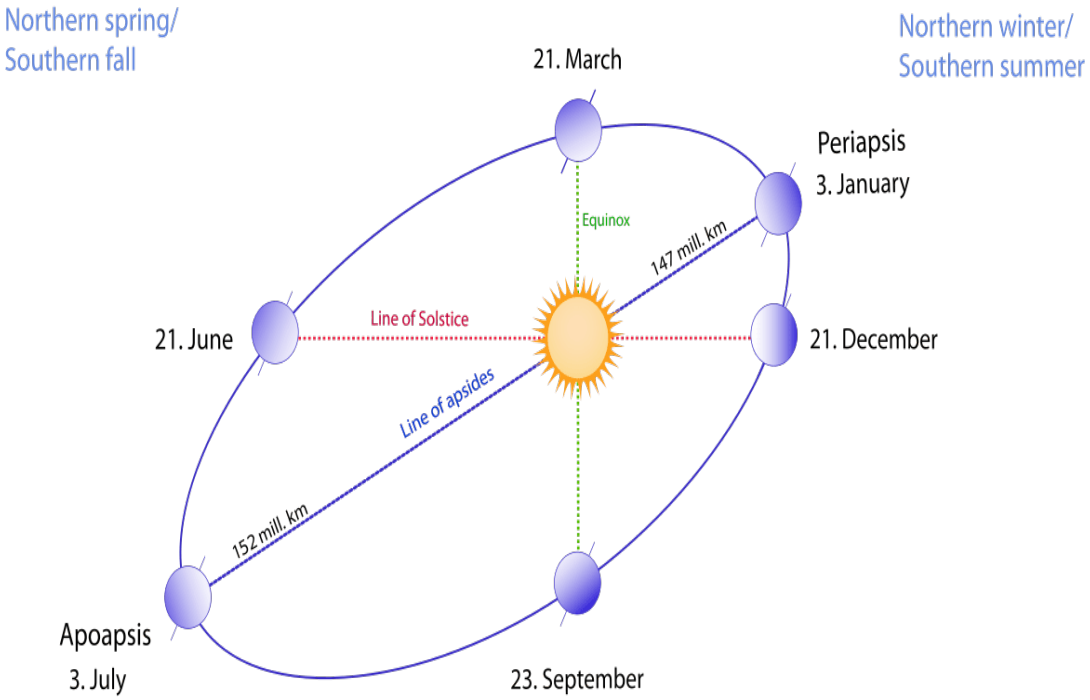
Northern spring/
Southern fall
21. March
Northern winter/
Southern summer
Periapsis
3. January
Equinox
147 mill. km
Line of Solstice
21. June
21. December
Line of apsides
152 mill. km
Apoapsis
3. July
23. September
Northern summer/
Southern winter
Northern fall/
Southern spring

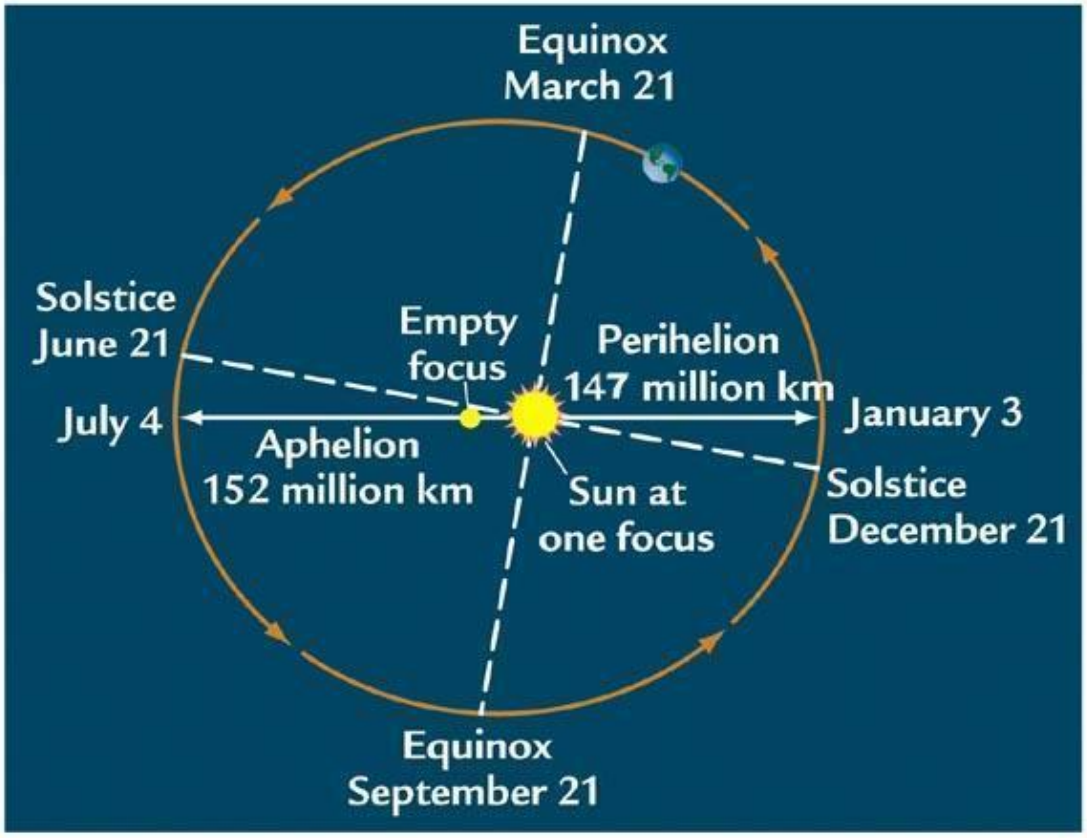
Equinox
March 21
Solstice
June 21
Empty
focus
Perihelion
147 million km
July 4
January 3
Aphelion
152 million km
Sun at
one focus
Solstice
December 21
Equinox
September 21

Chapter Two

Available of Solar Radiation

Solar radiation data are used in several forms and for a variety of purposes. The most detailed information available is beam and diffuse solar radiation on a horizontal surface, by hours, which is useful in simulations of solar processes. (A few measurements are available on inclined surfaces and for shorter time intervals.) Daily data are often available and hourly radiation can be estimated from daily data. Monthly total solar radiation on a horizontal surface can be used in some process design methods. However, as process performance is generally not linear with solar radiation, the use of averages may lead to serious errors if nonlinearities are not taken into account. It is also possible to reduce radiation data to more manageable forms by statistical methods.

Instruments for measuring solar radiation are of two basic types:

A **pyrheliometer** is an instrument using a collimated detector for measuring solar radiation from the sun and from a small portion of the sky around the sun (i.e., beam radiation) at normal incidence.

A **pyranometer** is an instrument for measuring total hemispherical solar (beam plus diffuse) radiation, usually on a horizontal surface. If shaded from the beam radiation by a shade ring or disc, a pyranometer measures diffuse radiation.

Solar Radiation Data:

Solar radiation data are available in several forms. The following information about radiation data is important in their understanding and use: whether they are instantaneous measurements (irradiance) or values integrated over some period of time (irradiation) (usually hour or day); the time or time period of the measurements; whether the measurements are of beam, diffuse, or total radiation; the instruments used; the receiving surface orientation (usually horizontal, sometimes inclined at a fixed slope, or normal to the beam radiation); and, if averaged, the period over which they are averaged (e.g., monthly averages of daily radiation).

Most radiation data available are for horizontal surfaces, include both direct and diffuse radiation, and were measured with thermopile pyranometers (or in some cases Robitzsch-type instruments). Most of these instruments provide radiation records as a function of time and do not themselves provide a means of integrating the records. The data were usually recorded in a form similar to that shown in Figure 2.5.1 by recording potentiometers and were integrated graphically. Uncertainties in integration add to uncertainties in pyranometer response; electronic integration is now common.

Two types of solar radiation data are widely available. The first is monthly average daily total radiation on a horizontal surface, $\overline{H}$. The second is hourly total radiation on a horizontal surface, I, for each hour for extended periods such as one or more years. The $\overline{H}$ data are widely available and are given for many stations in Appendix D. The

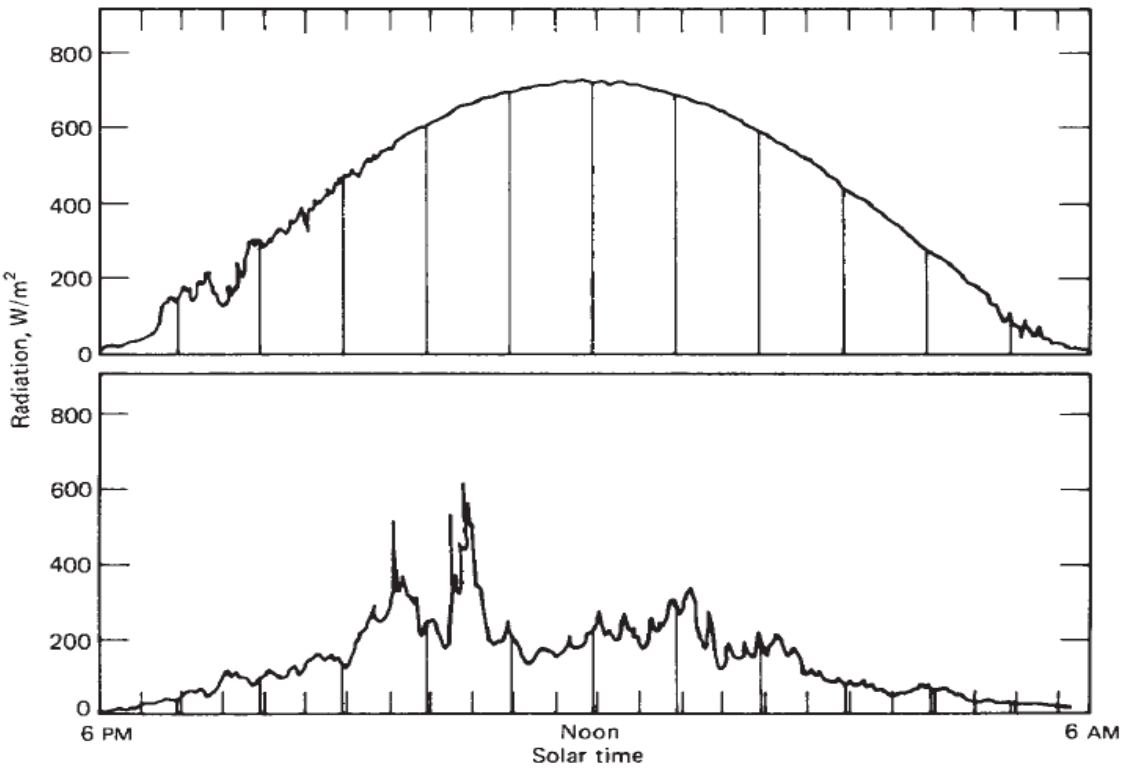

Figure 2.5.1 Total (beam and diffuse) solar radiation on a horizontal surface versus time for clear and largely cloudy day, latitude 43°, for days near equinox.

Atmospheric Attenuation for Solar Radiation:

Solar radiation at normal incidence received at the surface of the earth is subject to variations due to change in the extraterrestrial radiation as noted in Chapter 1 and to two additional and more significant phenomena: (1) atmospheric scattering by air molecules, water, and dust and (2) atmospheric absorption by O_3, H_2O, and CO_2. Iqbal (1983) reviews these matters in considerable detail.

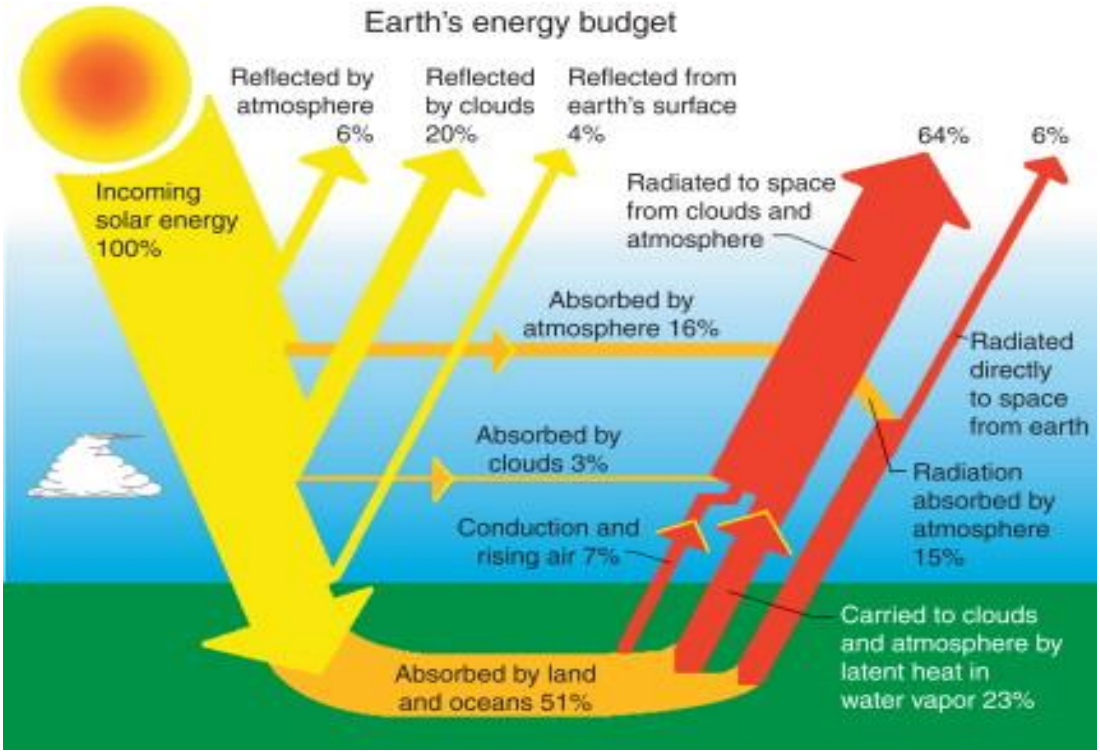
Earth's energy budget
Reflected by atmosphere 6%
Reflected by clouds 20%
Reflected from earth's surface 4%
64%
6%
Incoming solar energy 100%
Radiated to space from clouds and atmosphere
Absorbed by atmosphere 16%
Radiated directly to space from earth
Absorbed by clouds 3%
Radiation absorbed by atmosphere 15%
Conduction and rising air 7%
Carried to clouds and atmosphere by latent heat in water vapor 23%
Absorbed by land and oceans 51%

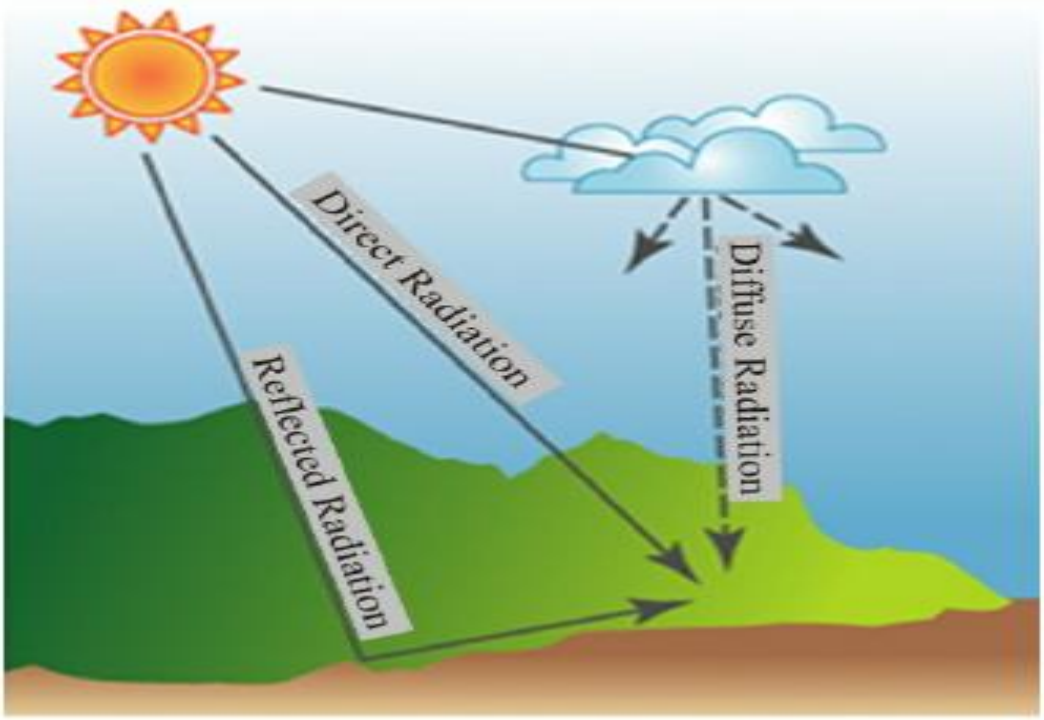
Direct Radiation
Diffuse Radiation
Reflected Radiation

Estimation of Average Solar Radiation:

The original Ångström-type regression equation related monthly average daily radiation to clear-day radiation at the location in question and average fraction of possible sunshine hours:

$$\frac{\overline{H}}{\overline{H}_c} = a' + b' \frac{\overline{n}}{\overline{N}} \tag{2.7.1}$$

Table 2.7.1 Examples of Monthly Average Hours per Day of Sunshine by Latitude and Altitude

Location Latitude Altitude, m	Hong Kong, 22° N, Sea Level	Paris, France, 48° N, 50 m	Bombay, India, 19° N, Sea Level	Sokoto, Nigeria, 13° N, 107 m	Perth, Australia, 32° S, 20 m	Madison, Wisconsin, 43° N, 270 m
January	4.7	2.1	9.0	9.9	10.4	4.5
February	3.5	2.8	9.3	9.6	9.8	5.7
March	3.1	4.9	9.0	8.8	8.8	6.9
April	3.8	7.4	9.1	8.9	7.5	7.5
May	5.0	7.1	9.3	8.4	5.7	9.1
June	5.3	7.6	5.0	9.5	4.8	10.1
July	6.7	8.0	3.1	7.0	5.4	9.8
August	6.4	6.8	2.5	6.0	6.0	10.0
September	6.6	5.6	5.4	7.9	7.2	8.6
October	6.8	4.5	7.7	9.6	8.1	7.2
November	6.4	2.3	9.7	10.0	9.6	4.2
December	5.6	1.6	9.6	9.8	10.4	3.9
Annual	5.3	5.1	7.4	8.8	7.8	7.3

where $\overline{H}$ = monthly average daily radiation on horizontal surface
$\overline{H}_c$ = average clear-sky daily radiation for location and month in question
a', b' = empirical constants
$\overline{n}$ = monthly average daily hours of bright sunshine
$\overline{N}$ = monthly average of maximum possible daily hours of bright sunshine (i.e., day length of average day of month)

A basic difficulty with Equation 2.7.1 lies in the ambiguity of the terms $\overline{n}/\overline{N}$ and $\overline{H}_c$. The former is an instrumental problem (records from sunshine recorders are open to interpretation). The latter stems from uncertainty in the definition of a clear day. Page (1964) and others have modified the method to base it on extraterrestrial radiation on a horizontal surface rather than on clear-day radiation:

$$\frac{\overline{H}}{\overline{H}_o} = a + b\,\frac{\overline{n}}{\overline{N}} \tag{2.7.2}$$

where $\overline{H}_o$ is the extraterrestrial radiation for the location averaged over the time period in question and a and b are constants depending on location. The ratio $\overline{H}/\overline{H}_o$ is termed the monthly average clearness index and will be used frequently in later sections and chapters.

Values of $\overline{H}_o$ can be calculated from Equation 1.10.3 using day numbers from Table 1.6.1 for the mean days of the month or it can be obtained from either Table 1.10.1 or Figure 1.10.1. The average day length $\overline{N}$ can be calculated from Equation 1.6.11 or it can be obtained from Figure 1.6.3 for the mean day of the month as indicated in Table 1.6.1. Löf et al. (1966a) developed sets of constants a and b for various climate types and locations based on radiation data then available. These are given in Table 2.7.2.

Example 2.7.1

Estimate the monthly averages of total solar radiation on a horizontal surface for Madison, Wisconsin, latitude 43°, based on the average duration of sunshine hour data of Table 2.7.1.

Solution

The estimates are based on Equation 2.7.2 using constants $a = 0.30$ and $b = 0.34$ from Table 2.7.2. Values of $\overline{H}_o$ are obtained from either Table or Figure 1.10.1 and day lengths from Equation 1.6.11, each for the mean days of the month. The desired estimates are obtained in the following table, which shows daily $\overline{H}$ in MJ/m^2. (For comparison, TMY3 data for Madison are shown, and in the last column estimates of Madison radiation determined by using constants a and b for Blue Hill.)

Month	$\overline{H}_o$ (MJ/m^2)	$\overline{N}$ (h)	$\overline{n}/\overline{N}$	Estimated $\overline{H}$ (MJ/m^2)	Measured $\overline{H}^a$ (MJ/m^2)	Estimated $\overline{H}^b$ (MJ/m^2)
January	13.36	9.2	0.49	6.3	6.9	6.2
February	18.80	10.3	0.55	9.2	9.7	9.3
March	26.01	11.7	0.59	13.0	13.1	13.4
April	33.75	13.2	0.57	16.6	16.9	17.0
May	39.39	14.5	0.63	20.2	21.0	21.0
June	41.74	15.2	0.67	22.0	23.4	23.1
July	40.52	14.0	0.66	21.2	22.2	22.2
August	35.88	13.8	0.73	19.6	19.6	20.9
September	28.77	12.3	0.70	15.5	14.5	16.4
October	20.89	19.8	0.67	11.0	9.7	11.6
November	14.61	9.5	0.44	6.6	6.2	6.4
December	11.90	8.8	0.44	5.4	5.6	5.3

[a] From TMY3 data.
[b] Using constants for Blue Hill.

Estimation of Daily Clear Sky Solar Radiation:

The effects of the atmosphere in scattering and absorbing radiation are variable with time as atmospheric conditions and air mass change. It is useful to define a standard ''clear'' sky and calculate the hourly and daily radiation which would be received on a horizontal surface under these standard conditions.

Hottel (1976) has presented a method for estimating the beam radiation transmitted through clear atmospheres which takes into account zenith angle and altitude for a standard atmosphere and for four climate types. The atmospheric transmittance for beam radiation τ_b is G_{bn}/G_{on} (or G_{bT}/G_{oT}) and is given in the form

$$\tau_b = a_0 + a_1 \exp\left(\frac{-k}{\cos\theta_z}\right) \tag{2.8.1a}$$

The constants a_0, a_1, and k for the standard atmosphere with 23 km visibility are found from a_0^*, a_1^*, and k^*, which are given for altitudes less than 2.5 km by

$$a_0^* = 0.4237 - 0.00821(6 - A)^2 \tag{2.8.1b}$$

$$a_1^* = 0.5055 + 0.00595(6.5 - A)^2 \tag{2.8.1c}$$

$$k^* = 0.2711 + 0.01858(2.5 - A)^2 \tag{2.8.1d}$$

where A is the altitude of the observer in kilometers. (Hottel also gives equations for a_0^*, a_1^*, and k^* for a standard atmosphere with 5 km visibility.)

Correction factors are applied to a_0^*, a_1^*, and k^* to allow for changes in climate types. The correction factors $r_0 = a_0/a_0^*$, $r_1 = a_1/a_1^*$, and $r_k = k/k^*$ are given in Table 2.8.1. Thus, the transmittance of this standard atmosphere for beam radiation can be determined for any zenith angle and any altitude up to 2.5 km. The clear-sky beam normal radiation is then

$$G_{cnb} = G_{on}\tau_b \tag{2.8.2}$$

where G_{on} is obtained from Equation 1.4.1. The clear-sky horizontal beam radiation is

$$G_{cb} = G_{on}\tau_b \cos\theta_z \tag{2.8.3}$$

For periods of an hour, the clear-sky horizontal beam radiation is

$$I_{cb} = I_{on}\tau_b \cos\theta_z \tag{2.8.4}$$

Table 2.8.1 Correction Factors for Climate Types[a]

Climate Type	r_0	r_1	r_k
Tropical	0.95	0.98	1.02
Midlatitude summer	0.97	0.99	1.02
Subarctic summer	0.99	0.99	1.01
Midlatitude winter	1.03	1.01	1.00

Example 2.8.1

Calculate the transmittance for beam radiation of the standard clear atmosphere at Madison (altitude 270 m) on August 22 at 11:30 AM solar time. Estimate the intensity of beam radiation at that time and its component on a horizontal surface.

Solution

On August 22, $n = 234$, the declination is 11.4°, and from Equation 1.6.5 the cosine of the zenith angle is 0.846.

The next step is to find the coefficients for Equation 2.8.1. First, the values for the standard atmosphere are obtained from Equations 2.8.1b to 2.8.1d for an altitude of 0.27 km:

$$a_0^* = 0.4237 - 0.00821(6 - 0.27)^2 = 0.154$$

$$a_1^* = 0.5055 + 0.00595(6.5 - 0.27)^2 = 0.736$$

$$k^* = 0.2711 + 0.01858(2.5 - 0.27)^2 = 0.363$$

The climate-type correction factors are obtained from Table 2.8.1 for midlatitude summer. Equation 2.8.1a becomes

$$\tau_b = 0.154 \times 0.97 + 0.736 \times 0.99 \exp\left(-0.363 \times \frac{1.02}{0.846}\right) = 0.62$$

The extraterrestrial radiation is 1339 W/m^2 from Equation 1.4.1. The beam radiation is then

$$G_{cnb} = 1339 \times 0.62 = 830 \text{ W/m}^2$$

The component on a horizontal plane is

$$G_{cb} = 830 \times 0.846 = 702 \text{ W/m}^2$$

It is also necessary to estimate the clear-sky diffuse radiation on a horizontal surface to get the total radiation. Liu and Jordan (1960) developed an empirical relationship between the transmission coefficients for beam and diffuse radiation for clear days:

$$\tau_d = \frac{G_d}{G_o} = 0.271 - 0.294\tau_b \tag{2.8.5}$$

where τ_d is G_d/G_o (or I_d/I_o), the ratio of diffuse radiation to the extraterrestrial (beam) radiation on the horizontal plane. The equation is based on data for three stations. The data used by Liu and Jordan predated that used by Hottel (1976) and may not be entirely consistent with it; until better information becomes available, it is suggested that Equation 2.8.5 be used to estimate diffuse clear-sky radiation, which can be added to the beam radiation predicted by Hottel's method to obtain a clear hour's total. These

Example 2.8.2

Estimate the standard clear-day radiation on a horizontal surface for Madison on August 22.

Solution

For each hour, based on the midpoints of the hour, the transmittances of the atmosphere for beam and diffuse radiation are estimated. The calculation of τ_b is illustrated for the hour 11 to 12 (i.e., at 11:30) in Example 2.8.1, and the beam radiation for a horizontal surface for the hour is 2.53 MJ/m^2 (702 W/m^2 for the hour).

The calculation of τ_d is based on Equation 2.8.5:

$$\tau_d = 0.271 - 0.294(0.62) = 0.089$$

Next G_{on}, calculated by Equation 1.4.1, is 1339 W/m^2. Then G_o is $G_{on}\ \cos\theta_z$ so that

$$G_{cd} = 1339 \times 0.846 \times 0.089 = 101 \text{ W/m}^2$$

Then the diffuse radiation for the hour is 0.36 MJ/m^2. The total radiation on a horizontal plane for the hour is 2.53 + 0.36 = 2.89 MJ/m^2. These calculations are repeated for each hour of the day. The result is shown in the tabulation, where energy quantities are in megajoules per square meter. The beam for the day H_{cb} is twice the sum of column 4, giving 19.0 MJ/m^2. The day's total radiation H_c is twice the sum of column 7, or 22.8 MJ/m^2.

		I_{cb}				
Hours	τ_b	Normal	Horizontal	τ_d	I_{cd}	I_c
11–12, 12–1	0.620	2.99	2.52	0.089	0.36	2.89
10–11, 1–2	0.607	2.93	2.33	0.092	0.35	2.69
9–10, 2–3	0.580	2.79	1.97	0.100	0.34	2.31
8–9, 3–4	0.530	2.56	1.46	0.115	0.32	1.78
7–8, 4–5	0.444	2.14	0.88	0.140	0.28	1.15
6–7, 5–6	0.293	1.41	0.32	0.185	0.20	0.53
5–6, 6–7	0.150	0.72	0.03	0.227	0.05	0.07

Distribution of Clear and Cloudy Days and Hours:

The frequency of occurrence of periods of various radiation levels, for example, of good and bad days, is of interest in two contexts. First, information on the frequency distribution is the link between two kinds of correlations, that of the daily fraction of diffuse with daily radiation and that of the monthly average fraction of diffuse with monthly average radiation. Second, later in this chapter the concept of utilizability is developed; it depends on these frequency distributions.

The monthly average clearness index $\overline{K}_T$ is the ratio[9] of monthly average daily radiation on a horizontal surface to the monthly average daily extraterrestrial radiation. In equation form,

$$\overline{K}_T = \frac{\overline{H}}{\overline{H}_o} \tag{2.9.1}$$

We can also define a daily clearness index K_T as the ratio of a particular day's radiation to the extraterrestrial radiation for that day. In equation form,

$$K_T = \frac{H}{H_o} \tag{2.9.2}$$

An hourly clearness index k_T can also be defined:

$$k_T = \frac{I}{I_o} \tag{2.9.3}$$

The data $\overline{H}$, H, and I are from measurements of total solar radiation on a horizontal surface, that is, the commonly available pyranometer measurements. Values of $\overline{H}_o$, H_o, and I_o can be calculated by the methods of Section 1.10.

Estimation of Hourly Solar Radiation Using ASHRAE Clear-Sky Model

Global Solar Radiation Calculation:-

The global solar radiation on horizontal surface is consisting of two main components, beam and diffuse solar radiation components. Then the global solar radiation can be presented as follows [1]:

$$I = I_b + I_d \quad \text{.....(1)}$$

Where I_b and I_d are hourly beam and diffuse solar radiation components in (w/m^2).

Beam Solar Radiation:-

The direct solar radiation component on the surface normal to the sun's ray, I_{bn}, can be presented as follows, [1]:

$$I_{bn} = A \times \exp[-B/\cos(\theta_H)] \quad \text{.....(2)}$$

Where: A is the apparent solar radiation in (w/m^2), B is the atmospheric extinction coefficient (dimensionless), while θ_H is the solar zenith angle in (degrees) which may defined as the angle between the sun's ray and the normal to horizontal surface as shown in Fig. (1).

So the beam radiation component I_b on horizontal surface can be re-written as follows, [1]:

$$I_b = I_{bn} \times \cos(\theta_H) \quad \ldots\ldots(3)$$

The solar zenith angle θ_H in (degrees) can be evaluated from the following equation, [16]:

Diffuse Solar Radiation:-

The diffuse solar radiation component on horizontal surface can be written in the following form [1]:

$$I_d = C \times I_{bn} \quad \ldots\ldots(11)$$

Where: C is the diffuse radiation factor (dimensionless). Finally, the hourly global solar radiation on horizontal surface can be represented using the following formula:

$$I = I_{bn} \times \cos(\theta_H) + C \times I_{bn} \quad \ldots\ldots(12)$$

Table (1) Constants for ASHRAE equations for average values of each month.

Months	Day no.	A (per month)	B	C
		W/m^2	Dimensionless	dimensionless
January	17	1229.88	0.142	0.058
February	16	1216.25	0.144	0.060
March	16	1190.40	0.153	0.068
April	15	1144.66	0.175	0.092
May	15	1109.68	0.192	0.116
June	11	1092.69	0.202	0.130
July	17	1084.88	0.207	0.136
August	16	1102.97	0.202	0.124
September	15	1142.12	0.182	0.098
October	15	1183.45	0.164	0.077
November	14	1213.61	0.151	0.065
December	10	1228.00	0.145	0.059

Beam and Diffuse Components of Hourly Radiation:

correlations are shown in Figure 2.10.2. They are essentially identical, although they were derived from three separate databases. The Erbs et al. correlation (Figure 2.10.3) is[11]

$$\frac{I_d}{I} = \begin{cases} 1.0 - 0.09k_T & \text{for } k_T \le 0.22 \\ 0.9511 - 0.1604k_T + 4.388k_T^2 & \\ \quad -16.638k_T^3 + 12.336k_T^4 & \text{for } 0.22 < k_T \le 0.80 \\ 0.165 & \text{for } k_T > 0.8 \end{cases} \tag{2.10.1}$$

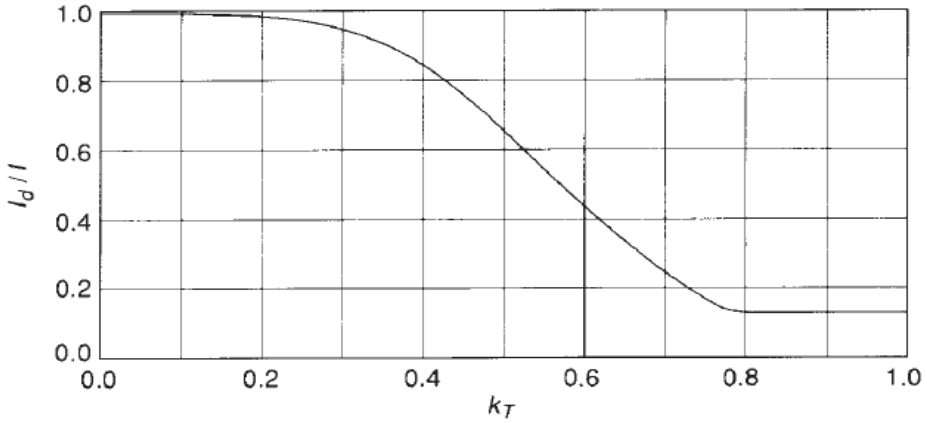

Figure 2.10.3 The ratio I_d/I as a function of hourly clearness index k_T. From Erbs et al. (1982).

Beam and Diffuse Components of Daily Radiation:

the sunset hour angle ω_s. Equations representing this set of correlations are as follows[12]: For $\omega_s \le 81.4^\circ$

$$\frac{H_d}{H} = \begin{cases} 1.0 - 0.2727K_T + 2.4495K_T^2 - 11.9514K_T^3 + 9.3879K_T^4 & \text{for } K_T < 0.715 \\ 0.143 & \text{for } K_T \ge 0.715 \end{cases} \tag{2.11.1a}$$

and for $\omega_s > 81.4^\circ$

$$\frac{H_d}{H} = \begin{cases} 1.0 + 0.2832K_T - 2.5557K_T^2 + 0.8448K_T^3 & \text{for } K_T < 0.722 \\ 0.175 & \text{for } K_T \ge 0.722 \end{cases} \tag{2.11.1b}$$

Example 2.11.1

The day's total radiation on a horizontal surface for St. Louis, Missouri (latitude 38.6°), on September 3 is 23.0 MJ/m^2. Estimate the fraction and amount that is diffuse.

Solution

For September 3, the declination is 7°. From Equation 1.6.10, the sunset hour angle is 95.6°. From Equation 1.10.3, the day's extraterrestrial radiation is 33.3 MJ/m^2. Then

$$K_T = \frac{H}{H_o} = \frac{23.0}{33.3} = 0.69$$

From Figure 2.11.2 or Equation 2.11.1b, $H_d/H = 0.26$, so an estimated 26% of the day's radiation is diffuse. The day's diffuse energy is $0.26 \times 23.0 = 6.0$ MJ/m^2. ■

Beam and Diffuse Components of Monthly Radiation:

Erbs et al. (1982) developed monthly average diffuse fraction correlations from the daily diffuse correlations of Figure 2.11.2. As with the daily correlations, there is a seasonal dependence; the winter curve lies below the other, indicating lower moisture and dust in the winter sky with resulting lower fractions of diffuse. The dependence of $\overline{H}_d/\overline{H}$ on $\overline{K}_T$ is shown for winter and for the other seasons in Figure 2.12.2. Equations for these correlations are as follows[13]: For $\omega_s \le 81.4°$ and $0.3 \le \overline{K}_T \le 0.8$

$$\frac{\overline{H}_d}{\overline{H}} = 1.391 - 3.560\overline{K}_T + 4.189\overline{K}_T^2 - 2.137\overline{K}_T^3 \qquad (2.12.1a)$$

and for $\omega_s > 81.4°$ and $0.3 \le \overline{K}_T \le 0.8$

$$\frac{\overline{H}_d}{\overline{H}} = 1.311 - 3.022\overline{K}_T + 3.427\overline{K}_T^2 - 1.821\overline{K}_T^3 \qquad (2.12.1b)$$

Example 2.12.1

Estimate the fraction of the average June radiation on a horizontal surface that is diffuse in Madison, Wisconsin.

Solution

From Appendix D, the June average daily radiation $\overline{H}$ for Madison is 23.0 MJ/m^2. From Equation 1.10.3, for June 11 (the mean day of the month, $n = 162$, from Table 1.6.1), when the declination is 23.1°, $H_o = 41.8$ MJ/m^2. Thus $\overline{K}_T = 23.0/41.8 = 0.55$. From Equation 1.6.10, $\omega_s = 113.4°$. Then, using either Equation 2.12.1b or the upper curve from Figure 2.12.2, $\overline{H}_d/\overline{H} = 0.38$. ■

Radiation on Sloped Surface Isotropic Sky:

Total solar radiation=Beam+diffuse+ground reflected

R_b=cos (inciedence angle/zenith angle)

It is clear that when ω_1 and ω_2 represent two adjacent hours in a day away from sunrise or sunset $R_{b,\text{ave}} \approx R_b$. However, when either ω_1 or ω_2 represent sunrise or sunset R_b changes rapidly and integration is needed:

$$R_{b,\text{ave}} = \frac{a}{b} \tag{2.14.6}$$

where

$$\begin{aligned} a = {} & (\sin\delta\ \sin\phi\ \cos\beta - \sin\delta\ \cos\phi\ \sin\beta\ \cos\gamma) \times \tfrac{1}{180}\,(\omega_2 - \omega_1)\pi \\ & + (\cos\delta\ \cos\phi\ \cos\beta + \cos\delta\ \sin\phi\ \sin\beta\ \cos\gamma) \times (\sin\omega_2 - \sin\omega_1) \\ & - (\cos\delta\ \sin\beta\ \sin\gamma) \times (\cos\omega_2 - \cos\omega_1) \end{aligned}$$

and

$$b = (\cos\phi\ \cos\delta) \times (\sin\omega_2 - \sin\omega_1) + (\sin\phi\ \sin\delta) \times \tfrac{1}{180}\,(\omega_2 - \omega_1)\,\pi.$$

Example 2.14.1

On March 4 at a latitude of 45° and a surface slope of 60° determine R_b at 6:30 AM and $R_{b,\text{ave}}$ for the hour 6 to 7 AM.

Solution

From Equation 1.6.1 the declination is −7.15°. The cosine of the incidence angle at 6:30 AM is found from Equation 1.6.7a with $\omega = -82.5°$,

$$\cos\theta = \cos(45-60)\ \cos(-7.15)\ \cos(-82.5) + \sin(45-60)\sin(-7.15) = 0.157$$

and the cosine of the zenith angle is found from Equation 1.6.5,

$$\cos\theta_z = \cos(45)\ \cos(-7.15)\ \cos(82.5) + \sin(45)\ \sin(-7.15) = 0.004$$

so that $R_b = \cos\theta/\cos\theta_z = 0.157/0.004 = 39.3$, a value that is much too high. If there is any significant beam radiation (measured or estimated), then multiplying it by 39.3 will probably produce a value that exceeds the solar constant. Clearly this is a situation to be avoided.

From Equation 1.6.10 sunrise occurs at $-82.79°/15$ deg/h $= 5.52$ h before noon, or 6:29 AM. Consequently $\omega_1 = -82.79°$ and $\omega_2 - 75.0°$ for use in Equation 2.14.6:

$$\begin{aligned} a = {} & [\sin(-7.15)\sin 45\ \cos 60 - \sin(-7.15)\cos 45\ \sin 60\ \cos 0] \\ & \times \tfrac{1}{180}[(-75) - (-82.79)]\pi \\ & + [\cos(-7.15)\cos 45\ \cos 60 + \cos(-7.15)\sin 45\ \sin 60\ \cos 0] \\ & \times [\sin(-75) - \sin(-82.79)] \\ & - \{\cos(-7.15)\sin 60\ \sin 0) \times [\cos(-75) - \cos(-82.79)\} = 0.0295 \\ b = {} & [\cos 45\ \cos(-7.15)] \times [\sin(-75) - \sin(-82.79)] \\ & + [\sin 45\ \sin(-7.15)] \times \tfrac{1}{180}[(-75) - (-82.79)]\pi = 0.00639 \end{aligned}$$

Therefore $R_{b,\text{ave}} = 0.0295/0.00639 = 4.62$, a much more reasonable value. An alternative is to neglect the hours that contain sunrise or sunset. ■

$$I_T = I_b R_b + I_d\left(\frac{1+\cos\beta}{2}\right) + I\rho_g\left(\frac{1-\cos\beta}{2}\right) \qquad (2.15.1)$$

and by the definition of R,

$$R = \frac{I_b}{I} R_b + \frac{I_d}{I}\left(\frac{1+\cos\beta}{2}\right) + \rho_g\left(\frac{1-\cos\beta}{2}\right) \tag{2.15.2}$$

Example 2.15.1

Using the isotropic diffuse model, estimate the beam, diffuse, and ground-reflected components of solar radiation and the total radiation on a surface sloped 60° toward the south at a latitude of 40° N for the hour 9 to 10 AM on February 20. Here $I = 1.04$ MJ/m^2 and $\rho_g = 0.60$.

Solution

For this hour, $I_o = 2.34$ MJ/m^2, so $k_T = 1.04/2.34 = 0.445$. From the Erbs correlation (Equation 2.10.1) $I_d/I = 0.766$. Thus

$$I_d = 0.766 \times 1.04 = 0.796 \text{ MJ/m}^2$$
$$I_b = 0.234 \times 1.04 = 0.244 \text{ MJ/m}^2$$

The hour angle ω for the midpoint of the hour is $-37.5°$. The declination $\delta = -11.6°$. Then for this south-facing surface

$$R_b = \frac{\cos(40-60)\ \cos(-11.6)\ \cos(-37.5) + \sin(40-60)\ \sin(-11.6)}{\cos(40)\ \cos(-11.6)\ \cos(-37.5) + \sin(40)\ \sin(-11.6)}$$
$$= \frac{0.799}{0.466} = 1.71$$

Equation 2.15.1 gives the three radiation streams and the total:

$$I_T = 0.244 \times 1.71 + 0.796\left(\frac{1+\cos 60}{2}\right) + 1.04 \times 0.60\left(\frac{1-\cos 60}{2}\right)$$
$$= 0.417 + 0.597 + 0.156 = 1.17 \text{ MJ/m}^2$$

Thus the beam contribution is 0.417 MJ/m^2, the diffuse is 0.597 MJ/m^2, and the ground reflected is 0.156 MJ/m^2. The total radiation on the surface for the hour is 1.17 MJ/m^2. There are uncertainties in these numbers, and while they are carried to 0.001 MJ in intermediate steps for purposes of comparing sky models, they are certainly no better than 0.01. ■

AVERAGE RADIATION ON SLOPED SURFACES: ISOTROPIC SKY

In Section 2.15, the calculation of total radiation on sloped surfaces from measurements on a horizontal surface was discussed. For use in solar process design procedures,[22] we also need the monthly average daily radiation on the tilted surface. The procedure for calculating $\overline{H}_T$ is parallel to that for I_T, that is, by summing the contributions of the beam radiation, the components of the diffuse radiation, and the radiation reflected from the ground. The state of development of these calculation methods for $\overline{H}_T$ is not as satisfactory as that for I_T.

The first method is that of Liu and Jordan (1962) as extended by Klein (1977), which has been widely used. If the diffuse and ground-reflected radiation are each assumed to be isotropic, then, in a manner analogous to Equation 2.15.1, the monthly mean solar radiation on an unshaded tilted surface can be expressed as

$$\overline{H}_T = \overline{H}_b \overline{R}_b + \overline{H}_d \left(\frac{1+\cos\beta}{2}\right) + \overline{H}\rho_g \left(\frac{1-\cos\beta}{2}\right) \tag{2.19.1}$$

and

$$\overline{R} = \frac{\overline{H}_T}{\overline{H}} = \left(1 - \frac{\overline{H}_d}{\overline{H}}\right) \overline{R}_b + \frac{\overline{H}_d}{\overline{H}} \left(\frac{1+\cos\beta}{2}\right) + \rho_g \left(\frac{1-\cos\beta}{2}\right) \tag{2.19.2}$$

where $\overline{H}_d/\overline{H}$ is a function of $\overline{K}_T$, as shown in Figure 2.12.2.

The ratio of the average daily beam radiation on the tilted surface to that on a horizontal surface for the month is $\overline{R}_b$, which is equal to $\overline{H}_{bT}/\overline{H}_b$. It is a function of transmittance of the atmosphere, but Liu and Jordan suggest that it can be estimated by assuming that it has the value which would be obtained if there were no atmosphere. For surfaces that are sloped toward the equator in the northern hemisphere, that is, for surfaces with $\gamma = 0°$,

$$\overline{R}_b = \frac{\cos(\phi-\beta)\ \cos\delta\ \sin\omega_s' + (\pi/180)\ \omega_s'\ \sin(\phi-\beta)\ \sin\delta}{\cos\phi\ \cos\delta\ \sin\omega_s + (\pi/180)\ \omega_s\ \sin\phi\ \sin\delta} \tag{2.19.3a}$$

where ω_s' is the sunset hour angle for the tilted surface for the mean day of the month, which is given by

$$\omega_s' = \min \begin{bmatrix} \cos^{-1}(-\tan\phi\ \tan\delta) \\ \cos^{-1}(-\tan(\phi-\beta)\ \tan\delta) \end{bmatrix} \tag{2.19.3b}$$

where "min" means the smaller of the two items in the brackets.

For surfaces in the southern hemisphere sloped toward the equator, with $\gamma = 180^\circ$, the equations are

$$\overline{R}_b = \frac{\cos(\phi+\beta)\ \cos\delta\ \sin\omega_s' + (\pi/180)\ \omega_s'\ \sin(\phi+\beta)\ \sin\delta}{\cos\phi\ \cos\delta\ \sin\omega_s + (\pi/180)\ \omega_s\ \sin\phi\ \sin\delta} \tag{2.19.4a}$$

and

$$\omega_s' = \min\begin{bmatrix}\cos^{-1}(-\tan\phi\ \tan\delta)\\ \cos^{-1}(-\tan(\phi+\beta)\ \tan\delta)\end{bmatrix} \tag{2.19.4b}$$

Example 2.19.1

A collector is to be installed in Madison, latitude 43°, at a slope of 60° to the south. Average daily radiation data are shown in Appendix D. The ground reflectance is 0.2 for all months except December and March ($\rho_g = 0.4$) and January and February ($\rho_g = 0.7$). Using the isotropic diffuse assumption, estimate the monthly average radiation incident on the collector.

Solution

The calculation is detailed below for January, and the results for the year are indicated in a table. The basic equation to be used is Equation 2.19.1. The first steps are to obtain $\overline{H}_d/\overline{H}$ and $\overline{R}_b$. The ratio $\overline{H}_d/\overline{H}$ is a function of $\overline{K}_T$ and can be obtained from Equation 2.12.1 or Figure 2.12.2.

For the mean January day, the 17th, from Table 1.6.1, $n = 17$, $\delta = -20.9^\circ$. The sunset hour angle is calculated from Equation 1.6.10 and is 69.1°. With $n = 17$ and

$\omega_s = 69.1^\circ$, from Equation 1.10.3 (or Figure 1.10.1 or Table 1.10.1), $\overline{H}_o = 13.36$ MJ/m^2. Then $\overline{K}_T = 6.44/13.36 = 0.48$.

The Erbs correlation (Equation 2.12.1a) is used to calculate $\overline{H}_d/\overline{H}$ from $\overline{K}_T$ and ω_s gives $\overline{H}_d/\overline{H} = 0.41$. The calculation of $\overline{R}_b$ requires the sunset hour angle on the sloped collector. From Equations 2.19.3

$$\cos^{-1}[-\tan(43-60)\ \tan(-20.8)] = 96.7^\circ$$

The angle ω_s was calculated as 69.1° and is less than 96.7°, so $\omega_s' = 69.1°$. Then

$$\overline{R}_b = \frac{\cos(-17)\ \cos(-20.9)\ \sin 69.1 + (\pi \times 69.1/180)\ \sin(-17)\ \sin(-20.9)}{\cos 43\ \cos(-20.9)\ \sin 69.1 + (\pi \times 69.1/180)\ \sin 43\ \sin(-20.9)}$$
$$= 2.79$$

The equation for $\overline{H}_T$ (Equation 2.19.1) can now be solved:

$$\overline{H}_T = 6.44\ (1 - 0.41)2.79 + 6.44 \times 0.41 \left(\frac{1 + \cos 60}{2}\right) + 6.44 \times 0.7 \left(\frac{1 - \cos 60}{2}\right)$$
$$= 10.60 + 1.98 + 1.13 = 13.7\ \text{MJ/m}^2$$

Month	$\overline{H}$	$\overline{H}_o$	$\overline{K}_T$	$\overline{H}_d/\overline{H}$	$\overline{R}_b$	ρ_s	$\overline{H}_T$
January	6.44	13.37	0.48	0.41	2.79	0.7	13.7
February	9.89	18.81	0.53	0.37	2.04	0.7	17.2
March	12.86	26.03	0.49	0.43	1.42	0.4	15.8
April	16.05	33.78	0.48	0.45	0.96	0.2	14.7
May	21.36	39.42	0.54	0.39	0.71	0.2	16.6
June	23.04	41.78	0.55	0.38	0.62	0.2	16.5
July	22.58	40.56	0.56	0.38	0.66	0.2	16.8
August	20.33	35.92	0.57	0.37	0.84	0.2	17.5
September	14.59	28.80	0.51	0.42	1.21	0.2	15.6
October	10.48	20.90	0.50	0.39	1.81	0.2	15.2
November	6.37	14.62	0.44	0.46	2.56	0.2	11.4
December	5.74	11.91	0.48	0.41	3.06	0.4	12.7

Selected Heat Transfer Topics

THE ELECTROMAGNETIC SPECTRUM

Thermal radiation is electromagnetic energy that is propagated through space at the speed of light. For most solar energy applications, only thermal radiation is important. Thermal radiation is emitted by bodies by virtue of their temperature; the atoms, molecules, or electrons are raised to excited states, return spontaneously to lower energy states, and in doing so emit energy in the form of electromagnetic radiation. Because the emission results from changes in electronic, rotational, and vibrational states of atoms and molecules, the emitted radiation is usually distributed over a range of wavelengths.

The spectrum of electromagnetic radiation is divided into wavelength bands. These bands and the wavelengths representing their approximate limits are shown in Figure 3.1.1. The wavelength limits associated with the various names and the mechanism producing the radiation are not sharply defined. There is no basic distinction between these ranges of radiation other than the wavelength λ; they all travel with the speed of light C and have a frequency ν such that

$$C = \frac{C_o}{n} = \lambda \nu \tag{3.1.1}$$

where C_o is the speed of light in a vacuum and n is the index of refraction.

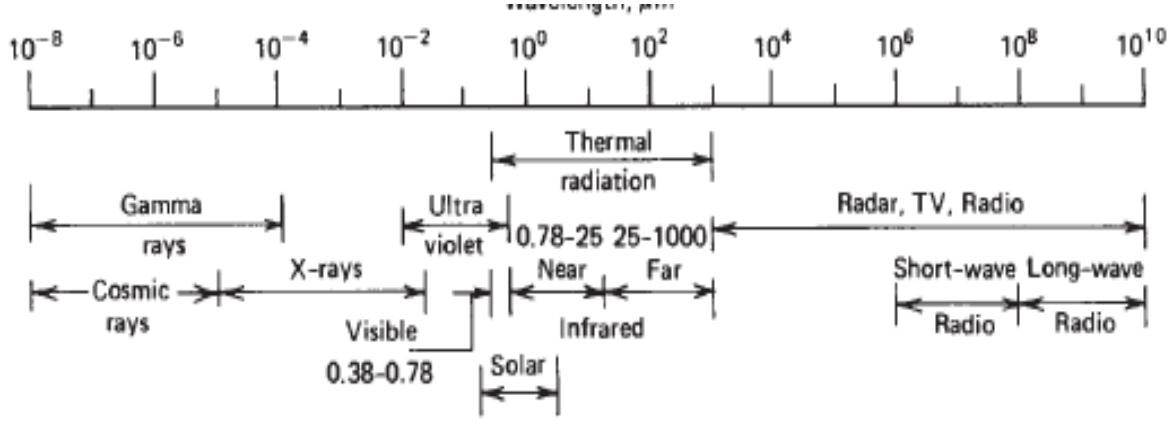

Figure 3.1.1 The spectrum of electromagnetic radiation.

BLACKBODY: PERFECT ABSORBER AND EMITTER

By definition, a blackbody is a perfect absorber of radiation. No matter what wavelengths or directions describe the radiation incident on a blackbody, all incident radiation will be absorbed. A blackbody is an ideal concept since all real substances will reflect some radiation.

PLANCK'S LAW AND WIEN'S DISPLACEMENT LAW

Radiation in the region of the electromagnetic spectrum from approximately 0.2 to approximately 1000 μm is called thermal radiation and is emitted by all substances by virtue of their temperature. The wavelength distribution of radiation emitted by a blackbody is given by Planck's law[1] (Richtmyer and Kennard, 1947):

$$E_{\lambda b} = \frac{2\pi hC_o^2}{\lambda^5[\exp(hC_o/\lambda kT) - 1]} \tag{3.4.1}$$

where h is Planck's constant and k is Boltzmann's constant. The groups $2\pi hC_o^2$ and hC_o/k are often called Planck's first and second radiation constants and given the symbols C_1 and C_2, respectively.[2] Recommended values are $C_1 = 3.7405 \times 10^8$ W μm^4/m^2 and $C_2 = 14,387.8$ μm K.

It is also of interest to know the wavelength corresponding to the maximum intensity of blackbody radiation. By differentiating Planck's distribution and equating to zero, the wavelength corresponding to the maximum of the distribution can be derived. This leads to Wien's displacement law, which can be written as

$$\lambda_{\max} T = 2897.8 \ \mu\text{m K} \tag{3.4.2}$$

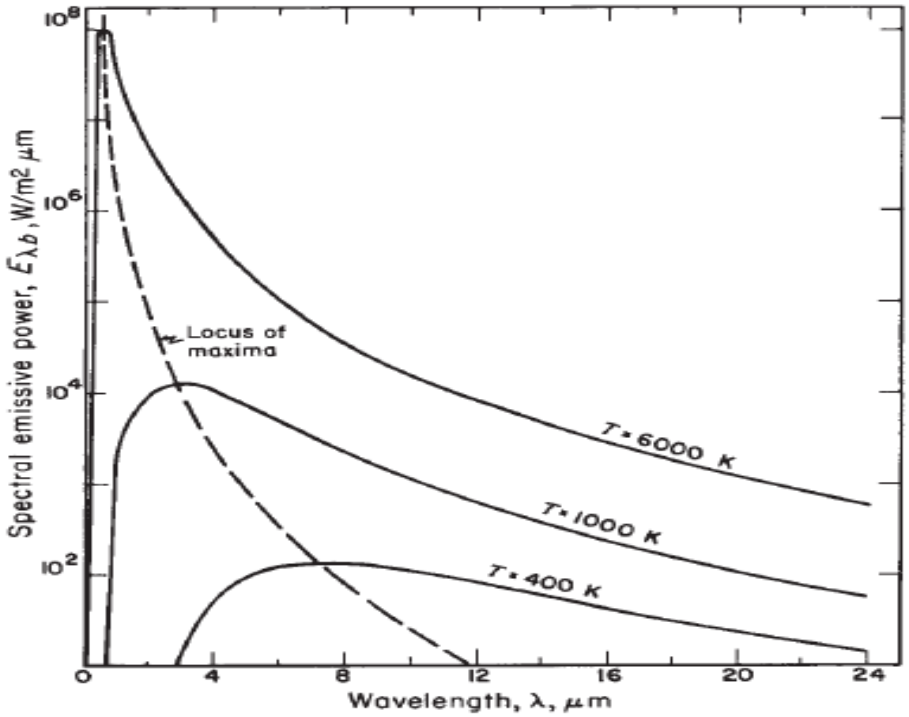

Figure 3.4.1 Spectral distribution of blackbody radiation.

STEFAN-BOLTZMANN EQUATION

Planck's law gives the spectral distribution of radiation from a blackbody, but in engineering calculations the total energy is often of more interest. By integrating Planck's law over all wavelengths, the total energy emitted per unit area by a blackbody is found to be

$$E_b = \int_0^\infty E_{\lambda b}\, d\lambda = \sigma T^4 \tag{3.5.1}$$

where σ is the Stefan-Boltzmann constant and is equal to 5.6697×10^{-8} W/m^2 K^4. This constant appears in essentially all radiation equations.

RADIATION TABLES

Starting with Planck's law (Equation 3.4.1) of the spectral distribution of blackbody radiation, Dunkle (1954) has presented a method for simplifying blackbody calculations. Planck's law can be written as

$$E_{\lambda b} = \frac{C_1}{\lambda^5[\exp(C_2/\lambda T) - 1]} \tag{3.6.1}$$

Equation 3.6.1 can be integrated to give the radiation between any wavelength limits. The total emitted from zero to any wavelength λ is given by

$$E_{0-\lambda b} = \int_0^\lambda E_{\lambda b}\, d\lambda \tag{3.6.2}$$

Substituting Equation 3.6.1 into 3.6.2 and noting that by dividing by σT^4 the integral can be made to be only a function of λT,

$$f_{0-\lambda T} = \frac{E_{0-\lambda T}}{\sigma T^4} = \int_0^{\lambda T} \frac{C_1\, d(\lambda T)}{\sigma(\lambda T)^5[\exp(C_2/\lambda T) - 1]} \tag{3.6.3}$$

Table 3.6.1a Fraction of Blackbody Radiant Energy between Zero and λT for Even Increments of λT

λT, μm K	$f_{0-\lambda T}$	λT, μm K	$f_{0-\lambda T}$	λT, μm K	$f_{0-\lambda T}$
1,000	0.0003	4,500	0.5643	8,000	0.8562
1,100	0.0009	4,600	0.5793	8,100	0.8601
1,200	0.0021	4,700	0.5937	8,200	0.8639
1,300	0.0043	4,800	0.6075	8,300	0.8676
1,400	0.0077	4,900	0.6209	8,400	0.8711
1,500	0.0128	5,000	0.6337	8,500	0.8745
1,600	0.0197	5,100	0.6461	8,600	0.8778
1,700	0.0285	5,200	0.6579	8,700	0.8810
1,800	0.0393	5,300	0.6693	8,800	0.8841
1,900	0.0521	5,400	0.6803	8,900	0.8871
2,000	0.0667	5,500	0.6909	9,000	0.8899
2,100	0.0830	5,600	0.7010	9,100	0.8927
2,200	0.1009	5,700	0.7107	9,200	0.8954
2,300	0.1200	5,800	0.7201	9,300	0.8980
2,400	0.1402	5,900	0.7291	9,400	0.9005
2,500	0.1613	6,000	0.7378	9,500	0.9030
2,600	0.1831	6,100	0.7461	9,600	0.9054
2,700	0.2053	6,200	0.7541	9,700	0.9076
2,800	0.2279	6,300	0.7618	9,800	0.9099
2,900	0.2506	6,400	0.7692	9,900	0.9120
3,000	0.2732	6,500	0.7763	10,000	0.9141
3,100	0.2958	6,600	0.7831	11,000	0.9318
3,200	0.3181	6,700	0.7897	12,000	0.9450
3,300	0.3401	6,800	0.7961	13,000	0.9550
3,400	0.3617	6,900	0.8022	14,000	0.9628
3,500	0.3829	7,000	0.8080	15,000	0.9689
3,600	0.4036	7,100	0.8137	16,000	0.9737
3,700	0.4238	7,200	0.8191	17,000	0.9776
3,800	0.4434	7,300	0.8244	18,000	0.9807
3,900	0.4624	7,400	0.8295	19,000	0.9833
4,000	0.4809	7,500	0.8343	20,000	0.9855
4,100	0.4987	7,600	0.8390	30,000	0.9952
4,200	0.5160	7,700	0.8436	40,000	0.9978
4,300	0.5327	7,800	0.8479	50,000	0.9988
4,400	0.5488	7,900	0.8521	∞	1.

Example 3.6.1

Assume that the sun is a blackbody at 5777 K.

a What is the wavelength at which the maximum monochromatic emissive power occurs?

b What is the energy from this source that is in the visible part of the electromagnetic spectrum (0.38 to 0.78 μm)?

Solution

a The value of λT at which the maximum monochromatic emissive power occurs is 2897.8 μm K, so the desired wavelength is 2897.8/5777, or 0.502 μm.

b From Table 3.6.1a the fraction of energy between zero and $\lambda T = 0.78 \times 5777 = 4506$ μm K is 56%, and the fraction of the energy between zero and $\lambda T = 0.38 \times 5777 = 2195$ μm K is 10%. The fraction of the energy in the visible is then 56% minus 10%, or 46%. These numbers are close to the values obtained from the actual distribution of energy from the sun as calculated in Example 3.6.1. ■

INFRARED RADIATION EXCHANGE BETWEEN GRAY SURFACES

The general case of infrared radiation heat transfer between many gray surfaces having different temperatures is treated in a number of textbooks (e.g., Hottel and Sarofim, 1967; Siegel and Howell, 2002). The various methods all make the same basic assumptions, which for each surface can be summarized as follows:

1. The surface is gray. (Radiation properties are independent of wavelength.)
2. The surface is diffuse or specular diffuse (see Section 4.3).
3. The surface temperature is uniform.
4. The incident energy over the surface is uniform.

Beckman (1971) also utilized these basic assumptions and defined a total exchange factor between pairs of surfaces of an N-surface enclosure such that the net heat transfer to a typical surface i is[4]

$$Q_i = \sum_{j=1}^{N} \varepsilon_i \varepsilon_j A_i \widehat{F}_{ij} \sigma (T_j^4 - T_i^4) \tag{3.8.1}$$

The majority of heat transfer problems in solar energy applications involve radiation between two surfaces. The solution of Equations 3.8.1 and 3.8.2 for diffuse surfaces with $N = 2$ is

$$Q_1 = -Q_2 = \frac{\sigma (T_2^4 - T_1^4)}{\dfrac{1 - \varepsilon_1}{\varepsilon A_1} + \dfrac{1}{A_1 F_{12}} + \dfrac{1 - \varepsilon_2}{\varepsilon_2 A_2}} \tag{3.8.3}$$

Two special cases of Equation 3.8.3 are of particular interest. For radiation between two infinite parallel plates (i.e., as in flat-plate collectors) the areas A_1 and A_2 are equal and the view factor F_{12} is unity. Under these conditions Equation 3.8.3 becomes

$$\frac{Q}{A} = \frac{\sigma (T_2^4 - T_1^4)}{\dfrac{1}{\varepsilon_1} + \dfrac{1}{\varepsilon_2} - 1} \tag{3.8.4}$$

The second special case is for a small convex object (surface 1) surrounded by a large enclosure (surface 2). Under these conditions, the area ratio A_1/A_2 approaches zero, the view factor F_{12} is unity, and Equation 3.8.3 becomes

$$Q_1 = \varepsilon_1 A_1 \sigma (T_2^4 - T_1^4) \tag{3.8.5}$$

RADIATION HEAT TRANSFER COEFFICIENT

To retain the simplicity of linear equations, it is convenient to define a radiation heat transfer coefficient. The heat transfer by radiation between two arbitrary surfaces is found from Equation 3.8.3. If we define a heat transfer coefficient so that the radiation between the two surfaces is given by

$$Q = A_1 h_r (T_2 - T_1) \tag{3.10.1}$$

then it follows that

$$h_r = \frac{\sigma (T_2^2 + T_1^2)(T_2 + T_1)}{\dfrac{1 - \varepsilon_1}{\varepsilon_1} + \dfrac{1}{F_{12}} + \dfrac{(1 - \varepsilon_2)A_1}{\varepsilon_2 A_2}} \tag{3.10.2}$$

SKY RADIATION

To predict the performance of solar collectors, it will be necessary to evaluate the radiation exchange between a surface and the sky. The sky can be considered as a blackbody at some equivalent sky temperature T_s so that the actual net radiation between a horizontal flat plate and the sky is given by Equation 3.8.5. The net radiation from a surface with emittance ε and temperature T to the sky at T_s is

$$Q = \varepsilon A \sigma (T^4 - T_s^4) \tag{3.9.1}$$

Example 3.10.1

The plate and cover of a flat-plate collector are large in extent, are parallel, and are spaced 25 mm apart. The emittance of the plate is 0.15 and its temperature is 70°C. The emittance of the glass cover is 0.88 and its temperature is 50°C. Calculate the radiation exchange between the surfaces and a radiation heat transfer coefficient for this situation.

Solution

Exact and approximate solutions are possible for this problem. The exact solution is based on Equations 3.8.4 and 3.10.1. The radiation exchange is given by Equation 3.8.4:

$$\frac{Q}{A} = \frac{\sigma(343^4 - 323^4)}{\frac{1}{0.15} + \frac{1}{0.88} - 1} = 24.6 \text{ W/m}^2$$

Then from the defining equation for the radiation coefficient (Equation 3.10.1),

$$h_r = \frac{24.6}{70 - 50} = 1.232 \text{ W/m}^2 \text{ °C}$$

(The use of Equation 3.10.2 produces the identical result.)

We can also get an approximate solution using the average of the two plate temperatures, 60°C or 333 K, in Equation 3.10.3: Then

$$h_r = \frac{\sigma \times 4 \times 333^3}{\frac{1}{0.15} + \frac{1}{0.88} - 1} = 1.231 \text{ W/m}^2 \text{ °C}$$

NATURAL CONVECTION BETWEEN FLAT PARALLEL PLATES AND BETWEEN CONCENTRIC CYLINDERS

The rate of heat transfer between two plates inclined at some angle to the horizon is of obvious importance in the performance of flat-plate collectors. Free-convection heat transfer data are usually correlated in terms of two or three dimensionless parameters: the Nusselt number Nu, the Rayleigh number Ra, and the Prandtl number Pr. Some authors correlate data in terms of the Grashof number, which is the ratio of the Rayleigh number to the Prandtl number.

The Nusselt, Rayleigh, and Prandtl numbers are given by[5]

$$\text{Nu} = \frac{hL}{k} \tag{3.11.1}$$

$$\text{Ra} = \frac{g\beta' \, \Delta T \, L^3}{\nu\alpha} \tag{3.11.2}$$

$$\text{Pr} = \frac{\nu}{\alpha} \tag{3.11.3}$$

Where h = heat transfer coefficient [W/m^2 K]
L = plate spacing [m]
k = thermal conductivity [W/m K]
g = gravitational constant [m/s^2]
β' = volumetric coefficient of expansion (for an ideal gas, $\beta' = 1/T$) [1/K]
ΔT = temperature difference between plates [K]
ν = kinematic viscosity [m^2/s]
α = thermal diffusivity [m^2/s]

In a more recent experimental study using air, Hollands et al. (1976) give the relationship between the Nusselt number and Rayleigh number for tilt angles from 0 to 75° as

$$\mathrm{Nu} = 1 + 1.44\left[1 - \frac{1708(\sin\ 1.8\beta)^{1.6}}{\mathrm{Ra}\ \cos\ \beta}\right]\left[1 - \frac{1708}{\mathrm{Ra}\ \cos\ \beta}\right]^{+} + \left[\left(\frac{\mathrm{Ra}\ \cos\ \beta}{5830}\right)^{1/3} - 1\right]^{+} \tag{3.11.4}$$

where the meaning of the + exponent is that only positive values of the terms in the square brackets are to be used (i.e., use zero if the term is negative).

Example 3.11.1

Find the convection heat transfer coefficient between two parallel plates separated by 25 mm with a 45° tilt. The lower plate is at 70°C and the upper plate is at 50°C.

Solution

At the mean air temperature of 60°C air properties are $k = 0.029$ W/m K, $T = 333$ K so $\beta' = 1/333$, $\nu = 1.88 \times 10^{-5}$ m^2/s, and $\alpha = 2.69 \times 10^{-5}$ m^2/s. (Property data are from EES; www.fchart.com.) The Rayleigh number is

$$\mathrm{Ra} = \frac{9.81 \times 20 \times (0.025)^3}{333 \times 1.88 \times 10^{-5} \times 2.69 \times 10^{-5}} = 1.82 \times 10^4$$

From Equation 3.11.4 or Figure 3.11.1 the Nusselt number is 2.4. The heat transfer coefficient is found from

$$h = \mathrm{Nu}\ \frac{k}{L} = \frac{2.4 \times 0.029}{0.025} = 2.78\ \mathrm{W/m^2\ K}$$

Example 3.14.1

What is the heat transfer coefficient inside the tubes of a solar collector in which the tubes are 10 mm in diameter and separated by a distance of 100 mm? The collector is 1.5 m wide and 3 m long and has total flow rate of water of 0.075 kg/s. The water is at 80°C.

Solution

The collector has 15 tubes so that the flow rate per tube is 0.005 kg/s. The Reynolds number is

$$\frac{VD}{\nu} = \frac{4\dot{m}}{\pi D\mu} = \frac{4 \times 0.005}{\pi \times 0.01 \times 3.6 \times 10^{-4}} = 1800$$

which indicates laminar flow. The Prandtl number is 2.2 so that

$$\frac{\mathrm{Re\ Pr}\ D_h}{L} = \frac{1800 \times 2.2 \times 0.01}{3} = 13$$

From Figure 3.14.1 the average Nusselt number is 4.6 so the average heat transfer coefficient is

$$h = \frac{\mathrm{Nu}\ k}{D} = \frac{4.6 \times 0.67}{0.01} = 308\ \mathrm{W/m^2\ °C}$$

■

EFFECTIVENESS-NTU CALCULATIONS FOR HEAT EXCHANGERS

It is convenient in solar process system calculations to use the effectiveness-NTU (number of transfer units) method of calculation of heat exchanger performance. A brief discussion of the method is provided here, based on the example of a countercurrent exchanger. The working equation is the same for other heat exchanger configurations; the expressions for effectiveness vary from one configuration to another (Kays and London, 1964).

A schematic of an adiabatic countercurrent exchanger with inlet and outlet temperatures and capacitance rates of the hot and cold fluids is shown in Figure 3.17.1. The overall heat transfer coefficient—area product is UA. The maximum possible temperature drop of the hot fluid is from T_{hi} to T_{ci}; the heat transfer for this situation would be

$$Q_{\max} = (\dot{m}C_p)_h(T_{hi} - T_{ci}) \tag{3.17.1}$$

The maximum possible temperature rise of the cold fluid would be from T_{ci} to T_{hi}. The corresponding maximum heat exchange would be

$$Q_{\max} = (\dot{m}C_p)_c(T_{hi} - T_{ci}) \tag{3.17.2}$$

The maximum heat transfer that could occur in the exchanger is thus fixed by the lower of the two capacitance rates, $(\dot{m}C_p)_{\min}$, and

$$Q_{\max} = (\dot{m}C_p)_{\min}\ (T_{hi} - T_{ci}) \tag{3.17.3}$$

The actual heat exchange Q is given by

$$Q = (\dot{m}C_p)_c(T_{co} - T_{ci}) = (\dot{m}C_p)_h(T_{hi} - T_{ho}) \tag{3.17.4}$$

Figure 3.17.1 Schematic of an adiabatic counterflow heat exchanger showing temperatures and capacitance rates of the hot and cold fluids.

Effectiveness ε is defined as the ratio of the actual heat exchange that occurs to the maximum possible, $Q/Q_{\max}$, so

$$\varepsilon = \frac{Q}{Q_{\max}} = \frac{(\dot{m}C_p)_h(T_{hi} - T_{ho})}{(\dot{m}C_p)_{\min}\ (T_{hi} - T_{ci})} = \frac{(\dot{m}C_p)_c(T_{co} - T_{ci})}{(\dot{m}C_p)_{\min}\ (T_{hi} - T_{ci})} \tag{3.17.5}$$

Since either the hot or cold fluid has the minimum capacitance rate, the effectiveness can always be expressed in terms of the temperatures only. The working equation for the heat exchanger is

$$Q = \varepsilon(\dot{m}C_p)_{\min}\ (T_{hi} - T_{ci}) \tag{3.17.6}$$

where NTU is the number of transfer units, defined as

$$NTU = \frac{UA}{(\dot{m}C_p)_{\min}} \tag{3.17.8}$$

and the dimensionless capacitance rate is given by

$$C^* = \frac{(\dot{m}C_p)_{\min}}{(\dot{m}C_p)_{\max}} \tag{3.17.9}$$

Example 3.17.1

A heat exchanger like that in Figure 3.17.1 is located between a collector and a storage tank. The fluid on the collector side is an antifreeze, a glycol-water mixture with $C_p = 3850$ J/kg K. Its flow rate is 1.25 kg/s. The fluid on the tank side is water, and its flow rate is 0.864 kg/s. The UA of the heat exchanger is estimated to be 6500 W/K.

If the hot glycol from the collector enters the exchanger at 62°C and the cool water from the tank enters at 35°C, what is the heat exchange rate and what are the outlet temperatures?

Solution

First calculate the capacitance rates on the hot (collector) and cold (tank) sides of the heat exchanger and C^*. Use the symbols C_h and C_c for the hot- and cold-side capacitance rates:

$$C_h = 1.25 \times 3850 = 4812 \text{ W/K}$$
$$C_c = 0.864 \times 4180 = 3610 \text{ W/K}$$

The cold-side capacitance rate is the minimum of the two, and from Equation 3.17.9,

$$C^* = \frac{3610}{4812} = 0.75$$

From Equation 3.17.8,

$$NTU = \frac{UA}{C_{\min}} = \frac{6500}{3610} = 1.80$$

The effectiveness is now calculated from Equation 3.17.7:

$$\varepsilon = \frac{1 - e^{-1.8(1-0.75)}}{1 - 0.75e^{-1.8(1-0.75)}} = 0.69$$

The heat transfer is now calculated from Equation 3.17.6:

$$Q = 0.69 \times 3610(62 - 35) = 67{,}300 \text{ W}$$

The temperatures of the fluids leaving the exchanger can also be calculated using Equation 3.17.4. The leaving-water temperature is

$$T_{co} = 35 + \frac{67{,}300}{3610} = 53.6^{\circ}\text{C}$$

and the leaving-glycol temperature is

$$T_{ho} = 62 - \frac{67{,}300}{4812} = 48.0^{\circ}\text{C}$$ ■

Flat-Plate Collectors

DESCRIPTION OF FLAT-PLATE COLLECTORS

The important parts of a typical liquid heating flat-plate solar collector, as shown in Figure 6.1.1, are the ''black'' solar energy-absorbing surface with means for transferring the absorbed energy to a fluid, envelopes transparent to solar radiation over the solar absorber surface that reduce convection and radiation losses to the atmosphere, and back insulation to reduce conduction losses. Figure 6.1.1 depicts a water heater, and most of the analysis of this chapter is concerned with this geometry. Air heaters are fundamentally the same except that the fluid tubes are replaced by ducts. Flat-plate collectors are almost

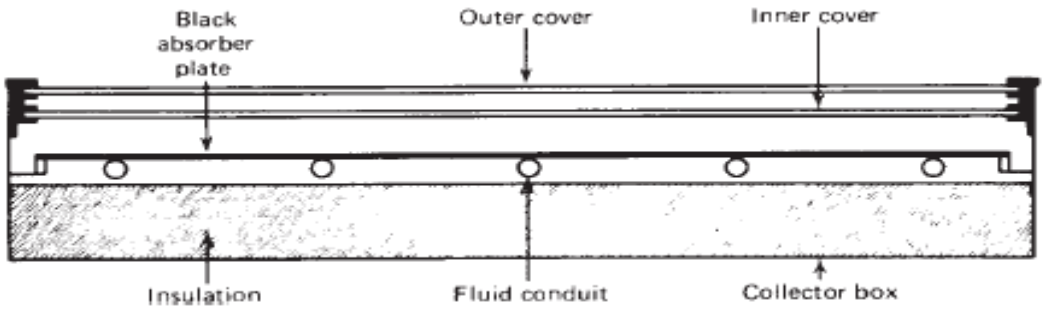

Figure 6.1.1 Cross section of a basic flat-plate solar collector.

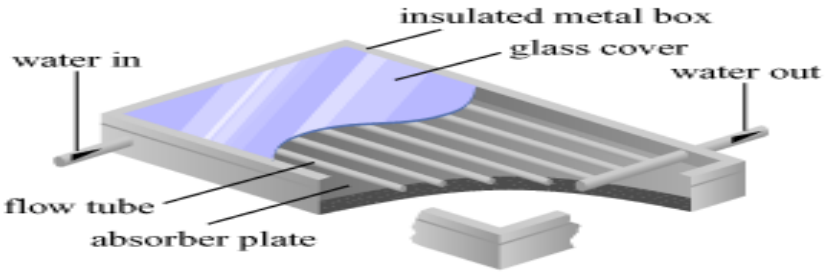

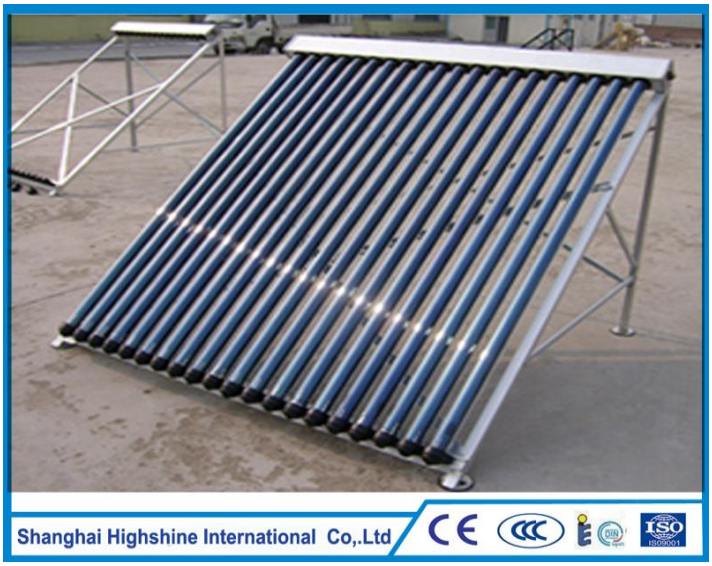

BASIC FLAT-PLATE ENERGY BALANCE EQUATION

In steady state, the performance of a solar collector is described by an energy balance that indicates the distribution of incident solar energy into useful energy gain, thermal losses, and optical losses. The solar radiation absorbed by a collector per unit area of absorber S is equal to the difference between the incident solar radiation and the optical losses as defined by Equation 5.9.1. The thermal energy lost from the collector to the surroundings by conduction, convection, and infrared radiation can be represented as the product of a heat transfer coefficient U_L times the difference between the mean absorber plate temperature T_{pm} and the ambient temperature T_a. In steady state the useful energy output of a collector of area A_c is the difference between the absorbed solar radiation and the thermal loss:

$$Q_u = A_c[S - U_L(T_{pm} - T_a)] \tag{6.2.1}$$

If conditions are constant over a time period, the efficiency reduces to

$$\eta = \frac{Q_u}{I_T A_C} \tag{6.2.2b}$$

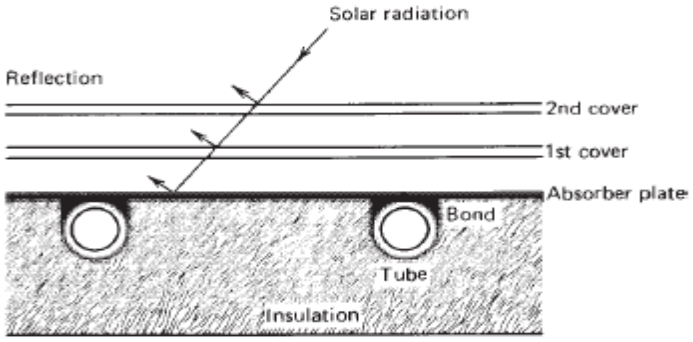

Figure 6.3.1 Sheet-and-tube solar collector.

COLLECTOR OVERALL HEAT LOSS COEFFICIENT

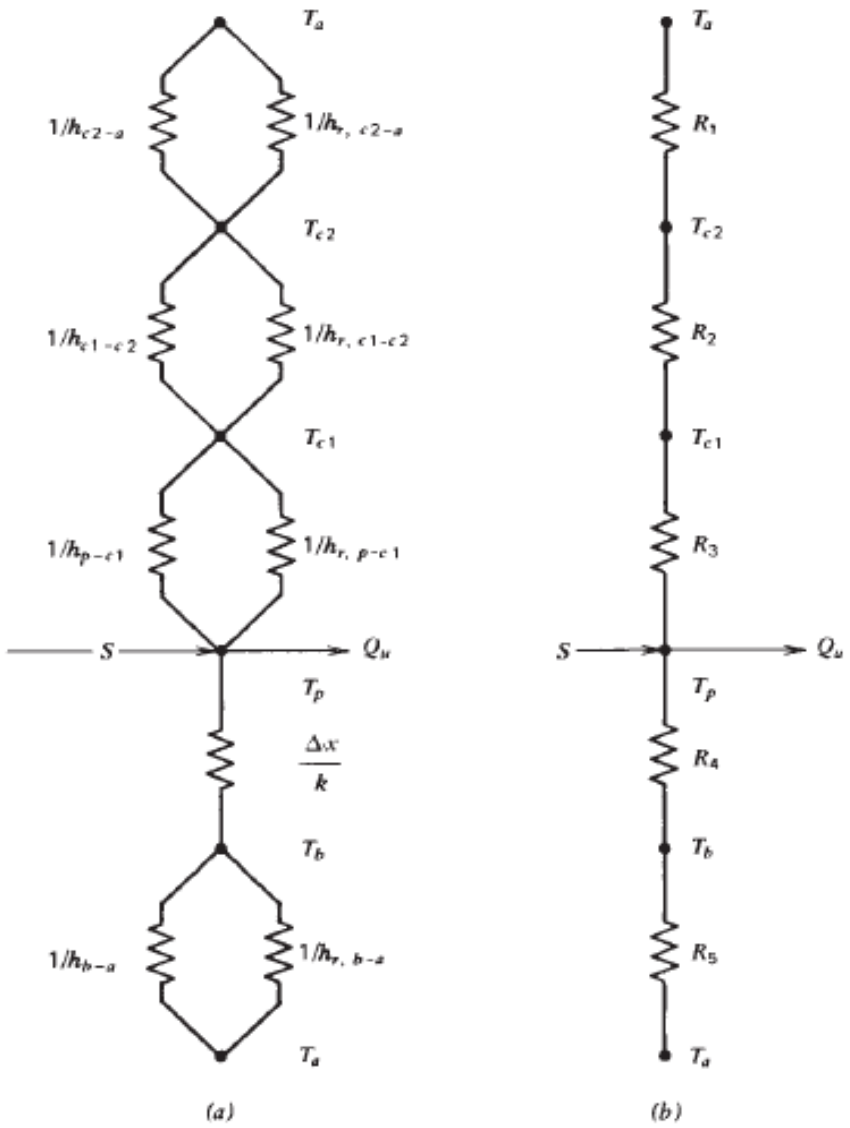

Thermal network for a two-cover flat-plate collector: (a) in terms of conduction, radiation resistances; (b) in terms of resistances between plates.

equal to the heat transfer from the absorber plate to the first cover:

$$q_{\text{loss,top}} = h_{c,p-c1}(T_p - T_{c1}) + \frac{\sigma(T_p^4 - T_{c1}^4)}{\frac{1}{\varepsilon_p} + \frac{1}{\varepsilon_{c1}} - 1} \tag{6.4.1}$$

where $h_{c,p-c1}$ is the convection heat transfer coefficient between two inclined parallel plates from Chapter 3. If the definition of the radiation heat transfer coefficient (Equation 3.10.1) is used, the heat loss becomes

$$q_{\text{loss,top}} = (h_{c,p-c1} + h_{r,p-c1})(T_p - T_{c1}) \tag{6.4.2}$$

where

$$h_{r,p-c1} = \frac{\sigma(T_p + T_{c1})(T_p^2 + T_{c1}^2)}{\dfrac{1}{\varepsilon_p} + \dfrac{1}{\varepsilon_{c1}} - 1} \tag{6.4.3}$$

The resistance R_3 can then be expressed as

$$R_3 = \frac{1}{h_{c,p-c1} + h_{r,p-c1}} \tag{6.4.4}$$

The resistance from the top cover to the surroundings has the same form as Equation 6.4.4, but the convection heat transfer coefficient h_w is given in Section 3.15. The radiation resistance from the top cover accounts for radiation exchange with the sky at T_s. For convenience, we reference this resistance to the ambient temperature T_a, so that the radiation heat transfer coefficient can be written as

$$h_{r,c2-a} = \frac{\sigma\varepsilon_c(T_{c2} + T_s)(T_{c2}^2 + T_s^2)(T_{c2} - T_s)}{T_{c2} - T_a} \tag{6.4.5}$$

The resistance to the surroundings R_1 is then given by

$$R_1 = \frac{1}{h_w + h_{r,c2-a}} \tag{6.4.6}$$

For this two-cover system, the top loss coefficient from the collector plate to the ambient is

$$U_t = \frac{1}{R_1 + R_2 + R_3} \tag{6.4.7}$$

temperature is used to find the next cover temperature, and so on. For any two adjacent covers or plate, the new temperature of plate or cover j can be expressed in terms of the temperature of plate or cover i as

$$T_j = T_j - \frac{U_t(T_p - T_a)}{h_{c,i-j} + h_{r,i-j}} \tag{6.4.8}$$

NATURAL CONVECTION BETWEEN FLAT PARALLEL PLATES AND BETWEEN CONCENTRIC CYLINDERS

The rate of heat transfer between two plates inclined at some angle to the horizon is of obvious importance in the performance of flat-plate collectors. Free-convection heat transfer data are usually correlated in terms of two or three dimensionless parameters: the Nusselt number Nu, the Rayleigh number Ra, and the Prandtl number Pr. Some authors correlate data in terms of the Grashof number, which is the ratio of the Rayleigh number to the Prandtl number.

The Nusselt, Rayleigh, and Prandtl numbers are given by[5]

$$\mathrm{Nu} = \frac{hL}{k} \tag{3.11.1}$$

$$\mathrm{Ra} = \frac{g\beta'\,\Delta T\,L^3}{\nu\alpha} \tag{3.11.2}$$

$$\mathrm{Pr} = \frac{\nu}{\alpha} \tag{3.11.3}$$

Where h = heat transfer coefficient [W/m^2 K]
L = plate spacing [m]
k = thermal conductivity [W/m K]
g = gravitational constant [m/s^2]
β' = volumetric coefficient of expansion (for an ideal gas, $\beta' = 1/T$) [1/K]
ΔT = temperature difference between plates [K]
ν = kinematic viscosity [m^2/s]
α = thermal diffusivity [m^2/s]

In a more recent experimental study using air, Hollands et al. (1976) give the relationship between the Nusselt number and Rayleigh number for tilt angles from 0 to 75° as

$$\mathrm{Nu} = 1 + 1.44\left[1 - \frac{1708(\sin\ 1.8\beta)^{1.6}}{\mathrm{Ra}\ \cos\ \beta}\right]\left[1 - \frac{1708}{\mathrm{Ra}\ \cos\ \beta}\right]^{+} + \left[\left(\frac{\mathrm{Ra}\ \cos\ \beta}{5830}\right)^{1/3} - 1\right]^{+} \tag{3.11.4}$$

where the meaning of the + exponent is that only positive values of the terms in the square brackets are to be used (i.e., use zero if the term is negative).

Example 3.11.1

Find the convection heat transfer coefficient between two parallel plates separated by 25 mm with a 45° tilt. The lower plate is at 70°C and the upper plate is at 50°C.

Solution

At the mean air temperature of 60°C air properties are $k = 0.029$ W/m K, $T = 333$ K so $\beta' = 1/333$, $\nu = 1.88 \times 10^{-5}$ m^2/s, and $\alpha = 2.69 \times 10^{-5}$ m^2/s. (Property data are from EES; www.fchart.com.) The Rayleigh number is

$$\mathrm{Ra} = \frac{9.81 \times 20 \times (0.025)^3}{333 \times 1.88 \times 10^{-5} \times 2.69 \times 10^{-5}} = 1.82 \times 10^4$$

From Equation 3.11.4 or Figure 3.11.1 the Nusselt number is 2.4. The heat transfer coefficient is found from

$$h = \mathrm{Nu}\,\frac{k}{L} = \frac{2.4 \times 0.029}{0.025} = 2.78\ \mathrm{W/m^2\ K}$$

Example 6.4.1

Calculate the top loss coefficient for an absorber with a single glass cover having the following specifications:

Plate-to-cover spacing	25 mm
Plate emittance	0.95
Ambient air and sky temperature	10°C
Wind heat transfer coefficient	10 W/m^2 °C
Mean plate temperature	100°C
Collector tilt	45°
Glass emittance	0.88

When :1) T_c=35 °C, 2) T_c=48.5 °C. Nu=3.19, k=0.0293 W/m. °C, Pr=0.7

Solution

For this single-glass-cover system, Equation 6.4.7 becomes

$$U_t = \left(\frac{1}{h_{c,p-c} + h_{r,p-c}} + \frac{1}{h_w + h_{r,c-a}} \right)^{-1}$$

The convection coefficient between the plate and the cover $h_{c,p-c}$ can be found using the methods of Section 3.11. The radiation coefficient from the plate to the cover $h_{r,p-c}$ is

$$h_{r,p-c} = \frac{\sigma (T_p^2 + T_c^2)(T_p - T_c)}{\frac{1}{\varepsilon_p} + \frac{1}{\varepsilon_c} - 1}$$

The radiation coefficient for the cover to the air $h_{r,c-a}$ is given as

$$h_{r,c-a} = \varepsilon_c \sigma (T_c^2 + T_s^2)(T_c + T_s)$$

The equation for the cover glass temperature is based on Equation 6.4.8:

$$T_c = T_p - \frac{U_t (T_p - T_a)}{h_{c,p-c} + h_{r,p-c}}$$

The procedure is to estimate the cover temperature, from which $h_{c,p-c}$, $h_{r,p-c}$ and $h_{r,c-a}$ are calculated. With these heat transfer coefficients and h_w, the top loss coefficient is calculated. These results are then used to calculate T_c from the preceding equation. If T_c is close to the initial guess, no further calculations are necessary. Otherwise, the newly calculated T_c is used and the process is repeated.

With an assumed value of the cover temperature of 35°C, the two radiation coefficients become

$$h_{r,p-c} = 7.60 \text{ W/m}^2 \text{ °C}, \quad h_{r,c-a} = 5.16 \text{ W/m}^2 \text{ °C}$$

Equation 3.11.4 is used to calculate the convection coefficient between the plate and the cover. The mean temperature between the plate and the cover is 67.5°C so the air properties are $\nu = 1.96 \times 10^{-5}$ m^2/s, $k = 0.0293$ W/m °C, $T = 340.5$ K, and Pr = 0.7. The Rayleigh number is

$$\text{Ra} = \frac{9.81(100 - 35)(0.025)^3(0.7)}{340.5(1.96 \times 10^{-5})^2} = 5.33 \times 10^4$$

and from Equation 3.11.4 the Nusselt number is 3.19. The convective heat transfer coefficient is

$$h = \text{Nu}\,\frac{k}{L} = 3.19\,\frac{0.0293}{0.025} = 3.73 \text{ W/m}^2 \text{ °C}$$

(The same result is obtained from Figures 3.11.1 and 3.11.2. From Figure 3.11.2, $F_1 = 0.46$ and $F_2 = 0.84$. The value of $F_1\,\Delta T\,l^3$ is 4.7×10^5. From Figure 3.11.1, $F_2 hl = 78$. Then $h = 3.7$ W/m^2 °C.) The first estimate of U_t is then

$$U_t = \left(\frac{1}{3.73 + 7.60} + \frac{1}{5.16 + 10.0}\right)^{-1} = 6.49 \text{ W/m}^2 \text{ °C}$$

The cover temperature is

$$T_c = 100 - \frac{6.49 \times 90}{3.73 + 7.60} = 48.5 \text{ °C}$$

With this new estimate of the cover temperature, the various heat transfer coefficients become

$$h_{r,p-c} = 8.03 \text{ W/m}^2 \text{ °C}, \quad h_{r,c-a} = 5.53 \text{ W/m}^2 \text{ °C}, \quad h_{c,p-c} = 3.52 \text{ W/m}^2 \text{ °C}$$

and the second estimate of U_t is

$$U_t = 6.62 \text{ W/m}^2 \text{ °C}$$

Hint:

$$R_a = \frac{g(T_p - T_c)L^3 \times \mathrm{Pr}}{T_{p-c} \times \upsilon^2}$$

$$\mathrm{Nu} = 1 + 1.44\left[1 - \frac{1708(\sin\ 1.8\beta)^{1.6}}{\mathrm{Ra}\ \cos\ \beta}\right]\left[1 - \frac{1708}{\mathrm{Ra}\ \cos\ \beta}\right]^{+} + \left[\left(\frac{\mathrm{Ra}\ \cos\ \beta}{5830}\right)^{1/3} - 1\right]^{+} \quad (3.11.4)$$

Wind heat transfer coefficient: $h_w=2.8+3\times V$
Convection heat transfer coefficient between plate-cover: $h_{c,p\text{-}c}=Nu\times k/L$

Another model to estimate the top loss coeffiecent:-

$$U_t = \left(\frac{N}{\frac{C}{T_{pm}}\left[\frac{(T_{pm} - T_a)}{(N + f)}\right]^e} + \frac{1}{h_w}\right)^{-1} + \frac{\sigma(T_{pm} + T_a)(T_{pm}^2 + T_a^2)}{\frac{1}{\varepsilon_p + 0.00591Nh_w} + \frac{2N + f - 1 + 0.133\varepsilon_p}{\varepsilon_g} - N} \quad (6.4.9)$$

where N = number of glass covers
$f = (1 + 0.089h_w - 0.1166h_w\varepsilon_p)(1 + 0.07866N)$
$C = 520(1 - 0.000051\beta^2)$ for $0^\circ < \beta < 70^\circ$; for $70^\circ < \beta < 90^\circ$, use $\beta = 70^\circ$
$e = 0.430(1 - 100/T_{pm})$
β = collector tilt (deg)
ε_g = emittence of glass (0.88)
ε_p = emittence plate
T_a = ambient temperature (K)
T_{pm} = mean plate temperature (K)
h_w = wind heat transfer coefficient (W/m^2 °C)

Example 6.4.2

Determine the collector top loss coefficient for a single glass cover with the following specifications:

Plate-to-cover spacing	25 mm
Plate emittance	0.95
Ambient temperature	10°C
Mean plate temperature	100°C
Collector tilt	45°
Wind heat transfer coefficient	10 W/m^2 °C

Solution

From the definitions of f, C, and e in Equation 6.4.9

$$f = [1.0 + 0.089(10) - 0.1166(10)(0.95)](1 + 0.07866) = 0.844$$

$$C = 520[1 - 0.000051(45)^2] = 466$$

$$e = 0.430\left(1 - \frac{100}{373}\right) = 0.315$$

From Equation 6.4.9

$$U_t = \left[\frac{1}{\frac{466}{373}\left(\frac{373 - 283}{1 + 0.844}\right)^{0.315}} + \frac{1}{10}\right]^{-1} + \frac{5.67 \times 10^{-8}(373 + 283)(373^2 + 283^2)}{\frac{1}{0.95 + 0.00591 \times 1 \times 10} + \frac{2 + 0.844 - 1 + 0.133 \times 0.95}{0.88} - 1}$$

$$= 2.98 + 3.65 = 6.6 \text{ W/m}^2\ ^\circ\text{C}$$

The energy loss through the bottom of the collector is represented by two series resistors, R_4 and R_5, in Figure 6.4.1, where R_4 represents the resistance to heat flow through the insulation and R_5 represents the convection and radiation resistance to the environment. The magnitudes of R_4 and R_5 are such that it is usually possible to assume R_5 is zero and all resistance to heat flow is due to the insulation. Thus, the back loss coefficient U_b is approximately[3]

$$U_b = \frac{1}{R_4} = \frac{k}{L} \tag{6.4.10}$$

where k and L are the insulation thermal conductivity and thickness, respectively.

For most collectors the evaluation of edge losses is complicated. However, in a well-designed system, the edge loss should be small so that it is not necessary to predict it with great accuracy. Tabor (1958) recommends edge insulation of about the same thickness as bottom insulation. The edge losses are then estimated by assuming one-dimensional sideways heat flow around the perimeter of the collector system. The losses through the edge should be referenced to the collector area. If the edge loss coefficient–area product is $(U/A)_{\text{edge}}$, then the edge loss coefficient, based on the collector area A_c, is

$$U_e = \frac{(UA)_{\text{edge}}}{A_c} \tag{6.4.11}$$

If it is assumed that all losses occur to a common sink temperature T_a, the collector overall loss coefficient U_L is the sum of the top, bottom, and edge loss coefficients:

$$U_L = U_t + U_b + U_e \tag{6.4.12}$$

Example 6.4.3

For the collector of Example 6.4.2 with a top loss coefficient of 6.6 W/m^2 °C, calculate the overall loss coefficient with the following additional specifications:

Back-insulation thickness	50 mm
Insulation conductivity	0.045 W/m °C
Collector bank length	10 m
Collector bank width	3 m
Collector thickness	75 mm
Edge insulation thickness	25 mm

Solution

The bottom loss coefficient is found from Equation 6.4.10:

$$U_b = \frac{k}{L} = \frac{0.045}{0.050} = 0.9 \text{ W/m}^2 \text{ °C}$$

The edge loss coefficient for the 26-m perimeter is found from Equation 6.4.11:

$$U_e = \frac{(0.045/0.025) \times 26 \times 0.075}{30} = 0.12 \text{ W/m}^2 \text{ °C}$$

The collector overall loss coefficient is then

$$U_L = 6.6 + 0.9 + 0.1 = 7.6 \text{ W/m}^2 \text{ °C}$$ ■

TEMPERATURE DISTRIBUTION BETWEEN TUBES AND THE COLLECTOR EFFICIENCY FACTOR

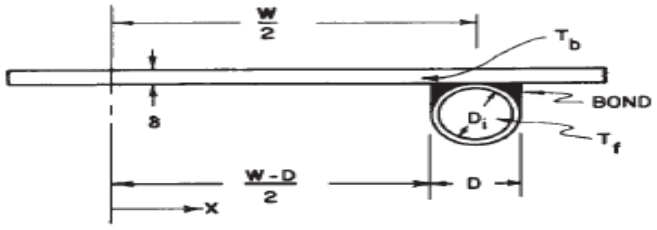

Figure 6.5.1 Sheet and tube dimensions.

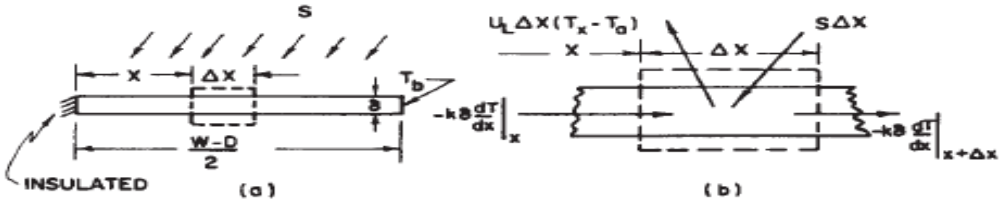

Figure 6.5.2 Energy balance on fin element.

$$m = \sqrt{\frac{U_L}{k\delta}} \tag{6.5.4a}$$

$$\frac{T - T_a - S/U_L}{T_b - T_a - S/U_L} = \frac{\cosh\, mx}{\cosh\, m(W - D)/2} \tag{6.5.8}$$

The energy conducted to the region of the tube per unit of length in the flow direction can now be found by evaluating Fourier's law at the fin base:

$$q'_{\text{fin}} = -k\,\delta \left.\frac{dT}{dx}\right|_{x=(W-D)/2} = \left(\frac{k\,\delta m}{U_L}\right)[S - U_L(T_b - T_a)]\,\tanh\,\frac{m(W - D)}{2} \tag{6.5.9}$$

but $k\,\delta m/U_L$ is just $1/m$. Equation 6.5.9 accounts for the energy collected on only one side of a tube; for both sides, the energy collection is

$$q'_{\text{fin}} = (W - D)[S - U_L(T_b - T_a)]\,\frac{\tanh\, m(W - D)/2}{m(W - D)/2} \tag{6.5.10}$$

It is convenient to use the concept of a fin efficiency to rewrite Equation 6.5.10 as

$$q'_{\text{fin}} = (W - D)F[S - U_L(T_b - T_a)] \tag{6.5.11}$$

where

$$F = \frac{\tanh[m(W - D)/2]}{m(W - D)/2} \tag{6.5.12}$$

The function F is the standard fin efficiency for straight fins with rectangular profile and is plotted in Figure 6.5.3.

We now wish to eliminate T_b from the equations and obtain an expression for the useful gain in terms of known dimensions, physical parameters, and the local fluid temperature. Solving Equation 6.5.15 for T_b, substituting it into Equation 6.5.14, and solving the result for the useful gain, we obtain

$$q'_u = W F'[S - U_L(T_f - T_a)] \tag{6.5.17}$$

where the collector efficiency factor F' is given as

$$F' = \frac{1/U_L}{W\left[\dfrac{1}{U_L\,[D + (W - D)\,F]} + \dfrac{1}{C_b} + \dfrac{1}{\pi D_i h_{fi}}\right]} \tag{6.5.18}$$

Example 6.5.1

Calculate the collector efficiency factor for the following specifications:

Overall loss coefficient	8.0 W/m^2 °C
Tube spacing	150 mm
Tube diameter (inside)	10 mm
Plate thickness	0.5 mm
Plate thermal conductivity (copper)	385 W/m °C
Heat transfer coefficient inside tubes	300 W/m^2 °C
Bond conductance	∞ W/m °C

Solution

The fin efficiency factor F, from Equations 6.5.4a and 6.5.12, is determined as follows:

$$m = \left(\frac{8}{385 \times 5 \times 10^{-4}}\right)^{1/2} = 6.45 \text{ [1/m]}$$

$$F = \frac{\tanh[6.45(0.15 - 0.01)/2]}{6.45(0.15 - 0.01)/2} = 0.937$$

The collector efficiency factor F' is found from Equation 6.5.18:

$$F' = \frac{1/8}{0.15\left[\frac{1}{8\,[0.01 + (0.15 - 0.01)\,0.937]} + \frac{1}{\infty} + \frac{1}{\pi \times 0.01 \times 300}\right]} = 0.841$$

COLLECTOR HEAT REMOVAL FACTOR AND FLOW FACTOR

It is convenient to define a quantity that relates the actual useful energy gain of a collector to the useful gain if the whole collector surface were at the fluid inlet temperature. This quantity is called the collector heat removal factor F_R. In equation form it is

$$F_R = \frac{\dot{m}C_p(T_{fo} - T_{fi})}{A_c[S - U_L(T_{fi} - T_a)]} \tag{6.7.1}$$

The collector heat removal factor can be expressed as

$$F_R = \frac{\dot{m}C_p}{A_c U_L}\left[\frac{T_{fo} - T_{fi}}{S/U_L - (T_{fi} - T_a)}\right]$$

$$= \frac{\dot{m}C_p}{A_c U_L}\left[\frac{[S/U_L - (T_{fi} - T_a)] - [S/U_L - (T_{fo} - T_a)]}{S/U_L - (T_{fi} - T_a)}\right] \tag{6.7.2}$$

or

$$F_R = \frac{\dot{m}C_p}{A_c U_L}\left[1 - \frac{S/U_L - (T_{fo} - T_a)}{S/U_L - (T_{fi} - T_a)}\right] \tag{6.7.3}$$

which from Equation 6.6.4 can be expressed as

$$F_R = \frac{\dot{m}C_p}{A_c U_L}\left[1 - \exp\left(-\frac{A_c U_L F'}{\dot{m}C_p}\right)\right] \tag{6.7.4}$$

To present Equation 6.7.4 graphically, it is convenient to define the collector flow factor F'' as the ratio of F_R to F'. Thus

$$F'' = \frac{F_R}{F'} = \frac{\dot{m}C_p}{A_c U_L F'}\left[1 - \exp\left(-\frac{A_c U_L F'}{\dot{m}C_p}\right)\right] \tag{6.7.5}$$

are then at a minimum. The collector heat removal factor times this maximum possible useful energy gain is equal to the actual useful energy gain Q_u :

$$Q_u = A_c F_R[S - U_L(T_i - T_a)] \tag{6.7.6}$$

Example 6.7.1

Calculate the daily useful gain and efficiency of an array of 10 solar collector modules installed in parallel near Boulder, Colorado, at a slope of 60° and a surface azimuth of 0°. The hourly radiation on the plane of the collector I_T, the hourly radiation absorbed by the absorber plate S, and the hourly ambient temperature T_a are given in the table at the end of this example. The methods of Sections 2.15, 2.16, and 5.9 can be used to find I_T and S knowing the hourly horizontal radiation, the collector orientation, and the collector optical properties. For the collector assume the overall loss coefficient U_L to be 8.0 W/m^2 °C and the plate efficiency factor F' to be 0.841 (from Example 6.5.1). The water flow rate through each 1 × 2-m collector panel is 0.03 kg/s and the inlet water temperature remains constant at 40°C. Assume a controller turns off the water flow whenever the outlet temperature is less than the inlet temperature.

Solution

The dimensionless collector mass flow rate is

$$\frac{\dot{m}C_p}{A_c U_L F'} = \frac{0.03 \times 4190}{2 \times 8 \times 0.841} = 9.35$$

so that the collector flow factor, from Equation 6.7.5 (or Figure 6.7.1), is

$$F'' = 9.35\left[1 - \exp\left(-\frac{1}{9.35}\right)\right] = 0.948$$

and the heat removal factor is

$$F_R = F'F'' = 0.841 \times 0.948 = 0.797$$

The average loss rate for the hour 10 to 11, based on an inlet temperature of 40°C, is

$$U_L(T_i - T_a) = 8(40 - 2) \times 3600 = 1.09 \text{ MJ/m}^2 \text{ h}$$

and the average useful energy gain per unit of collector area is

$$q_u = \frac{Q_u}{A_c} = 0.797(3.29 - 1.09) \times 10^6 = 1.76 \text{ MJ/m}^2 \text{ h}$$

The collector efficiency for this hour is found from Equation 6.2.2:

$$\eta = \frac{Q_u}{I_T A_c} = \frac{q_u}{I_T} = \frac{1.76}{3.92} = 0.45$$

and the day-long collector efficiency is

$$\eta_{\text{day}} = \frac{\sum q_u}{\sum I_T} = \frac{7.57}{19.79} = 0.38$$

The daily useful energy gain of the 10 collector modules in the array is

$$\sum Q_u = 10 \times 2 \times 7.57 \times 10^6 = 150 \text{ MJ}$$

Time	T_a (°C)	I_T (MJ/m² h)	S (MJ/m² h)	$U_L(T_i - T_a)$ (MJ/m² h)	q_u (MJ/m² h)	η
7–8	−11	0.02	0.01	1.46	0.00	0.00
8–9	−8	0.43	0.35	1.38	0.00	0.00
9–10	−2	0.99	0.82	1.21	0.00	0.00
10–11	2	3.92	3.29	1.09	1.76	0.45
11–12	3	3.36	2.84	1.07	1.42	0.42
12–1	6	4.01	3.39	0.98	1.93	0.48
1–2	7	3.84	3.21	0.95	1.81	0.47
2–3	8	1.96	1.63	0.92	0.57	0.29
3–4	9	1.21	0.99	0.89	0.08	0.07
4–5	7	0.05	0.04	0.95	0.00	0.00
Sum		19.79			7.57	

■

Solar Collectors Connection Types

Connection options

Legend

Corrugated hose return (cold)

Corrugated hose flow (hot) with collector sensor

Connection options for 1 collector
Caution: Sensor is positioned on the flow side (hot).

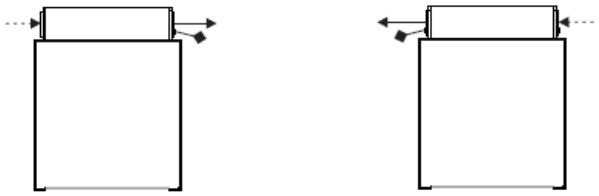

Connection options for 2 or more adjacent collectors
Caution: Sensor is positioned on the flow side (hot).

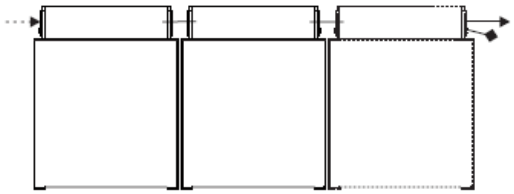

Reverse connection of the flow direction is possible.

Connection options for 2 or more collectors above one another
Caution: Sensor is positioned on the flow side (hot).

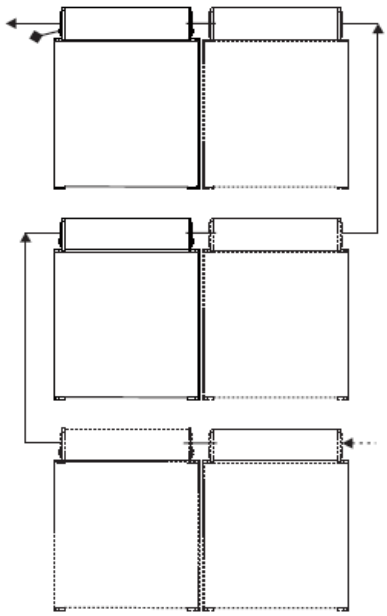

Connection options for 1 or 2 adjacent collectors and 2 or 3 collectors above one another
Caution: Sensor is positioned on the flow side (hot).

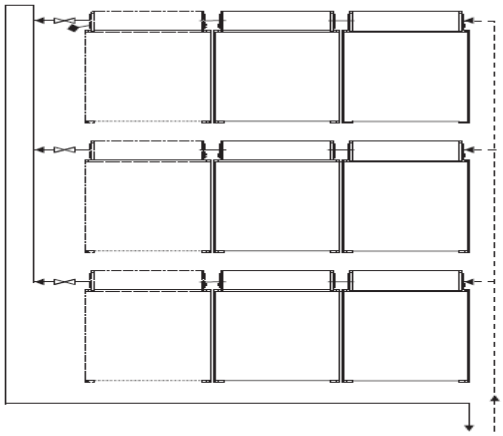

Note!
In order to facilitate bleeding and equalise the collector arrays, one shut-off ball valve should be built into each outlet.

Connection options for 1 or 2 adjacent series connections and multiple series connections above one another
Caution: Sensor is positioned on the flow side (hot).

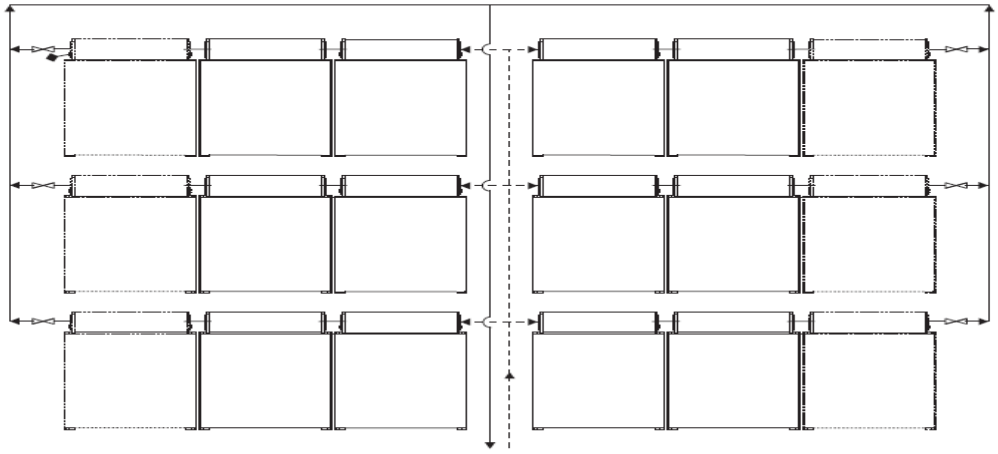

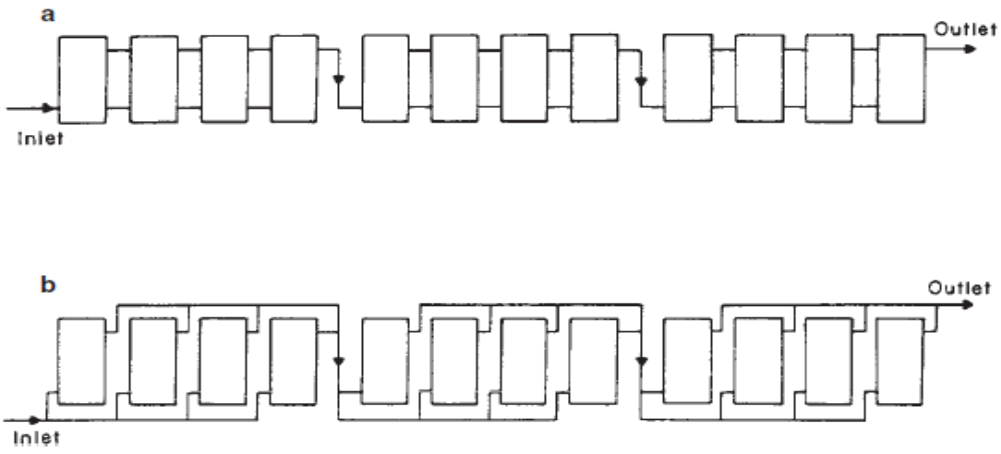

Figure 6.21.3 Examples of alternative methods of connecting arrays in (a) series–parallel and (b) parallel–series arrangements, as recommended by Dunkle and Davey (1970).

MEAN FLUID AND PLATE TEMPERATURES

To evaluate collector performance, it is necessary to know the overall loss coefficient and the internal fluid heat transfer coefficients. However, both U_L and h_{fi} are to some degree functions of temperature. The mean fluid temperature can be found by integrating Equation 6.6.3 from zero to L :

$$T_{fm} = \frac{1}{L}\int_0^L T_f(y)\,dy \tag{6.9.1}$$

Performing this integration and substituting F_R from Equation 6.7.4 and Q_u from Equation 6.7.6, the mean fluid temperature was shown by Klein et al. (1974) to be

$$T_{fm} = T_{fi} + \frac{Q_u/A_c}{F_R U_L}(1 - F'') \tag{6.9.2}$$

This is the proper temperature for evaluating fluid properties.

When a collector is producing useful energy, the mean plate temperature will always be greater than the mean fluid temperature due to the heat transfer resistance between the absorbing surface and the fluid. This temperature difference is usually small for liquid heating collectors but may be significant for air collectors.

The mean plate temperature can be used to calculate the useful gain of a collector,

$$Q_u = A_c[S - U_L(T_{pm} - T_a)] \tag{6.9.3}$$

If we equate Equations 6.9.3 and 6.7.6 and solve for the mean plate temperature, we have

$$T_{pm} = T_{fi} + \frac{Q_u/A_c}{F_R U_L}(1 - F_R) \tag{6.9.4}$$

Example 6.9.1

Find the mean fluid and plate temperatures for the hour 11 to 12 of Example 6.7.1.

Solution

Assume $U_L = 8.0\ \text{W/m}^2\ ^\circ\text{C}$, $F'' = 0.948$, $F_R = 0.797$, and $q_u = 1.42\ \text{MJ/m}^2\ \text{h}$. We have from Equation 6.9.2

$$T_{fm} = 40 + \frac{1.42 \times 10^6/3600}{8 \times 0.797}(1 - 0.948) = 43^\circ\text{C}$$

The mean plate temperature is found from Equation 6.9.4:

$$T_{pm} = 40 + \frac{1.42 \times 10^6/3600}{8 \times 0.797}(1 - 0.797) = 53^\circ\text{C}$$

■

AIR HEATERS

Figure 6.14.1 shows six designs for air heating collectors. Also on this figure are equations for the collector efficiency factors that have been derived for these geometries. For (e) and (f), the Löf overlapped glass plates and the matrix air heater, the analyses to date have not put the results in a generalized form. For these two situations, it is necessary to resort to numerical techniques for analysis. Selcuk (1971) has analyzed the overlapped glass plate system. Chiou et al. (1965), Hamid and Beckman (1971), and Neeper (1979) have studied the matrix-type air heaters. Hollands and Shewen (1981) have analyzed the effects of flow passage geometry on h_{fi} and F'.

To illustrate the procedure for deriving F' and U_L for an air heater, we derive the equation for type (a) of Figure 6.14.1. Although type (b) is the more common design for an air heater, type (a) is somewhat more complicated to analyze. Also, type (a) is similar

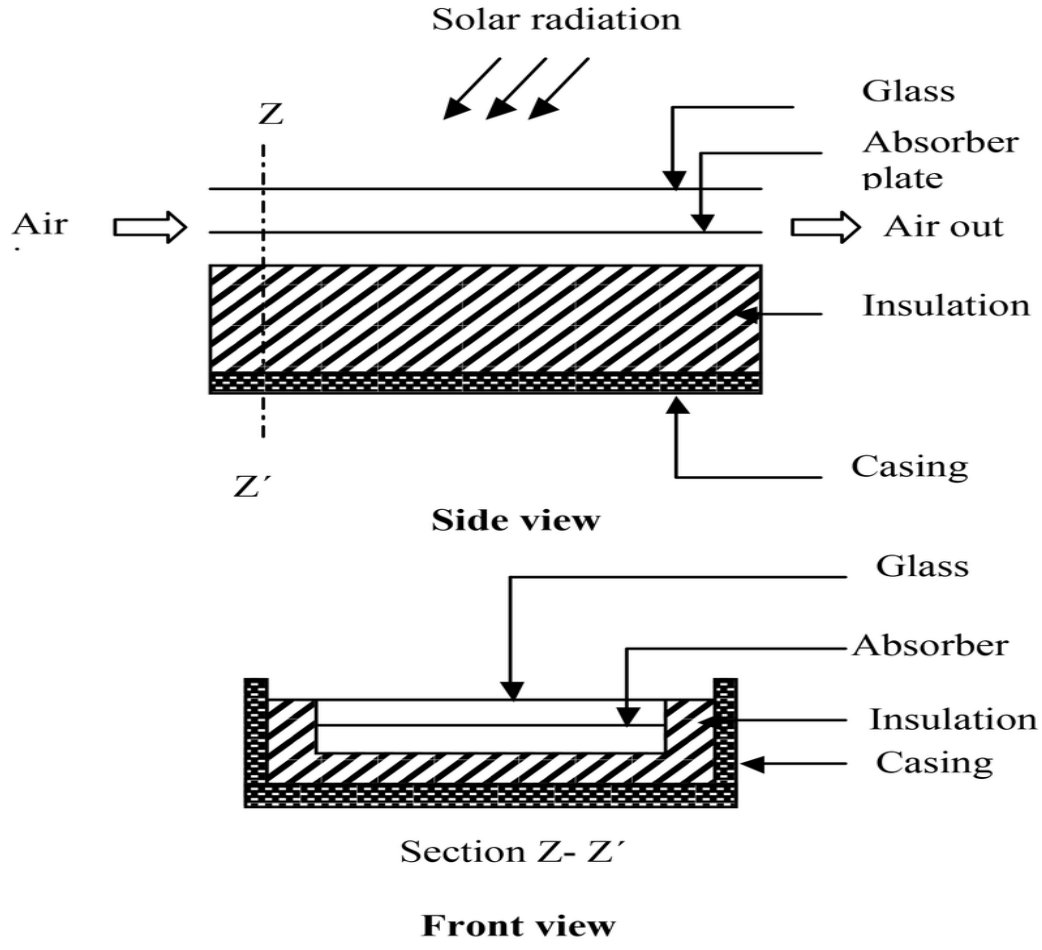

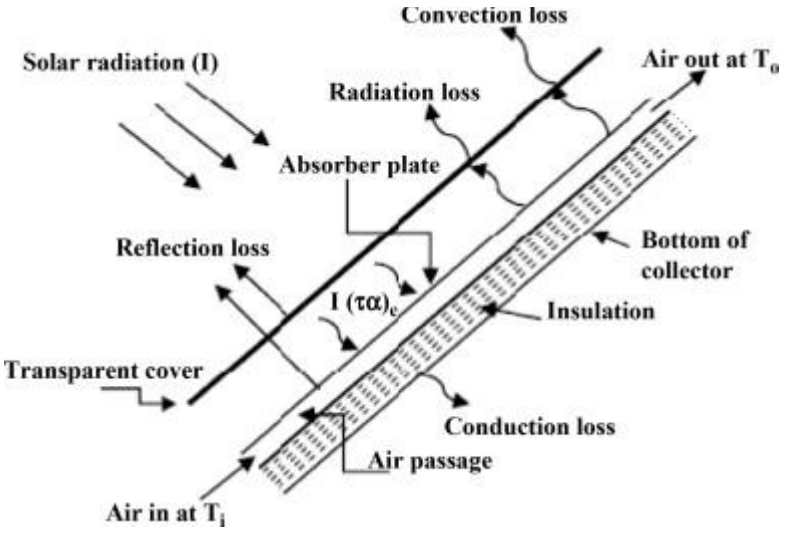
Convection loss
Solar radiation (I)
Air out at T_o
Radiation loss
Absorber plate
Reflection loss
Bottom of collector
$I\ (\tau\alpha)_e$
Insulation
Transparent cover
Conduction loss
Air passage
Air in at T_i

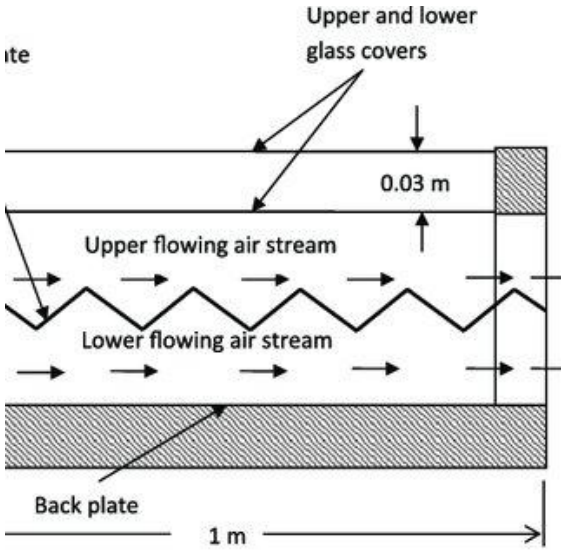
ıte
Upper and lower glass covers
0.03 m
Upper flowing air stream
Lower flowing air stream
Back plate
1 m

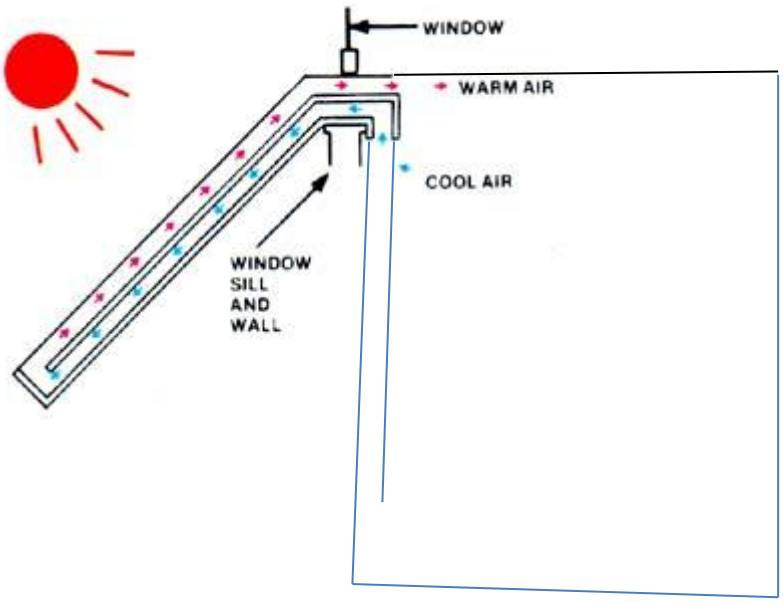
WINDOW
WARM AIR
COOL AIR
WINDOW SILL AND WALL

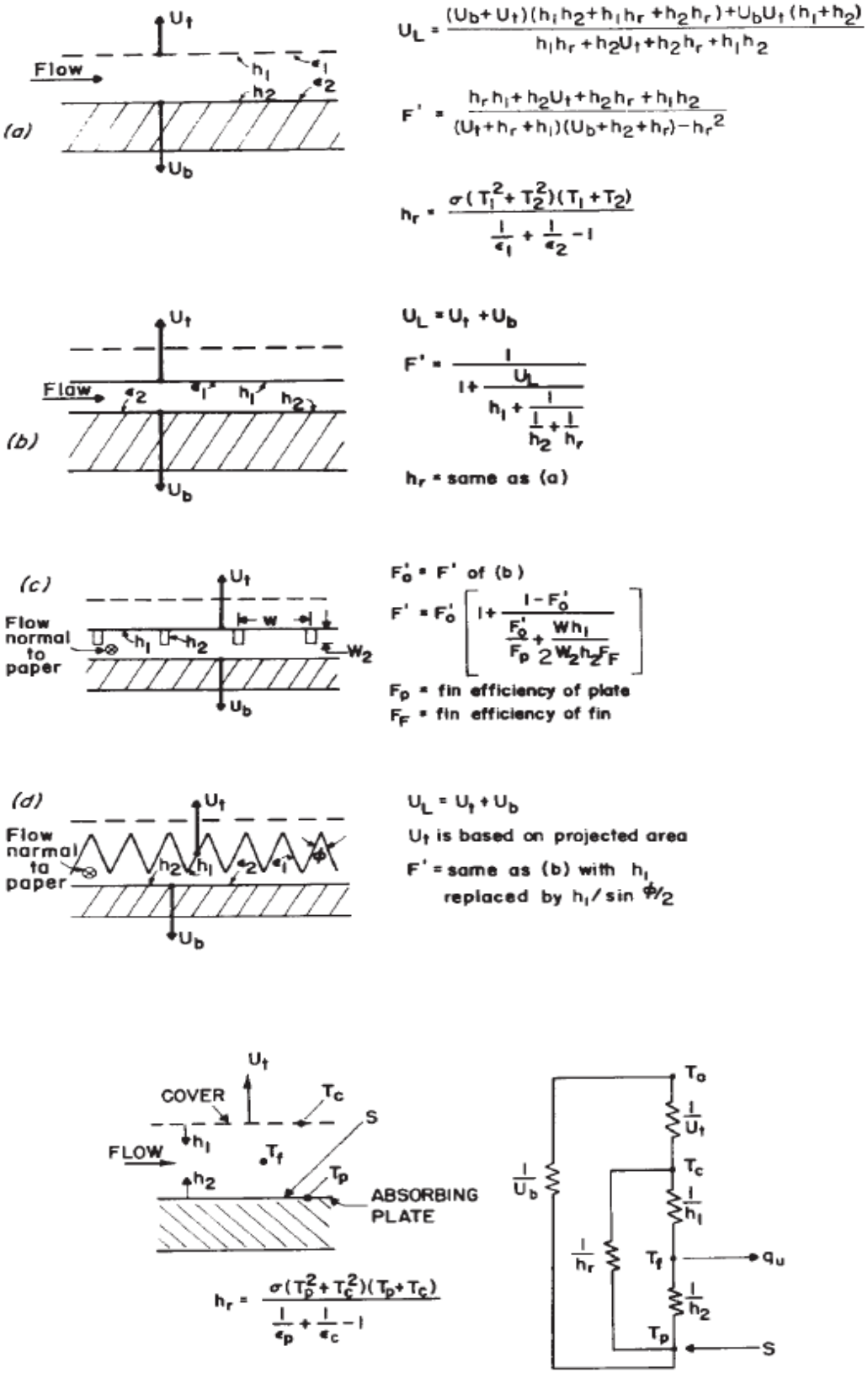

Figure 6.14.2 Type (a) solar air heater and thermal network.

where

$$F' = \frac{h_r h_1 + U_t h_2 + h_2 h_r + h_1 h_2}{(U_t + h_r + h_1)(U_b + h_2 + h_r) - h_r^2} \tag{6.14.7}$$

and

$$U_L = \frac{(U_b + U_t)(h_r h_1 + h_2 h_r + h_1 h_2) + U_b U_t (h_1 + h_2)}{h_r h_1 + U_t h_2 + h_2 h_r + h_1 h_2} \tag{6.14.8}$$

Example 6.14.1

Calculate the outlet temperature and efficiency of a single-cover type (b) air heater of Figure 6.14.1 at a 45° slope when the radiation incident on the collector is 900 W/m^2. The plate-to-cover spacing is 20 mm and the air channel depth is 10 mm. The collector is 1 m wide by 4 m long. The absorber plate is selective with an emittance of 0.1 and the effective transmittance-absorptance product is 0.82. The inlet air temperature is 60°C, the ambient air temperature is 10°C, and the mass flow rate of the air is 0.056 kg/s. The wind heat transfer coefficient is 10 W/m^2 °C and the sum of the back and edge loss coefficients is 1.0 W/m^2 °C (see Example 6.4.3). The emittances of the surfaces of the inside of the duct, ε_1 and ε_2, are both 0.95.

Assume: T_p=70 ^{0}C, U_{top}=3.3 W/m^2. ^{0}C, Re=5490, Nu=15.5, h_c=22 W/m^2. ^{0}C, C_p=1009 J/kg.k, K=

Solution

From Figure 6.4.4(e) with an assumed average plate temperature of 70°C, the top loss coefficient is 3.3 W/m^2 °C, and with the back and edge loss coefficient of 1.0 W/m^2 °C, the overall loss coefficient is 4.3 W/m^2 °C. The radiation coefficient between the two air duct surfaces is estimated by assuming a mean radiant temperature equal to the mean fluid temperature. With an estimated mean fluid temperature of 70°C,[11] we have, from Equations 3.10.2 and 3.10.3,

$$h_r = \frac{4\sigma \overline{T}^3}{1/\varepsilon_1 + 1/\varepsilon_2 - 1} = \frac{4 \times 5.67 \times 10^{-8} \times 343^3}{2/0.95 - 1} = 8.3 \text{ W/m}^2 \text{ °C}$$

plate spacing. The Reynolds number, at an assumed average fluid temperature of 70°C, is

$$\text{Re} = \frac{\rho V D_h}{\mu} = \frac{\dot{m} D_h}{A_f \mu} = \frac{0.056(2 \times 0.01)}{(0.01 \times 1)2.04 \times 10^{-5}} = 5490$$

The length-to-diameter ratio is

$$\frac{L}{D_h} = \frac{4}{2 \times 0.01} = 200$$

Since Re > 2100 and L/D_h is large, the flow is turbulent and fully developed. From Equation 3.14.6

$$\text{Nu} = 0.0158(5490)^{0.8} = 15.5$$

The heat transfer coefficients inside the duct, h_1 and h_2, are then

$$h = 15.5 \frac{k}{D_h} = \frac{15.5 \times 0.029}{2 \times 0.01} = 22 \text{ W/m}^2 \text{ °C}$$

From Figure 6.14.1(b), with $h_1 = h_2 = h$,

$$F' = \left[1 + \frac{U_L}{h + [(1/h) + (1/h_r)]^{-1}}\right]^{-1} = \left[1 + \frac{4.3}{22 + \left(\frac{1}{22} + \frac{1}{8.3}\right)}\right]^{-1} = 0.87$$

The dimensionless capacitance rate is

$$\frac{\dot{m}C_p}{A_c U_L F'} = \frac{0.056 \times 1009}{4 \times 4.3 \times 0.87} = 3.78$$

From Equation 6.7.5 or Figure 6.7.1,

$$F'' = 3.78[1 - e^{-1/3.78}] = 0.88$$

or

$$F_R = F''F' = 0.88 \times 0.87 = 0.77$$

The useful gain, from Equation 6.7.6, is

$$Q_u = 4 \times 0.77[900 \times 0.82 - 4.3(60 - 10)] = 1610 \text{ W}$$

The outlet temperature is

$$T_o = T_i + \frac{Q_u}{\dot{m}C_p} = 60 + \frac{1610}{0.056 \times 1009} = 89^\circ\text{C}$$

It is now necessary to check the assumed mean fluid and absorber plate temperatures. The mean plate temperature is found from Equation 6.9.4,

$$T_{pm} = 60 + \frac{1610/4}{4.3 \times 0.77}(1 - 0.77) = 88^\circ\text{C}$$

and the mean fluid temperature is found from Equation 6.9.2,

$$T_{fm} = 60 + \frac{1610/4}{4.3 \times 0.77}(1 - 0.88) = 74^\circ\text{C}$$

The efficiency is

$$\eta = \frac{Q_u}{A_c G_T} = \frac{1610}{4 \times 900} = 0.45, \ 45\%$$

■

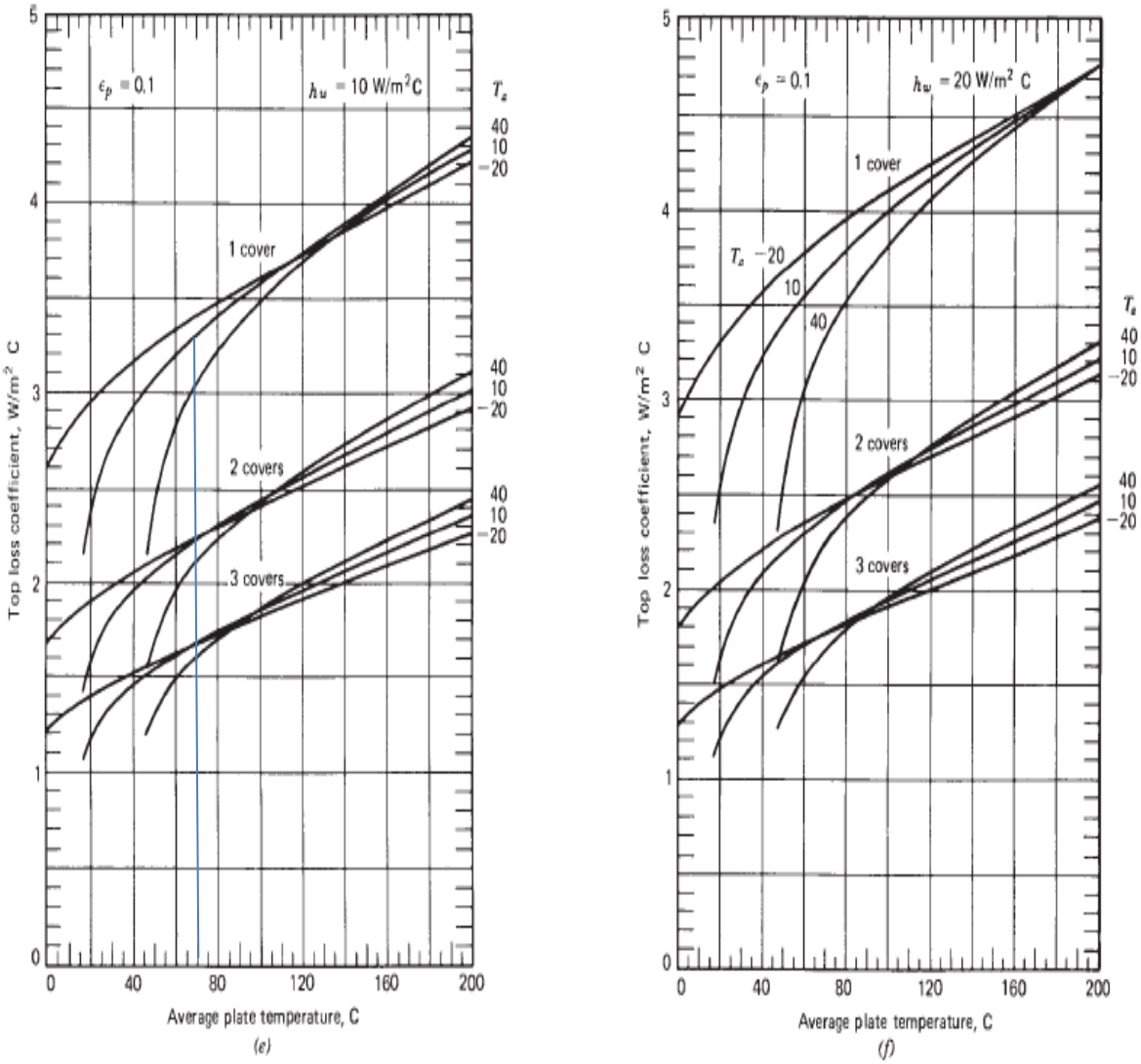

Figure 6.4.4 (*Continued*)

6.17 COLLECTOR TESTS: EFFICIENCY, INCIDENCE ANGLE MODIFIER, AND TIME CONSTANT

The basic method of measuring collector performance is to expose the operating collector to solar radiation and measure the fluid inlet and outlet temperatures and the fluid flow rate. The useful gain is then

$$Q_u = \dot{m}C_p(T_o - T_i) \tag{6.17.1}$$

In addition, radiation on the collector, ambient temperature, and wind speed are also recorded. Thus two types of information are available: data on the thermal output and data on the conditions producing that thermal performance. These data permit the characterization of a collector by parameters that indicate how the collector absorbs energy and how it loses energy to the surroundings.

Equation 6.7.6, which describes the thermal performance of a collector operating under steady conditions, can be written in terms of the incident radiation:

$$Q_u = A_c F_R[G_T(\tau\alpha)_{\text{av}} - U_L(T_i - T_a)] \tag{6.17.2}$$

Here $(\tau\alpha)_{\text{av}}$ is a transmittance-absorptance product that is weighted according to the proportions of beam, diffuse, and ground-reflected radiation on the collector, as discussed in Section 5.9. Testing standards generally require that during a collector test the beam

Equations 6.17.1 and 6.17.2 can be used to define an instantaneous efficiency:

$$\eta_i = \frac{Q_u}{A_c G_T} = F_R(\tau\alpha) - \frac{F_R U_L(T_i - T_a)}{G_T} \tag{6.17.3}$$

and

$$\eta_i = \frac{\dot{m}C_p(T_o - T_i)}{A_c G_T} \tag{6.17.4}$$

These equations are the basis of the standard test methods outlined in this section.

Other equations are also used. European practice is to base collector test results on $T_{f,\text{av}}$, the arithmetic average of the fluid inlet and outlet temperatures.[14] Thus

$$\eta_i = F_{\text{av}}(\tau\alpha) - \frac{F_{\text{av}} U_L(T_{f,\text{av}} - T_a)}{G_T} \tag{6.17.5}$$

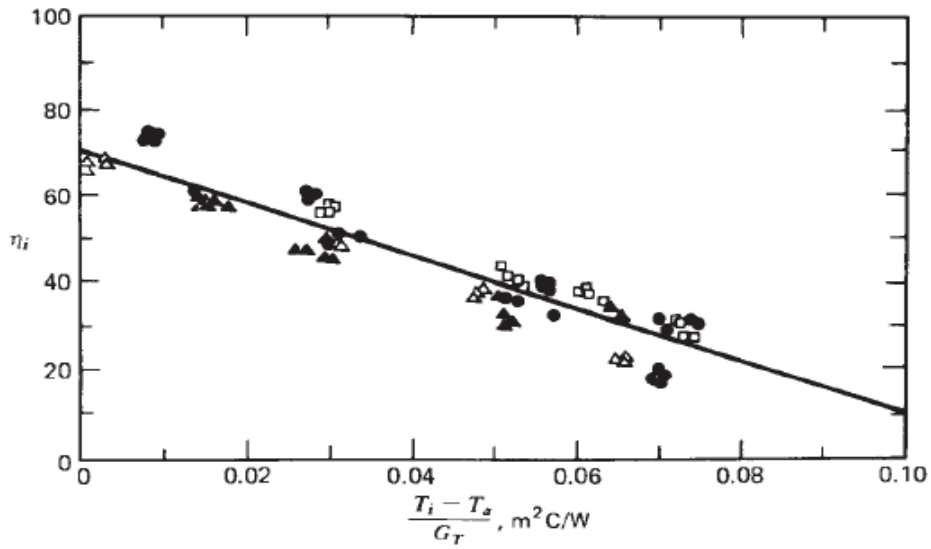

Figure 6.17.2 Experimental collector efficiency data measured for a liquid heating flat-plate collector with one cover and a selective absorber. Sixteen points are shown for each of five test sites. The curve represents the theoretical characteristic derived from points calculated for the test conditions. Adapted from Streed et al. (1979).

Example 6.17.1

A water heating collector with an aperture area of 4.10 m^2 is tested by the ASHRA method, with beam radiation nearly normal to the plane of the collector. The followi information comes from the test:

Q_u (MJ/h)	G_T (W/m^2)	T_i $(^\circ C)$	T_a $(^\circ C)$
9.05	864	18.2	10.0
1.98	894	84.1	10.0

What are $F_R(\tau\alpha)_n$ and $F_R U_L$ for this collector based on aperture area?

Solution

For the first data set,

$$\eta_i = \frac{9.05 \times 1000}{864 \times 3.6 \times 4.10} = 0.71$$

and

$$\frac{T_i - T_a}{G_T} = \frac{18.2 - 10.0}{864} = 0.0095 \text{ m}^2\text{C/W}$$

For the second data set, $\eta_i = 0.15$ and $(T_i - T_a)/G_T = 0.083$ m^{2}C/W. These two points are shown on the plot.

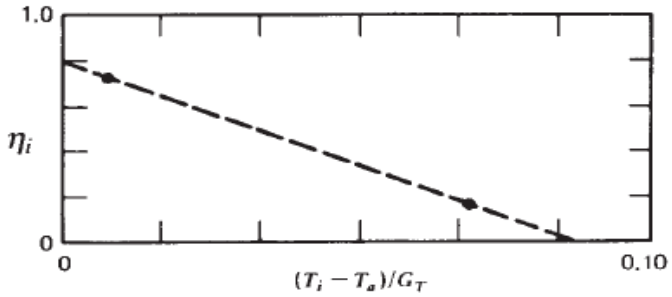

The slope is

$$\frac{0.71 - 0.15}{0.0095 - 0.083} = 7.62 \text{ W/m}^2\ ^\circ\text{C}$$

Then $F_R U_L = -\text{slope} = 7.62$ W/m^{2}C. The intercept of the line of the η_i axis is 0.78, which is $F_R(\tau\alpha)_n$. (In practice, tests produce multiple data points and a least-squares fit would be used to find the best constants.) ■

COLLECTOR PERFORMANCE

There is no fundamental reason why a collector would not operate as well installed in an application as it does on a test stand. However, there are some practical considerations that can influence measured performance on-site. Differences between predicted and measured performance may arise from several sources:

1. Flow of fluid through the collector may not be uniform through all parts of the collector array. Parts of a collector array receiving reduced fluid flow will have lower F_R and poorer performance, resulting in degradation of array performance.
2. Flow rates may not be those at which collectors were tested. The parameter F_R is a function of flow rate for both liquid and air heaters (particularly so for air heating collectors), and changes in flow rate can make significant differences in collector performance.
3. Leaks in air collectors may also introduce differences between predicted and measured performance. Collectors are usually operated at slightly less than atmospheric pressure, resulting in leakage of cool ambient air in and reduced collector outlet temperatures (Close and Yusoff, 1978).
4. Edge and back losses may be different in tests and applications. Edge losses may be reduced in large arrays resulting in smaller U_L than is obtained from measurements on a single module.
5. Duct and pipe losses may be more significant in applications than in tests, as runs may be longer and ducts and pipes may not be as well insulated.

THERMAL TEST DATA CONVERSION

Data from collector tests in the United States are usually expressed in terms of η_i and $(T_i - T_a)/G_T$ as shown in Figures 6.18.2. Practice in some other countries is to express η_i as a function of $(T_{av} - T_a)/G_T$. Test data for air systems are sometimes expressed as η_i as a function of $(T_o - T_a)/G_T$. In this section, methods are presented for converting test results from one format to another.

If test data are plotted as η_i versus $(T_{av} - T_a)/G_T$, where T_{av} is the arithmetic average of inlet and outlet fluid temperatures, the equation of the straight line is[19]

$$\eta_i = F_{av}(\tau\alpha)_n - F_{av}U_L \frac{T_{av} - T_a}{G_T} \tag{6.19.1}$$

If the flow rate of the fluid is known, the intercept $F_{av}(\tau\alpha)_n$ and slope $-F_{av}U_L$ of the curve of Equation 6.19.1 are related to F_RU_L and $F_R(\tau\alpha)_n$. Eliminating η and T_o from Equations 6.17.3 to 6.17.5 (Beckman et al., 1977), these relationships are found to be

$$F_R(\tau\alpha)_n = F_{av}(\tau\alpha)_n \left(1 + \frac{A_c F_{av} U_L}{2\dot{m}C_p}\right)^{-1} \tag{6.19.2a}$$

$$F_{av}(\tau\alpha)_n = F_R(\tau\alpha)_n \left(1 - \frac{A_c F_R U_L}{2\dot{m}C_p}\right)^{-1} \tag{6.19.2b}$$

and

$$F_RU_L = F_{av}U_L \left(1 + \frac{A_c F_{av} U_L}{2\dot{m}C_p}\right)^{-1} \tag{6.19.3a}$$

$$F_{av}U_L = F_RU_L \left(1 - \frac{A_c F_R U_L}{2\dot{m}C_p}\right)^{-1} \tag{6.19.3b}$$

For air heater test data that are presented as plots of η_i, versus $(T_o - T_a)/G_T$, the intercept $F_o(\tau\alpha)_n$ and slope $-F_oU_L$ of these curves can be converted to F_RU_L and

$F_R(\tau\alpha)_n$ by the following:

$$F_R(\tau\alpha)_n = F_o(\tau\alpha)_n\left(\frac{1 + A_c F_o U_L}{\dot{m} C_p}\right)^{-1} \tag{6.19.4a}$$

$$F_o(\tau\alpha)_n = F_R(\tau\alpha)_n\left(1 - \frac{A_c F_R U_L}{\dot{m} C_p}\right)^{-1} \tag{6.19.4b}$$

$$F_R U_L = F_o U_L\left(1 + \frac{A_c F_o U_L}{\dot{m} C_p}\right)^{-1} \tag{6.19.5a}$$

$$F_o U_L = F_R U_L\left(1 - \frac{A_c F_R U_L}{\dot{m} C_p}\right)^{-1} \tag{6.19.5b}$$

Example 6.19.1

What are $F_R U_L$ and $F_R(\tau\alpha)_n$ for the two-cover air heater having $F_o U_L = 3.70$ W/m^2 °C and $F_o(\tau\alpha)_n = 0.64$? The volumetric flow rate per unit area is 10.1 liters/m^2 s.

Solution

For air at 20°C, $C_p = 1006$ J/kg and $\rho = 1.204$ kg/m^3 or 0.001204 kg/liter. Then

$$\frac{A_c F_o U_L}{\dot{m} C_p} = \frac{3.7}{10.1 \times 0.001204 \times 1006} = 0.302$$

Then from Equations 6.19.4a and 6.19.5a,

$$F_R(\tau\alpha)_n = \frac{0.64}{1 + 0.302} = 0.49$$

$$F_R U_L = \frac{3.7}{1 + 0.302} = 2.84 \text{ W/m}^2\ ^\circ\text{C}$$

■

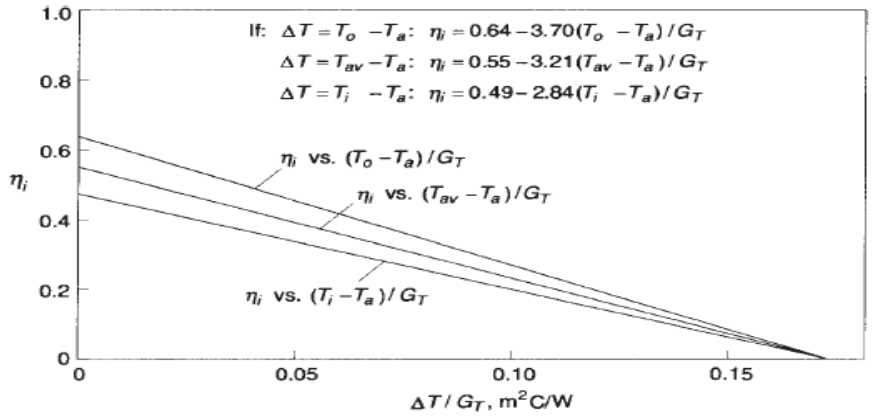

Figure 6.19.1 Efficiency curves for an air heating flat-plate collector plotted as functions of T_i, T_{av}, and T_o.

FLOW RATE CORRECTIONS TO $F_R(\tau\alpha)_n$ AND F_RU_L

Ideally, test data should be measured at flow rates corresponding to those to be used in applications. If a collector is to be used at a flow rate other than that of the test conditions, an approximate analytical correction to $F_R(\tau\alpha)_n$ and F_RU_L can be obtained from the ratios of values of F_R determined by use of Equation 6.7.4 or 6.7.5. Assume that the only effect of changing flow rate is to change the temperature gradient in the flow direction and that changes in F' due to changes of h_{fi} with flow rate are small (reasonable assumptions for liquid heating collectors operating at normal flow rates). The ratio r by which F_RU_L and $F_R(\tau\alpha)_n$ are to be corrected is then given by

$$r = \frac{F_RU_L|_{\text{use}}}{F_RU_L|_{\text{test}}} = \frac{F_R(\tau\alpha)_n|_{\text{use}}}{F_R(\tau\alpha)_n|_{\text{test}}} \tag{6.20.1}$$

$$r = \frac{\left.\dfrac{\dot{m}C_p}{A_cF'U_L}\left[1-\exp\left(-A_cF'U_L/\dot{m}C_p\right)\right]\right|_{\text{use}}}{\left.\dfrac{\dot{m}C_p}{A_cF'U_L}\left[1-\exp\left(-A_cF'U_L/\dot{m}C_p\right)\right]\right|_{\text{test}}} \tag{6.20.2}$$

or

$$r = \frac{\left.\dfrac{\dot{m}C_p}{A_c}\left[1-\exp\left(-A_cF'U_L/\dot{m}C_p\right)\right]\right|_{\text{use}}}{F_RU_L|_{\text{test}}} \tag{6.20.3}$$

To use these equations, it is necessary to know or estimate $F'U_L$. For the test conditions, it can be calculated from F_RU_L. Rearranging Equation 6.7.4 and solving for $F'U_L$ yields

$$F'U_L = -\frac{\dot{m}C_p}{A_c}\ln\left(1-\frac{F_RU_LA_c}{\dot{m}C_p}\right) \tag{6.20.4}$$

For liquid collectors, $F'U_L$ calculated for the test conditions is approximately equal to $F'U_L$ at use conditions and can be used in both numerator and denominator of Equation 6.20.2.

Example 6.20.1

The water heating collector of Example 6.17.1 is to be used at a flow rate of 0.020 kg/s rather than at the 0.040 kg/s at which the test data were obtained. Estimate the effect of reducing the flow rate on $F_R(\tau\alpha)_n$ and $F_R U_L$.

Solution

Equation 6.20.2 will be used but Equation 6.20.3 could have been used. First, calculate $F'U_L$ for the test conditions from Equation 6.20.4:

$$F'U_L = -\frac{0.040 \times 4187}{4.10} \ln\left(1 - \frac{7.62 \times 4.10}{0.040 \times 4187}\right) = 8.43 \text{ W/m}^2\ ^\circ\text{C}$$

Then r is obtained with Equation 6.20.2. For use conditions,

$$\frac{\dot{m}C_p}{A_c F'U_L} = \frac{0.020 \times 4187}{4.10 \times 8.43} = 2.42$$

For test conditions

$$\frac{\dot{m}C_p}{A_c F'U_L} = \frac{0.040 \times 4187}{4.10 \times 8.43} = 4.85$$

So

$$r = \frac{2.42[1 - \exp(-1/2.42)]}{4.85[1 - \exp(-1/4.85)]} = 0.91$$

Then at the reduced flow rate

$$F_R(\tau\alpha)_n = 0.78 \times 0.91 = 0.71$$

$$F_R U_L = 7.62 \times 0.91 = 6.91 \text{ W/m}^2\ ^\circ\text{C}$$

■

10.2 COLLECTOR HEAT EXCHANGER FACTOR

Collectors are often used in combination with a heat exchanger between collector and storage allowing the use of antifreeze solutions in the collector loop. A common circuit of this type is shown in Figure 10.2.1.

A useful analytical combination of the equations for the collector and the heat exchanger has been derived by deWinter (1975). In this development the collector equation and the heat exchanger equation are combined into a single expression that has the same form as the collector equation alone. The combination of a collector and a heat exchanger performs exactly like a collector alone but with a reduced value of F_R. The useful gain of the collector is represented by Equations 10.1.1 and 10.1.2 written in terms of T_{ci} and T_{co}. The heat exchanger performance is expressed in terms of effectiveness (Kays and London, 1964) by Equation 3.17.6:

$$Q_{HX} = \varepsilon(\dot{m}Cp)_{\min}(T_{co} - T_i) \tag{10.2.1}$$

where $(\dot{m}C_p)_{\min}$ is the smaller of the fluid capacitance rates (flow rate $\dot{m}$ times fluid heat capacity C_p) on the collector side $(\dot{m}C_p)_c$ and tank side $(\dot{m}C_p)_t$ of the heat exchanger, T_{co} is the outlet fluid temperature from the collector, and T_i is the inlet water temperature to the heat exchanger (very nearly the temperature in the bottom of the tank). For a counterflow heat exchanger, a common configuration, the effectiveness ε is given by Equation 3.17.7.

Combining Equations 10.1.1, 10.1.2, and 10.2.1,

$$Q_u = A_c F'_R[S - U_L(T_i - T_a)]^+ \tag{10.2.2}$$

where the modified collector heat removal factor F'_R accounts for the presence of the heat exchanger and is given by

$$\frac{F'_R}{F_R} = \left[1 + \left(\frac{A_c F_R U_L}{(\dot{m}C_p)_c}\right)\left(\frac{(\dot{m}C_p)_c}{\varepsilon(\dot{m}C_p)_{\min}} - 1\right)\right]^{-1} \tag{10.2.3}$$

The factor F'_R/F_R is an indication of the penalty in collector performance incurred because the heat exchanger causes the collector to operate at higher temperatures than it otherwise

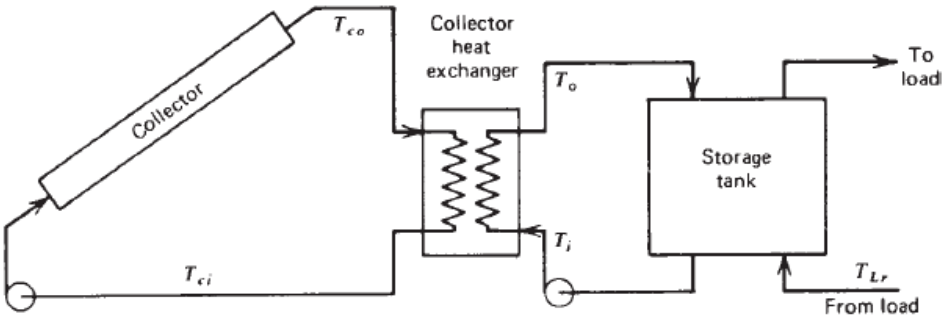

Figure 10.2.1 Schematic of liquid system with a collector heat exchanger between collector and tank.

Example 10.2.1

A collector to be used in a solar heating system such as that of Figure 10.2.1 heats antifreeze; heat is transferred to water through a collector heat exchanger. The collector $F_R U_L = 3.75$ W/m^2 °C. Flow rates through both sides of the heat exchanger are 0.0139 kg/s per square meter of collector. The fluid on the collector side is a glycol solution having $C_p = 3350$ J/kg °C. The effectiveness of the heat exchanger is 0.7. What is F'_R/F_R?

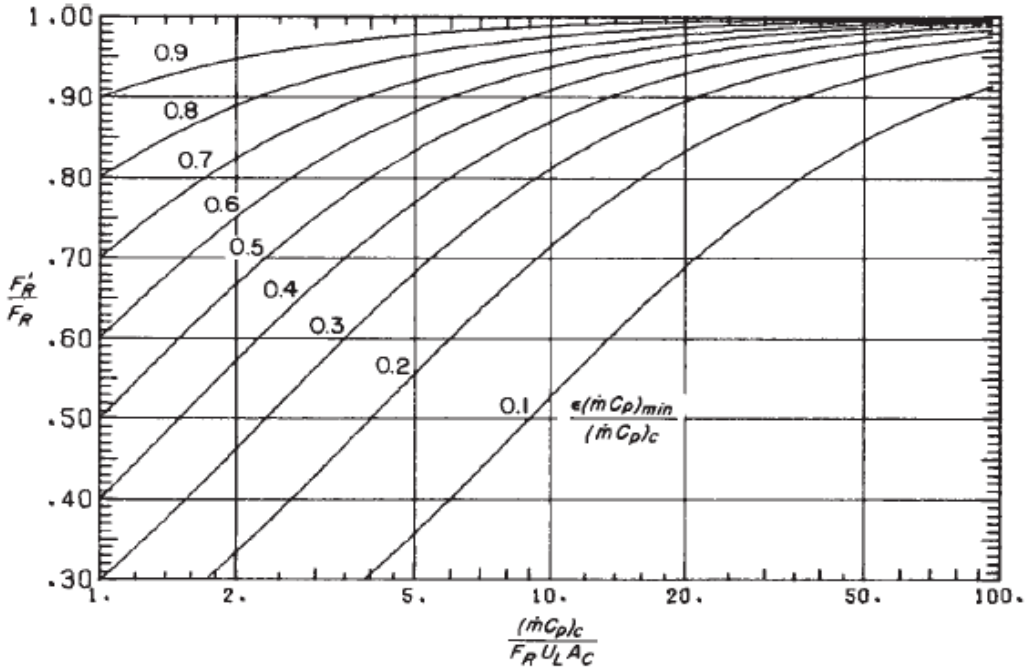

re **10.2.2** Collector heat exchanger correction factor as a function of $\varepsilon(\dot{m}C_p)_{\min}/(\dot{m}C_p)_c$ and $,)/F_R U_L A_c$. Adapted from Beckman et al. (1977).

Solution

The capacitance rate per unit area on the water side of the exchanger is $0.0139 \times 4190 = 58.2$ W/m^2 °C. On the glycol side it is $0.0139 \times 3350 = 46.6$ W/m^2 °C. Thus the minimum $(\dot{m}C_p)$ product is that of the glycol, $\varepsilon(\dot{m}C_p)_{\min}/(\dot{m}C_p)_c = \varepsilon = 0.7$, and

$$\frac{(\dot{m}C_p)_c}{A_c F_R U_L} = \frac{0.0139 \times 3350}{3.75} = 12.4$$

From Figure 10.2.2 or Equation 10.2.3, $F'_R/F_R = 0.97$. ■

COLLECTOR ARRAYS: SERIES CONNECTIONS

Collector modules in arrays may be connected in series, in parallel, or in combinations. The performance of collectors in arrays is dependent on how they are arranged, that is, on the flow rate through risers and on the inlet temperatures to individual modules.

Figure 10.5.1 shows arrays of two modules (or two groups of modules) with parallel and series connections. Assume for the moment that the modules are identical. If the flow rates to the arrays are the same, the velocity through the risers of the series-connected array will be twice that in the parallel array. If this difference in velocity does not make an appreciable difference in F' through its effect on h_{fi}, then there will be no appreciable difference in performance between the two arrays as the terms in Equation 6.7.6 will be identical. If there is a significant difference in F' and thus in F_R or if the design of the modules is not the same (e.g., with the first having one cover and the second two covers), the performance of the two arrays will not be the same. In the series arrangement, the performance of the second (and subsequent) module will not be the same as the first as its inlet temperature will be the outlet temperature of the first.

For collector modules in series, an analysis can be developed that results in an equation identical in form to that of Equation 6.7.6. It is not necessary that the modules be identical; the constraint is that each can be described by its set of two parameters, $F_R(\tau\alpha)_n$ and $F_R U_L$. The useful output of the combination is

$$Q_{u,1} + Q_{u,2} = A_1 F_{R1}[G_T(\tau\alpha)_1 - U_{L1}(T_i - T_a)] + A_2 F_{R2}[G_T(\tau\alpha)_2 - U_{L2}(T_{o,1} - T_a)] \tag{10.5.1}$$

where T_i is the inlet fluid temperature to the first collector and $T_{o,1}$ is the inlet temperature to the second collector, which is found from the outlet of the first collector:

$$T_{o,1} = T_i + \frac{Q_{u,1}}{\dot{m}C_p} \tag{10.5.2}$$

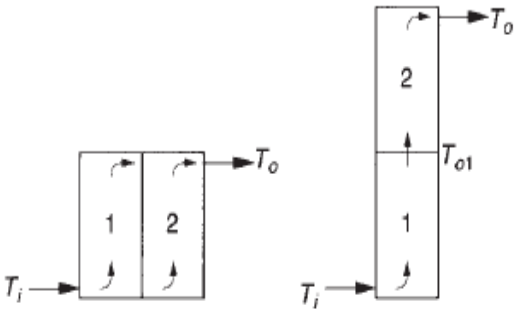

Figure 10.5.1 Collector modules in parallel and series. Flow divides in the parallel set; full flow goes through each module in the series set.

The values of $F_R(\tau\alpha)$ and $F_R U_L$ for each collector must be the values corresponding to the actual fluid flow through the collector (i.e., the flow rate through collector 1 in the parallel arrangement is one-half of the flow rate through collector 1 in the series arrangement). By eliminating $T_{o,1}$ from the previous two equations, the useful output of the combination can be expressed as

$$Q_{u,1+2} = [A_1 F_{R1}(\tau\alpha)_1(1-K) + A_2 F_{R2}(\tau\alpha)_2]G_T - [A_1 F_{R1} U_{L1}(1-K) + A_2 F_{R2} U_{L2}](T_i - T_a) \tag{10.5.3}$$

where

$$K = \frac{A_2 F_{R2} U_{L2}}{\dot{m} C_p} \tag{10.5.4}$$

The form of Equation 10.5.3 suggests that the combination of the two collectors can be considered as a single collector with the following characteristics:

$$A_c = A_1 + A_2 \tag{10.5.5}$$

$$F_R(\tau\alpha) = \frac{A_1 F_{R1}(\tau\alpha)_1 \ (1-K) + A_2 F_{R2}(\tau\alpha)_2}{A_c} \tag{10.5.6}$$

$$F_R U_L = \frac{A_1 F_{R1} U_{L1} \ (1-K) + A_2 F_{R2} U_{L2}}{A_c} \tag{10.5.7}$$

If three or more collectors are placed in series, then these equations can be used for the first two collectors to define a new equivalent first collector. The equations are applied again with this equivalent first collector and the third collector becoming the second collector. The process can be repeated for as many collectors as desired.

If the two collectors are identical, then Equations 10.5.6 and 10.5.7 reduce to the following:

$$F_R(\tau\alpha) = F_{R1}(\tau\alpha)_1 \left(1 - \frac{K}{2}\right) \tag{10.5.8}$$

$$F_R U_L = F_{R1} U_{L1} \left(1 - \frac{K}{2}\right) \tag{10.5.9}$$

For N identical collectors in series, Oonk et al. (1979) have shown that repeated applications of Equations 10.5.6 and 10.5.7 yield

$$F_R(\tau\alpha) = F_{R1}(\tau\alpha)_1 \left(\frac{1-(1-K)^N}{NK}\right) \tag{10.5.10}$$

$$F_R U_L = F_{R1} U_{L1} \left(\frac{1-(1-K)^N}{NK}\right) \tag{10.5.11}$$

Example 10.5.1

Calculate $F_R(\tau\alpha)$ and $F_R U_L$ for the combination of two air heating collectors connected in series with a flow rate of 0.056 kg/s. The characteristics of a single air heater are

$F_R(\tau\alpha) = 0.67$ and $F_R U_L = 3.6$ W/m^2 °C at a flow rate of 0.056 kg/s. Each collector is 1.00 m wide by 2.00 m long and $C_p = 1008$ J/kg °C.

Solution

From Equation 10.5.4,

$$K = \frac{3.63 \times 2.00}{0.056 \times 1008} = 0.129$$

From Equations 10.5.8 and 10.5.9,

$$F_R(\tau\alpha) = 0.67\left(1 - \frac{0.129}{2}\right) = 0.63$$

$$F_R U_L = 3.6\left(1 - \frac{0.129}{2}\right) = 3.4 \text{ W/m}^2 \text{ °C}$$

■

SERIES ARRAYS WITH SECTIONS HAVING DIFFERENT ORIENTATIONS

Collector arrays are occasionally constructed in sections, with the sections having different orientations (i.e., with different azimuth angles and/or slopes). These arrangements may be imposed by the locations and structure available to mount the collector. If these collector sections are series connected, the analysis of Section 10.6 can be applied to calculate the output.

Consider an array of two sections, 1 and 2, connected in series. Areas of the two sections A_1 and A_2 will be fixed. Flow is in the direction of 1 to 2. The F_R and U_L values will be the same for both sections, assuming that $\dot{m}/A_c$ is the same and neglecting effects of orientation and collector temperature on U_L. The values of $(\tau\alpha)$ for the two sections will be different and will depend on orientation. Equation 10.6.4 applies to this array, as shown in the following example.

Example 10.7.1

A collector array is in two sections of equal area. The slopes of both sections are 55°; section 1 has $\gamma = -45°$ and section 2 has $\gamma = 45°$. The latitude is 40°. The collector has

one glass cover with $KL = 0.0125$ and $\alpha_n = 0.93$; $F_R = 0.933$ and $U_L = 4.50$ W/ m^2 °C. Water is pumped in series through sections 1 and 2 at a rate of 0.01 kg/m^2 s.

For the hour 2 to 3 on May 15, $I = 2.83$ MJ/m^2. The ambient temperature is 10°C. The fluid inlet temperature is 45°C and ground reflectance is estimated to be 0.25. Estimate the output per square meter of total array area for this hour.

Solution

For this hour, $I_o = 3.72$ MJ/m^2, $k_T = 0.76$, and $I_d/I = 0.177$: $\delta = 18.8^\circ$ and $\omega = 37.5^\circ$.

For both sections, $I_d = 0.177 \times 2.83 = 0.50$ MJ/m^2 and $I_b = 2.33$ MJ/m^2. For the diffuse radiation, $\theta_e = 57^\circ$ (from Figure 5.4.1),

$$\tau_d = 0.85 \qquad \text{and} \qquad \left(\frac{\alpha}{\alpha_n}\right)_d = 0.94$$

$$1.01\tau\alpha = 1.01 \times 0.85 \times 0.93 \times 0.94 = 0.751$$

For the ground reflected radiation, $\theta_e = 66^\circ$,

$$\tau_g = 0.77 \qquad \text{and} \qquad \left(\frac{\alpha}{\alpha_n}\right)_g = 0.88$$

$$1.01\tau\alpha = 1.01 \times 0.77 \times 0.93 \times 0.88 = 0.636$$

For section 1; for beam radiation, from Equation 1.6.2,

$$\cos\ \theta = 0.277 \qquad \text{and} \qquad \theta = 74^\circ$$

$$\tau_b = 0.65 \qquad \text{and} \qquad \left(\frac{\alpha}{\alpha_n}\right)_b = 0.79$$

$$1.01\tau\alpha = 1.01 \times 0.65 \times 0.93 \times 0.79 = 0.482$$

From Equation 1.6.5, $\cos\ \theta_z = 0.782$,

$$R_{b,1} = \frac{0.277}{0.782} = 0.355$$

Then

$$I_{T,1} = 2.33 \times 0.355 + \frac{0.50(1 + \cos\ 55)}{2} + 2.83 \times \frac{0.25(1 - \cos\ 55)}{2}$$

$$= 0.827 + 0.393 + 0.151 = 1.37\ \text{MJ/m}^2$$

and

$$S_1 = 0.827 \times 0.482 + 0.393 \times 0.751 + 0.151 \times 0.636 = 0.790\ \text{MJ/m}^2$$

So

$$(\tau\alpha)_{\text{av},1} = \frac{0.790}{1.37} = 0.577$$

For section 2; for beam radiation,

$$\cos\ \theta = 0.942 \qquad \text{and} \qquad \theta = 19.6^\circ$$

$$\tau_b = 0.91 \qquad \text{and} \qquad \left(\frac{\alpha}{\alpha_n}\right)_b = 1.00$$

$$1.01\tau\alpha = 1.01 \times 0.91 \times 0.93 = 0.855$$

$$R_{b,2} = \frac{0.942}{0.782} = 1.18$$

Then

$$I_{T,2} = 2.33 \times 1.18 + 0.393 + 0.151 = 3.30\ \text{MJ/m}^2$$

and

$$S_2 = 2.33 \times 1.18 \times 0.855 + 0.393 \times 0.751 + 0.151 \times 0.636$$
$$= 2.75\ \text{MJ/m}^2$$

So

$$(\tau\alpha)_{\text{av},2} = \frac{2.75}{3.30} = 0.833$$

We now use Equations 10.6.4 and 10.6.5 to calculate the performance of the two sections in series:

$$K = 0.93 \times \frac{4.5}{0.01 \times 4190} = 0.100$$

$$\frac{Q_u}{A_c} = 0.933\{[0.5 \times 0.577(1 - 0.100)1.37 + 0.5 \times 0.833 \times 3.30]10^6$$
$$- 4.5 \times 3600[0.5(1 - 0.100) + 0.5](45 - 10)\}$$
$$= 1.11\ \text{MJ/m}^2$$

■

Note that for the hour 9 to 10 for this example, which corresponds to a reversal of flow direction for the hour 2 to 3, the output of the array would be 1.02 MJ/m^2, or about 8% less than for the conditions in the example. These calculations show how much difference flow direction makes and thus assists in determining control strategy. (Note that there may be conditions under which the section with the lower irradiation should be bypassed. This can be determined by calculating the output of the first section. If the output is negative, it should be bypassed. If its output is higher than that of the combined sections, the second section should be bypassed.)

Radiation Transmission through Glazing: Absorbed Radiation

The transmission, reflection, and absorption of solar radiation by the various parts of a solar collector are important in determining collector performance. The transmittance, reflectance, and absorptance are functions of the incoming radiation, thickness, refractive index, and extinction coefficient of the material. Generally, the refractive index n and the extinction coefficient K of the cover material are functions of the wavelength of the radiation.

REFLECTION OF RADIATION:

For smooth surfaces Fresnel has derived expressions for the reflection of unpolarized radiation on passing from medium 1 with a refractive index n_1 to medium 2 with refractive index n_2:

$$r_{\perp} = \frac{\sin^2(\theta_2 - \theta_1)}{\sin^2(\theta_2 + \theta_1)} \tag{5.1.1}$$

$$r_{\parallel} = \frac{\tan^2(\theta_2 - \theta_1)}{\tan^2(\theta_2 + \theta_1)} \tag{5.1.2}$$

$$r = \frac{I_r}{I_i} = \frac{r_{\perp} + r_{\parallel}}{2} \tag{5.1.3}$$

where θ_1 and θ_2 are the angles of incidence and refraction, as shown in Figure 5.1.1. Equation 5.1.1 represents the perpendicular component of unpolarized radiation $r_{\perp}$, and

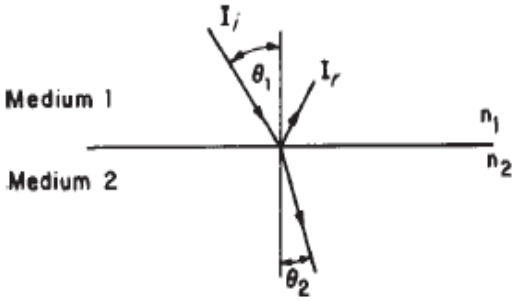

Figure 5.1.1 Angles of incidence and refraction in media with refractive indices n_1 and n_2.

Equation 5.1.2 represents the parallel component of unpolarized radiation $r_{\|}$. (Parallel and perpendicular refer to the plane defined by the incident beam and the surface normal.) Equation 5.1.3 then gives the reflection of unpolarized radiation as the average of the two components. The angles θ_1 and θ_2 are related to the indices of refraction by Snell's law,

$$n_1 \sin \theta_1 = n_2 \sin \theta_2 \tag{5.1.4}$$

Thus if the angle of incidence and refractive indices are known, Equations 5.1.1 through 5.1.4 are sufficient to calculate the reflectance of the single interface.

For radiation at normal incidence both θ_1 and θ_2 are zero, and Equations 5.1.3 and 5.1.4 can be combined to yield

$$r(0) = \frac{I_r}{I_i} = \left(\frac{n_1 - n_2}{n_1 + n_2}\right)^2 \tag{5.1.5}$$

If one medium is air (i.e., a refractive index of nearly unity), Equation 5.1.5 becomes

$$r(0) = \left(\frac{n - 1}{n + 1}\right)^2 \tag{5.1.6}$$

Example 5.1.1

Calculate the reflectance of one surface of glass at normal incidence and at 60°. The average index of refraction of glass for the solar spectrum is 1.526.

Solution

At normal incidence, Equation 5.1.6 can be used:

$$r(0) = \left(\frac{0.526}{2.526}\right)^2 = 0.0434$$

At an incidence angle of 60°, Equation 5.1.4 gives the refraction angle θ_2:

$$\theta_2 = \sin^{-1}\left(\frac{\sin\ 60}{1.526}\right) = 34.58$$

From Equation 5.1.3, the reflectance is

$$r(60) = \frac{1}{2}\left[\frac{\sin^2(-25.42)}{\sin^2(94.58)} + \frac{\tan^2(-25.42)}{\tan^2(94.58)}\right] = \frac{1}{2}(0.185 + 0.001) = 0.093$$

In solar applications, the transmission of radiation is through a slab or film of material so there are two interfaces per cover to cause reflection losses. At off-normal incidence, the radiation reflected at an interface is different for each component of polarization, so the transmitted and reflected radiation becomes partially polarized. Consequently, it is necessary to treat each component of polarization separately.

Neglecting absorption in the cover material shown in Figure 5.1.2 and considering for the moment only the perpendicular component of polarization of the incoming radiation, $(1 - r_\perp)$ of the incident beam reaches the second interface. Of this, $(1 - r_\perp)^2$ passes through the interface and $r_\perp(1 - r_\perp)$ is reflected back to the first, and so on. Summing the transmitted terms, the transmittance for the perpendicular component of polarization is

$$\tau_\perp = (1 - r_\perp)^2 \sum_{n=0}^{\infty} r_\perp^{2n} = \frac{(1 - r_\perp)^2}{1 - r_\perp^2} = \frac{1 - r_\perp}{1 + r_\perp} \tag{5.1.7}$$

Exactly the same expansion results when the parallel component of polarization is considered. The components $r_\perp$ and $r_\parallel$ are not equal (except at normal incidence), and the transmittance of initially unpolarized radiation is the average transmittance of the two components,

$$\tau_r = \frac{1}{2}\left(\frac{1 - r_\parallel}{1 + r_\parallel} + \frac{1 - r_\perp}{1 + r_\perp}\right) \tag{5.1.8}$$

where the subscript r is a reminder that only reflection losses have been considered.

For a system of N covers all of the same materials, a similar analysis yields

$$\tau_{rN} = \frac{1}{2}\left(\frac{1 - r_\parallel}{1 + (2N - 1)\, r_\parallel} + \frac{1 - r_\perp}{1 + (2N - 1) r_\perp}\right) \tag{5.1.9}$$

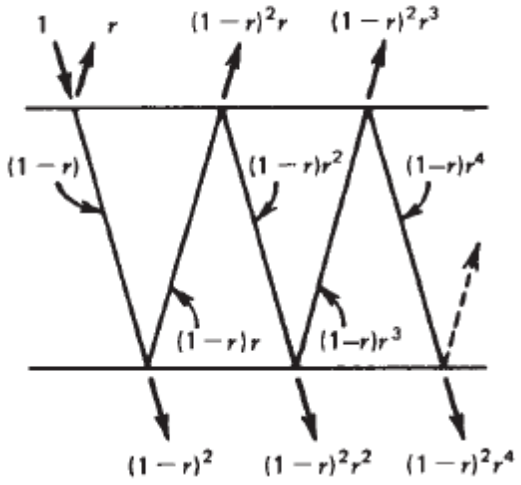

Figure 5.1.2 Transmission cover.

Example 5.1.2

Calculate the transmittance of two covers of nonabsorbing glass at normal incidence and at 60°.

Solution

At normal incidence, the reflectance of one interface from Example 5.1.1 is 0.0434. From Equation 5.1.9, with both polarization components equal, the transmittance is

$$\tau_r(0) = \frac{1 - 0.0434}{1 + 3(0.0434)} = 0.85$$

Also from Example 5.1.1 but at a 60° incidence angle, the reflectances of one interface for each component of polarization are 0.185 and 0.001. From Equation 5.1.9, the transmittance is

$$\tau_r(60) = \frac{1}{2}\left[\frac{1 - 0.185}{1 + 3\,(0.185)} + \frac{1 - 0.001}{1 + 3(0.001)}\right] = 0.76$$

■

ABSORPTION BY GLAZING

The absorption of radiation in a partially transparent medium is described by Bouguer's law, which is based on the assumption that the absorbed radiation is proportional to the local intensity in the medium and the distance x the radiation has traveled in the medium:

$$dI = -IK\,dx \tag{5.2.1}$$

where K is the proportionality constant, the extinction coefficient, which is assumed to be a constant in the solar spectrum. Integrating along the actual pathlength in the medium (i.e., from zero to $L/\cos\ \theta_2$) yields

$$\tau_a = \frac{I_{\text{transmitted}}}{I_{\text{incident}}} = \exp\left(-\frac{KL}{\cos\ \theta_2}\right) \tag{5.2.2}$$

where the subscript a is a reminder that only absorption losses have been considered. For glass, the value of K varies from approximately 4 m^{-1} for "water white" glass (which appears white when viewed on the edge) to approximately 32 m^{-1} for high iron oxide content (greenish cast of edge) glass.

OPTICAL PROPERTIES OF COVER SYSTEMS

The transmittance, reflectance, and absorptance of a single cover, allowing for both reflection and absorption losses, can be determined either by ray-tracing techniques similar to that used to derive Equation 5.1.7 or by the net radiation method as described by Siegel and Howell (2002). For the perpendicular component of polarization, the transmittance $\tau_\perp$, reflectance $\rho_\perp$, and absorptance $\alpha_\perp$ of the cover are

$$\tau_\perp = \frac{\tau_a(1-r_\perp)^2}{1-(r_\perp\tau_a)^2} = \tau_a\,\frac{1-r_\perp}{1+r_\perp}\left[\frac{1-r_\perp^2}{1-\left(r_\perp\tau_a\right)^2}\right] \tag{5.3.1}$$

$$\rho_\perp = r_\perp + r_\perp\,\frac{\tau_a^2(1-r_\perp)^2}{1-(r_\perp\tau_a)^2} = r_\perp\,(1+\tau_a\tau_\perp) \tag{5.3.2}$$

$$\alpha_\perp = (1-\tau_a)\left(\frac{1-r_\perp}{1-r_\perp\tau_a}\right) \tag{5.3.3}$$

transmittance of a single cover becomes

$$\tau \cong \tau_a\tau_r \tag{5.3.4}$$

This is a satisfactory relationship for solar collectors with cover materials and angles of practical interest.

The absorptance of a solar collector cover can be approximated by letting the last term in Equation 5.3.3 be unity so that

$$\alpha \cong 1 - \tau_a \tag{5.3.5}$$

The reflectance of a single cover is then found from $\rho = 1 - \alpha - \tau$, so that

$$\rho \cong \tau_a(1 - \tau_r) = \tau_a - \tau \tag{5.3.6}$$

Example 5.3.1

Calculate the transmittance, reflectance, and absorptance of a single glass cover 2.3 mm thick at an angle of 60°. The extinction coefficient of the glass is 32 m^{-1}.

Solution

At an incidence angle of 60°, the extinction coefficient—optical pathlength product is

$$\frac{KL}{\cos\ \theta_2} = \frac{32 \times 0.0023}{\cos\ 34.58} = 0.0894$$

where 34.58 is the refraction angle calculated in Example 5.1.1. The transmittance τ_a from Equation 5.2.2 is then

$$\tau_a = \exp(-0.0894) = 0.915$$

Using the results of Example 5.1.1 and Equation 5.3.1, the transmittance is found by averaging the transmittances for the parallel and perpendicular components of polarization,

$$\tau = \frac{0.915}{2}\left[\frac{1-0.185}{1+0.185}\left(\frac{1-0.185^2}{1-(0.185\times 0.915)^2}\right) + \frac{1-0.001}{1+0.001}\left(\frac{1-0.001^2}{1-(0.001\times 0.915)^2}\right)\right]$$

$$= 0.5(0.625 + 0.912) = 0.768$$

The reflectance is found using Equation 5.3.2 for each component of polarization and averaging:

$$\rho = 0.5[0.185\ (1 + 0.915 \times 0.625) + 0.001(1 + 0.915 \times 0.912)]$$
$$= 0.5(0.291 + 0.002) = 0.147$$

In a similar manner, the absorptance is found using Equation 5.3.3:

$$\alpha = \frac{1-0.915}{2}\left(\frac{1-0.185}{1-0.185\times 0.915} + \frac{1-0.001}{1-0.001\times 0.915}\right)$$

$$= \frac{0.085}{2}(0.981 + 1.000) = 0.085$$

Alternate Solution

The approximate equations can also be used to find these properties. From Equations 5.3.4 and 5.1.8 the transmittance is

$$\tau = \frac{0.915}{2}\left(\frac{1-0.185}{1+0.185}+\frac{1-0.001}{1+0.001}\right) = 0.771$$

From Equation 5.3.5, the absorptance is

$$\alpha = 1 - 0.915 = 0.085$$

and the reflectance is then

$$\rho = 1 - 0.771 - 0.085 = 0.144$$

Example 5.3.2

Calculate the solar transmittance at incidence angles of zero and 60° for two glass covers each 2.3 mm thick. The extinction coefficient of the glass is 16.1 m^{-1}, and the refractive index is 1.526.

Solution

For one sheet at normal incidence,

$$KL = 16.1 \times 2.3/1000 = 0.0370$$

The transmittance τ_a is given as

$$\tau_a(0) = \exp[-2(0.0370)] = 0.93$$

The transmittance accounting for reflection, from Example 5.1.2, is 0.85. The total transmittance is then found from Equation 5.3.4:

$$\tau(0) = \tau_r(0)\tau_a(0) = 0.85(0.93) = 0.79$$

From Example 5.1.1, when $\theta_1 = 60°$, $\theta_2 = 34.57°$, and

$$\tau_a(60) = \exp\left(-\frac{2\,(0.0370)}{\cos\ 34.57}\right) = 0.91$$

and the total transmittance (with $\tau_r = 0.76$ from Example 5.1.2) becomes

$$\tau(60) = \tau_r(60)\tau_a(60) = 0.76(0.91) = 0.69$$ ■

For a two-cover system with covers not necessarily identical the following equations are for transmittance and reflectance, where subscript 1 refers to the top cover and subscript 2 to the inner cover:

$$\tau = \frac{1}{2}(\tau_\perp + \tau_\parallel) = \frac{1}{2}\left[\left(\frac{\tau_1\tau_2}{1-\rho_1\rho_2}\right)_\perp + \left(\frac{\tau_1\tau_2}{1-\rho_1\rho_2}\right)_\parallel\right] \tag{5.3.7}$$

$$\rho = \frac{1}{2}(\rho_\perp + \rho_\parallel) = \frac{1}{2}\left[\left(\rho_1 + \frac{\tau\rho_2\tau_1}{\tau_2}\right)_\perp + \left(\rho_1 + \frac{\tau\rho_2\tau_1}{\tau_2}\right)_\parallel\right] \tag{5.3.8}$$

Example 5.3.3

Calculate the optical properties of a two-cover solar collector at an angle of 60°. The outer cover is glass with $K = 16.1\ \text{m}^{-1}$ and thickness of 2.3 mm. The inner cover is polyvinyl fluoride with refractive index equal to 1.45. The plastic film is thin enough so that absorption within the plastic can be neglected.

Solution

The optical properties of the glass and plastic covers alone, as calculated from Equations 5.3.1 through 5.3.3, are

Glass:	$\tau_\parallel = 0.953,$	$\tau_\perp = 0.655$
	$\rho_\parallel = 0.002,$	$\rho_\perp = 0.302$
	$\alpha_\parallel = 0.044,$	$\alpha_\perp = 0.044$
Plastic:	$\tau_\parallel = 0.995,$	$\tau_\perp = 0.726$
	$\rho_\parallel = 0.005,$	$\rho_\perp = 0.274$
	$\alpha_\parallel = 0.000,$	$\alpha_\perp = 0.000$

Equations 5.3.4 through 5.3.6 could have been used with each component of polarization to simplify the calculation of the preceding properties.

The transmittance of the combination is found from Equation 5.3.7:

$$\tau = \frac{1}{2}\left(\frac{0.655 \times 0.726}{1 - 0.302 \times 0.274} + \frac{0.953 \times 0.995}{1 - 0.002 \times 0.005}\right)$$
$$= 0.5(0.518 + 0.948) = 0.733$$

The reflectance, with the glass first, is found from Equation 5.3.8:

$$\rho = \frac{1}{2}\left(0.302 + \frac{0.518 \times 0.274 \times 0.655}{0.726} + 0.002 + \frac{0.948 \times 0.005 \times 0.953}{0.995}\right)$$
$$= 0.5(0.430 + 0.007) = 0.219$$

The absorptance is then

$$\alpha = 1 - 0.219 - 0.733 = 0.048$$

■

TRANSMITTANCE FOR DIFFUSE RADIATION

The preceding analysis applies only to the beam component of solar radiation. Radiation incident on a collector also consists of scattered solar radiation from the sky and possibly reflected solar radiation from the ground. In principle, the amount of this radiation that passes through a cover system can be calculated by integrating the transmitted radiation over all angles. However, the angular distribution of this radiation is generally unknown.

The dashed lines shown in Figure 5.4.1 are given for ground-reflected radiation by

$$\theta_{e,g} = 90 - 0.5788\beta + 0.002693\beta^2 \tag{5.4.1}$$

and for diffuse radiation by

$$\theta_{e,d} = 59.7 - 0.1388\beta + 0.001497\beta^2 \tag{5.4.2}$$

TRANSMITTANCE-ABSORPTANCE PRODUCT

To use the analysis of the next chapter, it is necessary to evaluate the transmittance-absorptance product $(\tau\alpha)$.[1] Of the radiation passing through the cover system and incident on the plate, some is reflected back to the cover system. However, all this radiation is not lost since some of it is, in turn, reflected back to the plate.

The situation is illustrated in Figure 5.5.1, where τ is the transmittance of the cover system at the desired angle and α is the angular absorptance of the absorber plate. Of the incident energy, $\tau\alpha$ is absorbed by the absorber plate and $(1-\alpha)\tau$ is reflected back to the cover system. The reflection from the absorber plate is assumed to be diffuse (and unpolarized) so the fraction $(1-\alpha)\tau$ that strikes the cover system is diffuse radiation and $(1-\alpha)\tau\rho_d$ is reflected back to the absorber plate. The quantity ρ_d refers to the reflectance of the cover system for diffuse radiation incident from the bottom side and can be estimated from Equation 5.3.6 as the difference between τ_a and τ at an angle of 60°.[2]

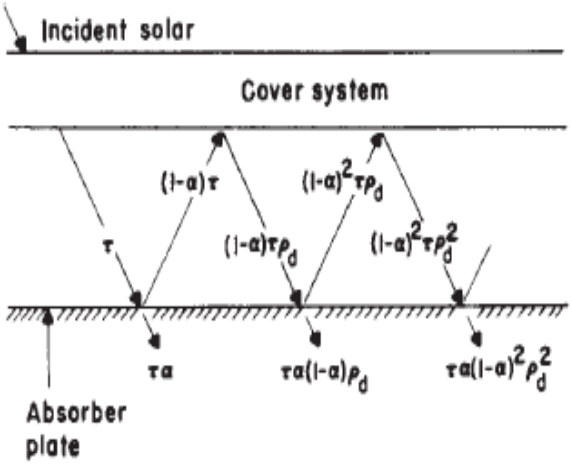

Figure 5.5.1 Absorption of solar radiation by absorber plate under a cover system.

If the cover system consists of two (or more) covers of dissimilar materials, ρ_d will be different (slightly) from the diffuse reflectance of the incident solar radiation (see Equation 5.3.8). The multiple reflection of diffuse radiation continues so that the fraction of the incident energy ultimately absorbed is[3]

$$(\tau\alpha) = \tau\alpha \sum_{n=0}^{\infty} [(1-\alpha)\rho_d]^n = \frac{\tau\alpha}{1-(1-\alpha)\rho_d} \tag{5.5.1}$$

Example 5.5.1

For a two-cover collector using glass with $KL = 0.0370$ per plate and an absorber plate with $\alpha = 0.90$ (independent of direction), find the transmittance-absorptance product at an angle of 50°.

Solution

From Figure 5.3.1, τ at 50° is 0.75 and τ at 60° (the effective angle of incidence of radiation reflected back to the cover) is 0.69. From Equation 5.2.2 with $\theta_2 = 34.58^\circ$, $\tau_a = 0.91$. From Equation 5.3.6, $\rho_d = 0.91 - 0.69 = 0.22$. From Equation 5.5.1

$$(\tau\alpha) = \frac{0.75 \times 0.90}{1-(1-0.90)\ 0.22} = 0.69$$

Note that it is also possible to estimate $\rho_d = 1 - \tau_r$, where τ_r can be estimated from Figure 5.1.3 at 60°. For two covers, $\tau_r = 0.77$, so $\rho_d = 0.23$. ■

The value of $(\tau\alpha)$ in this example is very nearly equal to 1.01 times the product of τ times α. This is a reasonable approximation for most practical solar collectors. Thus,

$$(\tau\alpha) \cong 1.01\tau\alpha \tag{5.5.2}$$

can be used as an estimate of $(\tau\alpha)$ in place of Equation 5.5.1.

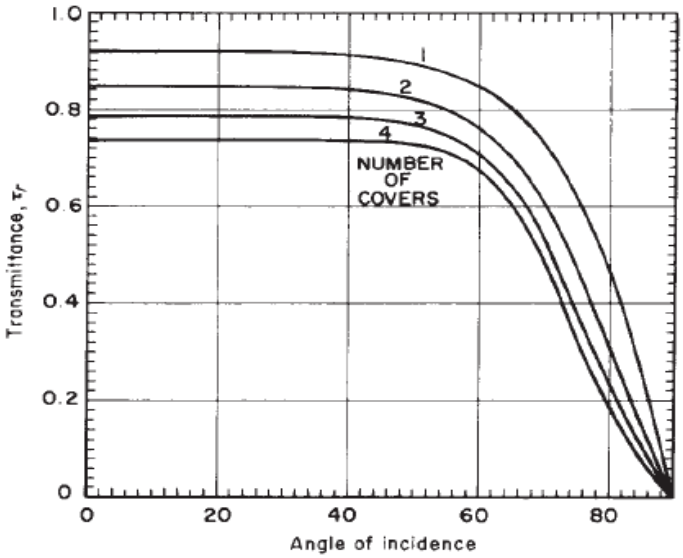

Figure 5.1.3 Transmittance of 1, 2, 3, and 4 nonabsorbing covers having an index of refraction of 1.526.

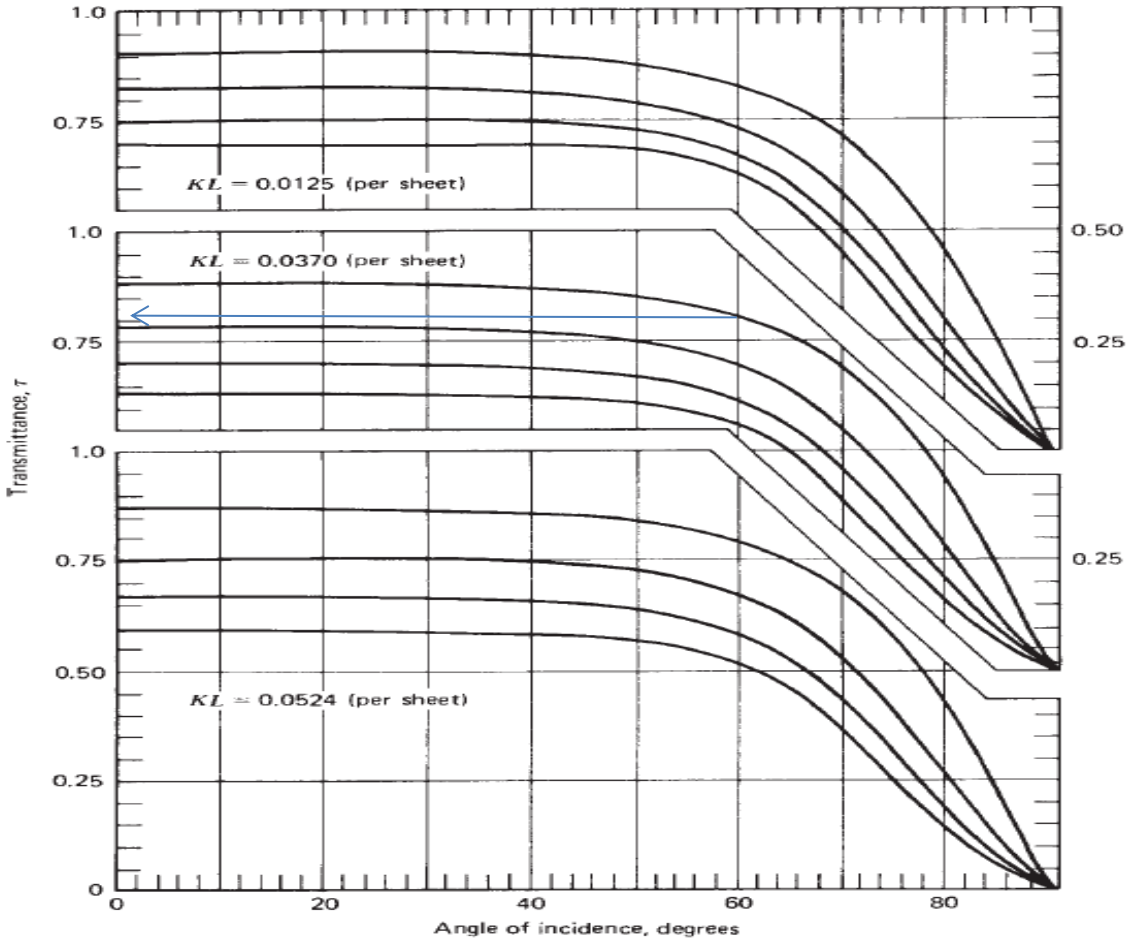

e 5.3.1 Transmittance (considering absorption and reflection) of one, two, three, and four s for three types of glass.

ABSORBED SOLAR RADIATION

$$S = I_b R_b (\tau\alpha)_b + I_d (\tau\alpha)_d \left(\frac{1 + \cos\ \beta}{2}\right) + \rho_g I (\tau\alpha)_g \left(\frac{1 - \cos\ \beta}{2}\right) \qquad (5.9.1)$$

where $(1 + \cos\ \beta)/2$ and $(1 - \cos\ \beta)/2$ are the view factors from the collector to the sky and from the collector to the ground, respectively. The subscripts b, d, and g represent beam, diffuse, and ground. For a given collector tilt, Figure 5.4.1 gives the effective angle of incidence of the diffuse and ground-reflected radiation, and Figures 4.11.1 and 5.4 can be used to find the proper absorptance and transmittance values. Equation 5.5.1 or 5.5.2 can then be used to find $(\tau\alpha)_d$ and $(\tau\alpha)_g$. The angle θ for the beam radiation, which is needed in evaluating R_b, is used to find $(\tau\alpha)_b$. Alternatively, $(\tau\alpha)_n$ can be found from the properties of the cover and absorber and Figure 5.6.1 can be used at the appropriate angles of incidence for each radiation stream to determine the three transmittance-absorptance products.

Example 5.9.1

For an hour 11 to 12 AM on a clear winter day, $I = 1.79$ MJ/m^2, $I_b = 1.38$ MJ/m^2, and $I_d = 0.41$ MJ/m^2. Ground reflectance is 0.6. For this hour, θ for the beam radiation is 7° and $R_b = 2.11$. A collector with one glass cover is sloped 60° to the south. The glass has $KL = 0.0370$, and the absorptance of the plate at normal incidence, α_n, is 0.93. Using the isotropic diffuse model (Equation 5.9.1), calculate the absorbed radiation per unit area of absorber.

Solution

Two approaches to the solution are possible. The angular dependence of τ and α can be individually determined or the angular dependence of $(\tau\alpha)$ can be determined.

In the first method, use Figure 4.11.1 to get angular dependence of α and Figure 5.3.1 to get angular dependence of τ. For the 60° slope, from Figure 5.4.1, the effective angle of incidence of the diffuse radiation is 57° and that of the ground-reflected radiation is 65°:

For the beam radiation, at $\theta = 7^\circ$:

From Figure 4.11.1, $\alpha/\alpha_n = 0.99$

From Figure 5.3.1, $\tau = 0.88$

$(\tau\alpha)_b = 1.01 \times 0.88 \times 0.99 \times 0.93 = 0.82$

For the (isotropic) diffuse radiation, at $\theta = 57^\circ$:

From Figure 4.11.1, $\alpha/\alpha_n = 0.94$

From Figure 5.3.1, $\tau = 0.83$

$(\tau\alpha)_d = 1.01 \times 0.83 \times 0.94 \times 0.93 = 0.73$

For the ground-reflected radiation, at $\theta = 65^\circ$:

From Figure 4.11.1, $\alpha/\alpha_n = 0.88$

From Figure 5.3.1, $\tau = 0.76$

$(\tau\alpha)_g = 1.01 \times 0.76 \times 0.88 \times 0.93 = 0.63$

Equation 5.9.1 is now used to calculate S:

$$S = 1.38 \times 2.11 \times 0.82 + 0.41 \times 0.73 \left(\frac{1 + \cos 60}{2}\right) + 1.79 \times 0.6 \times 0.63 \left(\frac{1 - \cos 60}{2}\right)$$

$$= 2.39 + 0.22 + 0.17 = 2.78 \text{ MJ/m}^2$$

In the second method, use Figure 5.6.1 to get the angular dependence of $(\tau\alpha)/(\tau\alpha)_n$. The effective angles of incidence of the diffuse and ground-reflected radiation are 57° and 65°, as before. From Figure 5.3.1, $\tau_n = 0.88$, $\alpha_n = 0.93$ (given), so

$$(\tau\alpha)_n = 1.01 \times 0.88 \times 0.93 = 0.83$$

From Figure 5.6.1 with the beam radiation at $\theta = 7^\circ$, $(\tau\alpha)/(\tau\alpha)_n = 0.99$ and

$$(\tau\alpha)_b = 0.83 \times 0.99 = 0.82$$

From Figure 5.6.1 with the diffuse radiation at $\theta = 57^\circ$, $(\tau\alpha)/(\tau\alpha)_n = 0.87$ and

$$(\tau\alpha)_d = 0.83 \times 0.87 = 0.72$$

From Figure 5.6.1 with the ground-reflected radiation at $\theta = 65^\circ$, $(\tau\alpha)/(\tau\alpha)_n = 0.76$ and

$$(\tau\alpha)_g = 0.83 \times 0.76 = 0.63$$

These are essentially identical to the results of the first solution. ■

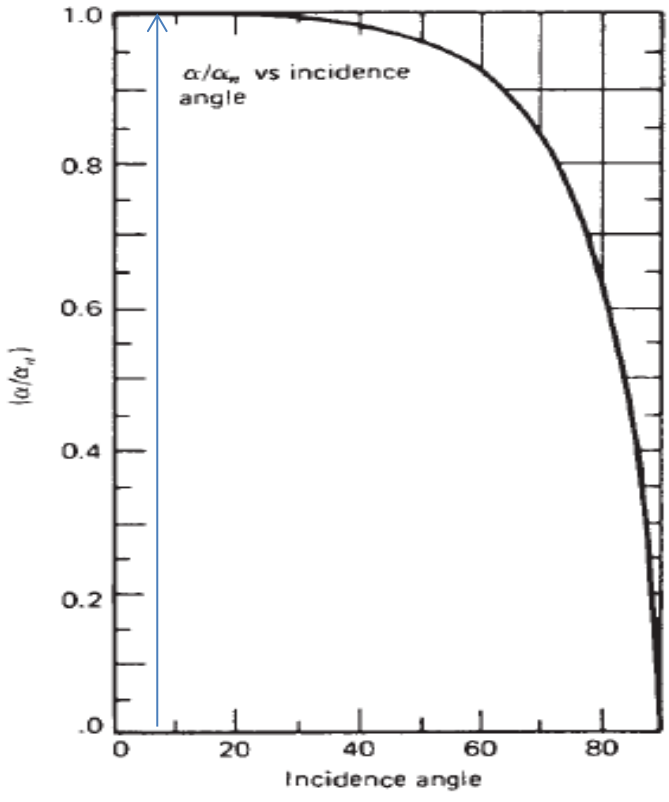

Figure 4.11.1 absorptance at n face. From Beck

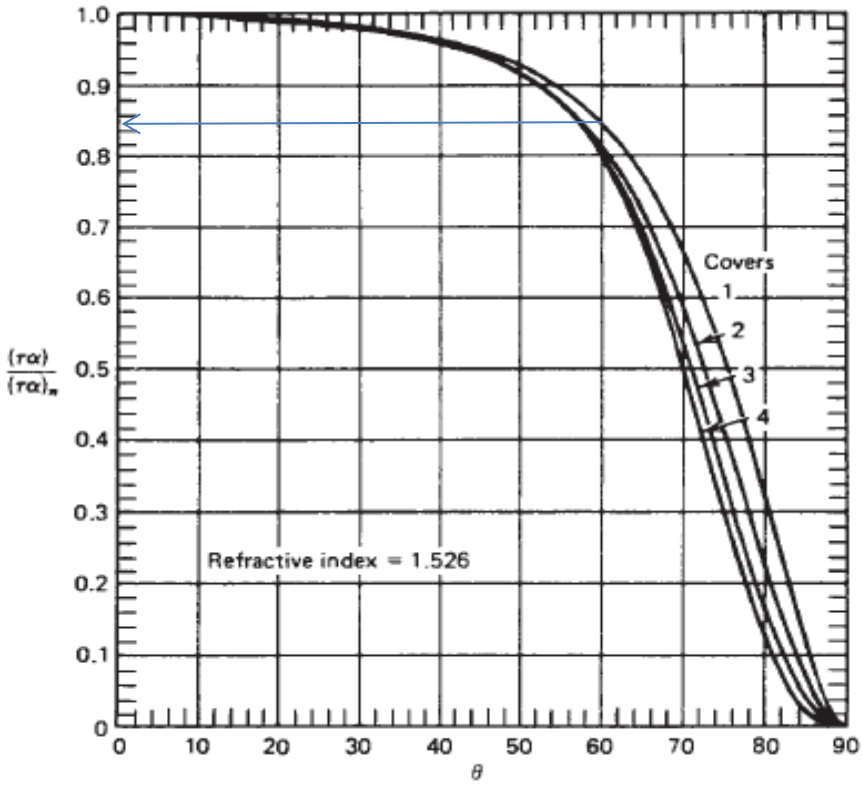

Figure 5.6.1 Typical $(\tau\alpha)/(\tau\alpha)_n$ curves for one to four covers. Adapted from Kle

MONTHLY AVERAGE ABSORBED RADIATION

Methods for the evaluation of long-term solar system performance[4] require that the average radiation absorbed by a collector be evaluated for monthly periods. The solar transmittance and absorptance are both functions of the angle at which solar radiation is incident on the collector. Example 5.9.1 illustrated how to calculate the absorbed solar radiation for an hour. This calculation can be repeated for each hour of each day of the month, from which the monthly average absorbed solar radiation can be found. Klein (1979) calculated the monthly average absorbed solar radiation in this manner using many years of data. He defined a monthly average transmittance-absorptance product[5] which when multiplied by the monthly average radiation incident on a collector yields the monthly average absorbed radiation $\overline{S}$:

$$(\overline{\tau\alpha}) = \frac{\overline{S}}{\overline{H}_T} = \frac{\overline{S}}{\overline{H}\,\overline{R}} \tag{5.10.1}$$

The following methods, analogous to the hourly evaluations of S, can be used to find $\overline{S}$.

Using the isotropic diffuse assumption, Equation 2.19.1 becomes

$$\overline{S} = \overline{H}_b \overline{R}_b\,(\overline{\tau\alpha})_b + \overline{H}_d\,(\overline{\tau\alpha})_d \left(\frac{1+\cos\,\beta}{2}\right) + \overline{H}\rho_g\,(\overline{\tau\alpha})_g \left(\frac{1-\cos\,\beta}{2}\right) \tag{5.10.2}$$

For the diffuse and ground-reflected terms, $(\overline{\tau\alpha})_d$ and $(\overline{\tau\alpha})_g$ can be evaluated using the effective incidence angles given in Figure 5.4.1. These are functions of the properties of the cover and absorber and β, the collector slope, and so do not change with time for collectors mounted at fixed β. The hourly and monthly values are thus the same, and they can be written with or without the overbars.

Example 5.10.1

Estimate $\overline{S}$ for a south-facing vertical collector-storage wall at Springfield, Illinois, 40° N latitude. The wall consists of double glazing with a black-finished absorbing surface behind the glass with α at normal incidence of 0.90. The monthly average daily radiation on a horizontal surface $\overline{H}$, in megajoules per square meter, is shown in the table that follows. The ground reflectance is assumed to be 0.3 for all months. The angular dependence of $(\tau\alpha)$ for the two-cover glazing is as shown in Figure 5.6.1. The glass has $KL = 0.0125$. Calculate the monthly radiation on the wall $\overline{H}_T$, the monthly absorbed radiation $\overline{S}$, and the monthly average $(\overline{\tau\alpha})$.

Solution

The calculations are shown in detail for January, and the results for all months are shown in the table.

For these two covers, from Figure 5.3.1 at normal incidence, the transmittance is 0.83. With the absorber normal-incidence absorptance of 0.90, $(\overline{\tau\alpha})_n = 1.01 \times 0.83 \times 0.90 = 0.754$. For the vertical collector the effective incidence angle of both the diffuse and the ground-reflected radiation is 59° from Figure 5.4.1. From Figure 5.6.1 at 59°, $(\overline{\tau\alpha})/(\tau\alpha)_n = 0.83$ so that $(\overline{\tau\alpha})_d = (\overline{\tau\alpha})_g = 0.83 \times 0.754 = 0.626$. These values apply to all months.

For January, from Figure 5.10.1(b), at 40° latitude and 90° slope, $\overline{\theta}_b = 41°$. From Figure 5.6.1, $(\overline{\tau\alpha})_b/(\tau\alpha)_n = 0.96$ for the two-cover system. Thus $(\overline{\tau\alpha})_b = 0.96 \times 0.754 = 0.724$.

For January, $\overline{H}_o = 15.21$ MJ/m^2, so $\overline{K}_T = 6.63/15.21 = 0.436$. For the mean day of the month, from Table 1.6.1, $\delta = -20.9°$. Thus

$$\omega_s = \cos^{-1}[-\tan(-20.9)\ \tan\ 40] = 71.3°$$

Equation 2.12.1 is used to calculate the diffuse fraction. For January this gives $\overline{H}_d/\overline{H} = 0.458$. Then

$$\overline{H}_d = 6.63 \times 0.458 = 3.04 \text{ MJ/m}^2$$

and

$$\overline{H}_b = 3.59 \text{ MJ/m}^2$$

From Equation 2.19.3, $\overline{R}_b = 2.32$.

We can now calculate $\overline{H}_T$ with Equation 2.19.1 based on the isotropic diffuse assumption:

$$\overline{H}_T = 3.59 \times 2.32 + 3.04 \left(\frac{1 + \cos\ 90}{2}\right) + 6.63 \times 0.3 \left(\frac{1 - \cos\ 90}{2}\right)$$
$$= 8.33 + 1.52 + 0.99 = 10.84 \text{ MJ/m}^2$$

With the transmittance-absorptance products determined above, again using the isotropic assumption (Equation 5.10.2),

$$\overline{S} = 3.59 \times 2.32 \times 0.724 + 3.04 \times 0.626 \left(\frac{1 + \cos\ 90}{2}\right)$$
$$+\ 6.63 \times 0.3 \times 0.626 \left(\frac{1 - \cos\ 90}{2}\right)$$
$$= 6.03 + 0.95 + 0.62 = 7.60 \text{ MJ/m}^2$$

The average transmittance-absorptance product for the month is then

$$(\overline{\tau\alpha}) = \frac{\overline{S}}{\overline{H}_T} = \frac{7.60}{10.84} = 0.70$$

The monthly results are as follows:

Month	$\overline{H}$	$\overline{K}_T$	$\overline{H}_T$	$(\overline{\tau\alpha})_b$	Absorbed Radiation, MJ/m^2				
					Beam	Diffuse	Gr. Refl.	$\overline{S}$	$(\overline{\tau\alpha})$
Jan.	6.63	0.44	10.84	0.72	6.03	0.95	0.62	7.60	0.70
Feb.	9.77	0.48	12.59	0.69	6.28	1.27	0.92	8.47	0.67
Mar.	12.97	0.47	11.65	0.63	4.25	1.85	1.22	7.32	0.63
Apr.	17.20	0.50	11.03	0.51	2.41	2.33	1.62	6.36	0.58
May	21.17	0.53	10.59	0.38	1.22	2.64	1.99	5.84	0.55
June	23.80	0.57	10.52	0.26	0.68	2.72	2.23	5.63	0.54
July	23.36	0.57	10.79	0.27	0.83	2.64	2.19	5.66	0.53
Aug.	20.50	0.56	11.69	0.44	2.11	2.39	1.92	6.42	0.55
Sep.	16.50	0.55	13.18	0.59	4.45	1.98	1.55	7.98	0.61
Oct.	12.13	0.54	14.23	0.67	6.72	1.49	1.14	9.35	0.66
Nov.	7.68	0.47	12.09	0.72	6.70	1.02	0.72	8.44	0.70
Dec.	5.57	0.40	9.46	0.72	5.22	0.86	0.52	6.61	0.70

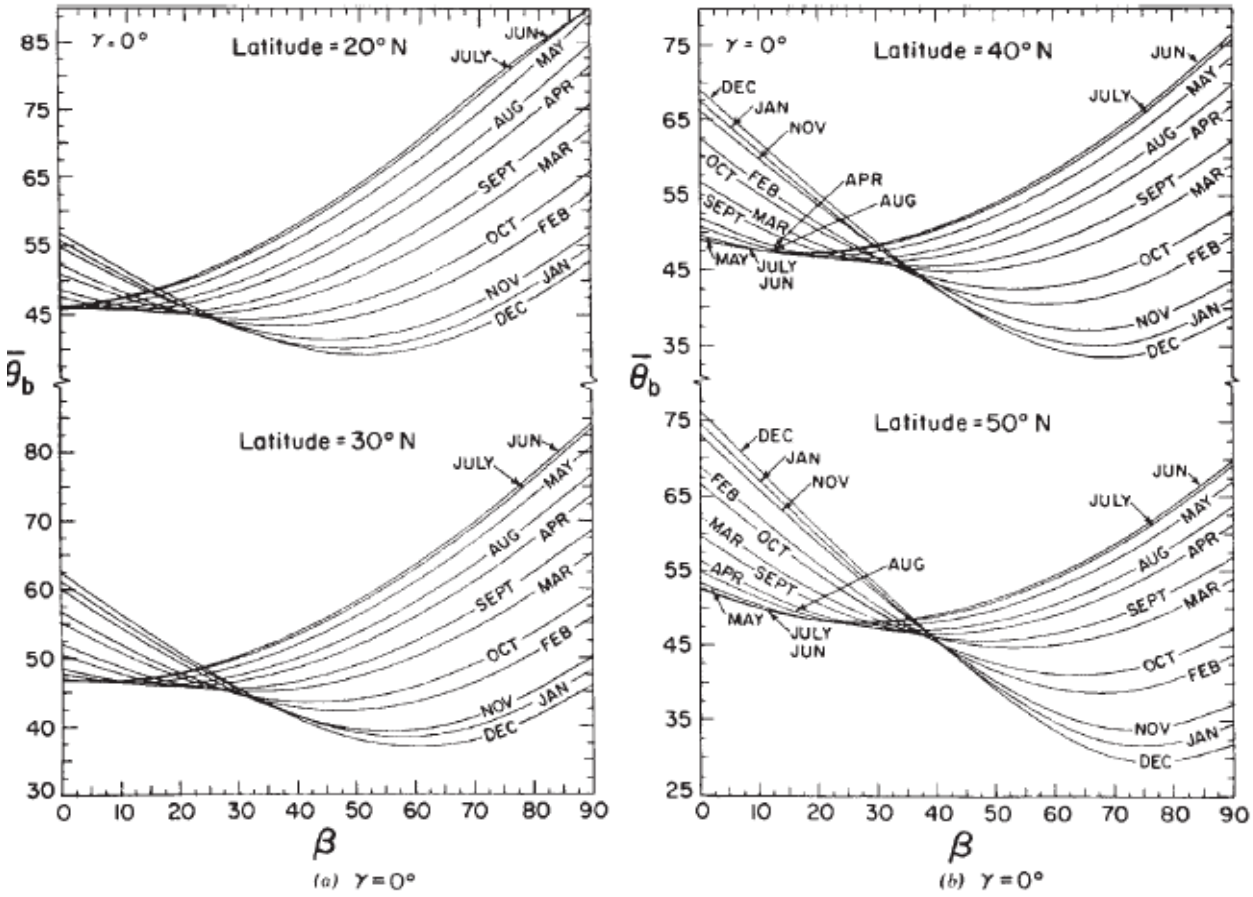

'igure 5.10.1 Monthly average beam incidence angle for various surface locations and orientations. For southern

Table 5.1.1 Average Refractive Index n in Solar Spectrum of Some Cover Materials

Cover Material	Average n
Glass	1.526
Polymethyl methacrylate	1.49
Polyvinylfluoride	1.45
Polyfluorinated ethylene propylene	1.34
Polytetrafluoroethylene	1.37
Polycarbonate	1.60

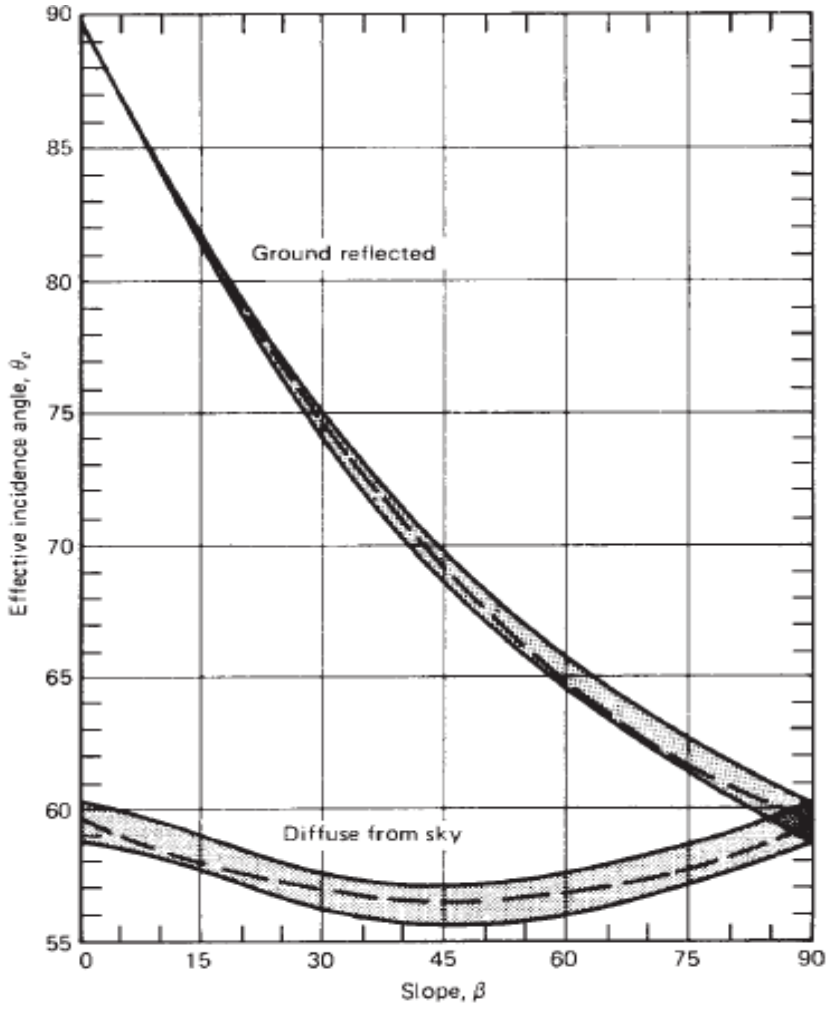

Figure 5.4.1 Effective incidence angle of isotropic diffuse radiation and isotropic ground-reflected

Solar Water Heating: Active and Passive

5. Solar collector applications

Solar collectors have been used in a variety of applications. These are described in this section. In Table 10 the most important technologies in use are listed together with the type of collector that can be used in each case.

5.1. Solar water heating systems

The main part of a SWH is the solar collector array that absorbs solar radiation and converts it into heat. This heat is then absorbed by a heat transfer fluid (water, non-freezing liquid, or air) that passes through the collector. This heat can then be stored or used directly. Portions of the solar energy system are exposed to the weather conditions, so they must be protected from freezing and from overheating caused by high insolation levels during periods of low energy demand.

In solar water heating systems, potable water can either be heated directly in the collector (direct systems) or

indirectly by a heat transfer fluid that is heated in the collector, passes through a heat exchanger to transfer its heat to the domestic or service water (indirect systems). The heat transfer fluid is transported either naturally (passive systems) or by forced circulation (active systems). Natural circulation occurs by natural convection (thermosyphoning), whereas for the forced circulation systems pumps or fans are used. Except for thermosyphon and integrated collector storage (ICS) systems, which need no control, solar domestic and service hot water systems are controlled using differential thermostats.

Five types of solar energy systems can be used to heat domestic and service hot water: thermosyphon, ICS, direct circulation, indirect, and air. The first two are called passive systems as no pump is employed, whereas the others are called active systems because a pump or fan is employed in order to circulate the fluid. For freeze protection, recirculation and drain-down are used for direct solar water heating systems and drain-back is used for indirect water heating systems.

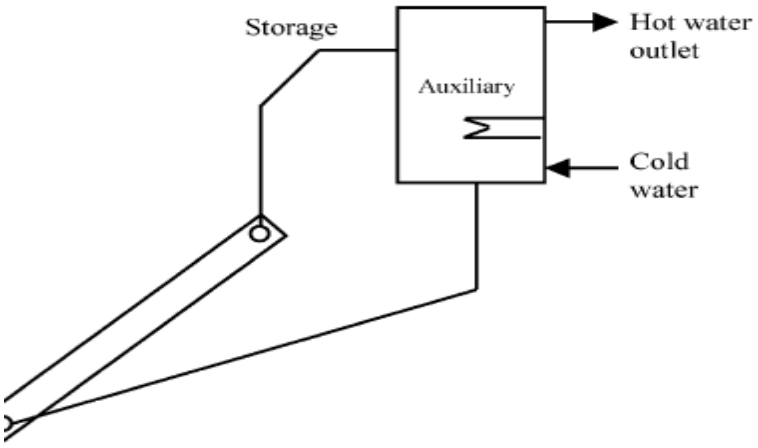

. 24. Schematic diagram of a thermosyphon solar water heater.

5.1.1. Thermosyphon systems (passive)

Thermosyphon systems, shown schematically in Fig. 24, heat potable water or heat transfer fluid and use natural convection to transport it from the collector to storage. The water in the collector expands becoming less dense as the sun heats it and rises through the collector into the top of the storage tank. There it is replaced by the cooler water that has sunk to the bottom of the tank, from which it flows down the collector. The circulation continuous as long as there is sunshine. Since the driving force is only a small density difference larger than normal pipe sizes must be used to minimise pipe friction. Connecting lines must be well insulated to prevent heat losses and sloped to prevent formation of air pockets which would stop circulation. At night, or whenever the collector is cooler than the water in the tank the direction of the thermosyphon flow will reverse, thus cooling the stored water. One way to prevent this is to place the top of the collector well below (about 30 cm) the bottom of the storage tank.

5.1.2. Integrated collector storage systems (passive)

ICS systems use hot water storage as part of the collector, i.e. the surface of the storage tank is used also as an absorber. As in all other systems, to improve stratification, the hot water is drawn from the top of the tank and cold make-up water enters to the bottom of the tank on the opposite side.

The main disadvantage of the ICS systems is the high thermal losses from the storage tank to the surroundings since most of the surface area of the storage tank cannot be thermally insulated as it is intentionally exposed for the absorption of solar radiation. In particular, the thermal losses are greatest during the night and overcast days with low ambient temperature. Due to these losses the water temperature drops substantially during the night especially during the winter. Various techniques have been used to avoid this from happening. Tripanagnostopoulos et al. [136] presented a number of experimental units in which the reduction of thermal losses was achieved by considering single and double cylindrical horizontal tanks properly placed in truncated symmetric and asymmetric CPC reflector troughs.

5.1.3. Direct circulation systems (active)

In direct circulation systems, shown schematically in Fig. 29, a pump is used to circulate potable water from storage to the collectors when there is enough available solar energy to increase its temperature and then return the heated water to the storage tank until it is needed. As a pump circulates the water, the collectors can be mounted either above or below the storage tank. The optimum flow rate for such units is about 0.015 l/m^2 of collector area. Direct circulation systems can be used in areas where freezing is not frequent. For extreme weather conditions, freeze protection is usually provided by recirculating warm water from the storage tank. Direct circulation systems often use a single storage tank equipped with an auxiliary water heater, but two-tank storage systems can also be used.

Direct circulation systems can be used with water supplied from a cold water storage tank or connected directly to city water mains. Pressure-reducing valves and pressure relief valves are required however when the city water pressure is greater than the working pressure of the collectors. Direct water heating systems should not be used in areas where the water is extremely hard or acidic because scale deposits may clog or corrode the collectors.

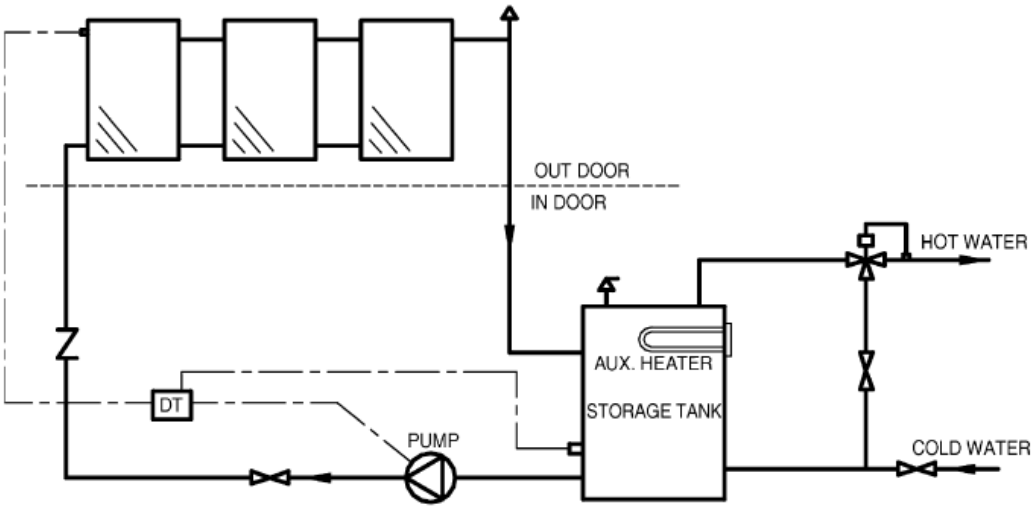

Fig. 29. Direct circulation system.

5.1.4. Indirect water heating systems (active)

Indirect water heating systems, shown schematically in Fig. 31, circulate a heat transfer fluid through the closed collector loop to a heat exchanger, where its heat is transferred to the potable water. The most commonly used heat transfer fluids are water/ethylene glycol solutions, although other heat transfer fluids such as silicone oils and refrigerants can also be used. When fluids that are non-potable or toxic are used double-wall heat exchangers should be employed. The heat exchanger can be located inside the storage tank, around the storage tank (tank mantle) or can be external. It should be noted that the collector loop is closed and therefore an expansion tank and a pressure relief valve are required. Additional over-temperature protection may be needed to prevent the collector heat transfer fluid from decomposing or becoming corrosive.

A variation of indirect water heating systems is the drain-back system. Drain-back systems are generally indirect water heating systems that circulate water through the closed collector loop to a heat exchanger, where its heat is transferred to the potable water. Circulation continues as long as usable energy is available. When the circulation pump stops the collector fluid drains by gravity to a drain-back tank. If the system is pressurised the tank serves also as

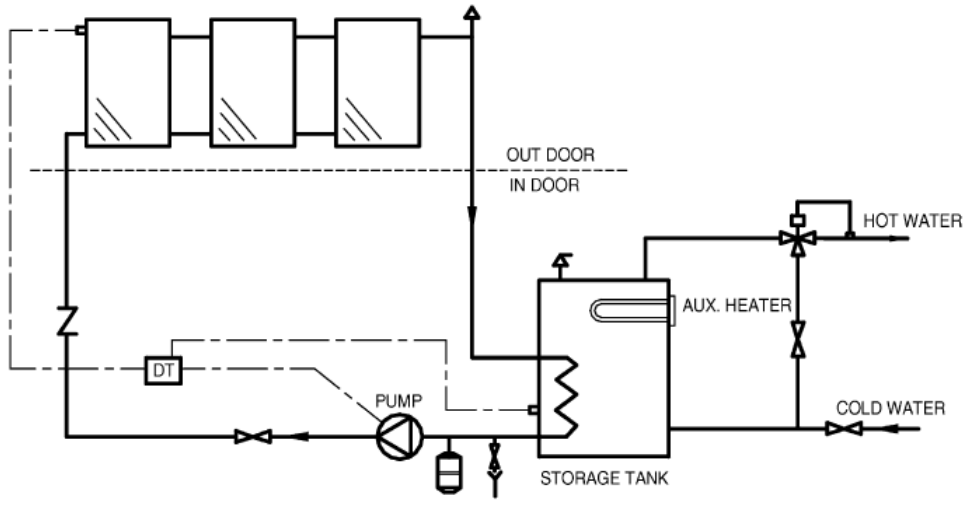

Fig. 31. Indirect water heating system.

5.1.5. Air systems

Air systems are indirect water heating systems that circulate air via ductwork through the collectors to an air-to-liquid heat exchanger. In the heat exchanger, heat is transferred to the potable water, which is also circulated through the heat exchanger and returned to the storage tank. Fig. 33 shows a double storage tank system. This type of system is used most often, because air systems are generally used for preheating domestic hot water and thus auxiliary is used only in one tank as shown.

The main advantage of the system is that air does not need to be protected from freezing or boiling, is non-corrosive, and is free. The disadvantages are that air handling equipment (ducts and fans) need more space than piping and pumps, air leaks are difficult to detect, and parasitic power consumption is generally higher than that of liquid systems.

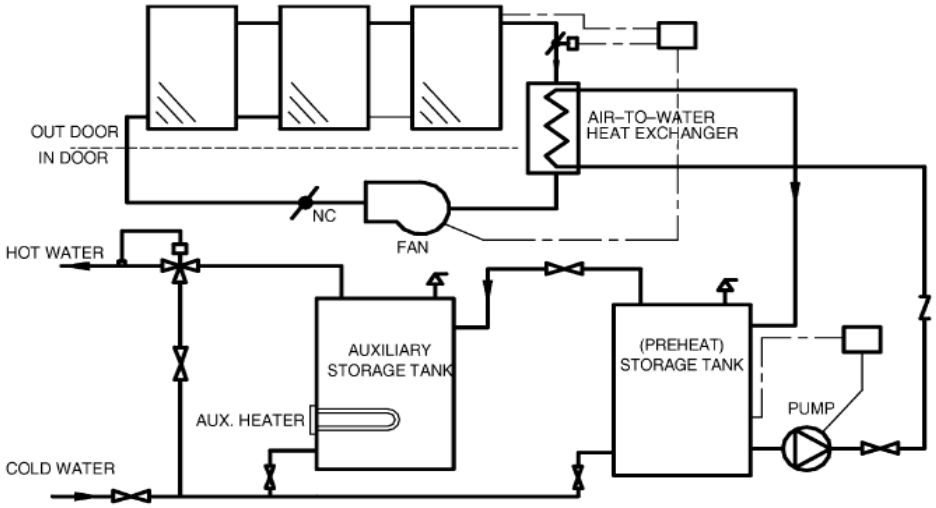

Fig. 33. Air system.

5.2.1. Space heating and service hot water

It is useful to consider solar systems as having five basic modes of operation, depending on the conditions that exist in the system at a particular time [97]:

1. If solar energy is available and heat is not needed in the building, energy gain from the collector is added to storage.
2. If solar energy is available and heat is needed in the building, energy gain from the collector is used to supply the building need.
3. If solar energy is not available, heat is needed in the building, and the storage unit has stored energy in it, the stored energy is used to supply the building need.
4. If solar energy is not available, heat is needed in the building, and the storage unit has been depleted, auxiliary energy is used to supply the building need.
5. The storage unit is fully heated, there are no loads to met, and the collector is absorbing heat.

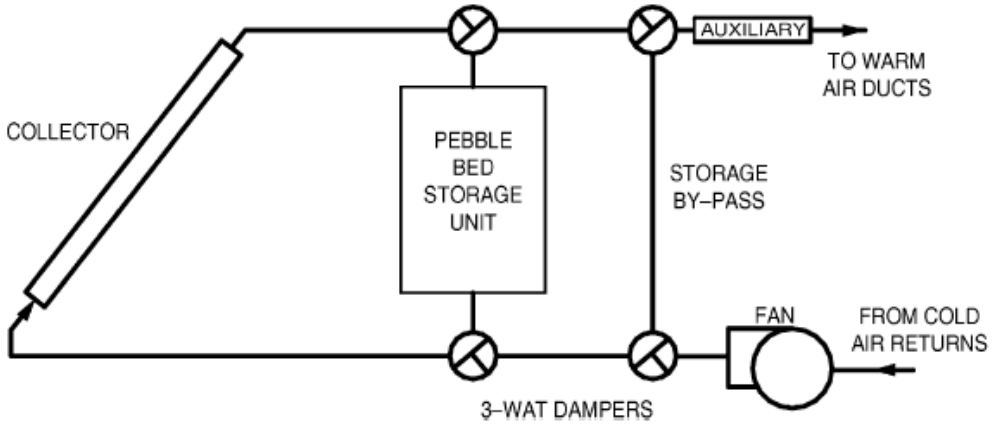

Fig. 34. Schematic of basic hot air system.

WATER HEATING SYSTEMS

The basic elements in solar water heaters can be arranged in several system configurations. The most common of these are shown in Figure 12.1.1. Auxiliary energy is shown added in three different ways; these are interchangeable among the four methods of transferring heat from the collector to the tank.

A passive water heater (also called natural circulation or thermosyphon) is shown in Figure 12.1.1(a). The tank is located above the collector, and water circulates by natural convection whenever solar energy in the collector adds energy to the water in the collector leg and so establishes a density difference. Auxiliary energy is shown added to the water in the tank near the top to maintain a hot-water supply. Sometimes the collector is ''close coupled'' with a horizontal cylindrical storage tank.

Figure 12.1.1(b) shows an example of a forced-circulation system. A pump is required; it is usually controlled by a differential thermostat turning on the pump when the temperature at the top header is higher than the temperature of the water in the bottom of the tank by a sufficient margin to assure control stability (as outlined in Section 10.4). A check valve is needed to prevent reverse circulation and resultant nighttime thermal losses from the collector. Auxiliary energy is shown added to the water in the pipe leaving the tank to the load.

In climates where freezing temperatures occur designs (a) and (b) need to be modified. Design (a) can include a heat exchanger in the tank and design (b) is sometimes provided with a drain-back tank that receives the entire collector and piping water whenever the pump does not operate. Examples of systems using nonfreezing fluids in the collector are shown in Figures 12.1.1(c) and (d). The collector heat exchangers can be either internal or external to the tank. In one modification of design (c) the heat exchanger forms a mantel around the tank (Furbo and Knudsen, 2004; Furbo et al., 2005). Auxiliary energy is shown added to the water in the storage tank in Figure 12.1.1(c) by a heat exchanger in the tank. The auxiliary energy supply can also be provided by a standard electric, oil, or gas water heater with storage capacity of its own; this is the two-tank system shown in Figure 12.1.1(d). Any of these systems may be fitted with tempering valves that mix cold supply water with heated water to put an upper limit on the temperature of the hot water going to the distribution system. Other equipment not shown can include surge tanks and pressure relief valves.

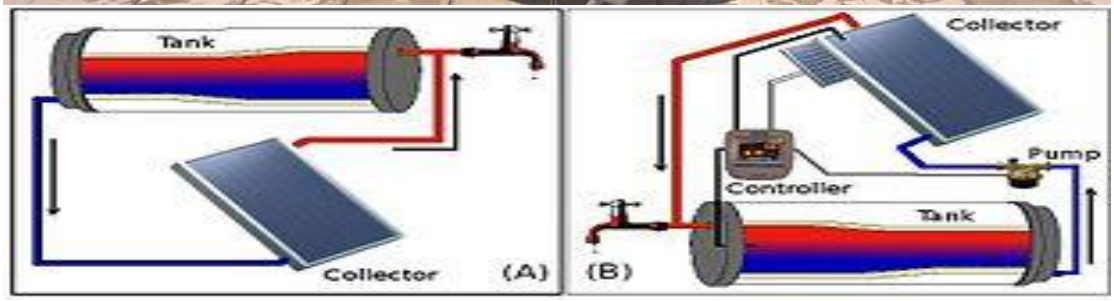
Tank
Collector
(A)
Collector
Pump
Controller
Tank
(B)

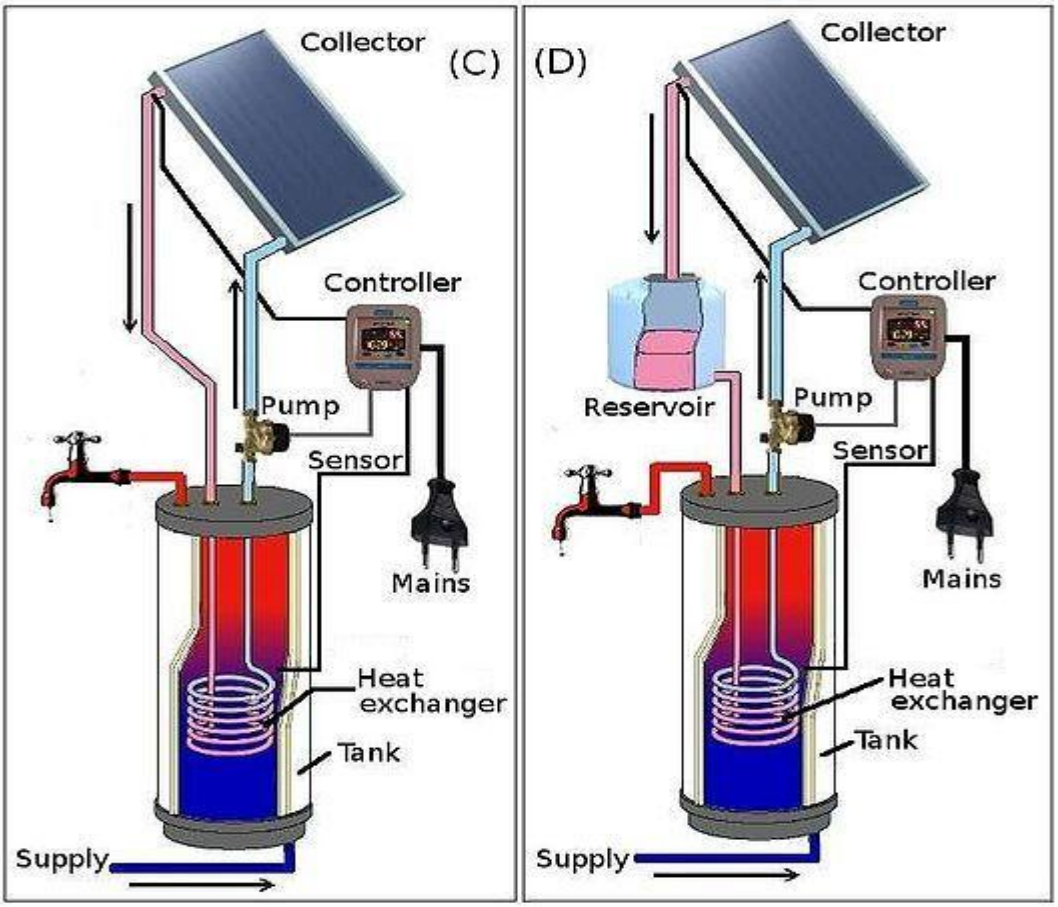
Collector
(C)
Controller
Pump
Sensor
Mains
Heat exchanger
Tank
Supply
Collector
(D)
Controller
Reservoir
Pump
Sensor
Mains
Heat exchanger
Tank
Supply

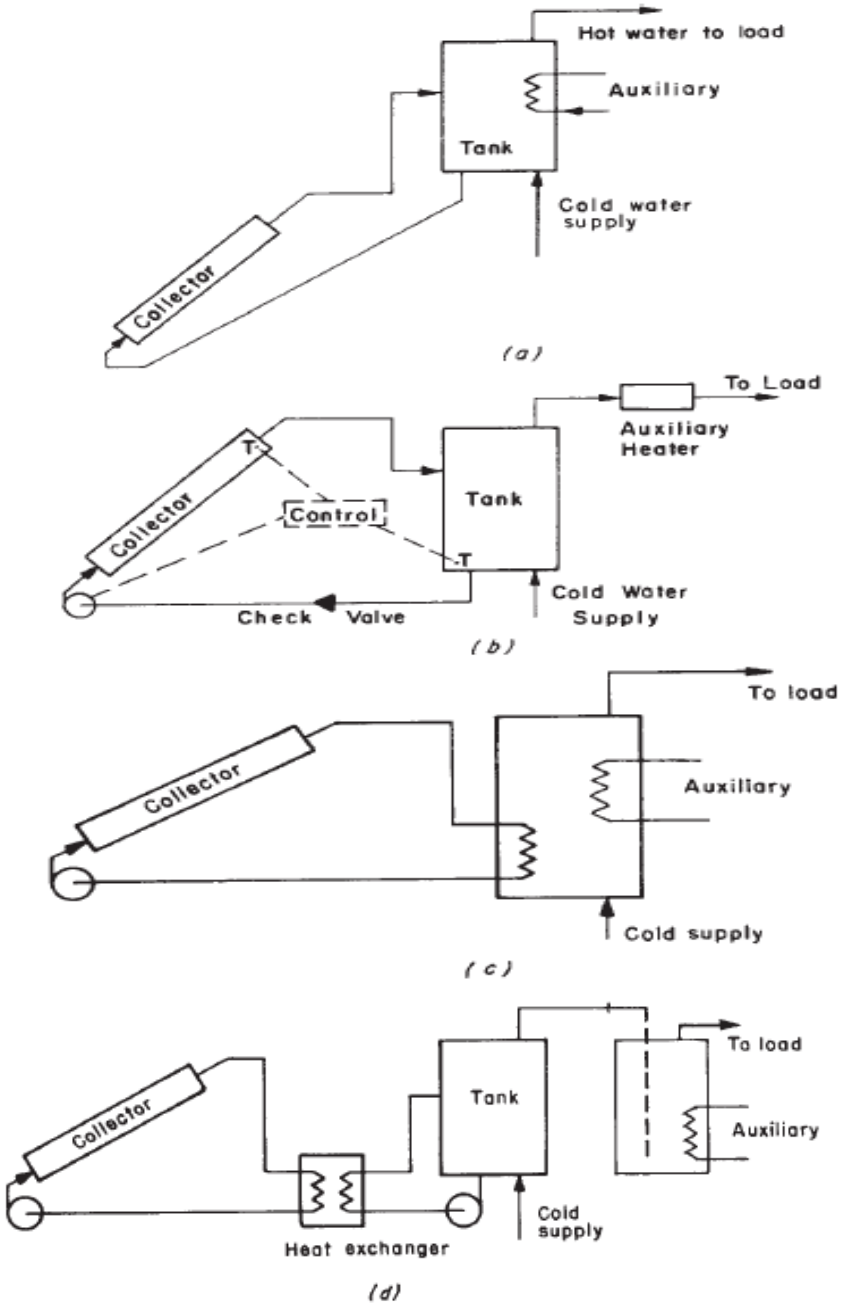

Figure 12.1.1 Schematic of common configurations of water heaters. (a) A natural-circulation system. (b) One-tank forced-circulation system. (c) System with antifreeze loop and internal heat exchanger. (d) System with antifreeze loop and external heat exchanger. Auxiliary is shown added in the tank, in a line heater, or in a second tank; any of these auxiliary methods can be used with any of the collector-tank arrangements.

Example 12.2.1

A collector with $(\tau\alpha) = 0.78$ has a temperature dependence of overall loss coefficient as shown in the figure. The fluid being heated is a 50% solution of propylene glycol in water. The glycol loop is pressurized to a limit of 4.0 atm. On a summer day the radiation on the collector is 1.15 kW/m^2 and ambient temperature is 38°C. Will the solution in the collector boil if the circulating pump does not operate?

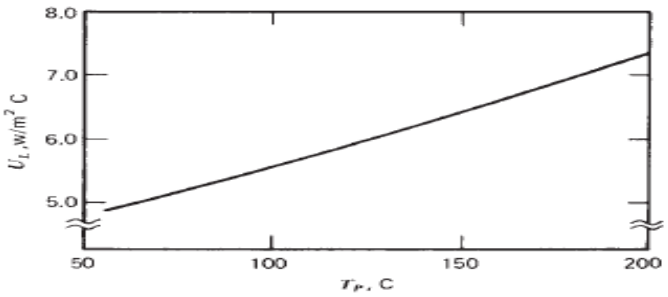

Solution

With no flow, absorbed energy equals losses:

$$G_T(\tau\alpha) = U_L(T_{p,m} - T_a) = 1150 \times 0.78 = 900 \text{ W/m}^2$$

so the plate temperature is

$$T_{p,m} = T_a + \frac{900}{U_L}$$

Since the loss coefficient is a function of plate temperature, it is necessary to simultaneously solve the energy balance equation and the equation for U_L as a function of T_p. Since the relationship between U_L and T_p is in graphical form, it is convenient to perform an iterative solution. Assume for a first estimate that $U_L = 6.5$ W/m^2 °C. Then

$$T_{p,m} = 38 + \frac{900}{6.5} = 176^\circ\text{C}$$

A second estimate of 6.8 W/m^2 °C yields

$$T_{p,m} = 38 + \frac{900}{6.8} = 170^\circ\text{C}$$

The boiling point of this solution is about 145 ^{O}C, so the solution would boil at these circumstances

APPROACHES HAVE BEEN DEVELOPED TO PROTECT COLLECTORS AGAINST DAMAGE BY FREEZING

First, antifreeze solutions can be used in the collector loop with a heat exchanger between the collector and the storage tank. As shown in Figures 12.1.1(c) and (d), the heat exchanger can be external to the tank, wrapped around the tank, or a coil within the tank relying on natural circulation of the water in the tank for heat transfer. The

Second, air can be used as the heat transfer fluid in the collector–heat exchanger loop of Figure 12.1.1(d). Air heating collectors have lower $F_R(\tau\alpha)$ and $F_R U_L$ than liquid heating collectors. However, no toxic fluids are involved, no second heat exchanger interface is needed, leakage is not critical, and boiling is not a problem.

The third method of freeze protection is to circulate warm water from the tank through the collector to keep it from freezing. Thermal losses from the system are significantly increased, and an additional control mode must be provided. This method can only be considered in climates where freezes are infrequent. In emergencies, when pump power is lost, the collector and piping subject to freezing temperatures must be drained.

The fourth method is based on draining water from the collectors when they are not operating. Draining systems must be vented at their highest point and must be arranged so that collectors and piping exposed to freezing temperatures are completely emptied. These systems are of two types: **drain-back** systems, in which the water drains back into the tank or a sump that is not exposed to freezing temperatures, and **drain-out** systems, which drain out of the system to waste.

AUXILIARY ENERGY

The degree of reliability desired of a solar process to meet a particular load can be provided by a combination of properly sized collector and storage units and an auxiliary energy source. In a few unique areas where there seldom are clouds of significant duration, it may be practical to provide all of the loads with the solar systems. However, in most climates auxiliary energy is needed to provide high reliability and avoid gross overdesign of the solar system.

Auxiliary energy can be provided in any of the three ways shown in Figure 12.3.1:

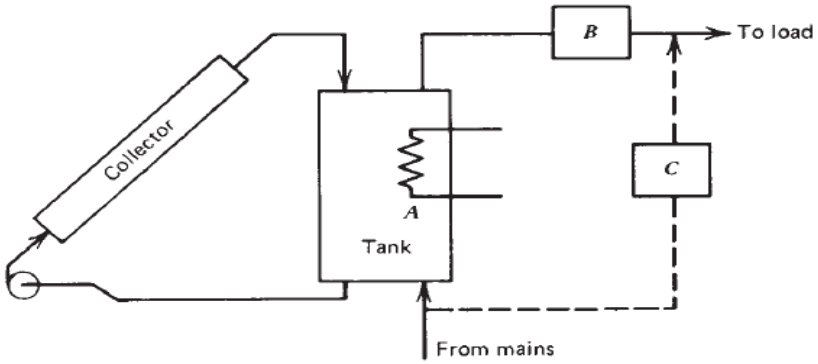

Figure 12.3.1 Schematic of alternative location for auxiliary energy supply to a one-tank forced-circulation solar water heater: A, in tank; B, in line to load; C, in a bypass around tank.

A Energy can be supplied to the water in the tank, at location A. Auxiliary energy is controlled by a thermostat in the top part of the tank which keeps the temperature in the top portion at or above a minimum setpoint. This is the simplest and probably the least expensive method. However, it has the disadvantage that the auxiliary energy supply may increase the temperature of the water in the bottom of the tank and thus the collector inlet temperature, resulting in reduction of solar gain. In standard electric domestic hot-water tanks there are two elements, one near the bottom and one about one-third of the way down from the top. When using such a tank in a solar system, it is common practice to disable the lower element so that the lower two-thirds of the tank is essentially solar energy storage and the upper one-third of the tank is auxiliary energy storage. The collector inlet and outlet must be suitably arranged.

B Auxiliary energy can be supplied to the water leaving the tank, thus ''topping off'' the solar energy with auxiliary energy. This requires a heater separate from the solar tank. This heater may be a simple line heater or it may be a conventional water heater with storage capacity of its own. Auxiliary energy is controlled to maintain the outlet temperature from the auxiliary heater at a desired level. This method has the advantage of using the maximum possible solar energy from the tank without driving up the collector temperature, but additional heat loss will occur from the auxiliary heater if it has storage capacity. If a second tank is used, it is not sufficient to just have a single pipe connecting the two tanks since energy would be transferred from the solar tank to the auxiliary tank only during periods of hot-water draw.

C Auxiliary energy can be added directly to the incoming supply water by bypassing the tank when auxiliary energy is needed. This is a simple method but has the disadvantage that either the solar heated water or the auxiliary heated water must have a temperature above the setpoint so that mixing the two streams produces the desired setpoint temperature. If low-temperature solar heated water is to be utilized, it is necessary that the auxiliary heated water be considerably above the set temperature, a potentially dangerous situation.

The major reasons for the differences in performance on changing the method of adding auxiliary energy concern the temperature at which the collector operates. Adding auxiliary energy to the top of the tank (method A) can result in a higher mean collector temperature, poorer collector performance, and higher requirements for auxiliary energy (depending on the degree of stratification in the tank). Method C, which bypasses the tank when its top section is not hot enough, results in failure to use some collected solar energy.

Method B, with a modulated auxiliary heater (or its equivalent in an on-off auxiliary heater), maximizes the solar collector output and minimizes collector losses by operating at the lowest mean collector temperature of any of the methods. The magnitude of the differences may depend on the degree of stratification in the tank and the insulation on the tank. Losses from the auxiliary heater must be maintained at very low levels or method B may not be best (see Section 12.4).

NATURAL-CIRCULATION SYSTEMS

Circulation in passive solar water heaters such as that shown in Figure 12.1.1(a) occurs when the collector warms up enough to establish a density difference between the leg including the collector and the leg including the tank and the feed line from tank to collector. The density difference is a function of temperature difference, and the flow rate is then a function of the useful gain of the collector which produces the temperature difference. Under these circumstances, these systems are self-adjusting, with increasing

difference at the estimated collector gain. The basic collector equations are

$$Q_u = A_c F_R [S - U_L (T_i - T_a)] \tag{12.6.1}$$

and

$$Q_u = \dot{m} C_p (T_o - T_i) = \dot{m} C_p \, \Delta T_f \tag{12.6.2}$$

Solving for the flow rate,

$$\dot{m} = \frac{A_c F_R [S - U_L (T_i - T_o)]}{C_p \, \Delta T_f} \tag{12.6.3}$$

This equation can be solved for $\dot{m}$ if it is assumed that F' is independent of flow rate. Substituting Equation 6.7.4 for F_R into Equation 12.6.3 and rearranging give

$$\dot{m} = \frac{-U_L F' A_c}{C_p \ln \left\{ 1 - \dfrac{U_L (T_o - T_i)}{S - U_L (T_i - T_a)} \right\}} \tag{12.6.4}$$

Example 12.6.1

A natural-circulation water heater operates with a nearly constant increase in water temperature of 10°C. The collector has an area of 4 m^2, an overall loss coefficient of 4.2 W/m^2 °C, and $F' = 0.91$. If the water inlet temperature is 30°C, the ambient temperature is 15°C, and the radiation absorbed by the collector plate is 780 W/m^2, what is the useful gain from the collector?

Solution

All of the information needed to estimate $\dot{m}$ using Equation 12.6.4 is available:

$$\dot{m} = \frac{-4.2 \times 0.91 \times 4}{4190 \ \ln \left\{ 1 - \dfrac{4.2 \times 10}{780 - 4.2 \, (30 - 15)} \right\}} = 0.060 \text{ kg/s}$$

$$Q_u = 0.060 \times 4190 \times 10 = 2550 \text{ W}$$

INTEGRAL COLLECTOR STORAGE SYSTEMS

Water heaters that combine the functions of collector and storage are manufactured in Japan (Tanishita, 1970), the United States, and elsewhere. The designs of these integral collector storage (ICS) systems vary. The basic configuration is that of a tank or set of interconnected tanks, with energy-absorbing surfaces on their exposed surfaces, enclosed in an insulated box with a transparent cover on the top to admit solar radiation. A cross-sectional schematic of a system of this type is shown in Figure 12.7.1. In the morning, water is put in the tubes, which in this configuration are black plastic cylinders about 0.2 m in diameter. Through the day, the water is heated by absorbed solar energy. The top cover and back insulation reduce energy losses from the cylinders. The performance of this type of collector can be

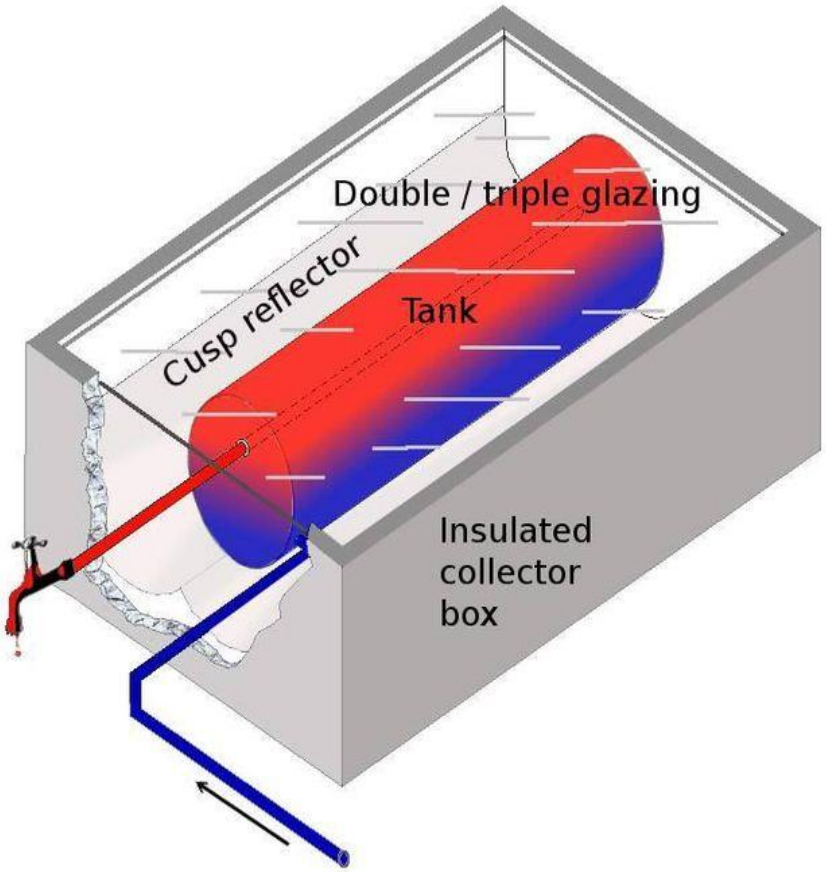

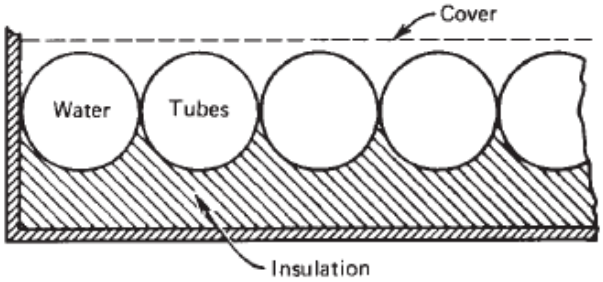

Figure 12.7.1 Schematic section of solar water heaters combining collector and storage.

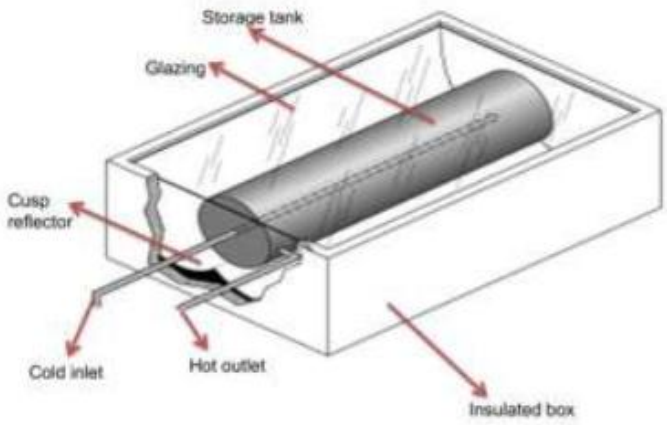

Active Solar Water Heating Systems

There are two Solar Water Heating System types: *Active and Passive*

There are two types of Active Solar Water Heating Systems:

- Direct Circulation Systems
- Indirect Circulation Systems

Direct Circulation Systems

Pump circulates domestic water through the collector(s) and into the building. This type of system works well in climates where it rarely freezes.

The direct pumped system has one or more solar energy collectors installed on the roof and a storage tank located somewhere within the building. A pump circulates the water from the tank up to the collector and back again. This is called a direct (or open loop) system because the sun's heat is transferred directly to the potable water circulating through the collector and storage tank. Neither an anti-freeze nor heat exchanger is involved.

This system has a differential controller that senses temperature differences between water leaving the solar collector and the coldest water in the storage tank. When the water in the collector is about 15-20°F warmer than the water in the storage tank, the pump is turned on by the controller. When the temperature difference drops to about 3-5°F, the pump is turned off.

In this way, the water always gains heat from the collector when the pump operates.

A flush-type freeze protection valve installed near the collector provides freeze protection. Whenever temperatures approach freezing, the valve opens to let warm water flow through the collector.

Direct System Advantages

- Service water used directly from collector loop.
- No heat exchanger – more efficient heat transfer to storage.
- Circulation pump (if needed) needs only to overcome friction losses – system pressurized.

Direct System Disadvantages

- Quality of service water must be good to prevent corrosion, scale or deposits in components.
- Freeze protection depends on mechanical valves.
- Recommended in climates with minimal/no freeze potential, and good water quality.

Indirect Circulation Systems

Pump circulates a non-freezing, heat transfer fluid through the collector(s) and a heat exchanger.

This heats the water that then flows into the home.

This type of system works well in climates prone to freezing temperatures.

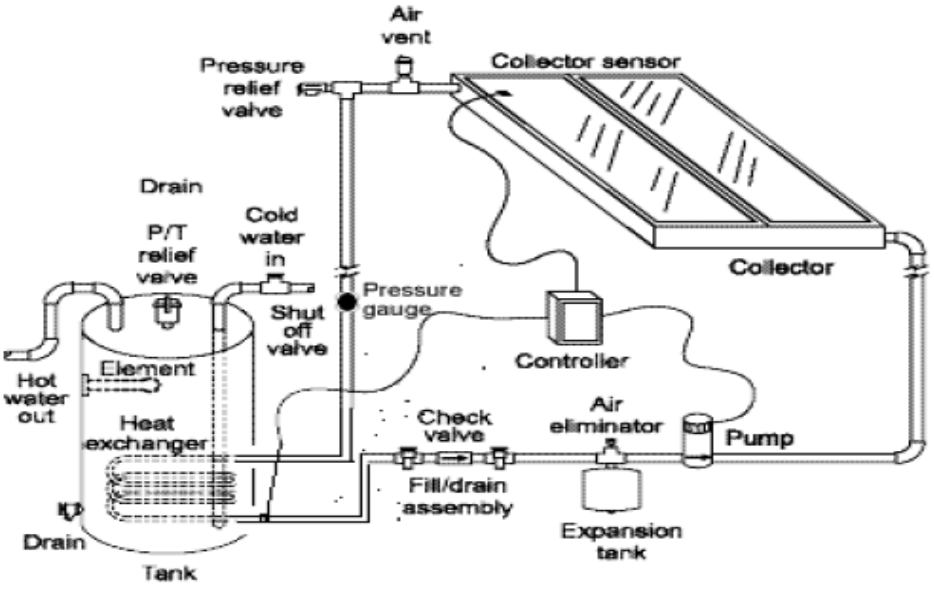

Indirect Pumped System Using Anti-Freeze Solution

This system design is common in northern climates, where freezing weather occurs more frequently. An anti-freeze solution circulates through the collector, and a heat exchanger transfers the heat from the anti-freeze solution to the storage tank water. When toxic heat exchanger fluids are used, a double-walled exchanger is required. Generally, if the heat exchanger is installed in the storage tank, it should be located in the lower half of the tank.

A heat transfer solution is pumped through the collector in a closed loop. The loop includes the collector, connecting piping, the pump, an expansion tank and a heat exchanger. A heat exchanger coil in the lower half of the storage tank transfers heat from the heat transfer solution to the potable water in the solar storage tank. An alternative of this design is to wrap the heat exchanger around the tank. This keeps it from contact with the potable water.

The differential controller, in conjunction with the collector and tank sensors, determines when the pump should be activated to direct the heat transfer fluid through the collector. The photovoltaic panel located on the roof supplies the power to operate the circulating pump.

Indirect System Advantages

- Freeze protection provided by antifreeze fluid or drainback.
- Collector/piping protected from aggressive water.

Indirect System Disadvantages

- Must account for reduced heat transfer efficiency through heat exchanger.
- Added materials = added cost.
- If not using water, fluids require maintenance.
- Most designs require added pumping cost.

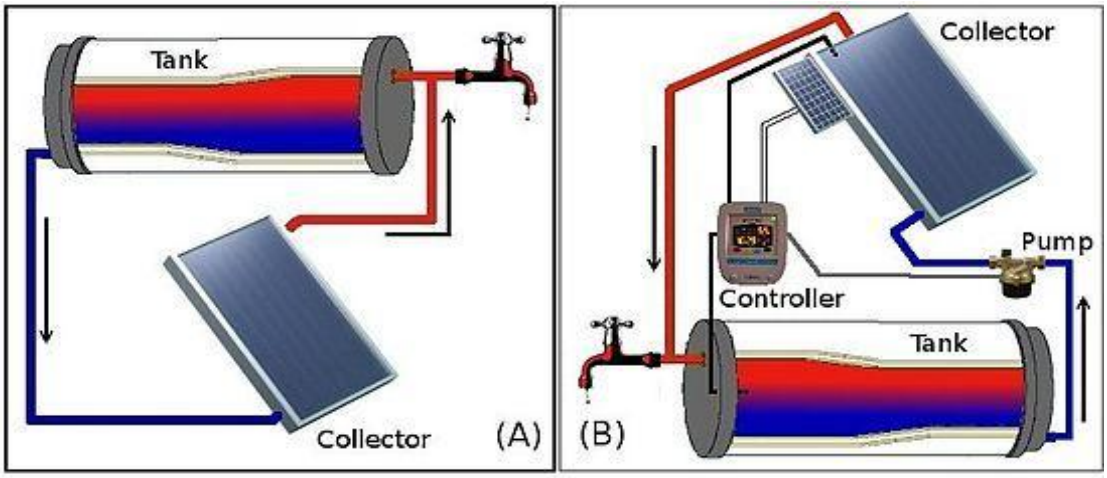

Passive Solar Water Heaters

Passive solar water heaters rely on gravity and the tendency for water to naturally circulate as it is heated.

Passive solar water heater systems contain no electrical components, are generally more reliable, easier to maintain, and possibly have a longer work life than active solar water heater systems.

The two most popular types of passive solar water heater systems are: Integral-Collector Storage (ICS) andThermosyphon systems.

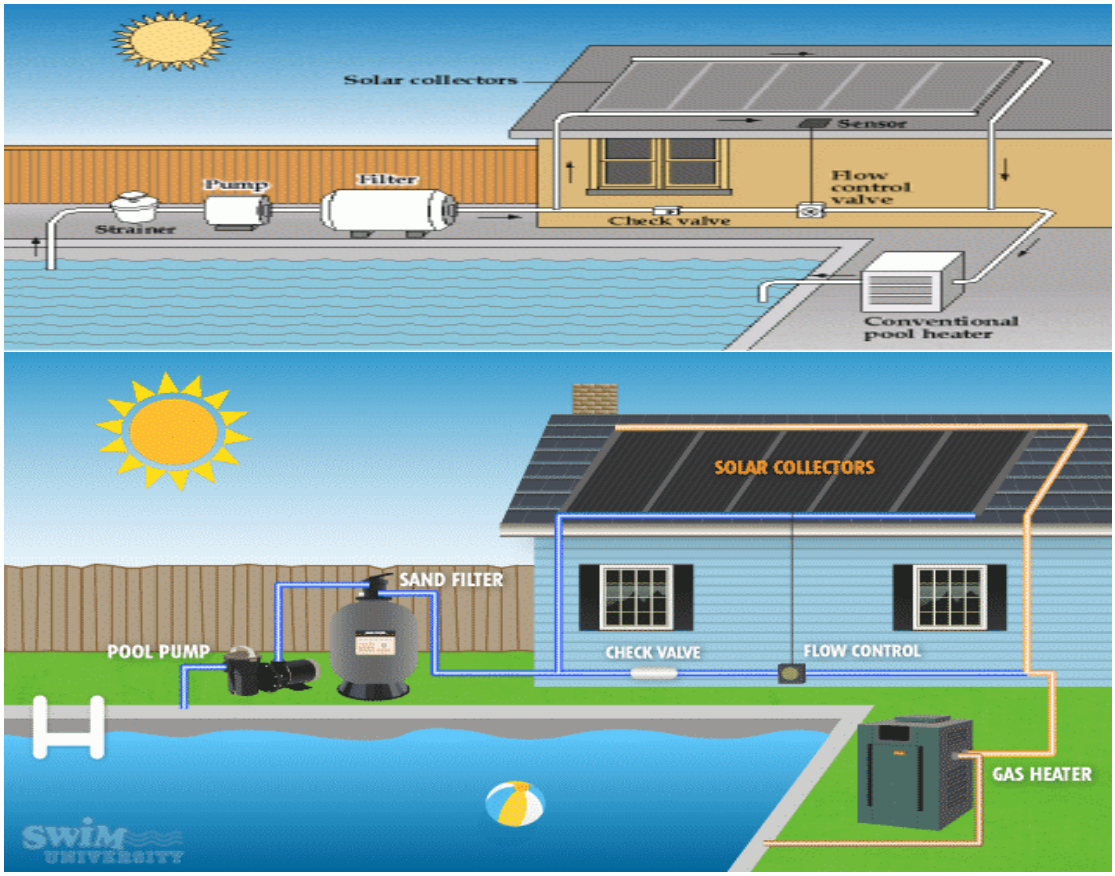

Environmental Benefits

- Solar water heaters do not pollute.
- Solar water heaters help to avoid carbon dioxide, nitrogen oxides, sulfur dioxide, and the other air pollution and wastes created when the local utility generates power or fuel is burned to heat domestic water.
- When a solar water heater replaces an electric water heater, the electricity displaced over 20 years represents more than 50 tons of avoided carbon dioxide emissions alone.

Solar Water Heaters (SWH) or Solar Hot Water Systems (SHWS) are one of the most successful thermal employment of solar energy. They proved to be feasible especially in providing hot water for domestic applications. They are commonly classified into two types:

a) Forced circulation systems.
b) Natural circulation systems (thermosyphon systems).

6.1 Forced circulation solar water heaters

In this type a pump is used to circulate the working fluid through the system. The typical solar heater consists of the following parts (Fig. 6.1):

a) Solar collector (usually flat–plate type)
b) Water storage tank.
c) Upriser (to carry the hot water from the collector to the tank).
d) Downcomer (to return the cold water from the tank to the collector).
e) Water pump (to circulate the fluid between the collector and the tank).
f) Thermal controller (to actuate the pump when the temperature difference between collector inlet and outlet exceeds certain limit.

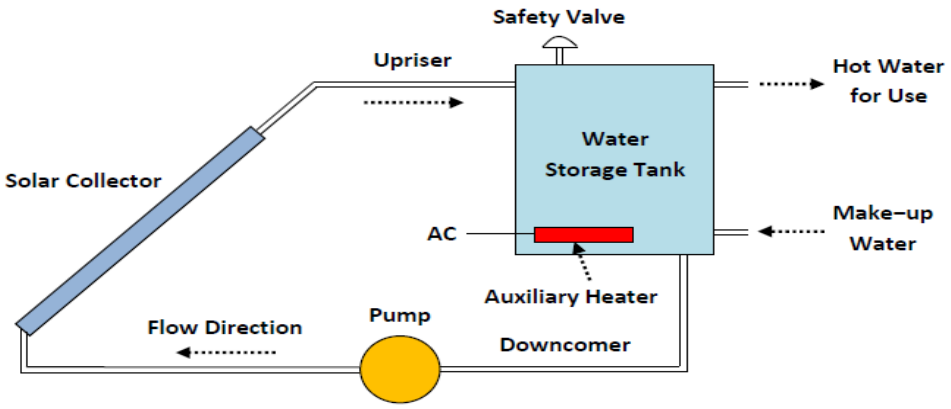

Fig. (6.1): Forced circulation solar water heater.

The water storage tank in forced circulation systems can be put anywhere regardless of the solar collector level since the pump will circulate the water at any condition. The pump is usually actuated when a certain temperature difference is reached between collector inlet and outlet. The freezing of water in the collector risers is a serious problem in cold weather nights. Anti-freeze solutions can be mixed with water inside risers which requires separating collector water from tank water via a heat exchanger.

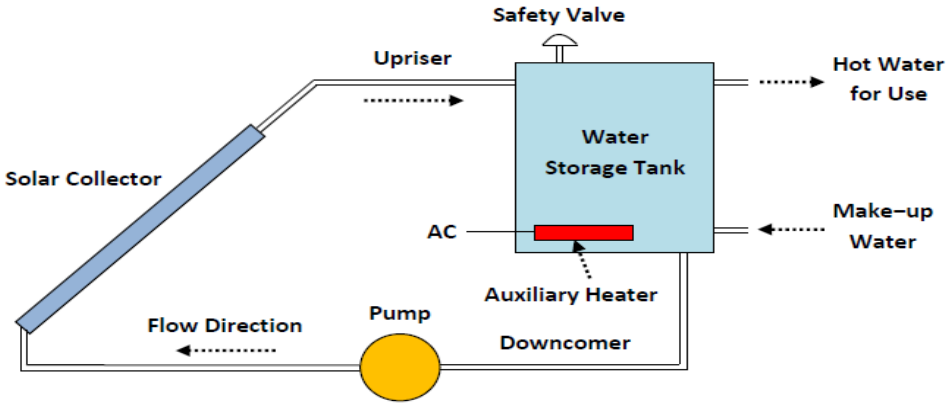

Fig. (6.1): Forced circulation solar water heater.

The water storage tank in forced circulation systems can be put anywhere regardless of the solar collector level since the pump will circulate the water at any condition. The pump is usually actuated when a certain temperature difference is reached between collector inlet and outlet. The freezing of water in the collector risers is a serious problem in cold weather nights. Anti-freeze solutions can be mixed with water inside risers which requires separating collector water from tank water via a heat exchanger.

6.2 Thermosyphon solar water heaters

These systems rely on natural convection to circulate the working fluid between the solar collector and storage tank without using a pump. The buoyancy forces generated by the density differences between the cold water at the bottom of the tank (high density) and the hot water at the top of the collector (low density), propels the circulation of the working fluid. It is therefore necessary to put the water storage tank at a position higher than the collector to ensure the continuity of circulation (Fig. 6.2).

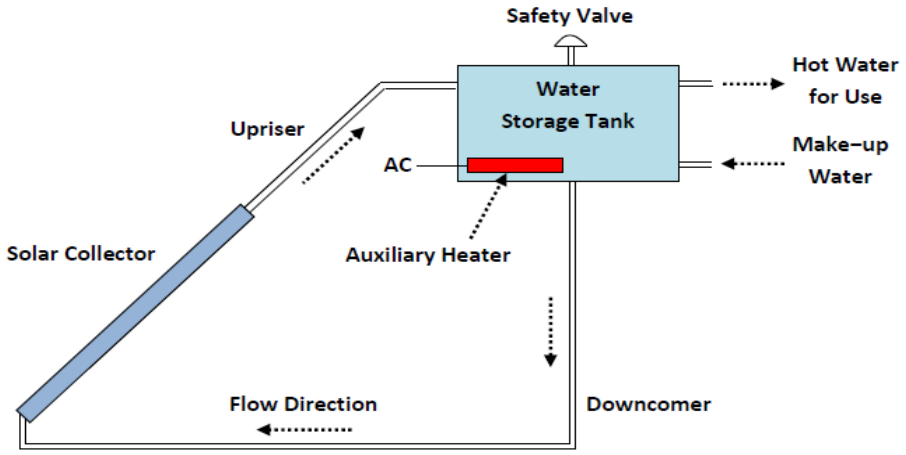

Fig. (6.2): Thermosyphon solar water heater.

6.3 Thermal analysis of solar water heaters

The aim of the thermal analysis of solar water heater is to estimate the tank water temperature at the end of daytime or after certain exposure time to solar radiation. The temperature of water depends on the solar collector area and the tank volume. As a rule of thumb, if a flat–plate solar collector of 1 m^2 area is connected to a storage tank of 50 L then the final tank water temperature at the end of daytime will be around 60 ^{o}C. However, the accurate estimation of tank temperature requires the incorporation of thermal models of all parts of the system in a process called (simulation). In the simulation of a solar system the real performance is imitated theoretically on computer to estimate the system performance for various imposing operation conditions (Irradiance, ambient temperature, working fluid flow rate and rate of hot water usage or water withdrawal from the tank). The following thermal models can be used in a simple simulation process:

a) Flat–plate solar collector

To evaluate the collector fluid outlet temperature T_{fo} equations 5.3, 5.41 and 5.42 can be used as follows:

$$T_{fo} = T_{fi} + \frac{Q_u}{\dot{m} c_{pf}} \qquad 5.3$$

Where: $$Q_u = A_c F_R [\tau\alpha I_T - U_L (T_{fi} - T_a)] \qquad 5.41$$

And: $$F_R = \frac{\dot{m} c_{pf}}{A_c U_L} \left(1 - e^{\frac{-A_c U_L F}{\dot{m} c_{pf}}}\right) \qquad 5.42$$

b) Upriser

The working fluid undergoes thermal losses to the environment when passes through the upriser. To estimate the working fluid temperate T_{uo} at the upriser outlet (before entering the tank) the following equation can be used:

$$T_{uo} = T_a + (T_{fo} - T_a) e^{\frac{-A_u U_u}{\dot{m} c_{pf}}} \qquad 6.1$$

Where U_u is the upriser heat loss coefficient and A_u is the outside surface area of the upriser.

c) Downcomer

The outlet fluid temperature of the downcomer T_{do} is the collector inlet temperature. It can be calculated similar to the upriser as follows:

$$T_{do} = T_{fi} = T_a + (T_{t2} - T_a) e^{\frac{-A_d U_d}{\dot{m} c_{pf}}} \qquad 6.2$$

Where T_{t2} is the tank water mean temperature after a period of operation time, U_d is the downcomer heat loss coefficient and A_d is the outside surface area of the downcomer.

d) Water storage tank

The working fluid enters the storage tank at a temperature T_{uo} and mixes with the tank water that is initially at T_{t1} . The resulting tank temperature T_{t2} after the system operates for a period of time Δt depends on the tank volume, ambient temperature and the water withdrawal rate from the tank. The following energy balance can be written for a fully mixed water storage tank:

$$\begin{pmatrix} Change\ of\ Tank \\ Internal\ Energy \\ in\ Joules \end{pmatrix} = \begin{pmatrix} Input\ Energy \\ from\ Upriser \end{pmatrix} + \begin{pmatrix} Input\ Energy \\ from\ the\ AC \\ Heater \end{pmatrix} - \begin{pmatrix} Thermal \\ Losses\ to \\ Environment \end{pmatrix} - \begin{pmatrix} Thermal\ Losses \\ due\ to\ Water \\ Withdrawal \end{pmatrix}$$

$$M_t c_{pt} (T_{t2} - T_{t1}) = \Delta t [Q_{up} + Q_{AC} - Q_{loss} - Q_w] \qquad 6.3$$

Where: $$Q_{up} = \dot{m} c_{pf} (T_{uo} - T_{t1}) \qquad 6.4$$

$$Q_{loss} = A_t U_{ta} (T_{t1} - T_a) \qquad 6.5$$

$$Q_w = \dot{m}_w c_{pw} (T_{t1} - T_w) \qquad 6.6$$

And, M_t is the tank water mass, Δt is the time period, U_{ta} is the tank heat loss coefficient, A_t is the outside surface area of the tank, $\dot{m}_w$ is the water withdrawal rate for usage and T_w is the temperature of the make–up water.

Equation 6.3 can be rearranged to evaluate the new tank temperature T_{t2}:

$$T_{t2} = T_{t1} + \frac{\Delta t [Q_{up} + Q_{AC} - Q_{loss} - Q_w]}{M_t c_{pt}} \qquad 6.7$$

Ex. 6.1 A solar water heater has a tank containing 100 kg of water initially at 20 °C. Water from a flat plate solar collector enters the tank at 40 °C at a rate of 0.03 kg/s. If the tank is equipped with auxiliary heater of 2000 W power, then find the tank temperature after one hour of operation with and without actuating the auxiliary heater. Neglect any losses from the tank whether to the environment or by the water withdrawal and take the value of specific heat of the working fluid and tank to be 4180 J/(kg °C). What would be the tank temperature after the same period if water is withdrawn during the second 15 minutes of the hour at a rate of 0.05 kg/s with a make–up water of 10 °C and the electric heater is turned on.

Sol. Rate of heat gain from the upriser:

$$Q_{up} = \dot{m} c_{pf} (T_{uo} - T_{t1}) = 0.03 \times 4180 \times (40 - 20) = 2508\ W$$

Final tank temp. after 1 hr without withdrawal (only solar):

$$T_{t2} = T_{t1} + \frac{\Delta t \times Q_{up}}{M_t c_{pt}} = 20 + \frac{3600 \times 2508}{100 \times 4180} = 41.6\ ^{\circ}\text{C}$$

Final tank temp. after 1 hr without withdrawal (solar and AC):

$$T_{t2} = T_{t1} + \frac{\Delta t[Q_{up} + Q_{AC}]}{M_t c_{pt}} = 20 + \frac{3600[2508 + 2000]}{100 \times 4180} = 58.82\ ^{\circ}\text{C}$$

Final tank temp. after the first 15 min without withdrawal (solar and AC):

$$T_{t2} = T_{t1} + \frac{\Delta t[Q_{up} + Q_{AC}]}{M_t c_{pt}} = 20 + \frac{900[2508 + 2000]}{100 \times 4180} = 29.7\ ^{\circ}\text{C}$$

Rate of heat losses due to water withdrawal from the tank:

$$Q_w = \dot{m}_w c_{pw} (T_{t1} - T_w) = 0.05 \times 4180 \times (29.7 - 10) = 4117.3\ W$$

Final tank temp. after the second 15 min. with withdrawal (solar and AC):

$$T_{t2} = T_{t1} + \frac{\Delta t[Q_{up} + Q_{AC} - Q_w]}{M_t c_{pt}} = 29.7 + \frac{900[2508 + 2000 - 4117.3]}{100 \times 4180} = 30.54\ ^{\circ}\text{C}$$

Final tank temp. after 1 hr with withdrawal in the second 15 min. (solar and AC):

$$T_{t2} = T_{t1} + \frac{\Delta t[Q_{up} + Q_{AC}]}{M_t c_{pt}} = 30.54 + \frac{1800[2508 + 2000]}{100 \times 4180} = 49.95\ ^{\circ}\text{C}$$

SUMMARY

Water heating is a practical application of solar energy in many parts of the world. Natural-circulation systems are widely used in climates where freezing does not occur. Forced-circulation systems using drain-down or nonfreezing fluids in collector–heat exchanger loops are used in climates where freezing is a problem. Auxiliary energy is used in essentially all systems where high reliability is wanted, and care must be taken to use auxiliary in such a way that it does not drive up collector temperatures.

As an example of a simple system that yields a single differential equation, consider a solar house heater with an unstratified storage unit supplying energy through a heat exchanger to the house maintained at T_h. Except for the heat exchanger supplying energy to the house, this is illustrated in Figure 10.2.1. Equation 10.1.1 for the collector can be combined with Equation 10.1.3 for the tank to give

$$(mC_P)_s \frac{dT_s}{dt} = A_c F_R[S - U_L(T_s - T_a)]^+ - (UA)_s(T_s - T_a) - \varepsilon_L(\dot{m}C_p)_{\min}(T_s - T_h) \tag{10.9.1}$$

Once the collector parameters, the storage size and loss coefficient, the magnitude of the load, and the meteorological data are specified, the storage tank temperature can be calculated as a function of time. Also, gain from the collector, losses from storage, and energy to load can be determined for any desired period of time by integration of the appropriate rate quantities.

Various methods are available to numerically integrate equations such as Equation 10.9.1. For example, simple Euler integration can be used, the same technique that was used in Example 8.3.1. Using simple Euler integration, we express the temperature derivative dT_s/dt as $(T_s^+ - T_s)/\Delta t$ and obtain an expression for the change in storage tank temperature for the time period in terms of known quantities. Equation 10.9.1 then be comes

$$T_s^+ = T_s + \frac{\Delta t}{(mC_p)_s}\{A_c F_R[S - U_L(T_s - T_a)]^+ - (UA)_s(T_s - T_a') - \varepsilon_L(\dot{m}C_p)_{\min}(T_s - T_h)\} \tag{10.9.2}$$

Integration schemes must be used with care to ensure that they are stable for the desired time step and that reasonably accurate solutions are being attained. When performing hand calculations, both stability and accuracy can be problems. However, most computer facilities have subroutines that will solve systems of differential equations to a specified accuracy and automatically take care of stability problems.

In order to ensure stability in Equation 10.9.2, the time step Δt must be small enough so that the coefficient on T_s is positive. The critical time step occurs when the coefficient on T_s is zero. In order to minimize truncation errors on a digital computer, use about one-sixth of the critical time step. However, weather data are usually known in hour increments so hour time steps are often used if stability is maintained.

Example 10.9.1

The performance of the collector of Example 6.7.1 was based upon a constant water supply temperature of 40°C to the collector. Assume the collector area is 4 m^2, $F_R = 0.80$, and $U_L = 8.0$ W/m^2 °C. The collector is connected to a water storage tank containing 150 kg of water initially at 40°C. The storage tank loss coefficient–area product is 1.70 W/°C and the tank is located in a room at 25°C. Assume water is withdrawn to meet a load at a constant rate of 10 kg/h and is replenished from the mains at a temperature of 15°C. Calculate the performance of this system for the period from 7 AM to 5 PM using the collector and meteorological data from Example 6.11.1. Check the energy balance on the tank.

Solution

Equation 10.9.2 (modified due to lack of a load heat exchanger) is used to calculate hourly temperatures of the tank. For this problem a time step of 1 h is sufficient to guarantee stability. The equations will be left uncombined in order that the individual terms in the energy balance can be seen.

$$T_s^+ = T_s + \frac{1}{150 \times 4190}\{4 \times 0.80[S - 8.0 \times 3600(T_s - T_a)]^+ - 1.70 \times 3600(T_s - 25) - 10 \times 4190(T_s - 15)\}$$

The first term in the brackets is the useful output of the collector and can have only positive values. The second term is the thermal loss from the tank. The third term is the energy delivered to the load. Simplifying the individual terms, this equation becomes

$$T_s^+ = T_s + 1.59\{3.20[S - 0.0288(T_s - T_a)]^+ - 0.00612(T_s - 25) - 0.0419(T_s - 15)\}$$

where S and all energy terms are in megajoules per square meter. The data in the first four columns of the table below are from Example 6.11.1. The new tank temperature calculated for the end of the hour is T_s^+. The three terms in the brackets of the equation are Q_u, load met by solar, and loss, assuming T_s to be fixed for the hour at its initial value. The change in internal energy of the water should be equal to $\Sigma\ Q_u - \Sigma\ L_s - \Sigma$ losses.

$$150 \times 4190\ (53.0 - 40.0) = (23.43 - 1.41 - 13.87) \times 10^6$$

$$8.17\ \text{MJ} \cong 8.15\ \text{MJ}$$

Hour	I_T (MJ/m^2)	S (MJ/m^2)	T_a (°C)	T_s^+ (°C)	Q_u (MJ)	Loss (MJ)	Load (MJ)
Start				40.0			
7–8	0.02	—	−11	38.2	0	0.09	1.05
8–9	0.43	0.34	−8	36.5	0	0.08	0.97
9–10	0.99	0.79	−2	35.0	0	0.07	0.90
10–11	3.92	3.16	2	44.8	7.07	0.06	0.84
11–12	3.36	2.73	3	50.4	4.88	0.12	1.25
12–1	4.01	3.25	6	57.8	6.31	0.16	1.48
1–2	3.84	3.08	7	62.9	5.17	0.20	1.79
2–3	1.96	1.56	8	59.3	0	0.23	2.01
3–4	1.21	0.95	9	56.0	0	0.21	1.86
4–5	0.05	—	7	53.0	0	0.19	1.72
Total	19.79				23.43	1.41	13.87

The day's efficiency is

$$\eta_{\text{day}} = \frac{23.4}{19.8 \times 4} = 0.30 = 30\%$$

■

Ocean Energy Technology Overview

This paper presents an overview of ocean energy technology as a source of renewable energy for U.S. Federal sites. It investigates ocean energy resources and new technologies under development to capture that energy. These technologies span:

- Wave energy
- Tidal energy
- Marine current energy
- Ocean thermal energy conversion (OTEC)

1.3 Technology Types

Four types of ocean energy conversion exist: wave energy, tidal energy, marine current energy, and ocean thermal energy conversion.

Wave Energy

Wave energy is generated by the movement of a device either floating on the surface of the ocean or moored to the ocean floor. Many different techniques for converting wave energy to electric power have been studied.

Wave conversion devices that float on the surface have joints hinged together that bend with the waves. This kinetic energy pumps fluid through turbines and creates electric power. Stationary wave energy conversion devices use pressure fluctuations produced in long tubes from the waves swelling up and down. This bobbing motion drives a turbine when critical pressure is reached. Other stationary platforms capture water from waves on their platforms. This water is allowed to runoff through narrow pipes that flow through a typical hydraulic turbine.

Tidal Energy

The tidal cycle occurs every 12 hours due to the gravitational force of the moon. The difference in water height from low tide and high tide is potential energy.

Similar to traditional hydropower generated from dams, tidal water can be captured in a barrage across an estuary during high tide and forced through a hydro-turbine during low tide. To capture sufficient power from the tidal energy potential, the height of high tide must be at least five meters (16 feet) greater than low tide. There are only approximately 20 locations on earth with tides this high. The Bay of Fundy between Maine and Nova Scotia features the highest tides in the world, reaching 17 meters (56 feet). This area has the potential to produce 10,000 MW [3].

Current Energy

Marine current is ocean water moving in one direction. In the U.S., it is found primarily off the coast of Florida. This ocean current is known as the Gulf Stream. Tides also create currents that flow in two directions. Kinetic energy can be captured from the Gulf Stream and other tidal currents with submerged turbines that are very similar in appearance to miniature wind turbines. As with wind turbines, the constant movement of the marine current moves the rotor blades to generate electric power.

Ocean Thermal Energy Conversion

Ocean thermal energy conversion, or OTEC, uses ocean temperature differences from the surface to depths lower than 1,000 meters, to extract energy. A temperature difference of only 20°C (36°F) can yield usable energy.

Research focuses on two types of OTEC technologies to extract thermal energy and convert it to electric power: closed cycle and open cycle. In the closed cycle method, a working fluid, such as ammonia, is pumped through a heat exchanger and vaporized. This vaporized steam runs a turbine. The cold water found at the depths of the ocean condenses the vapor back to a fluid where it returns to the heat exchanger. In the open cycle system, the warm surface water is pressurized in a vacuum chamber and converted to steam to run the turbine. The steam is then condensed using cold ocean water from lower depths [3].

2 Wave Energy

2.1 Overview

Wave energy is captured by devices that are stationary or move up and down with the frequency of waves. Energy conversion devices also capture waves in reservoirs by overtopping the device and channeling sea water through a hydro turbine to generate electricity. Wave height and frequency determine wave energy. Section 2.3 discusses categories of wave technology and current technology development in more detail.

2.2 Resources

Figure 4 maps the kilowatt per meter (kW/m) crest length of wave energy around global coastlines. The crest length is measured from one crest, or peak, to the next.

Note that wave energy increases as latitudes increase north or south. Latitudes greater than 40° generate the highest energy. The largest wave energy in the U.S. is found in Alaska, reaching 67 kW/m. Conversely, there is virtually no wave energy in the Gulf Coast.

Figure 4: Wave Energy Levels in kW/m Crest Length
Courtesy of the European Ocean Energy Association

2.3 Energy Conversion Technologies

Wave energy technology is rapidly growing and varies widely in application of conversion devices. Energy conversion devices can be situated on or off shore.

Four categories of wave energy technology exist: attenuators, point absorbers, overtopping terminators, and oscillating wave column (OWC) terminators. Point absorbers and attenuators capture wave energy as they are placed in the path of the wave. Attenuators are situated parallel to the waves and energy is captured over the surface area. Point absorbers are moored to the sea bed or float near the surface, collecting wave energy from all directions. Terminators restrain wave motion and capture energy through long arms. OWC terminators capture water from an opening into a partially submerged platform and let that water rise in an air column. The air is compressed, which drives a turbine to generate electricity.

Technology - Point Absorber: Developed in 2004, this device is a buoy moored to the seabed. Waves move over a submerged air-filled upper casing and push against the fixed cylinder. Air inside the cylinder is compressed, serving as a point absorber. The compressed air drives a hydraulic system and generator set to convert the wave energy to electricity.	**Projects:** Pilot power plant installed off the coast of Portugal in 2004. Power plant in Portugal was designed to test technology at full scale but was not designed as a long-term demonstrator. Pre-commercial 250 kW device is planned for testing during 2009 and 2010 at Orkney's European Marine Energy Center (EMEC) in Scotland.	**Test Performance:** Pilot plant delivered wave power to the Portuguese grid at predicted levels (250 kW). Pre-commercial 250 kW prototype to be tested in Scotland (EMEC). The technology is scalable and the commercial system will be in excess of 1 MW.	 *Figure 5: Archimedes Waveswing* *Courtesy of AWS Ocean Energy*
Technology - Point Absorber: Moored to the seabed and completely submerged, movement produces high-pressure sea water that is delivered to shore through pipes. The high-pressure sea water can be desalinated with reverse osmosis and used to drive the on-shore hydro-turbine. There is no need for underwater cabling or high voltage transmission. CETO will operate in waters between 15-50 meters below breaking waves.	**Projects:** First CETO wave energy conversion device was tested in Western Australia in January 2008.	**Test Performance:** Produced sustained high-pressure sea water greater than 1,000 pounds per square inch (psi) during testing. CETO is the only wave energy technology that produces fresh water directly from sea water. Commercially availability expected in 2009.	 *Figure 6: CETO* *Courtesy of Renewable Energy Holdings*

Technology - Attenuator: Semi-submerged structure composed of cylindrical sections linked by hydraulic joints. Ram pumps resist wave motion in the joints that in turn pump high-pressure oil through motors. The hydraulic motors drive generators to produce electricity. Each device is 140 meters long and 3.5 meters in diameter with three wave energy conversion modules.	**Projects:** PWP is working on three full scale trials with the initial one deployed in Portugal summer 2008: 2.25 MW Agucadoura wave project off the coast of Portugal for Enersis and Babcock & Brown. 3 MW project under development off the coast of Orkney for Scottish Power Renewables. 5 MW wave station for Cornwall, United Kingdom, as part of the Cornwall Wave Hub.	**Test Performance:** The multiple PWP units in Agucadoura make up the world's first multi-unit commercial wave farm tied to Portuguese grid. Each Pelamis is capable of generating 750 kW with an expected average of 25-40% of this power being continuously generated. **Cost:** Estimated (2004) $2 million to $3 million per device.	 *Figure 7: Pelamis* *Courtesy of Pelamis Wave Power*
Technology - Point Absorber: A moored buoy floats on the surface of the waves. As the buoy moves up and down, sea water inside a 25-meter (82-foot) tube drives a piston that then drives a hose pump. Sea water inside the elongated hose becomes pressurized and is released to drive the Pelton turbine. Underwater transmission lines transmit electric energy to shore. The AquaBuoy must be deployed where water depth is greater than 50 meters (164 feet).	**Projects:** 1 MW project in Makah Bay, Washington, pending a FERC environmental impact study. 2 MW project with 200 MW planned for Figueira de Foz, Portugal. 5 MW wave energy device off Ucluelet, British Columbia, granted an investigative permit. 20 MW wave energy project off Western Cape, South Africa. 200 MW wave park under development in Coos Bay, Oregon. FERC granted a preliminary permit for this project.	**Test Performance:** Each 40-ton AquaBuoy is rated for up to 250 kW. Unfortunately, the prototype device failed before power tests were complete, springing a leak that caused the pump to malfunction after only one month of deployment. The AquaBuoy sank off the coast of Oregon. The test was intended to measure power output of the AquaBuoy 2.0. No reports from this test have been released. **Cost:** The cost for the project in Makah Bay, Washington, including grid connection cable and four AquaBuoys, was $3 million (2004).	 *Figure 8: AquaBuoy* *Courtesy of Finavera Renewables*

Technology - Point Absorber: Converts wave motion into electricity with a moored buoy that floats freely up and down in the water. A structure with a piston moves as the PowerBuoy bobs in the waves. This movement drives a turbine and electric generator.	**Projects:** 1 MW wave park deployed for the U.S. Navy in Oahu, Hawaii. 5 MW wave station for Cornwall, United Kingdom, as part of the Cornwall Wave Hub. 1.25 MW commercial wave power station off the Spanish coast. Agreement signed with Iberdrola. Still in development. 100 MW project in Coos Bay, Oregon. Application filed with FERC for permits. 2 MW to 50 MW wave park near Reedsport, Oregon. Agreement signed with Pacific Northwest Generating Cooperative (PNGC) Power.	**Test Performance:** PowerBuoys installed in Hawaii and New Jersey rated at 40 kW each. Operational 2005 in Atlantic City, New Jersey. Demonstrated feasibility of wave power in New Jersey. Testing and grid connection deployed for the U.S. Navy in Kaneohe Bay, Hawaii. Completed extensive environmental assessment. Demonstrated wave power for use at US Navy bases, worldwide.	 *Figure 9: PowerBuoy* *Courtesy of Ocean Power Technologies, Inc.*
Technology - Overtopping Terminator: Secured on shore, the Limpet is an inclined Oscillating Water Column (OWC). An air chamber captures wave energy from an opening in the bottom. Water compresses the air as it moves up the column, which turns a turbine at the top. The turbine spins the same direction no matter the air direction.	**Projects:** The Limpet prototype has been installed since 2000 on the island of Islay in Scotland.	**Test Performance:** The Limpet on Islay has three chambers that generate a combined average of 100 kW. Typical ratings for shore wave energy stations are 100 kW to 500 kW per unit.	 *Figure 10: Limpet* *Courtesy of Voith Hydro*
Technology – OWC Terminator: Oceanlinx patented oscillating water column (OWC) technology. As waves pass the Oceanlinx device, water enters from beneath the column and compresses the air inside the chamber. This compressed air drives the turbine located in a narrow tapered part of the column. The Oceanlinx OWC can be deployed on the shoreline or in water depths of up to 50 meters.	**Projects:** 450 kW prototype power purchase agreement with Integral Energy in Port Kembla, New South Wales, Australia. 5 MW facility letter of intent signed with Cornwall, United Kingdom, as part of the Cornwall Wave Hub. 1.5 MW signed memorandum of understanding with Rhode Island. 2.7 MW wave generator memorandum of understanding signed with Hawaii. 1.5 MW under contract with GPP, Namibia.	**Test Performance:** Each OWC produces 100 kW to 1.5 MW depending on wave climate. **Cost:** Estimated (2004) $2.5 million to $3 million	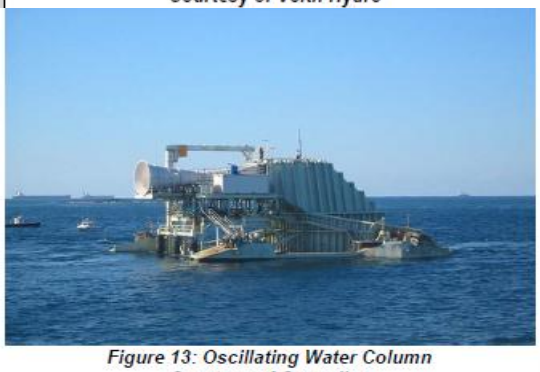 *Figure 13: Oscillating Water Column* *Courtesy of Oceanlinx*

3 Tidal and Marine Current Energy

3.1 Overview

Tidal current is created from the gravitational pull of the moon and sun. Tidal current moves in two directions and reverses four times per day. Tidal current energy conversion devices are the most common of the two ocean current technologies. Tidal turbines are similar to wind turbines but can be made smaller due to the high energy density of water.

Marine current refers to water that moves continuously and is driven by the motion of the ocean from solar heating and wind near the equator. Marine current moves in one direction with relatively constant flow.

3.2 Resources

Figure 14 shows available tidal current resources [9]. Figure 15 shows available marine current resource. The highest resource for tidal current in the U.S. is located in the upper northeast, northwest, and Alaska. The highest U.S. resource for marine current is primarily in the Gulf Coast around the tip of Florida. Energy conversion from the Gulf Stream could potentially supply Florida with 35 percent of its electricity needs [6].

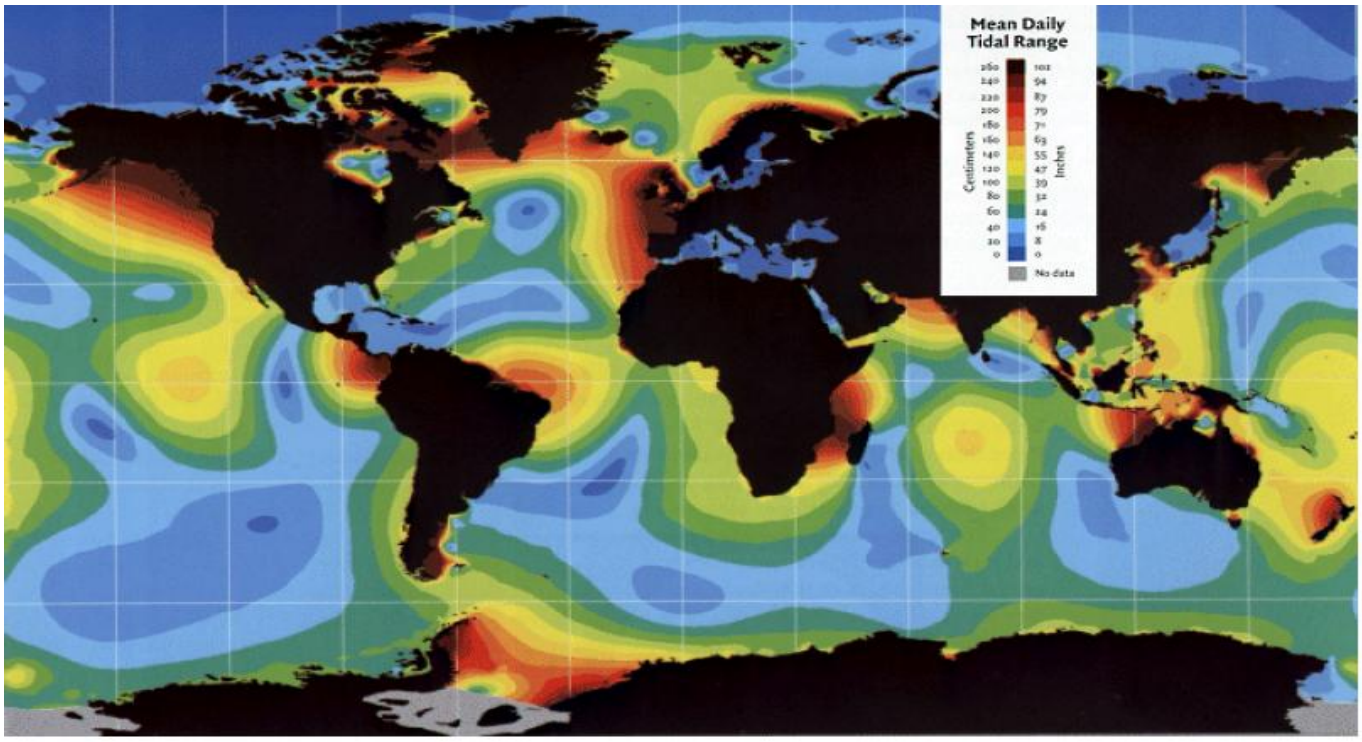

Figure 14: Global Distribution of Mean Tidal Range
Courtesy of the Electric Power Research Institute

3.3 Energy Conversion Technologies

Ocean current energy conversion devices are submerged in sea water and capture energy from the ocean similar to the way wind turbines capture energy from the wind. Ocean water is more than 800 times denser than wind. Energy available from ocean currents is estimated at 5,000 GW worldwide with energy densities as high as 15 kW/m^2 [6].

Turbines are oriented cross flow or axial flow. Axial-flow turbines feature open or shrouded rotors. Table 3 shows examples of each type of turbine. Ocean current and tidal current technologies are in the early stages of development and only prototypes have been tested to date.

Technology - Axial Flow, Open Rotor: Works similar to wind turbines. Submerged in sea water, the turbines are driven by marine current or tidal current if velocities are high (in excess of 4 knots). SeaGen turbines consist of two axial rotors 15 to 20 meters across that rotate to drive a generator. The pair of rotors can be pitched to a neutral position to stop or limit the turbines when velocities are too high. The turbines are designed to operate in bi-directional flows by allowing the blades to be pitched 180°. The power trains are mounted on a cross beam that is raised up the supporting structure when maintenance is required.	**Projects:** 300 kW unit installed in 2003 off the coast of Devon, UK, The device is still operating today. 1.2 MW single SeaGen system deployed in April 2008 in Strangford Lough, Northern Ireland. ESB Independent Energy has a power purchase agreement for the output power. 10.5 MW marine current farm off the coast of Anglesey, Wales, planned for 2011/2012, subject to financing. The turbines will sit approximately 25 meters deep. 3.6 MW tidal farm proposed by MCT and BC Tidal Energy Corp. in Vancouver, Canada's Campbell River. No date targeted for deployment.	**Test Performance:** The SeaGen commercial scale tidal turbine can produce 1.2 MW. MCT plans to increase SeaGen's capacity to 1.5 MW for future projects.

Figure 16: SeaGen
Courtesy of Marine Current Turbines Limited

Technology - Axial Flow, Shrouded Rotor: Bi-directional turbine housed in a symmetrically curved duct that is narrow at the center to draw the tidal current through the turbine with accelerated energy. The design is modular so the blades can be removed from the platform for easy maintenance and repair. Can be deployed in depths in excess of 40 meters.	**Projects:** 8 MW marine current farm off the coast of Welsh, United Kingdom, expected to be complete in 2011. 300 MW deployed off Korea in the Wando Hoenggan waterway expected to be complete in 2015. The memorandum of understanding was signed with Hyundai Samho Heavy Industries and Korean Midland Power.	**Test Performance:** The Rotech Tidal Turbine can produce 1 MW of energy. **Cost:** The 300 MW marine farm in Korea is expected to cost $763 million.	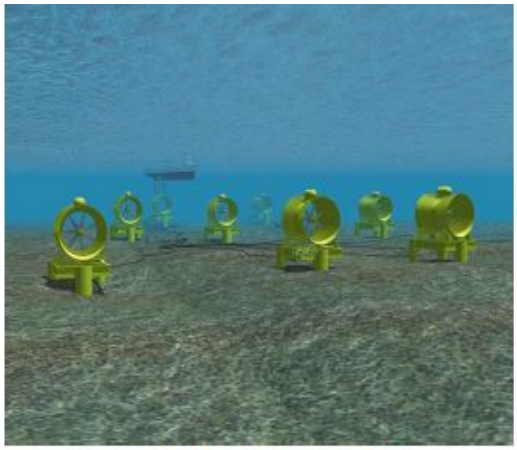 **Figure 17: Rotech Tidal Turbine** **Courtesy of Lunar Energy Ltd.**
Technology - Axial Flow, Shroded Rotor: Slow-moving, single-piece rotor with lubricant-free operation. The turbine is considered environmentally safe with no oils or exposed blade tips. It sits directly on the sea bed out of sight and away from harsh storm environment.	**Projects:** 250 kW installed off the coast of Orkney, Scotland, by EMEC. It was tested for more than a year and then connected to the grid in May 2008. Array of turbines installed in the English Channel off the coast of Alderney, UK for Alderney Renewable Energy in 2008 and 2009. 200 MW array under consideration by Crest Energy in New Zealand.	**Test Performance:** The Open-Centre Turbine produces 250 kW.	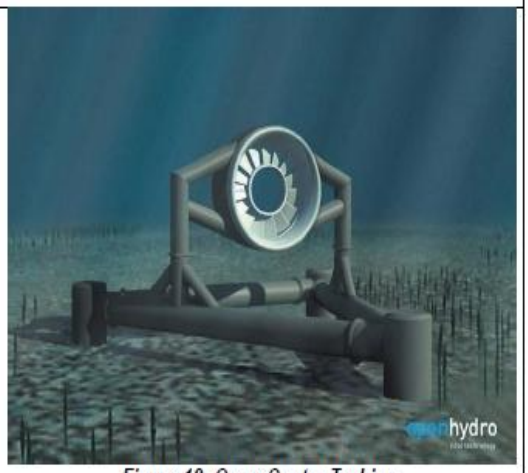 *Figure 18: Open-Centre Turbine* *Courtesy of OpenHydro*
Technology - Axial Flow, Shroded Rotor: Uses a tapered turbine with blades that rotate with marine currents. Similar to wind turbines, the blades are bi-directional and operate in the ebb and flow of tides. The turbine tested successfully at currents exceeding 3.5 meters per second.	**Projects:** Generator was tested for 9 months in 2006 near Race Rocks, British Columbia. Chosen in January 2008 as one of three technologies to be tested in the Bay of Fundy at the Fundy Institute of Tidal Energy in Nova Scotia, Canada. The Clean Current Mark III will supply 400 GWh of power per year.	**Test Performance:** Three commercial scale tidal turbines are available: 1) Clean Current 2.2 can produce 960 kW at current speeds of 3 meters per second and 2.2 MW at current speeds of 4.1 meters per second. 2) Clean Current 1.5 can produce 1.5 MW at current speeds of 3.25 meters per second. 3) Clean Current 1.0 can produce 1.0 MW at current speeds of 2.6 meters per second.	 *Figure 19: Tidal Turbine* *Courtesy of Clean Current Power Systems*

Technology - Axial Flow, Open Rotor: Verdant Power systems are modular, three-blade horizontal-axis turbines that move slowly with the natural currents (~32 rpm) and offer a low-impact kinetic hydropower solution. The turbines are like wind turbines and can pivot with the changing direction of the tide. The free flow systems are completely submerged in water and operate without being seen.	**Projects:** 6-turbine marine current farm in New York City's East River will expand to more than 300 turbines. The project produces 1 MWh of electricity per day. 2002-2006: Phase 1 Prototype Testing 2006-2008: Phase 2 Demonstration 2009-2012: Phase 3 Commercial MW scale	**Test Performance:** The Free Flow Turbine can be scaled in unit size and number. One Free Flow turbine produces 7 kW of energy with an average marine current velocity of 2.0 meters per second. 1 MW is projected from a future 11 meter blade turbine.

Figure 21: Free Flow Turbine
Courtesy of Verdant Power

4 Ocean Tidal Energy

4.1 Overview

High and low tides occur every 12 hours. With ocean tidal energy, potential energy from these tides is captured similarly to a dam in an estuary. The first commercial-scale ocean energy project was in St. Malo, France, in 1966, which still produces 240 MWh/year.

4.2 Resources

To capture viable power from tidal energy, in most cases, the difference in high tide and low tide height must be at least five meters (16 feet). Only 20 to 40 locations on earth have this potential, most of which are located in the Bay of Fundy by Nova Scotia.

4.3 Energy Conversion Technologies

Building barrages or dams is unpopular in the U.S. because of the environmental considerations. Barrages block navigation, impede fish migration, and change the tidal regime downstream.

With the use of low-head hydroelectric generating equipment, new trials are in process to build lagoons in shallow, offshore rock mound impoundments of tidal flats. The impoundments have less environmental impact than a barrage since migratory fish can simply swim around the structure and boats can navigate past. Table 4 provides an example of this technology.

5 Ocean Thermal Energy Conversion

5.1 Overview

In 1881, a French physicist named Jacques Arsene d'Arsonval discovered the concept of ocean thermal energy conversion (OTEC). His student, Georges Claude, built the first open cycle OTEC plant in Cuba in 1930. With this technology, temperature gradient from the ocean surface to deeper waters converts heat energy to electricity. It functions best when there is a temperature difference of at least 20°C (36°F).

In 1979, the first 18 kW closed cycle OTEC demonstration plant was built in Keahole Point, Hawaii. This project was known as "Mini-OTEC." In 1990, a 103 kW open cycle OTEC demonstration plant was built in Keahole Point, Hawaii. A planned commercial project to produce 1 MW was also expected in 2009 [10].

In 2006, DOE assigned FEMP and the National Renewable Energy Laboratory (NREL) to team with the U.S. Navy and U.S. Army to develop an OTEC facility in the Republic of Marshall Islands (RMI) on or near Kwajalein Island, RMI [11]. According to the memorandum, the facility will produce 7MW/yr and displace 47,000MWh/yr, saving Kwajalein 38 percent of its baseline diesel use.

5.2 Resources

Figure 23 outlines temperature differences between the ocean surfaces and 1,000 meters deep. OTEC works best with temperature differences of at least 20°C (36°F).

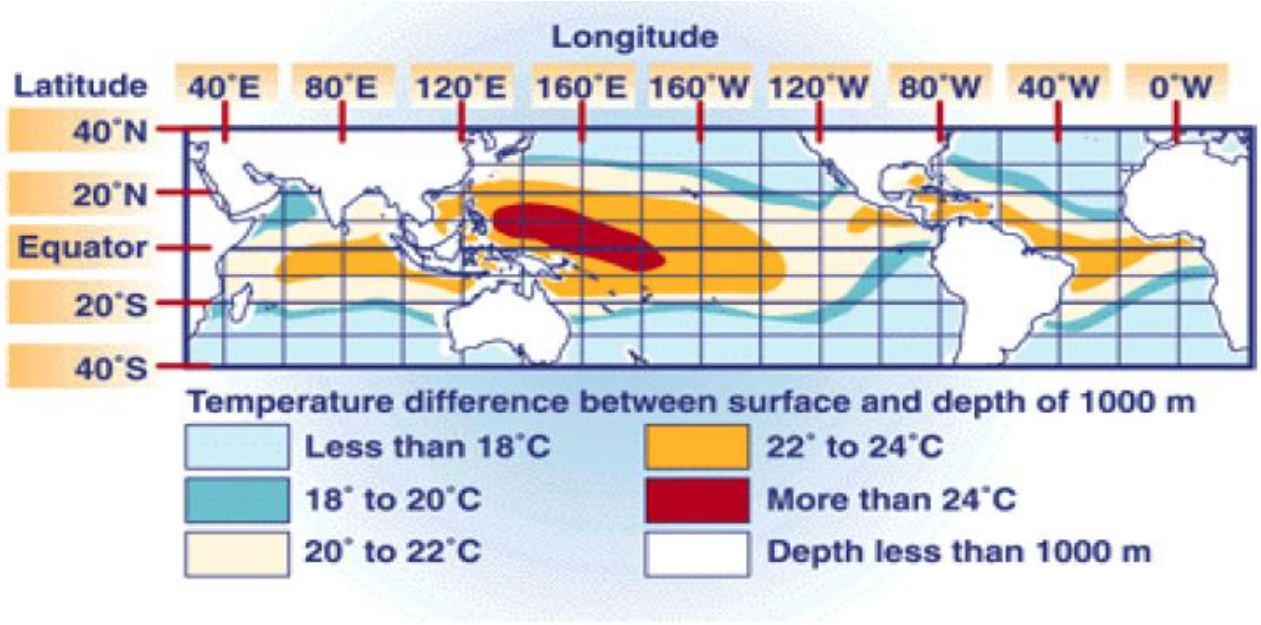

Figure 23: Ocean Temperature Differences between Surface and 1,000 Meters Deep
Courtesy of National Renewable Energy Laboratory

5.3 Energy Conversion Technologies

Two types of OTEC technologies exist: open loop cycle and closed loop cycle. Each is discussed below. Table 5 outlines options for both open loop and closed loop OTEC technologies.

Open Loop Cycle OTEC

Open loop cycle technologies use warm surface ocean water placed in a pressurized receptacle, which causes it boil. Steam from the boiling water turns a turbine that is connected to a generator. The steam, almost fresh water, is then condensed with the cold ocean water as shown in Figure 24. The desalinated water produced in open loop cycle OTEC can be used as fresh drinking water, an additional advantage of this methodology.

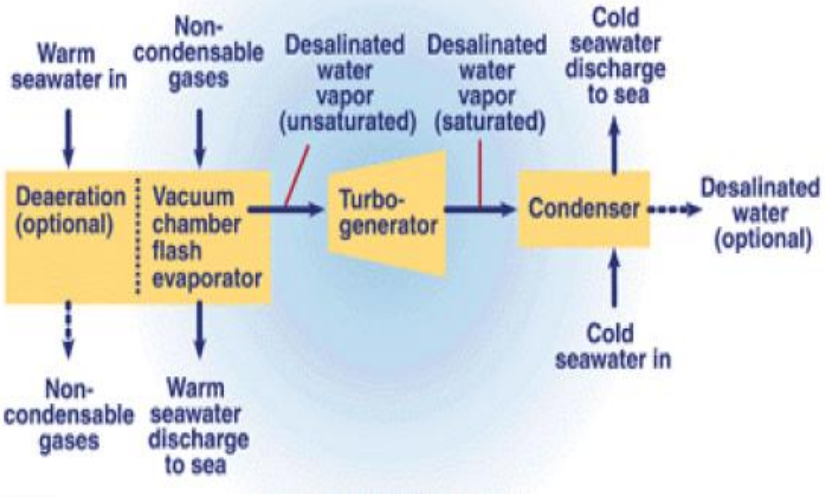

Closed Loop Cycle OTEC

Closed loop cycle OTEC is similar to open loop cycle OTEC, but uses a working fluid, like ammonia, that boils at a lower temperature than water. The working fluid creates steam and runs a turbo generator as shown in Figure 25. The steam is condensed with the cold water from lower depths, and the ammonia condenses to the working fluid.

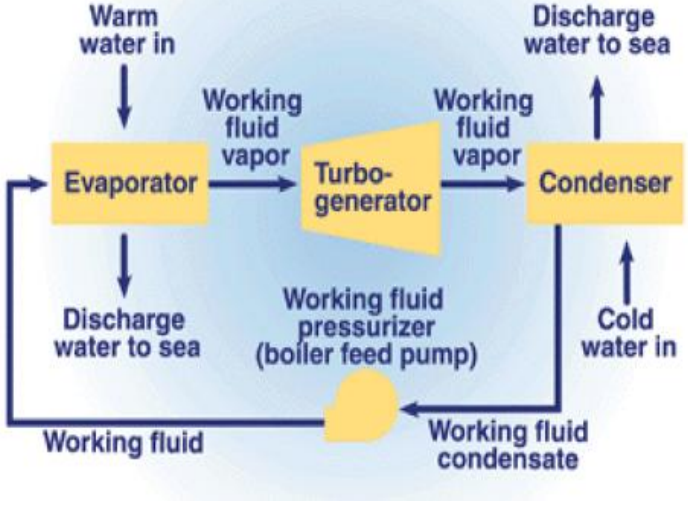

1.1 Benefits

Using waves as a source of renewable energy offers significant advantages over other methods of energy generation including the following:

1. Sea waves offer the highest energy density among renewable energy sources [6]. Waves are generated by winds, which in turn are generated by solar energy. Solar energy intensity of typically 0.1–0.3 kW/m^2 horizontal surface is converted to an average power flow intensity of 2–3 kW/m^2 of a vertical plane perpendicular to the direction of wave propagation just below the water surface [9].
2. Limited negative environmental impact in use. Thorpe [3] details the potential impact and presents an estimation of the life cycle emissions of a typical nearshore device. In general, offshore devices have the lowest potential impact.
3. Natural seasonal variability of wave energy, which follows the electricity demand in temperate climates [6].
4. Waves can travel large distances with little energy loss. Storms on the western side of the Atlantic Ocean will travel to the western coast of Europe, supported by prevailing westerly winds.
5. It is reported that wave power devices can generate power up to 90 per cent of the time, compared to ~20–30 per cent for wind and solar power devices

2.2 Type

Despite the large variation in designs and concepts, WECs can be classified into three predominant types.

2.2.1 Attenuator (A)

Attenuators lie parallel to the predominant wave direction and 'ride' the waves. An example of an attenuator WEC is the Pelamis, developed by Ocean Power Delivery Ltd (now known as Pelamis Wave Power [**15**]). Figure 1 shows an artist's impression of a Pelamis wave farm. See section 2.4.1 for more details about this particular WEC.

2.2.2 Point absorber (B)

A point absorber is a device that possesses small dimensions relative to the incident wavelength. They can be floating structure that heave up and down on the surface of the water or submerged below the surface relying on pressure differential. Because of their small size, wave direction is not important for these devices. There are numerous examples of point absorbers, one of which is Ocean Power Technology's Powerbuoy [**16**]. Figure 2 shows an artist's impression of a wave farm using Powerbuoys.

2.2.3 Terminator (C)

Terminator devices have their principal axis parallel to the wave front (perpendicular to the predominant wave direction) and physically intercept waves. One example of a terminator-type WEC is the Salter's Duck, developed at the Unviersity of Edinburgh, as shown in Fig. 3 (for more details, see section 2.4.2).

Fig. 1 Attenuator device: Pelamis wave farm [**17**]

Fig. 2 Point absorber device: OPT Powerbuoy [18]

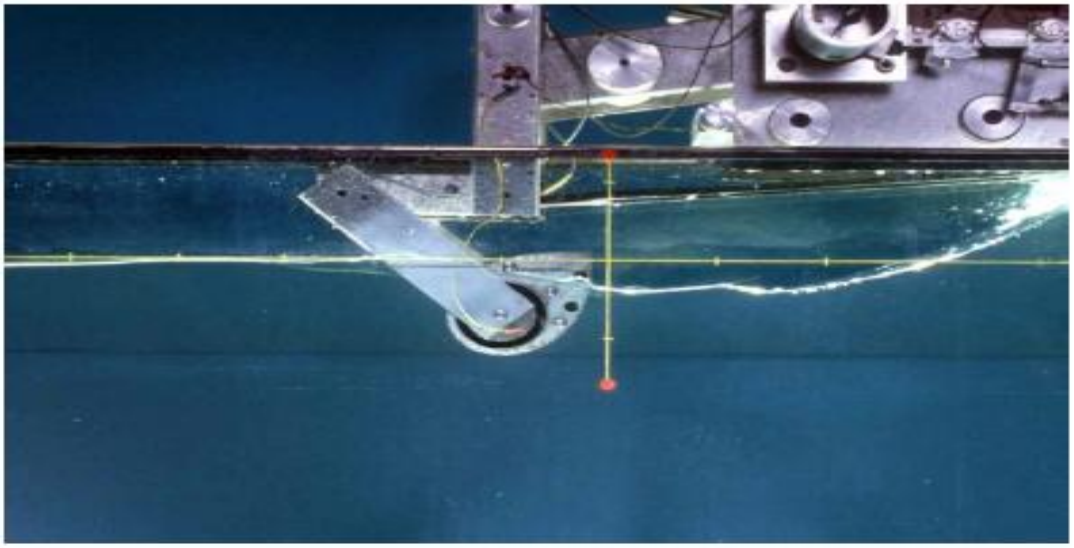

Fig. 3 Terminator device: Salter's Duck [19]

2.3 Modes of operation

Within the categories identified above, there is a further level of classification of devices, determined by their mode of operation. Some significant examples are given below.

2.3.1 *Submerged pressure differential*

The submerged pressure differential device is a submerged point absorber that uses the pressure difference above the device between wave crests and troughs. It comprises two main parts: a sea bed fixed air-filled cylindrical chamber with a moveable upper cylinder. As a crest passes over the device, the water pressure above the device compresses the air within the cylinder, moving the upper cylinder down. As a trough passes over, the water pressure on the device reduces and the upper cylinder rises. An advantage of this device is that since it is fully submerged, it is not exposed to the dangerous slamming forces experienced by floating devices [**20**], and reduces the visual impact of the device. Maintenance of the device is a possible issue however. Owing to part of the device being attached to the sea bed, these devices are typically located nearshore. An example of this device is the Archimedes Wave Swing, an artist's impression of which is shown in Fig. 4.

2.3.4 *Overtopping device*

An overtopping device captures sea water of incident waves in a reservoir above the sea level, then releases the water back to sea through turbines. An example of such a device is the Wave Dragon, which is shown in Fig. 7. This device uses a pair of large curved reflectors to gather waves into the central receiving part, where they flow up a ramp and over the top into a raised reservoir, from which the water is allowed to return to the sea via a number of low-head turbines.

direction, removing the need to rectify the airflow. It has been suggested that one of the advantages of the OWC concept is its simplicity and robustness [4].

There are examples of OWCs as point absorbers, as well as being built into the shoreline, where it acts as a terminator. An example of a shoreline mounted device is the Wavegen Limpet. The device is installed on the island of Islay, Western Scotland, and produces power for the national grid. Figure 6 shows the design of the Limpet. The OWC concept has also been proposed by Oceanlinx, an Australian wave energy developer, in a nearshore tethered device [24].

Fig. 6 OWC: the Limpet [25]

(a)

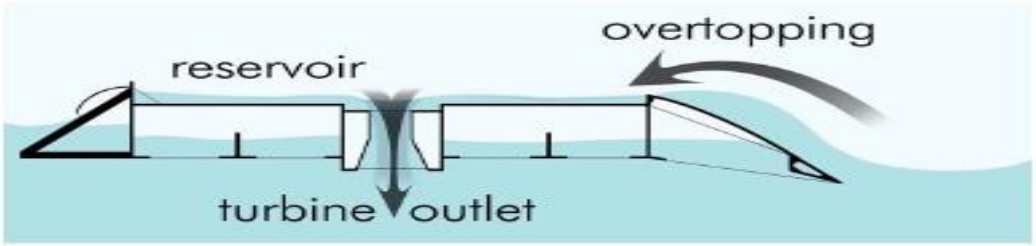

(b)

Fig. 7 Overtopping WEC: the Wave Dragon [26, 27]

2.3.4 *Overtopping device*

An overtopping device captures sea water of incident waves in a reservoir above the sea level, then releases the water back to sea through turbines. An example of such a device is the Wave Dragon, which is shown in Fig. 7. This device uses a pair of large curved reflectors to gather waves into the central receiving part, where they flow up a ramp and over the top into a raised reservoir, from which the water is allowed to return to the sea via a number of low-head turbines.

3 POWER TAKE OFF METHODS

The method of energy capture varies from device to device, but with the exception of linear electrical generation, discussed later, the general method of producing electrical power is through conventional high-speed rotary electrical generators [**42**]. One of the major challenges of WECs is concerned with how to drive these generators. Heaving- and nodding-type devices are not directly compatible with conventional rotary electrical machines, and a transmission system is required to interface the WEC with the electrical generator [**20**].

In this section, different types of rotary generators are briefly presented, followed by an overview of different energy transfer methods. This starts with turbine transfer, moving on to hydraulic conversion methods, and then discussing direct electrical linear generators,

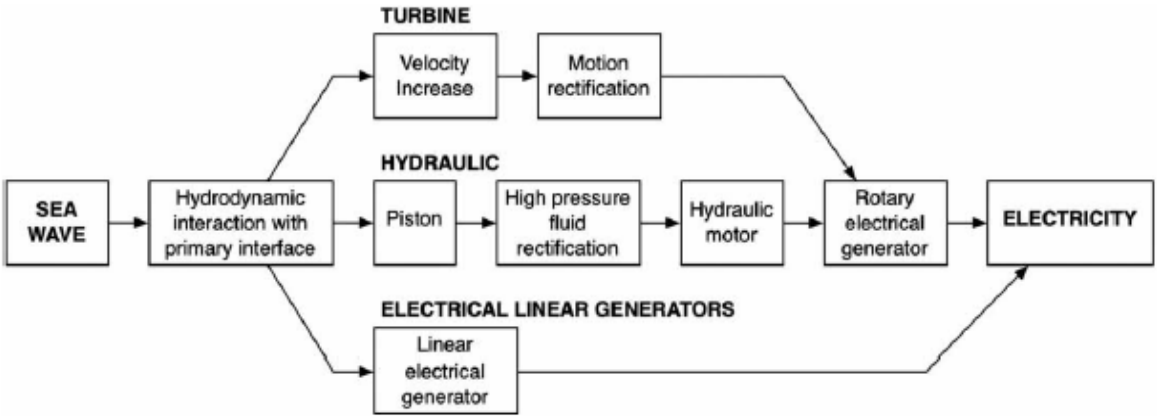

Fig. 8 Alternative PTO mechanisms

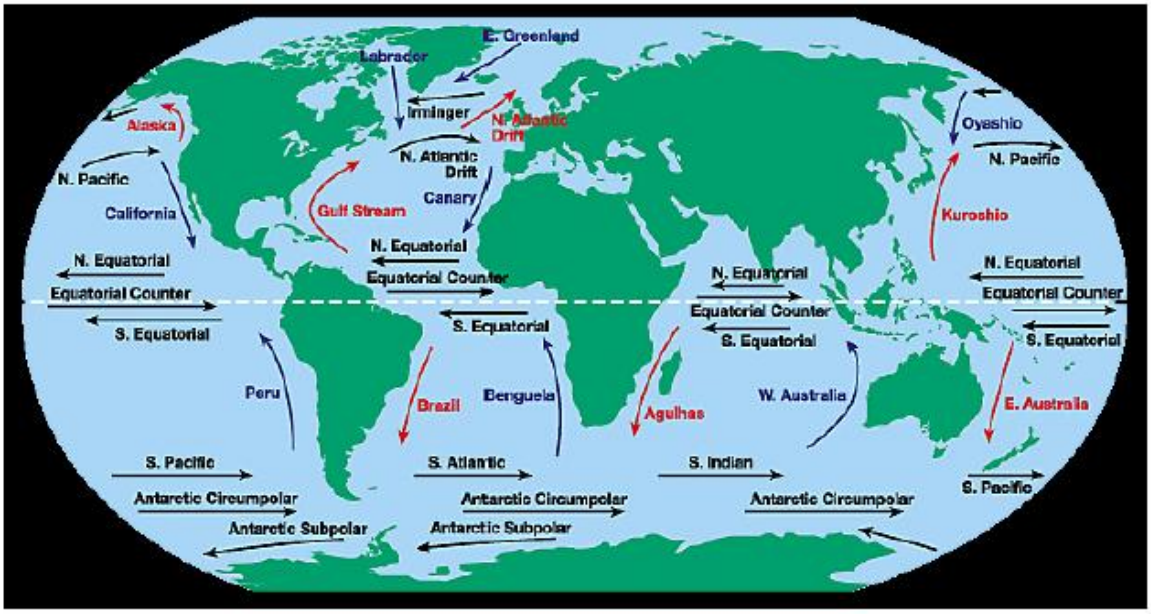

Figure 6.4: Surface ocean currents, showing warm (red) and cold (blue) systems (Windows to the Universe, 2009).

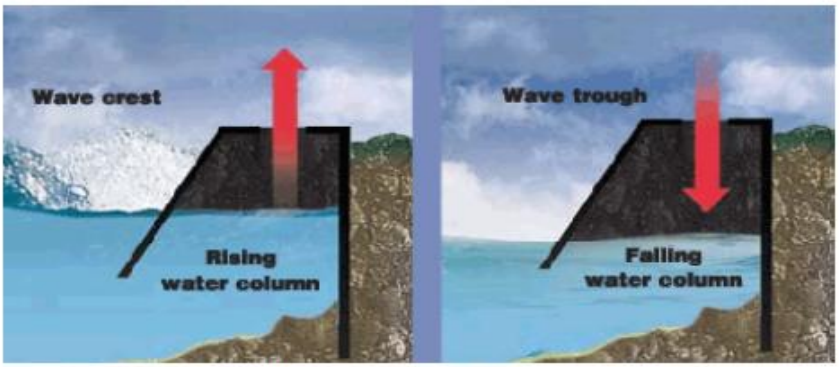

(a): Chambers Under Wave Action

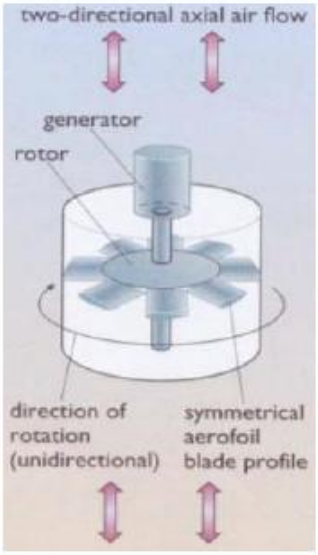

(b): Wells Turbine

Figure 6.10: Oscillating Water Column

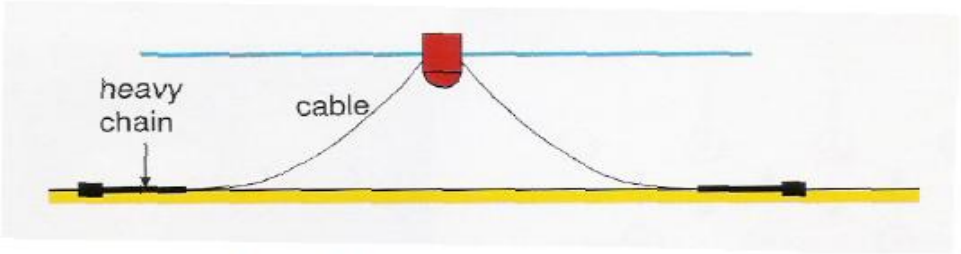

Figure 6.11: Oscillating-Body System

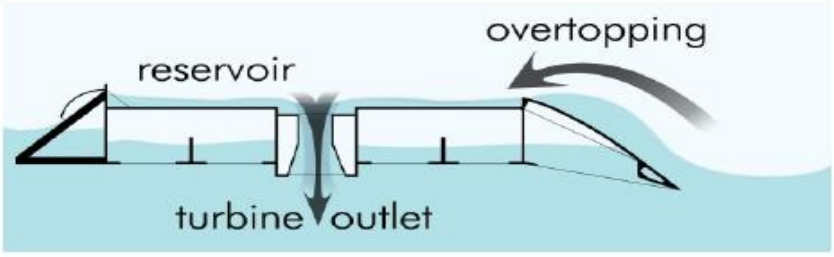

Figure 6.12: Overtopping Wave Terminator

Figure 6.15: 20 MW tidal power plant at Annapolis Royal, Nova Scotia, Canada. [TSU

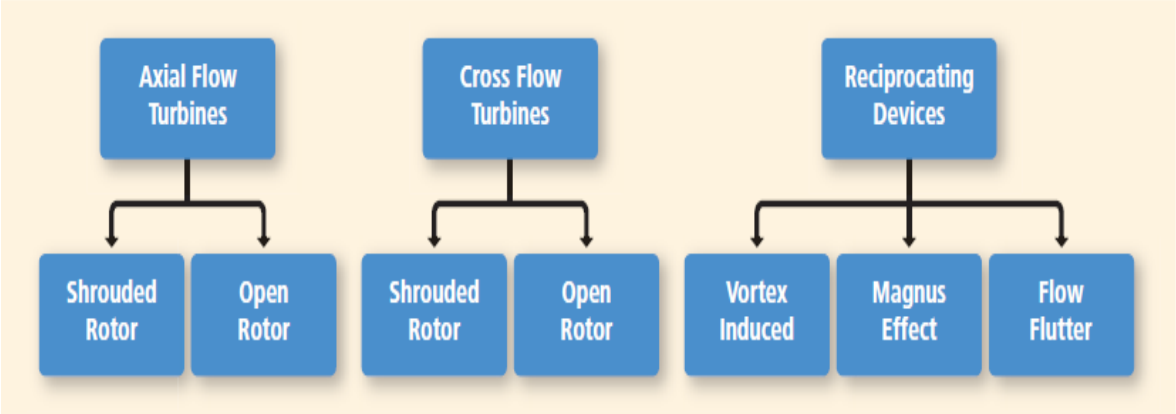

igure 6.7 | Classification of current tidal and ocean energy technologies (principles of operation).

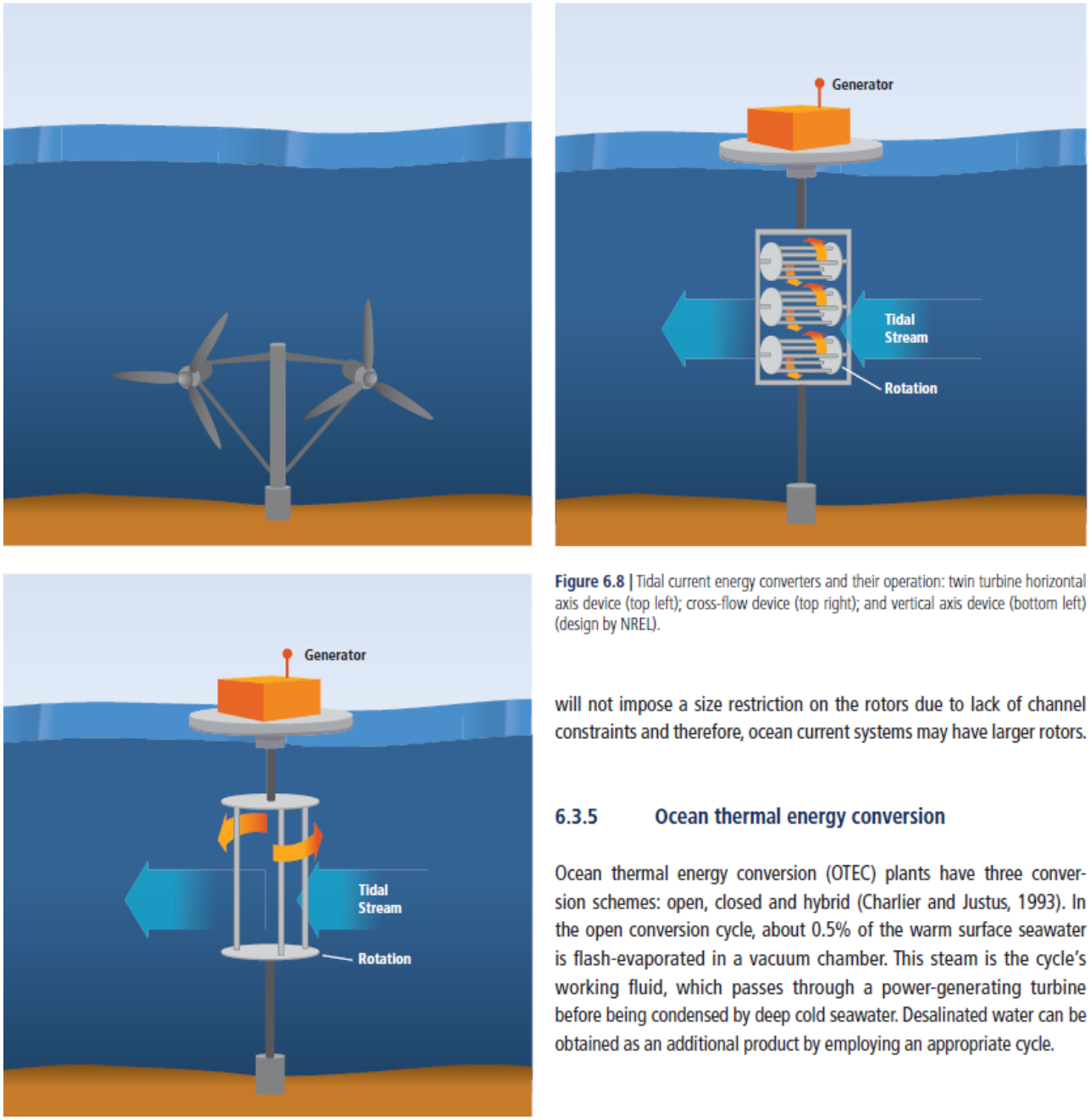

Figure 6.8 | Tidal current energy converters and their operation: twin turbine horizontal axis device (top left); cross-flow device (top right); and vertical axis device (bottom left) (design by NREL).

will not impose a size restriction on the rotors due to lack of channel constraints and therefore, ocean current systems may have larger rotors.

6.3.5 Ocean thermal energy conversion

Ocean thermal energy conversion (OTEC) plants have three conversion schemes: open, closed and hybrid (Charlier and Justus, 1993). In the open conversion cycle, about 0.5% of the warm surface seawater is flash-evaporated in a vacuum chamber. This steam is the cycle's working fluid, which passes through a power-generating turbine before being condensed by deep cold seawater. Desalinated water can be obtained as an additional product by employing an appropriate cycle.

7.4 SOLAR DRYERS

Solar drying is another very important application of solar energy. Solar dryers use air collectors to collect solar energy. Solar dryers are used primarily by the agricultural industry. The purpose of drying an agricultural product is to reduce its moisture content to a level that prevents its deterioration. In drying, two processes take place: One is a heat transfer to the product using energy from the heating source, and the other is a mass transfer of moisture from the interior of the product to its surface and from the surface to the surrounding air.

Traditionally, farmers used the open-to-the-sun or natural drying technique, which achieves drying by using solar radiation, ambient temperature, relative humidity of ambient air, and natural wind. In this method, the crop is placed on the ground or concrete floors, which can reach higher temperatures in open sun, and left there for a number of days to dry. Capacity wise, and despite the very rudimentary nature of the process, natural drying remains the most common method of solar drying. This is because the energy requirements, which come from solar radiation and the air enthalpy, are readily available in the ambient environment and no capital investment in equipment is required. The process, however, has some serious limitations. The most obvious ones are that the crops suffer the undesirable effects of dust, dirt, atmospheric pollution, and insect and rodent attacks. Because of these limitations, the quality of the resulting product can be degraded, sometimes beyond edibility. All these disadvantages can be eliminated by using a solar dryer.

The purpose of a dryer is to supply more heat to the product than that available naturally under ambient conditions, thus increasing sufficiently the vapor pressure of the crop moisture. Therefore, moisture migration from the crop is improved. The dryer also significantly decreases the relative humidity of the drying air, and by doing so, its moisture-carrying capability increases, thus ensuring a sufficiently low equilibrium moisture content.

There are two types of solar dryers: the ones that use solar energy as the only source of heat and the ones that use solar energy as a supplemental source. The airflow can be either natural convection or forced, generated by a fan. In the dryer, the product is heated by the flow of the heated air through the product, by directly exposing the product to solar radiation or a combination of both.

The transfer of heat to the moist product is by convection from the flowing air, which is at a temperature above that of the product, by direct radiation from the sun, and by conduction from heated surfaces in contact with the product.

Absorption of heat by the product supplies the energy necessary for vaporization of water from the product. From the surface of the product, the moisture is removed by evaporation. Moisture starts to vaporize from the surface of the product when the absorbed energy increases its temperature sufficiently and the vapor pressure of the crop moisture exceeds the vapor pressure of the

surrounding air. Moisture replacement to the surface is by diffusion from the interior, and it depends on the nature of the product and its moisture content. If the diffusion rate is slow, it becomes the limiting factor in the drying process, but if it is fast enough, the controlling factor is the rate of evaporation from the surface, which occurs at the initiation of the drying process.

In direct radiation drying, part of the solar radiation penetrates the material, and it is absorbed within the product, thus generating heat both in the interior of the product and on its surface. Therefore, the solar absorptance of the product is an important factor in direct solar drying. Because of their color and texture, most agricultural materials have relatively high absorptance.

The maximum drying rate is required so that drying is economically viable.

Solar energy dryers are classified according to the heating mode employed, the way the solar heat is utilized, and their structural arrangement. With respect to the heating mode employed, the two main categories are active and passive dryers. In active systems, a fan is used to circulate air through the air collector to the product, whereas in passive or natural circulation solar energy dryers, solar-heated air is circulated through the crop by buoyancy forces as a result of wind pressure. Therefore, active systems require, in addition to solar energy, other non-renewable energy sources, usually electricity, for powering fans for forced air circulation or for auxiliary heating.

With respect to the mode of solar energy utilization and structural arrangements, the three major sub classes are distributed, integral, and mixed-mode-type dryers. These sub-classes belong to both active and passive solar energy dryers. In a distributed-type solar energy dryer, the solar energy collector and the drying chamber are separate units. In an integral-type solar energy dryer, the same piece of equipment is used for both solar energy collection and drying, i.e., the dryer is capable of collecting solar energy directly, and no solar collectors are required. In the mixed-mode–type, the two systems are combined, i.e., the dryer is able to absorb heat directly but the process is enhanced by the use of a solar collector. These types are explained in more detail in the following sections.

7.4.1 Active Solar Energy Dryers

DISTRIBUTED TYPE

A typical distributed-type active solar dryer is shown in Figure 7.10. It comprises four components: a drying chamber, a solar energy air heater, a fan, and ducting to transfer the hot air from the collector to the dryer.

INTEGRAL TYPE

Large-scale, commercial, forced-convection, greenhouse-type dryers are like transparent roof solar barns and are used for solar timber drying kilns (see Figure 7.11). Small-scale forced dryers are often equipped with auxiliary heating.

Another variation of this type of dryer is the solar collector–roof/wall, in which the solar heat collector forms an integral part of the roof and/or wall of

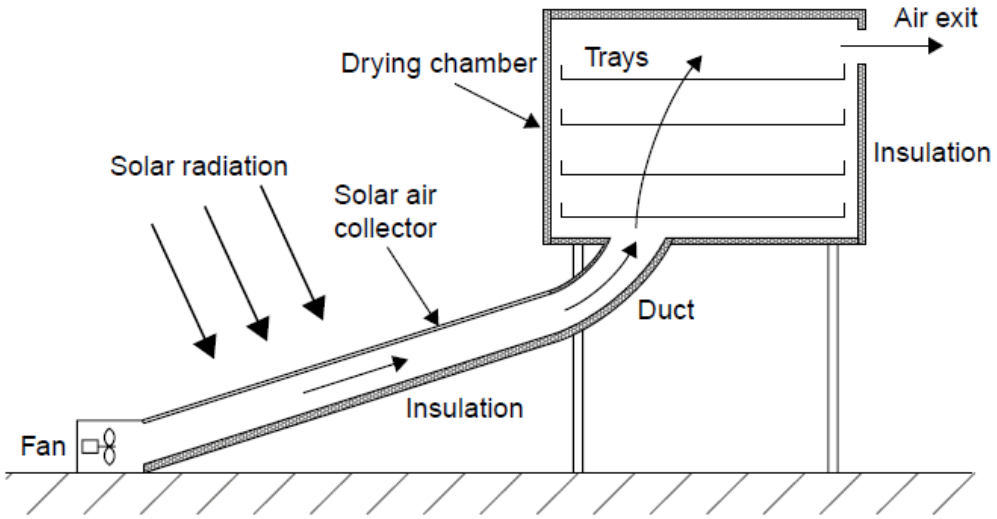

FIGURE 7.10 Schematic diagram of a distributed-type active solar dryer.

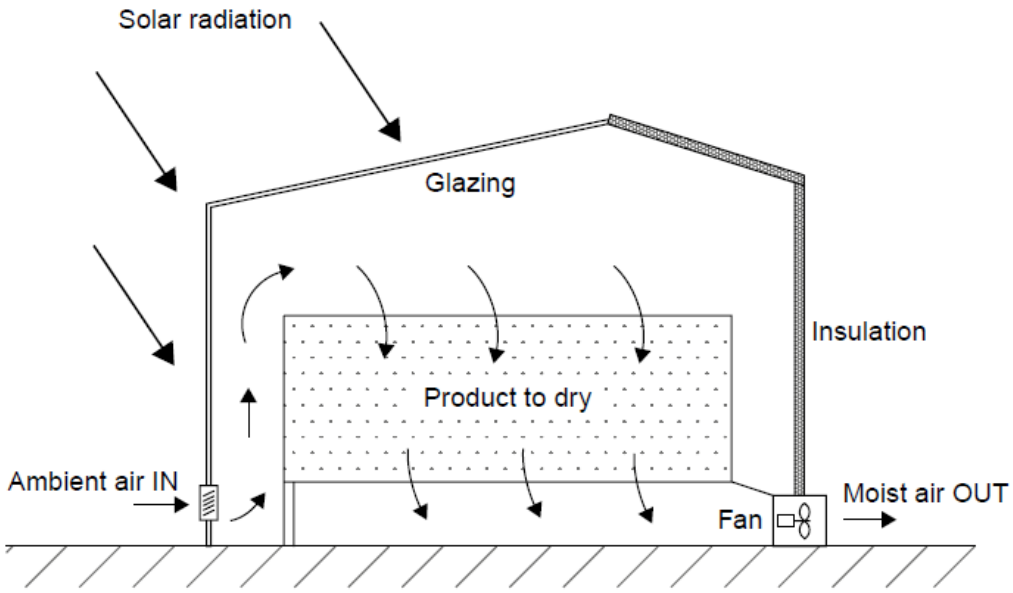

FIGURE 7.11 Schematic diagram of a forced-convection, transparent-roof solar barn.

the drying chamber. A solar-roof dryer is shown in Figure 7.12. A collector-wall system is like a Trombe wall, described in Chapter 6, where a black painted concrete block wall with outside glazing forms the solar collector and serves also as a thermal storage.

MIXED-MODE TYPE

The mixed-mode dryer is similar to the distributed type with the difference that the walls and roof of the dryer are made from glass, to allow solar energy to warm the products directly, as shown in Figure 7.13.

It should be noted that, because drying efficiency increases with temperature, in conventional dryers the maximum possible drying temperature that would not deteriorate the product quality is used. In solar dryers, however, the maximum drying temperature is determined by the solar collectors, because their efficiency

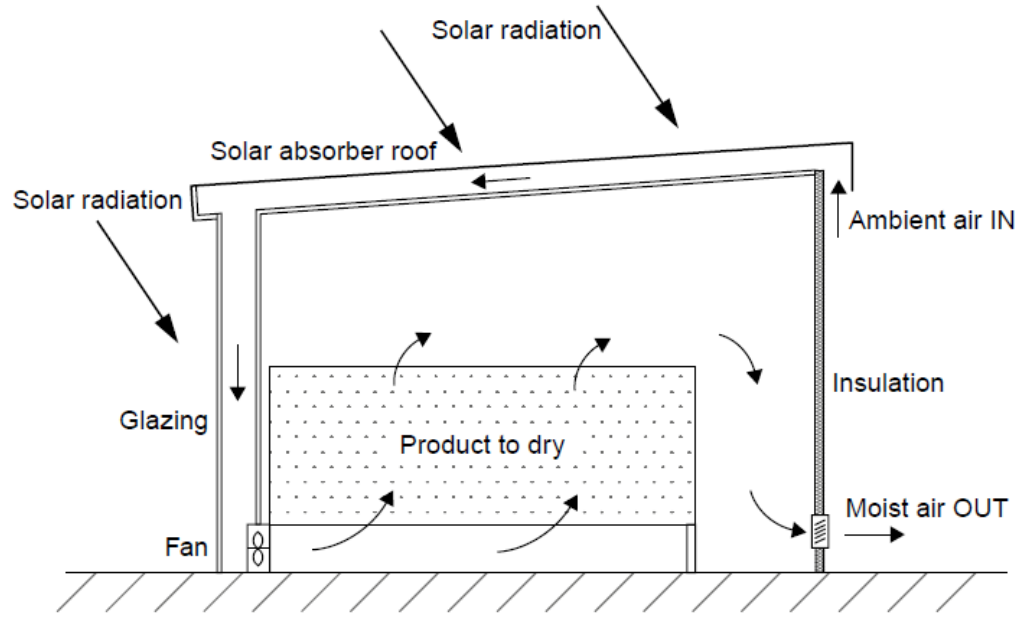

FIGURE 7.12 Schematic diagram of an active collector–roof solar energy storage dryer.

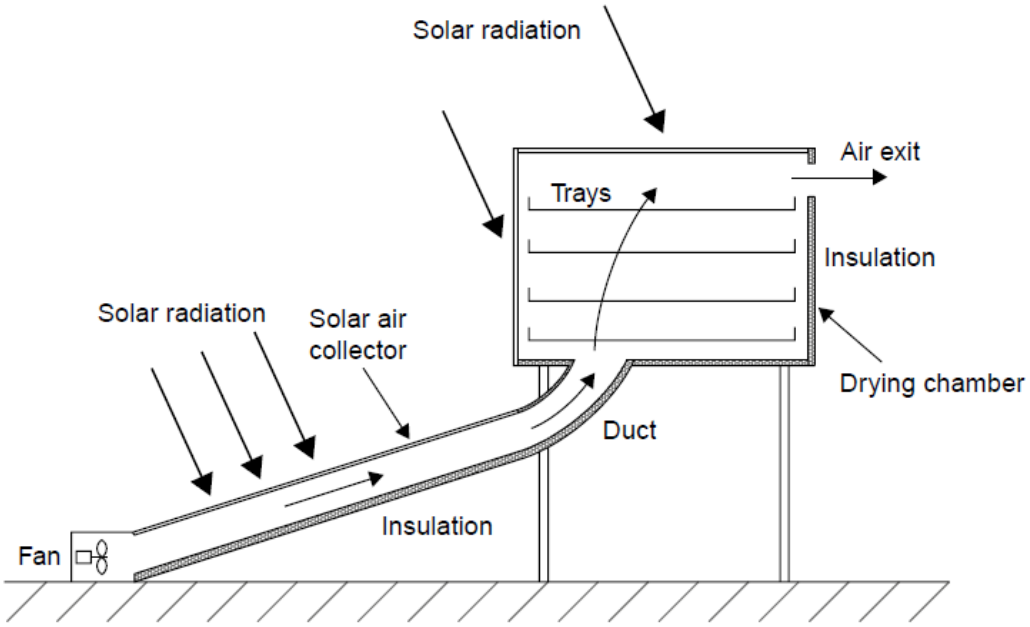

FIGURE 7.13 Schematic diagram of a mixed-mode-type active solar dryer.

decreases with higher operating temperatures and this may not yield an optimal dryer design.

Most air heaters use metal or wood absorbers, whereas black polythene absorbers have been used in a few designs in an attempt to minimize cost.

7.4.2 Passive Solar Energy Dryers

Passive or natural circulation solar energy dryers operate by using entirely renewable sources of energy, such as solar and wind.

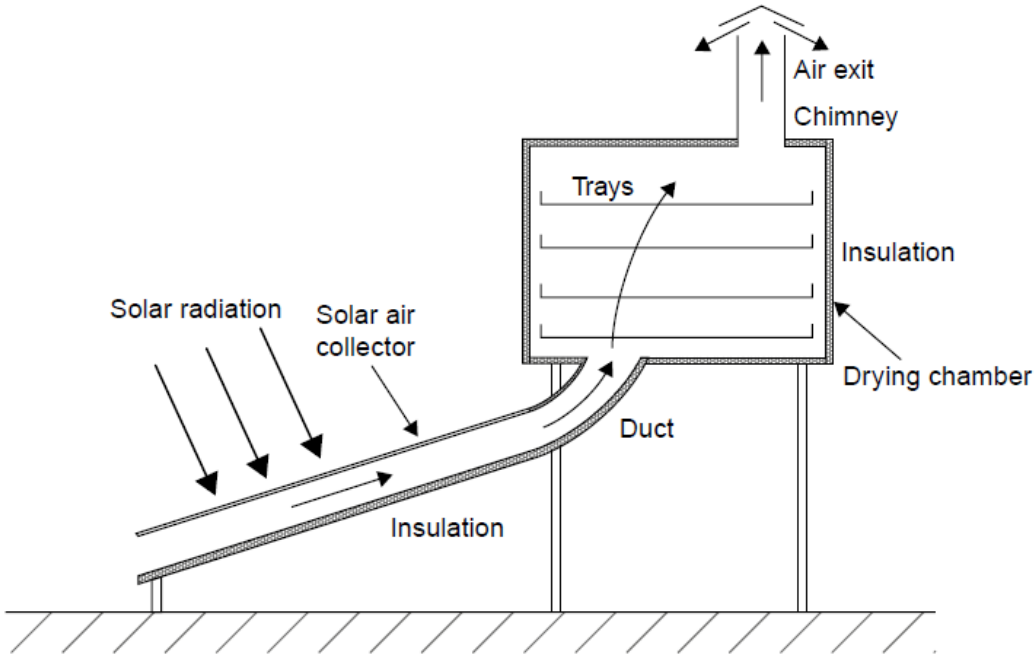

FIGURE 7.14 Schematic diagram of a distributed-type passive solar dryer.

DISTRIBUTED TYPE

Distributed, natural circulation, solar energy dryers are also called *indirect passive dryers*. A typical distributed natural circulation solar energy dryer comprises an air heating solar energy collector, appropriate insulated ducting, a drying chamber, and a chimney, as shown in Figure 7.14. In this design, the crop is located on trays or shelves inside an opaque drying chamber, which does not allow the solar radiation to reach the product directly. Air, which is heated during its passage through an air solar collector, is ducted to the drying chamber to dry the product. Because the crops do not receive direct sunshine, caramelization (formation of sugar crystals on the crop surface) and localized heat damage do not occur. Therefore, indirect dryers are usually used for some perishables and fruits, for which the vitamin content of the dried product is reduced by the direct exposure to sunlight. The color retention in some highly pigmented commodities is also very adversely affected when they are exposed directly to the sun (Norton, 1992).

INTEGRAL TYPE

Integral-type, natural circulation, solar energy dryers are also called *direct passive solar energy dryers*. In this system, the crop is placed in a drying chamber,

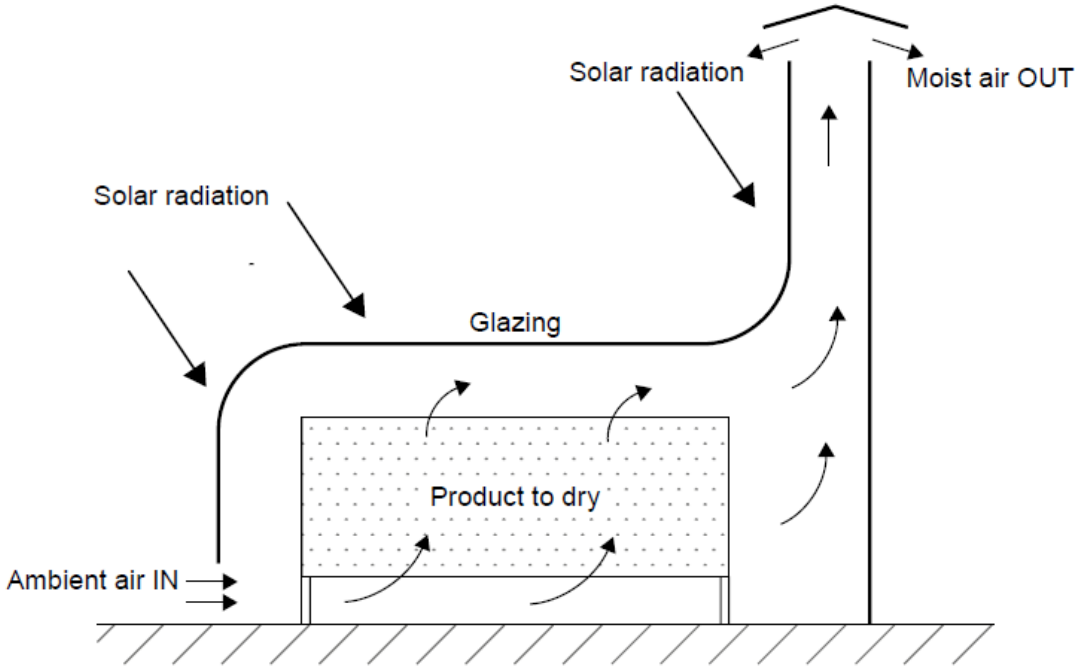

FIGURE 7.15 Schematic diagram of an integral-type passive solar dryer.

which is made with transparent walls; therefore, the necessary heat is obtained by the direct absorption of solar radiation at the product, from the internal surfaces of the chamber, and by convection from the heated air mass within the chamber. The heat removes the moisture from the product and, at the same time, lowers the relative humidity of the resident air mass, thus increasing its moisture-carrying capacity. The air in the chamber is also expanded because the density of the hot air is lower than the cold, thus generating natural circulation, which also helps in the removal of moisture, along with the warm air. Because heat is transferred to the crop by both convection and radiation, the rate of drying for direct dryers is greater than that for indirect dryers.

Integral-type, natural circulation solar energy dryers can be of a very simple construction, as shown in Figure 7.15, which consists of a container insulated at its sides and covered with a single glazing or roof. The interior walls are blackened; therefore, solar radiation transmitted though the cover is absorbed by the blackened interior surfaces as well as by the product, thus raising the internal temperature of the container. At the front, special openings provide ventilation, with warm air leaving via the upper opening under the action of buoyant forces. The product to be dried is placed on perforated trays inside the container. This type of dryer has the advantage of easy construction from cheap, locally available materials and is used commonly to preserve fruits, vegetables, fish, and meat. The disadvantage is the poor air circulation obtained, which results in poor moist air removal and drying at high air temperatures (70–100°C), which is very high for most products, particularly perishables.

MIXED-MODE TYPE

Mixed-mode, natural circulation, solar energy dryers combine the features of the integral-type and the distributed-type natural circulation solar energy dryers.

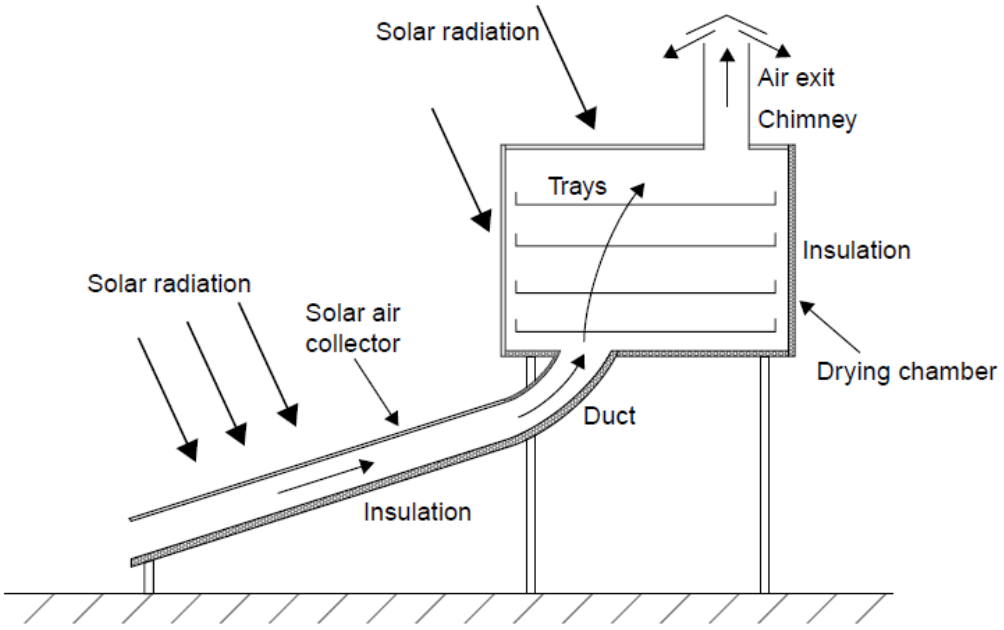

FIGURE 7.16 Schematic diagram of a natural circulation, mixed-mode solar energy dryer.

In this case, the combined action of solar radiation incident directly on the product to be dried and the air heated in a solar air collector provide the necessary heat required for the drying process. A mixed-mode, natural circulation solar energy dryer has the same structural characteristics as the distributed type, i.e., a solar air heater, a separate drying chamber, and a chimney; in addition, the drying chamber walls are glazed so that the solar radiation can reach the product directly as in the integral-type dryers, as shown in Figure 7.16.

Wind Turbines

2.3 Classification of wind turbines

2.3.1 Horizontal axis wind turbines

Horizontal axis wind turbines (HAWT) have their axis of rotation horizontal to the ground and almost parallel to the wind stream (Fig. 2.3). Most of the commercial wind turbines fall under this category. Horizontal axis machines have some distinct advantages such as low cut-in wind speed and easy furling. In general, they show relatively high power coefficient. However, the generator and gearbox of these turbines are to be placed over the tower which makes its design more complex and expensive. Another disadvantage is the need for the tail or yaw drive to orient the turbine towards wind.

Depending on the number of blades, horizontal axis wind turbines are further classified as single bladed, two bladed, three bladed and multi bladed, as shown in Fig. 2.4. Single bladed turbines are cheaper due to savings on blade materials. The drag losses are also minimum for these turbines. However, to balance the blade, a counter weight has to be placed opposite to the hub. Single bladed designs are not very popular due to problems in balancing and visual acceptability. Two bladed rotors also have these drawbacks, but to a lesser extent. Most of the present commercial turbines used for electricity generation have three blades.

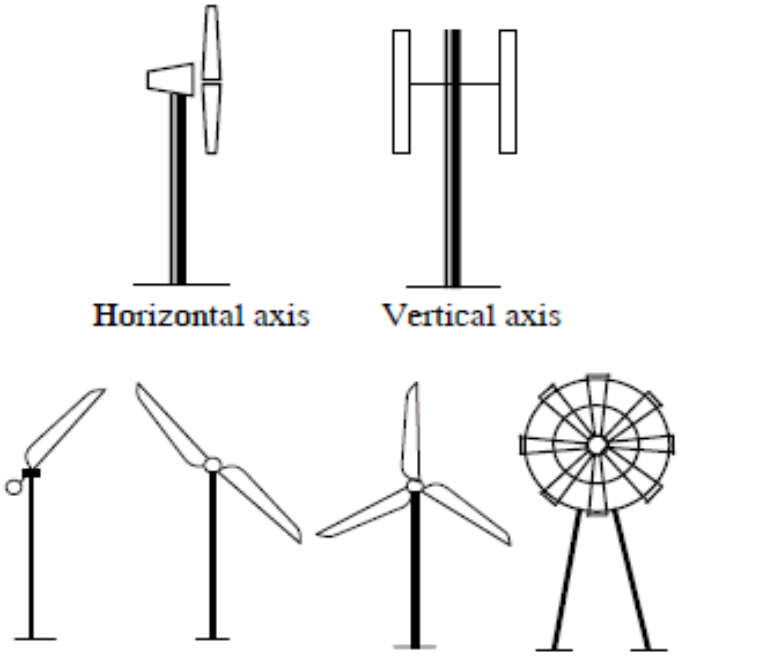

Fig. 2.4. Classification of wind turbines

Horizontal wind turbines may be classified according to position of blades and Nacelle as:
1-Upwind HAWT:
2-Downwind HAWT:

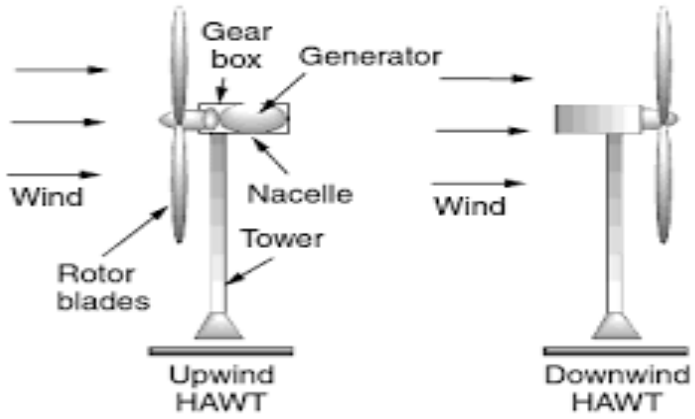

2.3.2 Vertical axis wind turbines

Darrieus rotor

Darrieus rotor, named after its inventor Georges Jeans Darrieus, works due to the lift force generated from a set of airfoils (Fig. 2.6). In the original design the blades are shaped like egg beaters or *troposkein* (turning rope) and are under pure tension while in operation. This typical blade configuration helps in minimizing the bending stress experienced by the blades. There are several variations in the Darrieus design of which some are with straight vertical blades, usually called

Savonius rotor

The Savonius wind turbine, invented by S.J. Savonius, is a vertical axis machine consisting of two half cylindrical (or elliptical) blades arranged in 'S' shape (Fig. 2.7). Convex side of one of the half cylinder and the concave side of the other are facing the wind at a time as shown in Fig. 2.8. The basic driving force of Savonius rotor is drag. The drag coefficient of a concave surface is more than the convex surface. Hence, the half cylinder with concave side facing the wind will experience more drag force than the other cylinder, thus forcing the rotor to rotate. Some times two or more rotors fixed one over the other at 90^{o} offset may be used to smoothen the torque fluctuations during rotation. Another way to improve the performance is to attach deflector augmenters with the rotor. The augmenter shades the convex half facing the wind and directs the flow to the concave half thus enhancing the performance.

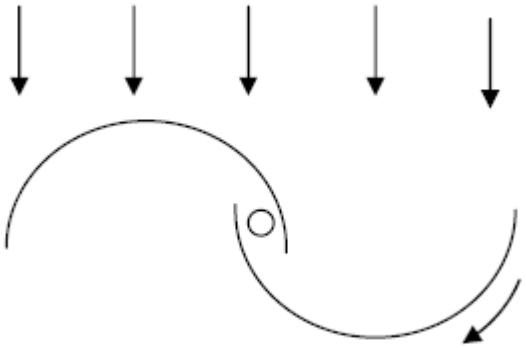

Fig. 2.8. Principle of Savonius rotor

Musgrove rotor

Musgrove rotor was developed by a research team under Prof. Musgrove at the Reading University, UK. It is basically a vertical axis lift machine having 'H' shaped blades and a central shaft (Fig. 2.9). At high wind speeds the rotor feathers and turn about a horizontal point due to the centrifugal force. This eliminates the risk of higher aerodynamic forces on the blades and the structure.

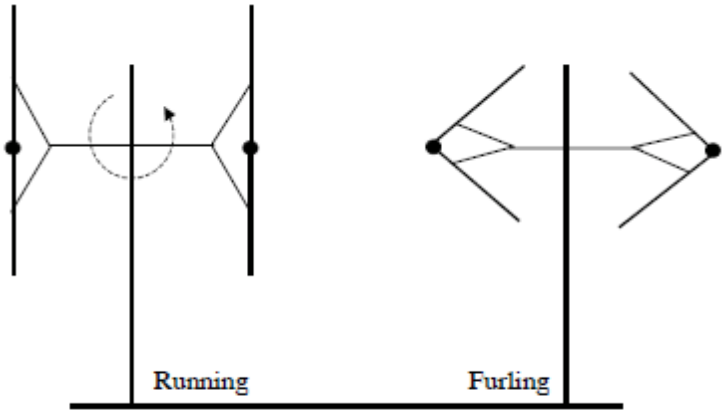

Fig. 2.9. Principle of Musgrove turbine

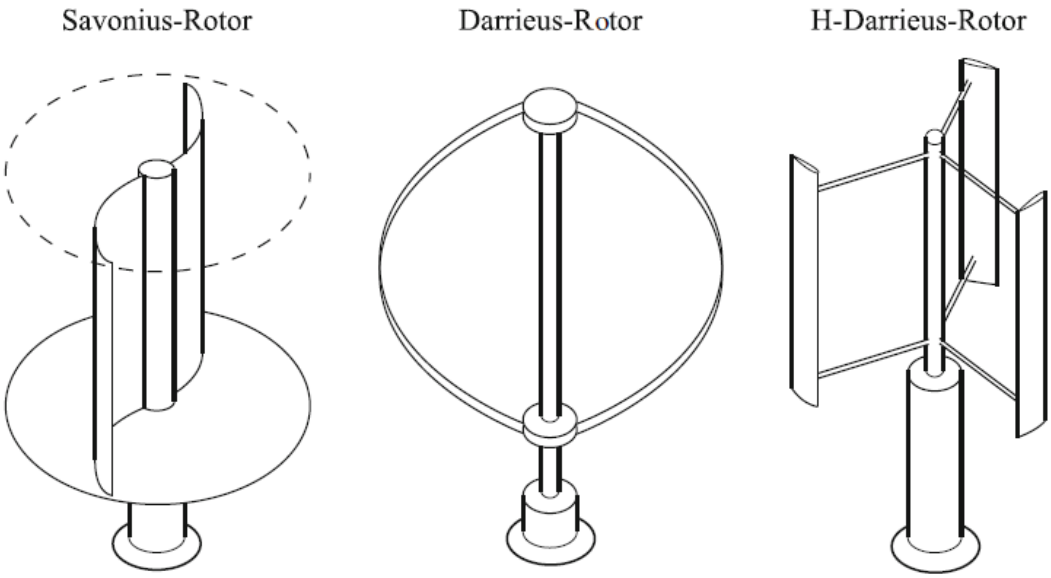

2.4 Characteristics of wind rotors

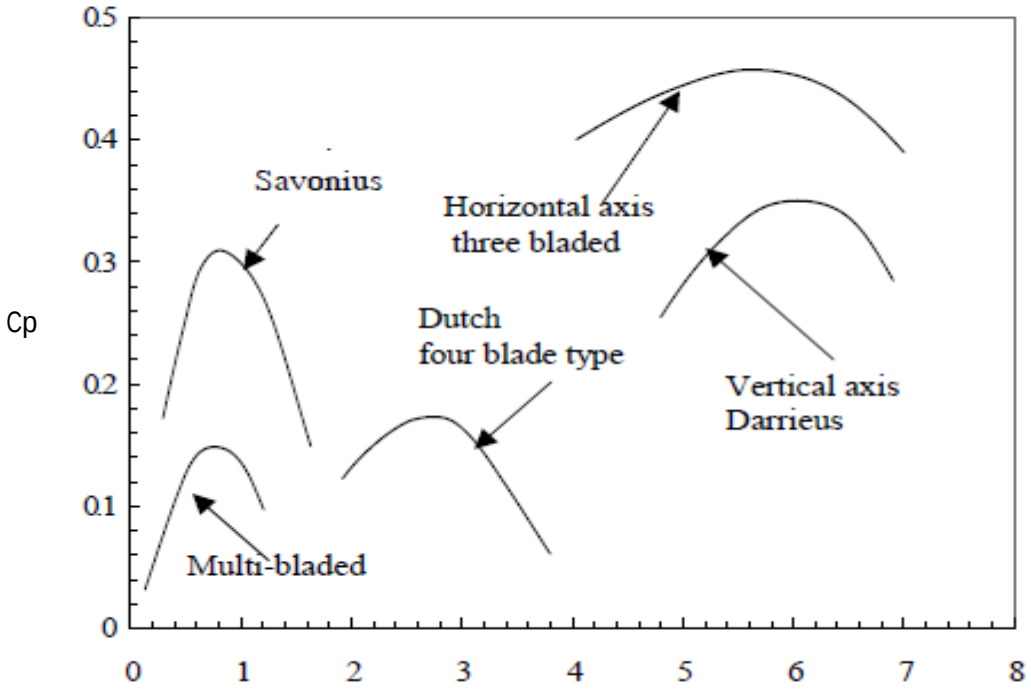

Fig. 2.10. Performance characteristics of wind rotors

Power curve versus turbine blade pitch angle

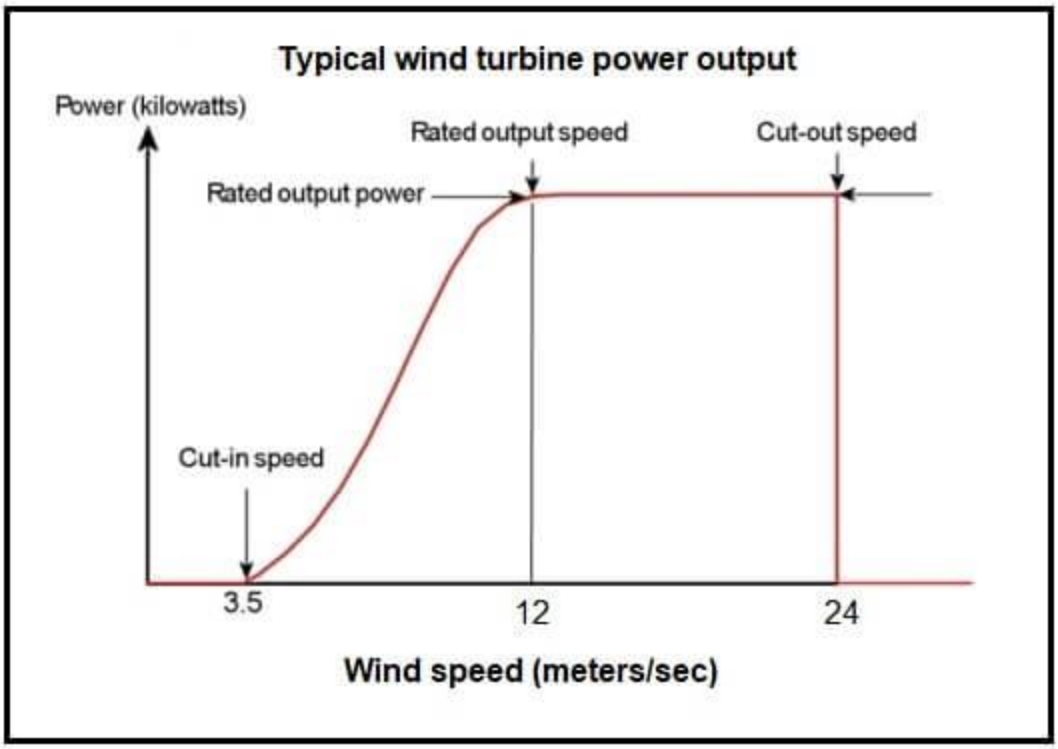

Ex: explain the following terms for the following curve:

1- Cut-in speed
2- Rated power
3- Cut-out speed

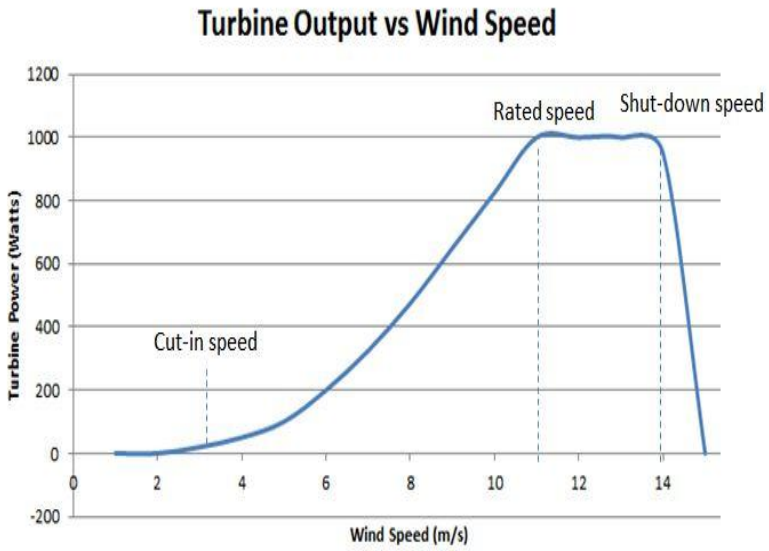

Ans: the rated power is the power must be extracted from the turbine at a certain range of wind speed. So, rated power=1000 watt, and this value was satisfyed at wind speed range (11-14 m/s) as shown in that curve and to keep the turbine work at same rated power , the turbine pitch angle must be change at each values of wind speed.

Cut-in speed mean the minimum wind speed value here(3m/s) beyond the turbine start extract power from wind. See when wind speed =1m/s, there is no power was extracted. Byeond the cut-in speed, (3-11m/s) as the wind speed increase causes rise in turbine power.

Cut-out or shut down speed here (14m/s) is the speed which causes turbine blades stall, or causes quick drop in rated power.

2.5 Aerodynamics of wind turbines

2.5.1 Airfoil

For the efficient energy extraction, blades of modern wind turbine are made with airfoil sections. Major features of such an airfoil are shown in Fig. 2.11. The airfoils used for the earlier day's wind turbines were the aviation air foils under the NACA (National Advisory Committee for Aeronautics) series. NACA specifies the features of the airfoil by numbers.

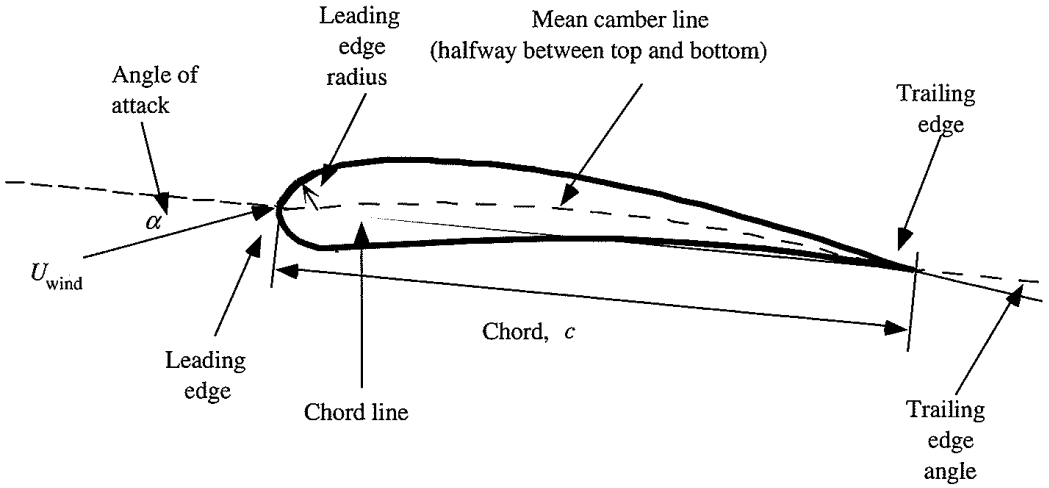

Figure 3.7 Airfoil nomenclature

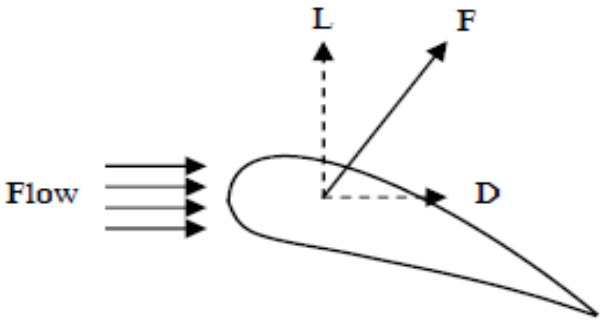

Fig. 2.12. Airfoil lift and drag

The lift force is given by

$$L = C_L \frac{1}{2} \rho_a A V^2 \tag{2.15}$$

and the drag force (D) by

$$D = C_D \frac{1}{2} \rho_a A V^2 \tag{2.16}$$

where C_L and C_D are the lift and drag coefficients respectively.

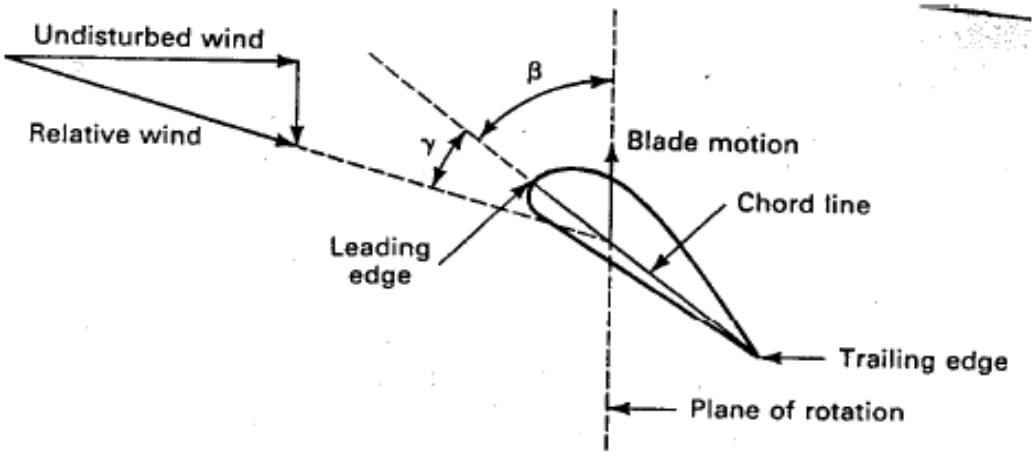

Figure 6: Definition of pitch angle β and angle of attack γ.

Axial momentum theory

The conventional analysis of HAWT originates from the axial momentum concept introduced by Rankine, which was further improved by Froudes for marine propellers. Ideal flow conditions are considered for this analysis. The flow is assumed to be incompressible and homogeneous. The rotor is considered to be made up of infinite number of blades. Static pressures far in front and behind the rotor are considered to be equal to the atmospheric pressure. Frictional drag over the blades and wake behind the rotor are neglected.

Consider a wind turbine with rotor of area A_T, placed in a wind stream as shown in Fig. 2.15. Let A and A' be the areas of the sections 1-1, and 2-2 and V and V' are the respective wind velocities at these sections.

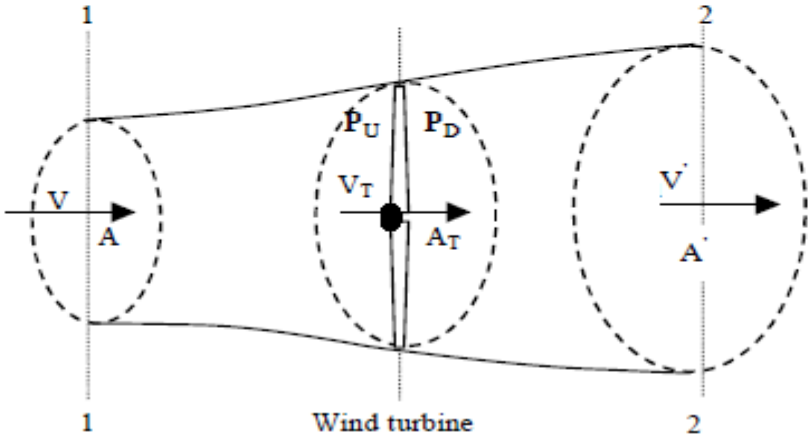

Fig. 2.15. The axial stream tube model

V=wind velocity upstream of turbine disc
A= Upstream turbine disc(rotor) swept area
V_T=Wind velocity at turbine rotor disc station
A_T= Turbine disc(rotor) swept area
V'= wind velocity downstream of turbine disc
A'= Downstream turbine disc(rotor) swept area

V_T is the velocity at the turbine section. According to the law of conservation of mass, the mass of air flowing through these sections is equal. Thus:

$$\rho_a A V = \rho_a A_T V_T = \rho_a A' V' \tag{2.18}$$

The thrust force experienced by the rotor is due to the difference in momentum of the incoming and outgoing wind, which is given by

$$F = \rho_a A V^2 - \rho_a A' V'^2 \tag{2.19}$$

As $A V = A' V' = A_T V_T$ from (2.18), the thrust can be expressed as

$$F = \rho_a A_T V_T \left(V - V'\right) \tag{2.20}$$

The thrust can also be represented as the pressure difference in the upstream and down stream sides of the rotor. Let p_U and p_D be the pressure at the upstream and down stream side of the rotor respectively. Hence:

$$F = \left(p_U - p_D\right) A_T \tag{2.21}$$

Applying the Bernoulli's equation at the sections and considering the assumption that the static pressures at sections 1-1 and 2-2 are equal to the atmospheric pressure p, we get

$$p + \frac{\rho_a V^2}{2} = p_U + \frac{\rho_a V_T^2}{2} \tag{2.22}$$

and

$$p + \frac{\rho_a V'^2}{2} = p_D + \frac{\rho_a V_T^2}{2} \tag{2.23}$$

From Eqs. (2.22) and (2.23),

$$p_U - p_D = \frac{\rho_a \left(V^2 - V'^2\right)}{2} \tag{2.24}$$

Substituting the above expression for $(p_U - p_D)$ in Eq. (2.21),

$$F = \frac{\rho_a A_T \left(V^2 - V'^2\right)}{2} \tag{2.25}$$

Comparing Eqs. (2.20) and (2.25) we get

$$V_T = \frac{\left(V + V'\right)}{2} \tag{2.26}$$

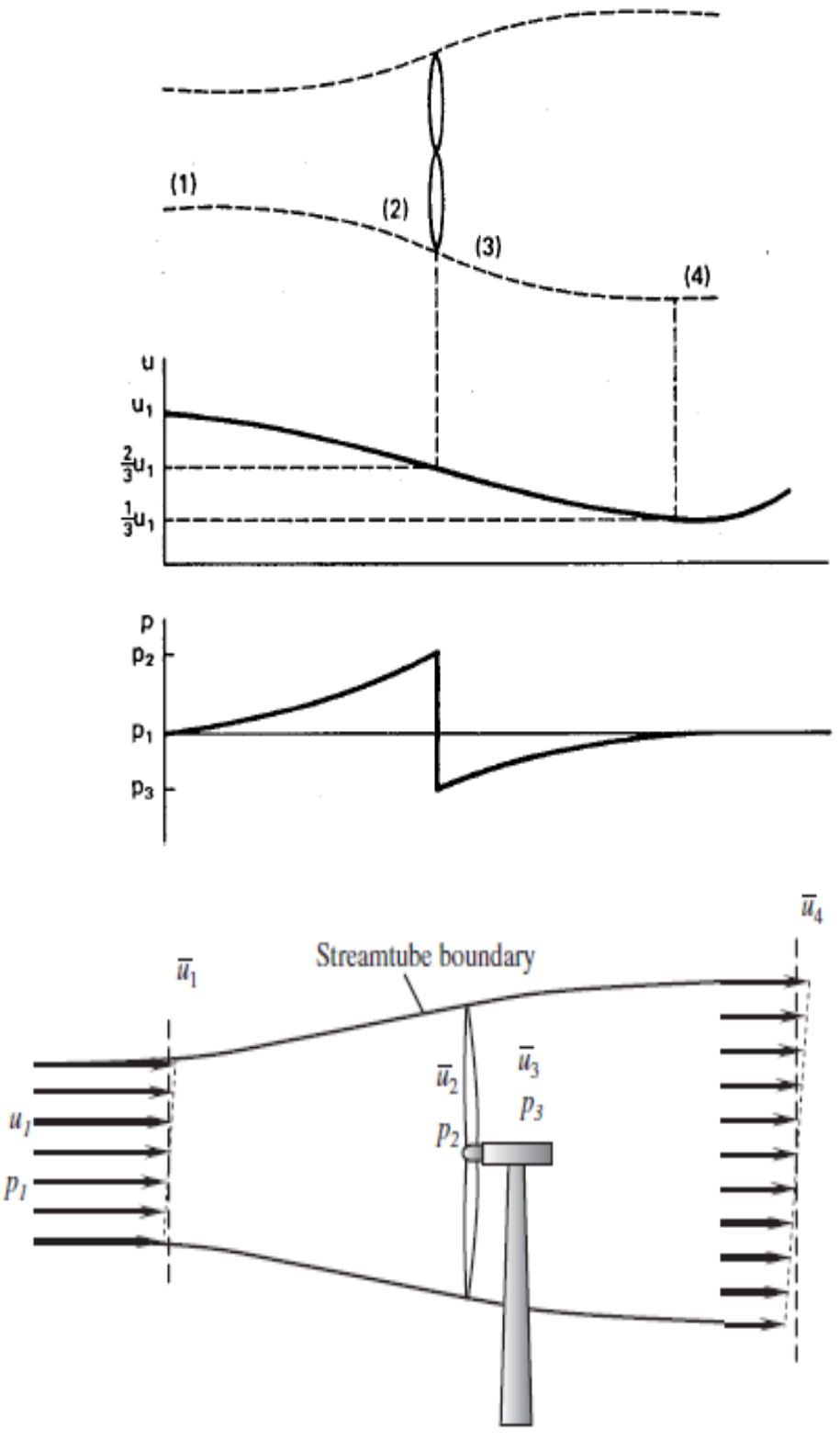
(1)
(2)
(3)
(4)
u
u1
2/3 u1
1/3 u1
p
p2
p1
p3
Streamtube boundary
ū1
ū2
ū3
ū4
u1
p1
p2
p3
u4
p4

At this stage, we introduce a parameter, termed as the axial induction factor into our analysis. The axial induction factor a indicates the degree with which the wind velocity at the upstream of the rotor is slowed down by the turbine. Thus

$$a = \frac{V - V_T}{V} \tag{2.27}$$

From Eqs. (2.26) and (2.27),

$$V_T = V(1-a) \tag{2.28}$$

and

$$V' = V(1-2a) \tag{2.29}$$

As we have seen earlier, the power imparted to the wind turbine is due to the transfer of kinetic energy from the air to the rotor. The mass flow through the rotor over a unit time is

$$m = \rho A_T V_T \tag{2.30}$$

Hence the power developed by the turbine due to this transfer of kinetic energy is

$$P_T = \frac{1}{2}\rho_a A_T V_T (V^2 - V'^2) \tag{2.31}$$

Substituting for V_T and V' from Eqs. (2.28) and (2.29), we get

$$P_T = \frac{1}{2}\rho_a A_T V^3 \; 4a(1-a)^2 \tag{2.32}$$

Comparing Eq. (2.32) with the expression for power coefficient in Eq. (2.8), we can see that

$$C_P = 4a(1-a)^2 \tag{2.33}$$

For C_p to be maximum,

$$\frac{dC_p}{da} = 0 \tag{2.34}$$

Thus differentiating Eq. (2.33), equating it to zero and solving, we get a=1/3.

Substituting for a in Eq. (2.33), the maximum theoretical power coefficient of a horizontal axis wind turbine is 16/27 and the maximum power produced is

$$P_{TMAX} = \frac{1}{2}\rho_a A_T V^3 \; \frac{16}{27} \tag{2.35}$$

EXAMPLE 1.2. Calculate the Betz limit for a horizontal-axis wind turbine whose blades sweep a circular area with a diameter of 80 m, and for an upstream wind speed of $v_1 = 12$ m/s.

The answer is found by substituting the given parameters in (1.8):

$$P_{\max} = \left(\frac{16}{27}\right)\left(\frac{1}{2}\right)(1.25)(3.14)(40^2)(12^3) = 3.2 \text{ MW}. \tag{1.9}$$

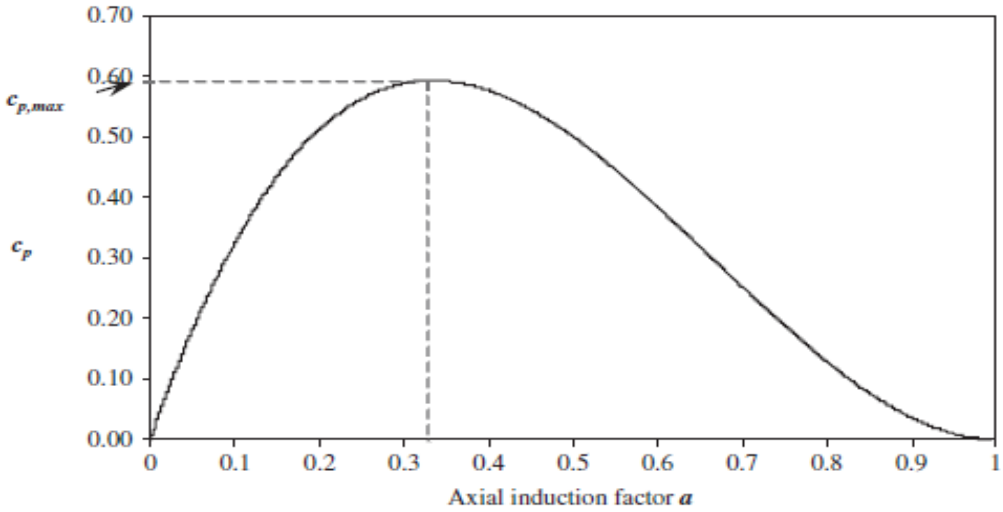

Figure 9: Power coefficient as a function of axial induction factor a.

5.4 Wind turbine controls

Wind turbine control systems continue to play important roles for ensuring wind turbine reliable and safe operation and to optimize wind energy capture. The main control systems in a modern wind turbine include pitch control, stall control (passive and active), yaw control, and others.

Under high wind speed conditions, the power output from a wind turbine may exceed its rated value. Thus, power control is required to control the power output within allowable fluctuations for avoiding turbine damage and stabilizing the power output. There are two primary control strategies in the power control: pitch control and stall control. The wind turbine power control system is used to control the power output within allowable fluctuations.

5.4.1 Pitch control

The pitch control system is a vital part of the modern wind turbine. This is because the pitch control system not only continually regulates the wind turbine's blade pitch angle to enhance the efficiency of wind energy conversion and power generation stability, but also serves as the security system in case of high wind speeds or emergency situations. It requires that even in the event of grid power failure, the rotor blades can be still driven into their feathered positions by using either the power of backup batteries or capacitors [51] or mechanical energy storage devices [52].

5.4.2 Stall control

Besides pitch control, stall control is another approach for controlling and protecting wind turbines. The concept of stall control is that the power is regulated through stalling the blades after rated speed is achieved.

Stall control can be further divided into passive and active control approaches. Passive stall control is basically used in wind turbines in which the blades are bolted to the hub at a fixed installing angle. In a passive stall-regulated wind turbine, the power regulation relies on the aerodynamic features of blades. In low and moderate wind speeds, the turbine operates near maximum efficiency. At high wind speeds, the turbine is automatically controlled by means of stalled blades to limit the rotational speed and power output, protecting the turbine from excessive wind speeds.

5.4.3 Yaw control

In order to maximize the wind power output and minimize the asymmetric loads acting on the rotor blades and the tower, a horizontal-axis wind turbine must be oriented with rotor against the wind by using an active yaw control system. Like wind pitch systems, yaw systems can be driven either electrically or hydraulically. Generally, hydraulic yaw systems were used in the earlier time of the wind turbine development [54]. In modern wind turbines, yaw control is done by electric motors. The yaw control system usually consists of an electrical motor with a speed reducing gearbox, a bull gear which is fixed to the tower, a wind vane to gain the information about wind direction, a yaw deck, and a brake to lock the turbine securely in yaw when the required position is reached. For a large wind turbine with high driving loads, the yaw control system may use two or more yaw motors to work together for driving a heavy nacelle (see Figure 7).

5.2 Wind turbine configuration

Most of the modern large wind turbines are horizontal-axis turbines with typically three blades. As shown in Fig. 7, a wind turbine is comprised of a nacelle, which

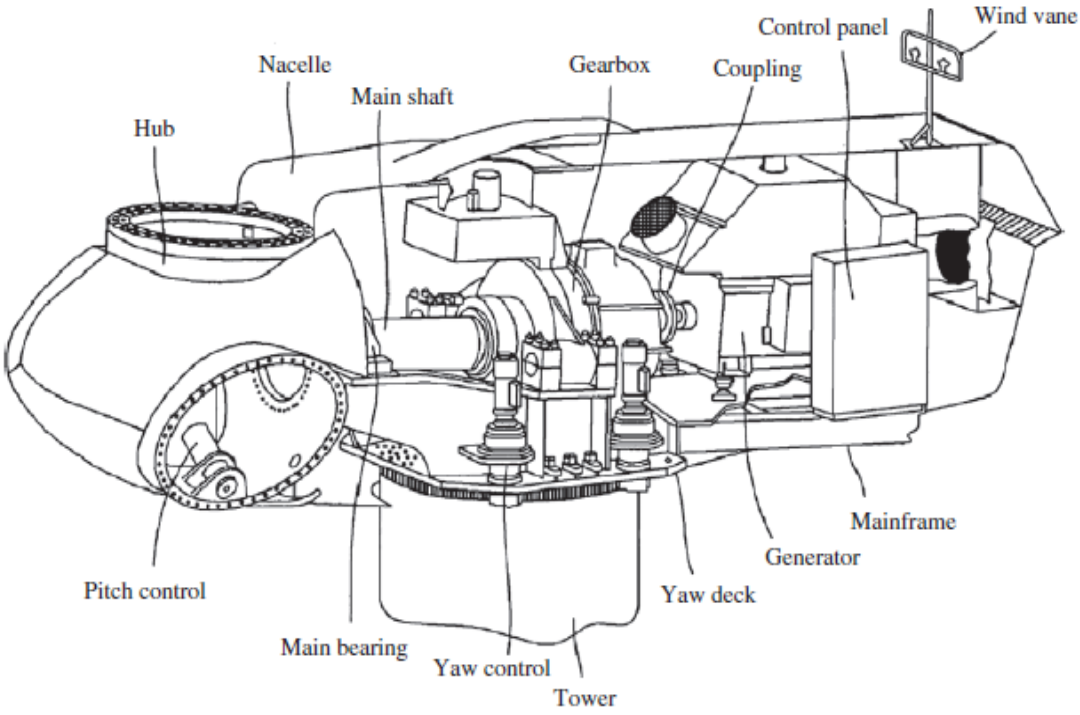

Figure 7: A horizontal-axis wind turbine configuration. Courtesy of the US Patent & Trademark Office.

2.2 Wind turbine power and torque

Theoretical power available in a wind stream is given by Eq. (2.3). However, a turbine cannot extract this power completely from the wind. When the wind stream passes the turbine, a part of its kinetic energy is transferred to the rotor and the air leaving the turbine carries the rest away. Actual power produced by a rotor would thus be decided by the efficiency with which this energy transfer from wind to the rotor takes place. This efficiency is usually termed as the power coefficient (C_p). Thus, the power coefficient of the rotor can be defined as the ratio of actual power developed by the rotor to the theoretical power available in the wind. Hence,

$$C_p = \frac{2\ P_T}{\rho_a\ A_T\ V^3} \tag{2.8}$$

where P_T is the power developed by the turbine. The power coefficient of a turbine depends on many factors such as the profile of the rotor blades, blade arrangement and setting etc. A designer would try to fix these parameters at its optimum level so as to attain maximum C_p at a wide range of wind velocities.

The thrust force experienced by the rotor (F) can be expressed as

$$F = \frac{1}{2}\rho_a\ A_T\ V^2 \tag{2.9}$$

Hence we can represent the rotor torque (T) as

$$T = \frac{1}{2}\rho_a\ A_T\ V^2 R \tag{2.10}$$

where R is the radius of the rotor. This is the maximum theoretical torque and in practice the rotor shaft can develop only a fraction of this maximum limit. The ratio between the actual torque developed by the rotor and the theoretical torque is termed as the torque coefficient (C_T). Thus, the torque coefficient is given by

$$C_T = \frac{2\ T_T}{\rho_a\ A_T\ V^2 R} \tag{2.11}$$

where T_T is the actual torque developed by the rotor.

The ratio between the velocity of the rotor tip and the wind velocity is termed as the tip speed ratio (λ). Thus,

$$\lambda = \frac{R\,\Omega}{V} = \frac{2\pi N R}{V} \tag{2.12}$$

where Ω is the angular velocity and N is the rotational speed of the rotor. The power coefficient and torque coefficient of a rotor vary with the tip speed ratio. There is an optimum λ for a given rotor at which the energy transfer is most efficient and thus the power coefficient is the maximum ($C_{P\,max}$).

Now, let us consider the relationship between the power coefficient and the tip speed ratio.

$$C_p = \frac{2\ P_T}{\rho_a\ A_T\ V^3} = \frac{2\ T_T\ \Omega}{\rho_a\ A_T\ V^3} \tag{2.13}$$

Dividing Eq. (2.13) by Eq. (2.11) we get

$$\frac{C_p}{C_T} = \frac{R\,\Omega}{V} = \lambda \tag{2.14}$$

Thus, the tip speed ratio is given by the ratio between the power coefficient and torque coefficient of the rotor.

Example

Consider a wind turbine with 5 m diameter rotor. Speed of the rotor at 10 m/s wind velocity is 130 r/min and its power coefficient at this point is 0.35. Calculate the tip speed ratio and torque coefficient of the turbine. What will be the torque available at the rotor shaft? Assume the density of air to be 1.24 kg/m^3.

Area of the rotor is

$$A_T = \frac{\pi}{4} \times 5^2 = 19.63\,\text{m}^2$$

As the speed of the rotor is 130 r/min, its angular velocity is

$$\Omega = \frac{2 \times \pi \times 130}{60} = 13.6 \text{ rad/s}$$

The tip speed ratio at this velocity is

$$\lambda = \frac{2.5 \times 13.6}{10} = 3.4$$

The torque coefficient is

$$C_T = \frac{0.35}{3.4} = 0.103$$

From this, torque developed can be calculated as

$$T_T = \frac{1}{2} \times 1.24 \times \frac{\pi}{4} \times 5^2 \times 10^2 \times 0.103 = 313.39 \quad \text{Nm}$$

Example

A wind turbine model of 1 m diameter was tested in a wind tunnel. Test results are given in Table 2.3. Generate the CP-λ curve of the rotor.

Table 2.3. Observations of the wind tunnel test

4 m/s		6 m/s		8 m/s	
Rotor speed (r/min)	Power (W)	Rotor speed (r/min)	Power (W)	Rotor speed (r/min)	Power (W)
306	12.30	482	42.55	673	104.54
352	13.37	550	45.66	764	109.46
397	13.68	619	47.73	856	113.15
443	14.33	688	48.46	948	110.69
489	13.53	757	44.62	1039	100.85
535	11.99	768	43.58	1055	98.39

The power-speed curve of the rotor at 4 m/s, 6 m/s and 8 m/s are shown in Fig. 2.22. The power coefficient of the model rotor can be estimated from the relationship

$$C_P = \frac{8\,P}{\pi\,\rho_a\,d^2\,V^3} \tag{2.72}$$

The tip speed ratio may be calculated as

$$\lambda = \frac{\pi\,D\,N}{V} \tag{2.73}$$

λ and the corresponding C_P for the rotor, at different wind velocities and loads, are calculated using the above expressions and plotted in Fig. 2.23.

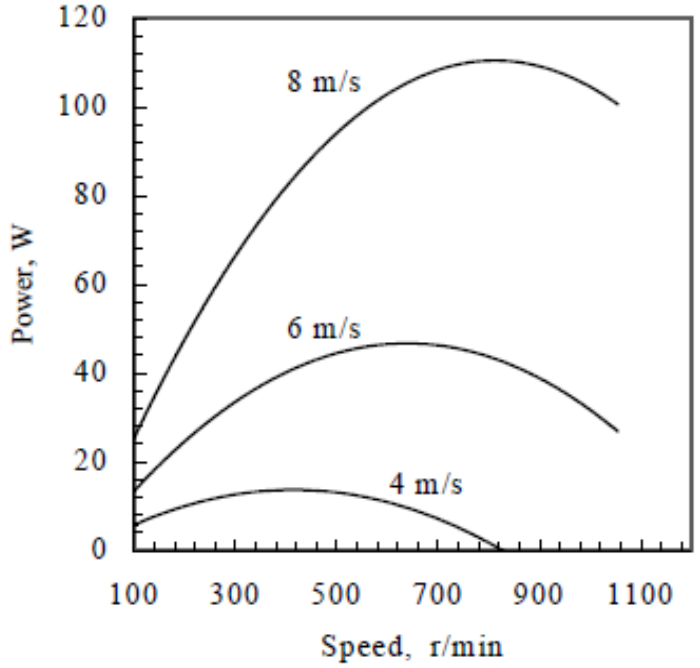

Fig. 2.22. Power- speed curves of the rotor

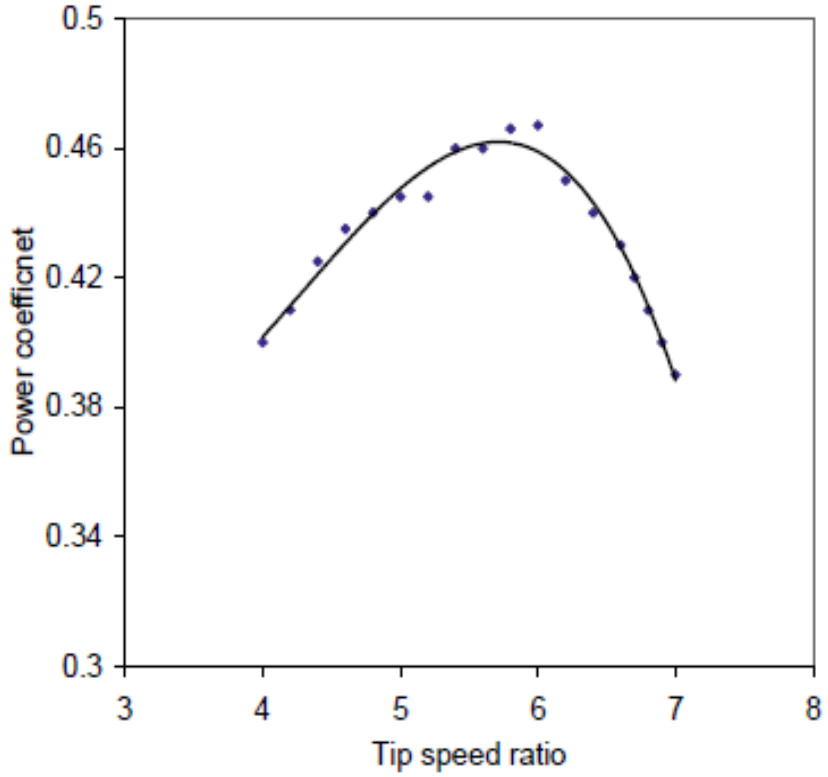

Fig. 2.23. C_P - λ curve of the rotor

Ex1: Based on average speed data only, estimate the wind power from a horizontal axis wind turbine with a 12 m diameter operating in a wind regime with an average wind speed of 8 m/s. Assume that the wind turbine is operating under standard atmospheric conditions (ρ = 1.225 kg/m3).

Where P is determined from Equation 2.7, $P = \pi R^2 \frac{1}{2} \rho U^3$. For an average wind speed of 8 m/s:

$$P = \pi(6)^2 \frac{1}{2}(1.225)(8)^3 = 35.46\ kW$$

Ex2: A 40 m diameter, three bladed wind turbine produces 700 kW at a wind speed (hub height) of 14 m/s. The air density is 1.225 kg/m^3. Find:
a) The rotational speed (rpm) of the rotor at a tip-speed ratio of 5.0.
b) What is the tip-speed in (m/s)?
c) If the generator turns at 1800 rpm, what gear ratio is needed to match the rotor speed to the generator speed?
d) What is the efficiency of the wind turbine system (including blades, transmission, shafts, and generator) under these conditions?

a) $\lambda = 5$

$$\lambda = \frac{\Omega R}{U} \text{ (Equation 2.76)}$$

$$\Omega = \frac{\lambda U}{R} = \frac{(5.0)(14\,m/s)}{20\,m} = 3.5\,rad/s$$

$$N_{rotor} = \frac{(\Omega\,rad/s)(60\,s/\min)}{2\pi\,rad/rev} = 33.42\,rpm$$

b) $U_{tip} = \Omega R = (20\,m)(3.5\,rad/s) = 70\,m/s$

c) N_{gen} =1800 rpm; N_{rotor} = 33.42 rpm

gearbox ratio = N_{gen} / N_{rotor} = 53.86

(d) $P = \frac{1}{2} \rho \pi R^2 C_p \eta U^3$; assume Betz limit: C_P =16/27

$$\eta = \frac{P}{\frac{1}{2}\rho\pi R^2 C_p U^3} = 0.56$$

Ex3: Find the size of a wind turbine rotor (diameter in m) that will generate 100 kW of electrical power in a steady wind (hub height) of 7.5 m/s. Assume that the air density is ρ = 1.225 kg/m3, Cp = 16/27, η = 1.

a) $P = 100$ kW; $U = 7.5$ m/s, $\rho = 1.225$ kg/m^3, $C_P = 16/27$, $\eta = 1$

$P = \frac{1}{2}\rho\pi R^2 C_p \eta U^3$; therefore:

$$D = 2\sqrt{\frac{P}{\frac{1}{2}\rho\pi C_p \eta U^3}} = 28.8\ m$$

Ex4:The Darrieus (vertical axis wind turbine) that shown in Fig.(1) has a disc diameter of 20 m. A wind stream of 29 Km/hr velocity is blowing the turbine which cause rotates the turbine at 40 rev/min. For this condition, estimate:

(a) the blades speed in (m/s),

(b) the power available of wind stream in (watt),

(c) the power coefficient,

(d) the maximum axial thrust in (N).

Take the air density equal to 1.225 Kg/m^3.

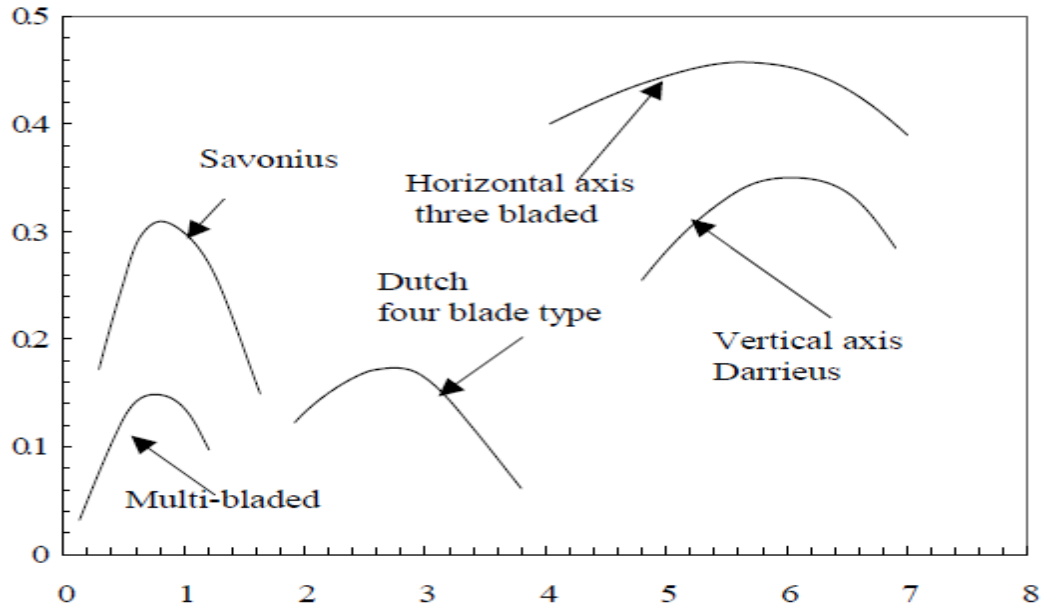

V=29 km/hr=29*1000/3600=8.05 m/sec.

N=40 rev/min, w=2πN/60=2π*40/60=4.189rad/sec.

a) u=w*r=4.189*10=41.89 m/sec.
b) P=0.5*ρ*A*V^3=0.5*1.225*π*$(20)^2$/4*$(8.05)^3$ =100379.17 watt.
c) From chart, (ω*r)/V=(4.189*10)/8.05=5.20 →Cp=0.30-0.32. not maximum value.
d) Axial thrust=889N

Ex6: An American 6 ft diameter multi-blade (HAWT) is used to pump water to a height of 10 ft through 3 in diameter cast-iron pipe. If the winds are 17.6 ft/s, estimate:

a.the power developed in (Ib.ft/s).

b.velocity behind the wind turbine disc in (ft/s).

c.the force exerted by wind on turbine disc in (Ib)

Take $\rho_{air} = 0.0023 slug / ft^3$

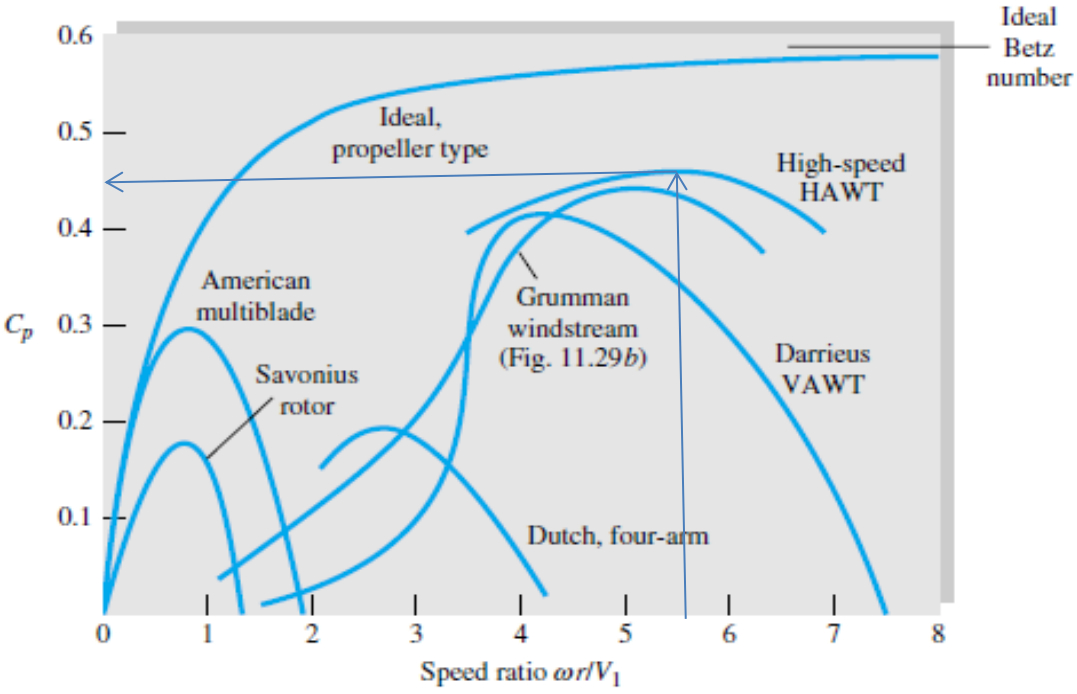

a) For best operations, $Cp_{max}=0.29$ and

$$u/V=0.9$$

then, $Pmax=0.5*0.0023*0.29*(\frac{\pi}{4}d^2)*V^3=51.4$ Ib.ft/sec

b) $V_2=1/3*V_1=5.86$ ft/s

c) $F= 0.5*0.0023*(\frac{\pi}{4}d^2)*V^2=10.07$ Ib.

Wind mill:

Consider the control volume enclosed by the slipstream boundary and planes 1 and 4. Momentum equation in the x-direction is:

$$F_x = \dot{m}_{out} u_{out_x} - \dot{m}_{in} u_{in_x} = \dot{m}(u_4 - u_1),$$

where we have employed the mass conservation equation:

$$\dot{m}_{out} = \dot{m}_{in} \Rightarrow \dot{m}_4 = \dot{m}_1 = \dot{m} = \rho u_2 A.$$

The pressure all around the control volume is atmospheric hence $F_x = F_{Rx}$, which is the force from the propeller to the fluid. The thrust force from the fluid to the propeller is $R_x = -F_{Rx}$. We can obtain another equation for F_{Rx}, if we take a control volume between sections 2 and 3, and assume that $u_2 \approx u_3$. The momentum equation is simply

$$F_x = 0 \Rightarrow F_{Rx} + F_{px} = 0 \Rightarrow F_{Rx} = -F_{px} = (p_3 - p_2)A.$$

Combining this with the momentum equation gives:

$$u_2 = \frac{u_1 + u_4}{2}$$

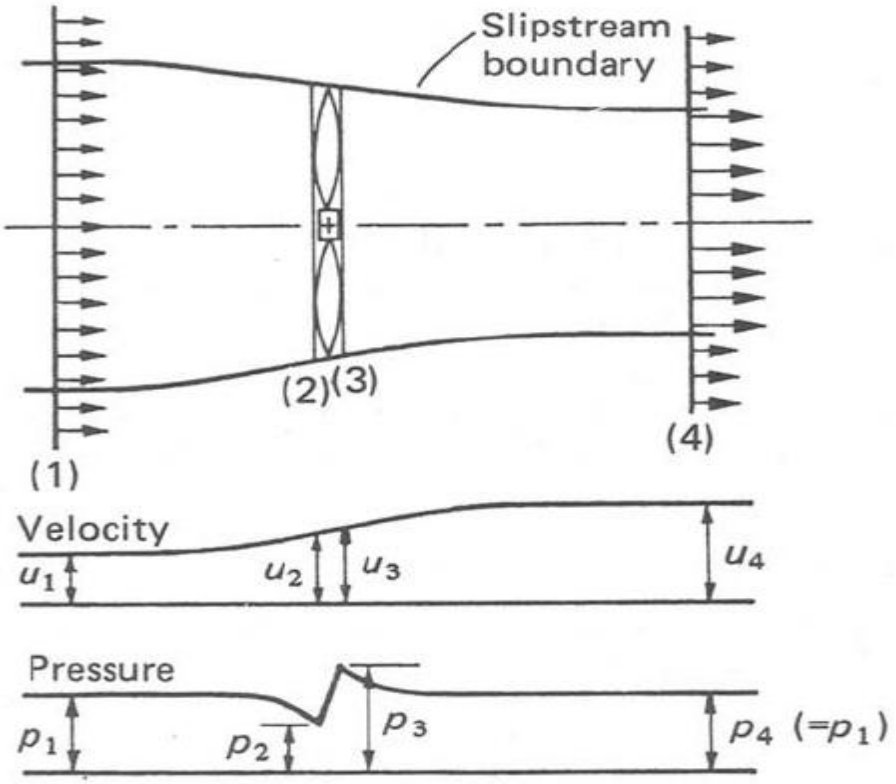

$$F_x = \rho A \frac{(u_1 + u_4)(u_4 - u_1)}{2}:$$

Ex: An ideal windmill, 12 m diameter, operates at a wind speed of 14 m/s. If the air density is 1.235 kg/m^3 , and the air velocity downstream of turbine is equal to 8.65 m/s. Determine the thrust on the windmill, and the air velocity through the disc.

Sol:

$$F_x = \rho A \frac{(u_1 + u_4)(u_4 - u_1)}{2} \quad = 1.235 \times \pi \frac{12^2}{4} \frac{\left(8.65^2 - 14^2\right)}{2} = 8460 \text{ N}$$

$$u_2 = \frac{u_1 + u_4}{2}$$

So, u_2=(14+8.65)/ (2)=11.3 m/s

11.100 One of the largest wind generators in operation today is the ERDA/NASA two-blade propeller HAWT in Sandusky, Ohio. The blades are 125 ft in diameter and reach maximum power in 19 mi/h winds. For this condition estimate (a) the power generated in kW, (b) the rotor speed in r/min, and (c) the velocity V_2 behind the rotor.

Solution: For air in Ohio (?), take $\rho \approx 0.0023$ slug/ft^3. Convert 19 mi/h = 27.9 ft/s. From Fig. 11.34 for the propeller HAWT, read optimum power coefficient and speed ratio:

$$C_{P,max} \approx 0.46 = \frac{P}{(1/2)\rho A V_1^3} = \frac{P_{max}}{(1/2)(0.0023)(\pi/4)(125)^2(27.9)^3}$$

Solve for $P_{max} \approx 1.4E6$ ft·lbf/s $\approx$ **190 kW** *Ans.* (a)

$$\frac{\omega r}{V_1}\Big|_{optimum} \approx 5.7 = \frac{\omega(125/2)}{27.9}, \quad \text{or} \quad \omega \approx 2.54 \frac{\text{rad}}{\text{s}} \times \frac{60}{2\pi} \approx \textbf{24 rpm} \quad \textit{Ans.} \text{ (b)}$$

From ideal-windmill theory, $V_{behind} = V_2 = \frac{1}{3} V_1 = \frac{27.9}{3} \approx$ **9.3 ft/s** *Ans.* (c)

4 TRANSMISSION AND GENERATOR EFFICIENCIES

The shaft power output that we have been discussing is not normally used directly, but is usually coupled to a load through a transmission or gear box. The load may be a pump, compressor, grinder, electrical generator, and so on. For purposes of illustration, we will consider the load to be an electrical generator. The basic system is then as shown in Fig. 12. We start with the power in the wind, P_w. After this power passes through the turbine, we have a mechanical power P_m at the turbine angular velocity ω_m, which is then supplied to the transmission. The *transmission output power* P_t is given by the product of the turbine output power P_m and the *transmission efficiency* η_m:

$$P_t = \eta_m P_m \qquad \text{W} \tag{12}$$

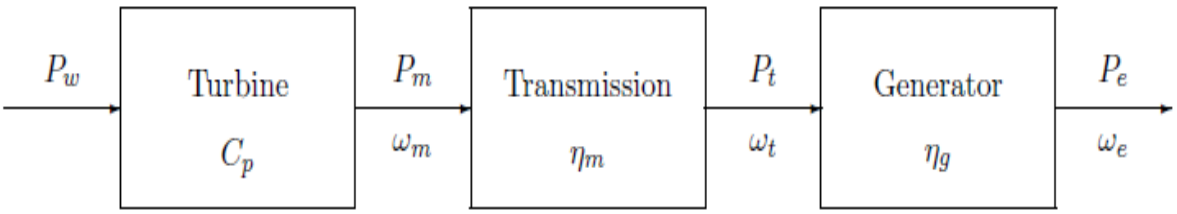

Figure 12: Wind electric system

Similarly, the generator output power P_e is given by the product of the transmission output power and the generator efficiency η_g:

$$P_e = \eta_g P_t \qquad \text{W} \tag{13}$$

Equations 9, 12, and 13 can be condensed to a single equation relating electrical power output to wind power input:

$$P_e = C_p \eta_m \eta_g P_w \qquad \text{W} \tag{14}$$

At rated wind speed, the rated electrical power output can be expressed as

- Gearbox efficiency η_{gear} – The power losses in a gearbox can be classified as load-dependent and no-load power losses. The load-dependent losses consist of gear tooth friction and bearing losses and no-load losses consist of oil churning, windage, and shaft seal losses. The planetary gearboxes, which are widely used in wind turbines, have higher power transmission efficiencies over traditional gearboxes.
- Generator efficiency η_{gen} – It is related to all electrical and mechanical losses in a wind generator, such as copper, iron, load, windage, friction, and other miscellaneous losses.
- Electric efficiency η_{ele} – It encompasses all combined electric power losses in the converter, switches, controls, and cables.

Therefore, the total power conversion efficiency from wind to electricity η_t is the production of these parameters, i.e.:

$$\eta_t = C_p \eta_{gear} \eta_{gen} \eta_{ele} \tag{17}$$

The effective power output from a wind turbine to feed into a grid becomes

$$P_{eff} = C_p \eta_{gear} \eta_{gen} \eta_{ele} P_w = \eta_t P_w = \tfrac{1}{2}(\eta_t \rho A \overline{u}^3) \tag{18}$$

Example

The Sandia 17-m Darrieus is rated at 60 kW at 15.5 m/s and 52.5 r/min, and at 25 kW at 11 m/s and 42 r/min. The area A is 187 m^2. Compute the rated overall efficiency at each rating and standard conditions.

At standard conditions, $\rho/2 = 0.647$. Inserting this value in Eqs. 15 and 16 we get

$$\eta_{0,25} = \frac{25,000}{0.647(187)(11)^3} = 0.155$$

$$\eta_{0,60} = \frac{60,000}{0.647(187)(15.5)^3} = 0.133$$

4.1.3 Wind power density

Wind power density is a comprehensive index in evaluating the wind resource at a particular site. It is the available wind power in airflow through a perpendicular cross-sectional unit area in a unit time period. The classes of wind power density at two standard wind measurement heights are listed in Table 1.

Some of wind resource assessments utilize 50 m towers with sensors installed at intermediate levels (10 m, 20 m, etc.). For large-scale wind plants, class rating of 4 or higher is preferred.

Table 1: Classes of wind power density [17].

	10 m height		50 m height	
Wind power class	Wind power density (W/m^2)	Mean wind speed (m/s)	Wind power density (W/m^2)	Mean wind speed (m/s)
1	<100	<4.4	<200	<5.6
2	100–150	4.4–5.1	200–300	5.6–6.4
3	150–200	5.1–5.6	300–400	6.4–7.0
4	200–250	5.6–6.0	400–500	7.0–7.5
5	250–300	6.0–6.4	500–600	7.5–8.0
6	300–350	6.4–7.0	600–800	8.0–8.8
7	>400	>7.0	>800	>8.8

4.2.6 Wind shear

Wind shear is a meteorological phenomenon in which wind increases with the height above the ground. The effect of height on the wind speed is mainly due to roughness on the earth's surface and can be estimated using the Hellmann power equation that relates wind speeds at two different heights [33]:

$$u(z) = u(z_0)\left(\frac{z}{z_0}\right)^{\alpha} \tag{15}$$

where z is the height above the earth's surface, z_0 is the reference height for which wind speed $u(z_0)$ is known, and α is the wind shear coefficient. In practice, α depends on a number of factors, including the roughness of the surrounding landscape, height, time of day, season, and locations. The wind shear coefficient is generally lower in daytime and higher at night. Empirical results indicate that wind shear often follows the "1/7 power law" (i.e. $\alpha = 1/7$). The values of wind shear coefficient for different surface roughness are provided in [34].

Because the power output of wind turbine strongly depends on the wind speed at the hub height, modern wind turbines are built at the height greater than 80 m, for capturing more wind energy and lowering cost per unit power output.

Problem 1: An anemometer mounted at a height of 10 *m* above a surface (Hellman exponent $\alpha = 0.2$) shows a wind speed of 10 *m/s* at the temperature of 0°C, when the air density 1.291 kg/m^3

(*i*) **Evaluate** the wind power density in W/m^2 where the anemometer is mounted (20 points)

(*ii*) **Determine** the wind speed in *m/s* at the height of 40 *m* (20 points)

(*iii*) **Estimate** the wind power density in terms of W/m^2 at the height of 40 *m* if the temperature is 30°C at the height of 40 *m*. (20 points)

If air density at elevation of 40 m is 1.16 kg/m^3

i) Power density $= \frac{P}{A} = \frac{1}{2}\rho v^3 = \frac{1}{2}(1.291)(10)^3 = 645\ W/m^2$

ii) $\left(\frac{v_{40}}{v_{10}}\right) = \left(\frac{H_{40}}{H_{10}}\right)^{\alpha} \Rightarrow v_{40} = v_{10}\left(\frac{H_{40}}{H_{10}}\right)^{\alpha} = 10\left(\frac{40}{10}\right)^{0.2} = 13.2\ m/s$

Power density $= \frac{P}{A} = \frac{1}{2}\left(\rho_{30°C,40m}\right) v_{40m}^3 = \frac{1}{2}(1.16)(13.2)^3 = 1331\ W/m^2$

Ex3: A 30 m diameter wind turbine is placed on a 50 m tower in terrain with a power law coefficient (α) of 0.2. Find the ratio of available power in the wind at the highest point the rotor reaches to its lowest point.

D = 30 m, hub height = 50 m, α = 0.2

$z_{low} = 50 - 15 = 35$ m

$z_{high} = 50 + 15 = 65$ m

The ratio of the wind speeds is:

$$\frac{U(z_{high})}{U(z_{low})} = \left(\frac{z_{high}}{z_{low}}\right)^{\alpha} = \left(\frac{65}{35}\right)^{\alpha} = 1.13$$

The ratio of the powers is the cube of the ratio of the wind speeds:

$$\frac{P(z_{high})}{P(z_{low})} = \left[\frac{U(z_{high})}{U(z_{low})}\right]^3 = 1.13^3 = 1.44$$

HYDRAULIC TURBINES

Introduction:

The device which converts hydraulic energy into mechanical energy or vice versa is known as ***Hydraulic Machines.*** The hydraulic machines which convert hydraulic energy into mechanical energy are known as ***Turbines*** and that convert mechanical energy into hydraulic energy is known as ***Pumps.***

Fig. shows a general layout of a hydroelectric plant.

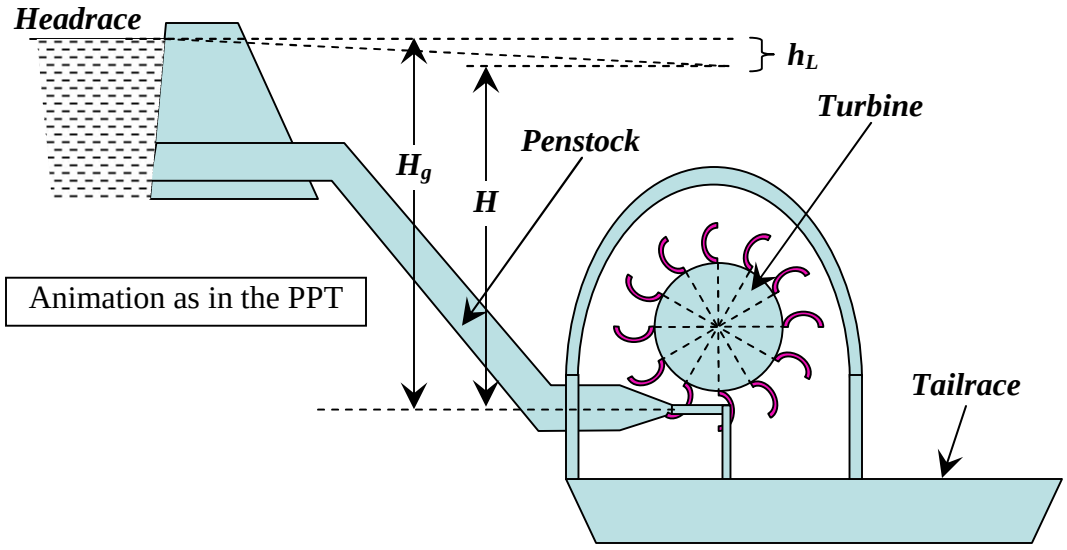

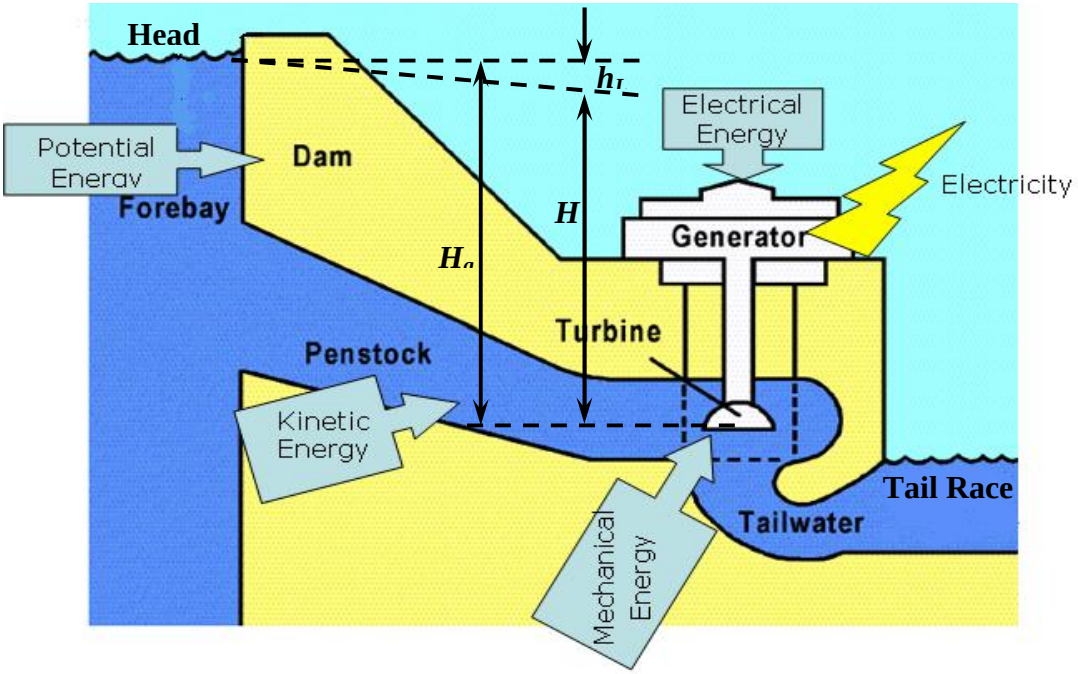

It consists of the following:

1. A ***Dam*** constructed across a river or a channel to store water. The reservoir is also known as ***Headrace.***
2. Pipes of large diameter called ***Penstocks*** which carry water under pressure from storage reservoir to the turbines. These pipes are usually made of steel or reinforced concrete.
3. ***Turbines*** having different types of vanes or buckets or blades mounted on a wheel called runner.
4. ***Tailrace*** which is a channel carrying water away from the turbine after the water has worked on the turbines. The water surface in the tailrace is also referred to as tailrace.

Important Terms:

Gross Head (H_g): It is the vertical difference between headrace and tailrace.

Net Head:(H): Net head or effective head is the actual head available at the inlet of the to work on the turbine.

$\boldsymbol{H = H_g - h_L}$

Where $\boldsymbol{h_L}$ is the total head loss during the transit of water from the headrace to tailrace which is mainly head loss due to friction, and is given by

$$h_f = \frac{4 f L V^2}{2 g d}$$

Where ***f*** is the coefficient of friction of penstock depending on the type of material of penstock

L is the total length of penstock

V is the mean flow velocity of water through the penstock

D is the diameter of penstock and

g is the acceleration due to gravity

TYPES OF EFFICIENCIES

Depending on the considerations of input and output, the efficiencies can be classified as

(i) Hydraulic Efficiency
(ii) Mechanical Efficiency
(iii) Overall efficiency

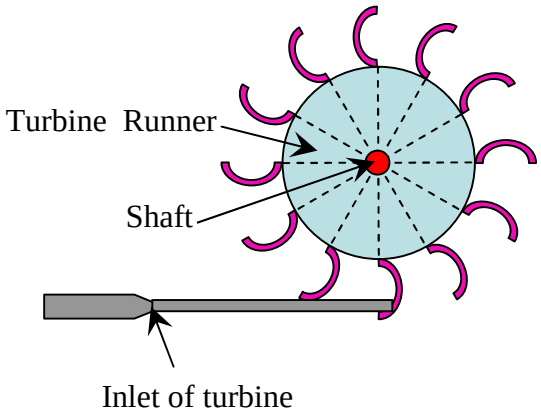

(i) Hydraulic Efficiency: (η_h)

It is the ratio of the power developed by the runner of a turbine to the power supplied at the inlet of a turbine. Since the power supplied is hydraulic, and the probable loss is between the striking jet and vane it is rightly called hydraulic efficiency.

If R.P. is the Runner Power and W.P. is the Water Power

$$\eta_h = \frac{\text{R.P.}}{\text{W.P.}} \qquad (01)$$

(ii) Mechanical Efficiency: (η_m)

It is the ratio of the power available at the shaft to the power developed by the runner of a turbine. This depends on the slips and other mechanical problems that will create a loss of energy between the runner in the annular area between the nozzle and spear, the amount of water reduces as the spear is pushed forward and vice-versa.

and shaft which is purely mechanical and hence mechanical efficiency.

If S.P. is the Shaft Power

$$\eta_m = \frac{\text{S.P.}}{\text{R.P.}} \qquad (02)$$

(iii) Overall Efficiency: (η)

It is the ratio of the power available at the shaft to the power supplied at the inlet of a turbine. As this covers overall problems of losses in energy, it is known as overall efficiency. This depends on both the hydraulic losses and the slips and other mechanical problems

that will create a loss of energy between the jet power supplied and the power generated at the shaft available for coupling of the generator.

$$\eta = \frac{\text{S.P.}}{\text{W.P.}}$$

(03)

From Eqs 1,2 and 3, we have

$$\eta = \eta_h \times \eta_m$$

Classification of Turbines

The hydraulic turbines can be classified based on type of energy at the inlet, direction of flow through the vanes, head available at the inlet, discharge through the vanes and specific speed. They can be arranged as per the following table:

Turbine		Type of energy	Head	Discharge	Direction of flow	Specific Speed
Name	Type					
Pelton Wheel	Impulse	Kinetic	High Head > 250m to 1000m	Low	Tangential to runner	Low <35 Single jet 35 – 60 Multiple jet
Francis Turbine	Reaction Turbine	Kinetic + Pressure	Medium 60 m to 150 m	Medium	Radial flow	Medium 60 to 300
					Mixed Flow	
Kaplan Turbine			Low < 30 m	High	Axial Flow	High 300 to 1000

As can be seen from the above table, any specific type can be explained by suitable construction of sentences by selecting the other items in the table along the row.

PELTON WHEEL OR TURBINE

Pelton wheel, named after an eminent engineer, is an impulse turbine wherein the flow is tangential to the runner and the available energy at the entrance is completely kinetic energy. Further, it is preferred at a very high head and low discharges with low specific speeds. The pressure available at the inlet and the outlet is atmospheric.

Animation:
(i) The water jet has to reduce and increase as the spear is brought forward and backward
(ii) The wheel has to rotate as the jet strikes

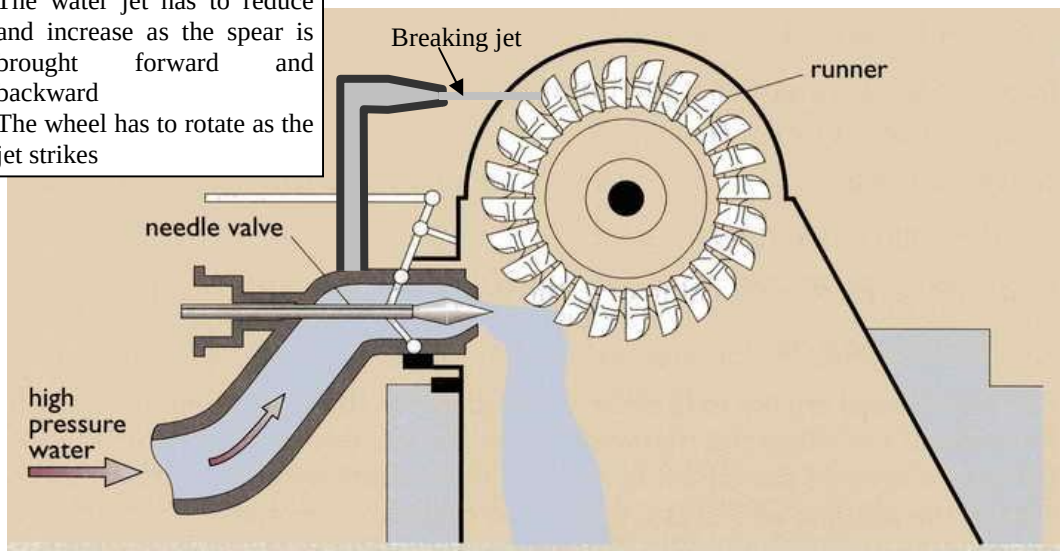

The main components of a Pelton turbine are:

(i) *Nozzle and flow regulating arrangement:*

Water is brought to the hydroelectric plant site through large penstocks at the end of which there will be a nozzle, which converts the pressure energy completely into kinetic energy. This will convert the liquid flow into a high-speed jet, which strikes the buckets or vanes mounted on the runner, which in-turn rotates the runner of the turbine. The amount of water striking the vanes is controlled by the forward and backward motion of the spear. As the water is flowing in the annular area between the annular area between the

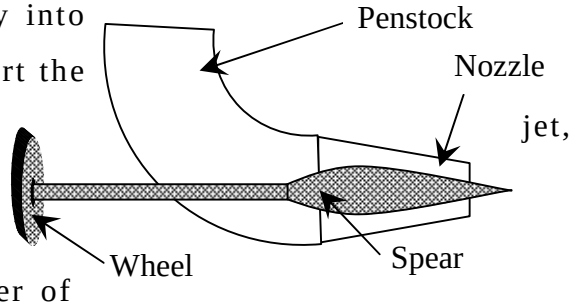

nozzle opening and the spear, the flow gets reduced as the spear moves forward and vice-versa.

(ii) *Runner with buckets:*

Runner is a circular disk mounted on a shaft on the periphery of

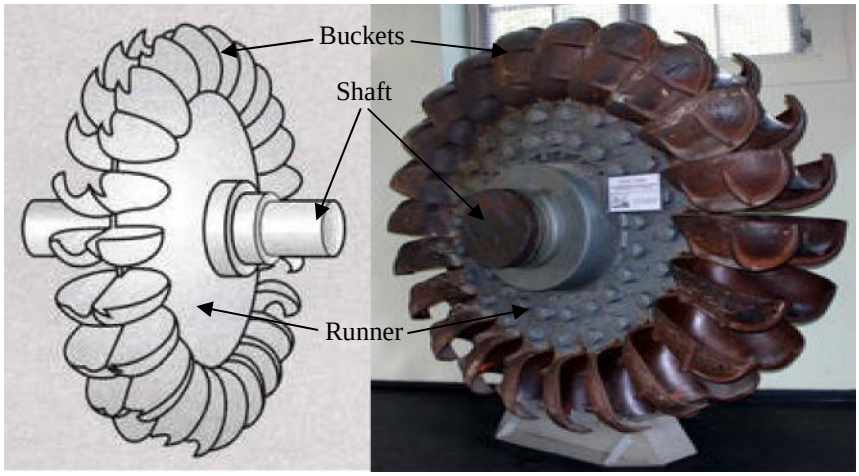

which a number of buckets are fixed equally spaced as shown in Fig. The buckets are made of cast-iron cast-steel, bronze or stainless steel depending upon the head at the inlet of the turbine. The water jet strikes the bucket on the splitter of the bucket and gets deflected through (~) 160-170^0.

(iii) *Casing:*

It is made of cast-iron or fabricated steel plates. The main function of the casing is to prevent splashing of water and to discharge the water into tailrace.

(iv) *Breaking jet:*

Even after the amount of water striking the buckets is completely stopped, the runner goes on rotating for a very long time due to inertia. To stop the runner in a short time, a small nozzle is provided which directs the jet of water on the back of bucket with which the rotation of the runner is reversed. This jet is called as breaking jet.

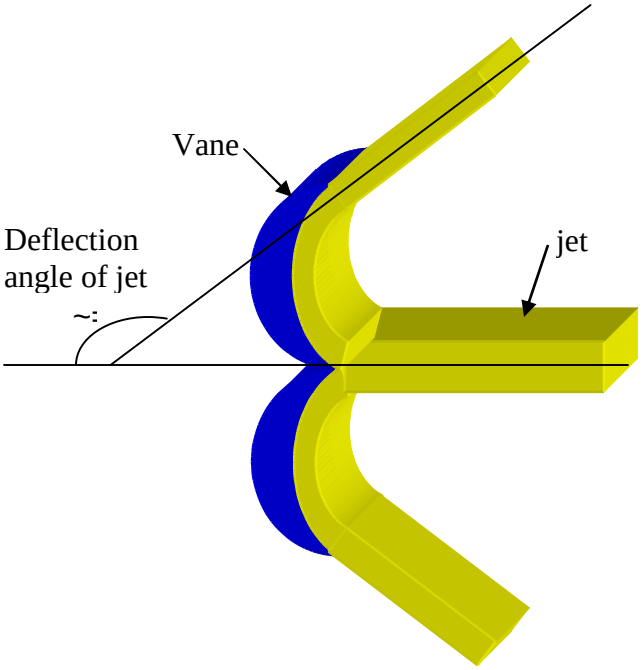

3 D Picture of a jet striking the splitter and getting split in to two parts and deviating.

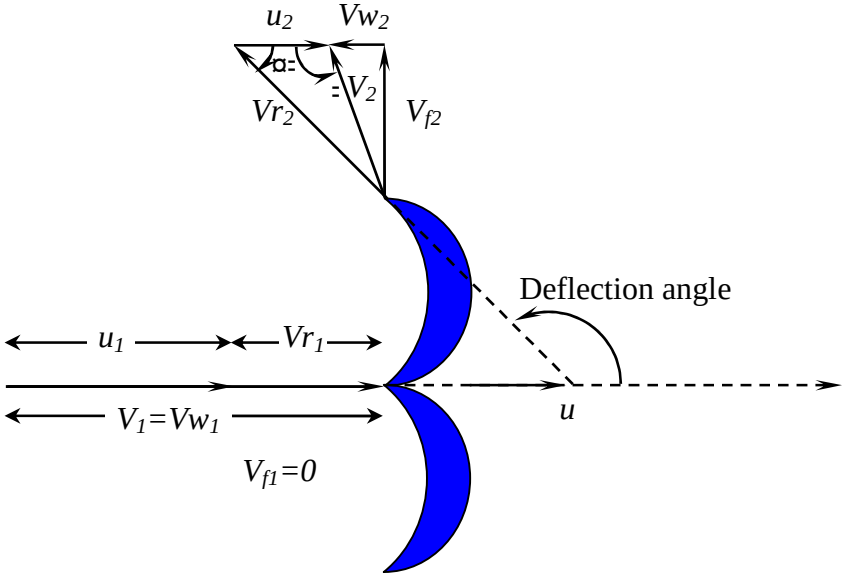

Velocity triangles for the jet striking the bucket

From the impulse-momentum theorem, the force with which the jet strikes tthe bucket along the direction of vane is given by

F_x = rate of change of momentum of the jet along the direction of vane motion

F_x = (Mass of water / second) x change in velocity along the *x* direction

$$= \rho a V_1 [V_{w1} - (-V_{w2})]$$

$$= \rho a V_1 [V_{w1} + V_{w2}]$$

Work done per second by the jet on the vane is given by the product of Force exerted on the vane and the distance moved by the vane in one second

W.D./S = F_x x u

$$= \rho a V_1 [V_{w1} + V_{w2}] u$$

Input to the jet per second = Kinetic energy of the jet per second

$$= \frac{1}{2} \rho a V_1^3$$

Efficiency of the jet = $\frac{Output/second}{Input/second} = \frac{Workdone/second}{Input/second}$

$$\eta = \frac{\rho a V_1 [V_{w1} + V_{w2}] u}{\frac{1}{2} \rho a V_1^3}$$

$$\eta = \frac{2u[V_{w1} + V_{w2}]}{V_1^2}$$

From inlet velocity triangle, $V_{w1} = V_1$

Assuming no shock and ignoring frictional losses through the vane, we have $V_{r1} = V_{r2} = (V_1 - u_1)$

In case of Pelton wheel, the inlet and outlet are located at the same radial distance from the centre of runner and hence $u_1 = u_2 = u$

From outlet velocity triangle, we have $V_{w2} = V_{r2} Cos\phi - u_2$

$$= (V_1 - u) Cos\phi - u$$

$$F_x = \rho a V_1 [V_1 + (V_1 - u) Cos\phi - u]$$

$$F_x = \rho a V_1 (V_1 - u)[1 + Cos\phi]$$

Substituting these values in the above equation for efficiency, we have

$$\eta = \frac{2u[V_1 + (V_1 - u)\cos\phi - u]}{V_1^2}$$

$$\eta = \frac{2u}{V_1^2}[(V_1 - u) + (V_1 - u)\cos\phi]$$

$$\eta = \frac{2u}{V_1^2}(V_1 - u)[1 + \cos\phi]$$

The above equation gives the efficiency of the jet striking the vane in case of Pelton wheel.

To obtain the maximum efficiency for a given jet velocity and vane angle, from maxima-minima, we have

$$\frac{d\eta}{du} = 0$$

$$\Rightarrow \frac{d\eta}{du} = \frac{2}{V_1^2}[1 + \cos\phi]\frac{d}{du}\left(uV_1 - u^2\right) = 0$$

$$V_1 - 2u = 0$$

or $$u = \frac{V_1}{2}$$

i.e. When the bucket speed is maintained at half the velocity of the jet, the efficiency of a Pelton wheel will be maximum. Substituting we get,

$$\eta_{max} = \frac{2u}{(2u)^2}(2u - u)[1 + \cos\phi]$$

$$\eta_{max} = \frac{1}{2}[1 + \cos\phi]$$

From the above it can be seen that more the value of cos¤, more will be the efficiency. Form maximum efficiency, the value of cos¤ should be 1 and the value of ¤ should be 0^0. This condition makes the jet to completely deviate by 180^0 and this, forces the jet striking the bucket to strike the successive bucket on the back of it acting like a breaking jet. Hence to avoid this situation, at least a small angle of ¤ $=5^0$ should be provided.

Dec-06/Jan07

6 a.i)Sketch the layout of a PELTON wheel turbine showing the details of nozzle, buckets and wheel when the turbine axis is horizontal(04)

ii) Obtain an expression for maximum-efficiency of an impulse turbine. (06)

July 06

6 (a) With a neat sketch explain the layout of a hydro-electric plant(06)

(b) With a neat sketch explain the parts of an Impulse turbine. (06)

Jan 06

6 (a) What Is specific speed of turbine and state Its significance. (04)

(b) Draw a neat sketch of a hydroelectric plant and mention the function of each component. (08)

Jan 05

6 (a) Classify the turbines based on head, specific speed and hydraulic actions. Give examples for each. (06)

(b) What is meant by Governing of turbines? Explain with a neat sketch the governing of an impulse turbine (06)

July 04

5 (a) Explain the classification of turbines. (08)

The head at the base of the nozzle of a Pelton wheel is 640 m. The outlet vane angle of the bucket is 15°. The relative velocity at the outlet is reduced by 15% due to friction along the vanes. If the discharge at outlet is without whirl find the ratio of bucket speed to the jet speed. If the jet diameter is 100 mm while the wheel diameter is 1.2 m, find the speed of the turbine in rpm, the force exerted by the jet on the wheel, the Power developed and the hydraulic efficiency. Take C_v=0.97.

Solution:

H = 640 m; ¤=15°; V_{r1} = 0.85 V_{r2}; V_{w2} = 0; d = 100 mm; D = 1.2 m;

C_v = 0.97; K_u = ?; N = ?; F_x = ?; P = ?; ¦$_h$ = ?

We know that the absolute velocity of jet is given by

$$V = C_v\sqrt{2gH} = 0.97\sqrt{2\times10\times640} = 109.74\,\text{m/s}$$

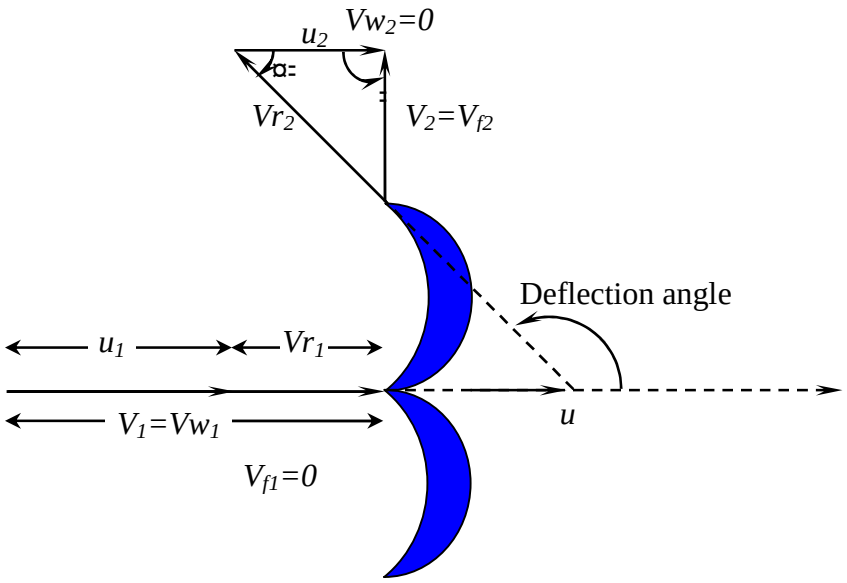

Let the bucket speed be u

Relative velocity at inlet = V_{r1} = V_1-u = 109.74-u

Relative velocity at outlet = V_{r2} = (1-0.15)V_{r1} = 0.85(109.74-u)

But V_{r2}cos¤ = u ⇨ 0.85(109.74-u)cos15

Hence u = 49.48 m/s

But $u = \frac{®\,D\,N}{60}$ and hence

$$N = \frac{60u}{® D} = \frac{60 \times 49.48}{® \times 1.2} = 787.5 \text{ rpm (Ans)}$$

Jet ratio = $m = \frac{u}{V} = \frac{49.48}{109.74} = 0.45$

Weight of water supplied = γ Q = $10 \times 1000 \times \frac{®}{4} \times 0.1^2 \times 109.74^2 = 8.62$ kN/s

Force exerted = $F_x = ° a V_1 (V_{w1} - V_{w2})$

But $V_{w1} = V_1$ and $V_{w2} = 0$ and hence

$$F_x = 1000 \times \frac{®}{4} \times 0.1^2 (109.74)^2 = 94.58 \text{ kN}$$

Work done/second = F_x x u = 94.58 x 49.48 = 4679.82 kN/s

Kinetic Energy/second = $\frac{1}{2} ° a V_1^3 = \frac{1}{2} \times 1000 \times \frac{®}{4} \times 0.1^2 \times 109.74^3 = 5189.85$ kN/s

Hydraulic Efficiency = $¦_h = \frac{\text{Work done/s}}{\text{Kinetic Energy/s}} = \frac{4679.82}{5189.85} \times 100 = 90.17\%$

Dec 06-Jan 07

A PELTON wheel turbine is having a mean runner diameter of 1.0 m and is running at 1000 rpm. The net head is 100.0 m. If the side clearance is 20° and discharge is 0.1 m^3/s, find the power available at the nozzle and hydraulic efficiency of the turbine. (10)

Solution:

D = 1.0 m; N = 1000 rpm; H = 100.0 m; ¤ = 20°; Q = 0.1 m^3/s; WD/s = ? and $¦_h$ = ?

Assume $C_v = 0.98$

We know that the velocity of the jet is given by

$$V = C_v \sqrt{2gH} = 0.98 \sqrt{2 \times 10 \times 1000} = 43.83 \text{ m/s}$$

The absolute velocity of the vane is given by

$$u = \frac{® DN}{60} = \frac{® \times 1 \times 1000}{60} = 52.36 \text{ m/s}$$

This situation is impracticable and hence the data has to be modified. Clearly state the assumption as follows:

Assume H = 700 m (Because it is assumed that the typing and seeing error as 100 for 700)

Absolute velocity of the jet is given by

$V = C_v\sqrt{2gH} = 0.98\sqrt{2\times10\times700} = 115.96$ m/s

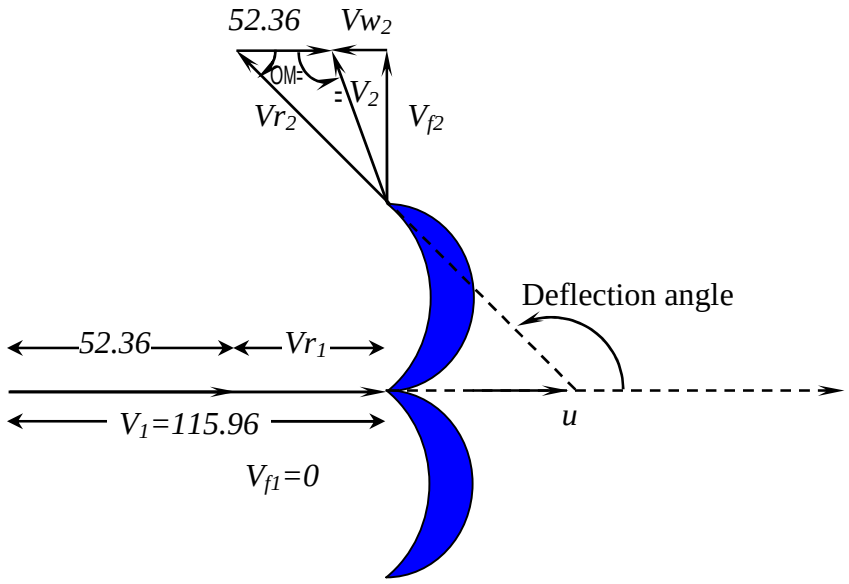

Power available at the nozzle is the given by work done per second

WD/second = ¥ Q H = ° g Q H = 1000x10x0.1x700 = 700 kW

Hydraulic Efficiency is given by

$$\eta_h = \frac{2u}{V_1^2}(V_1 - u)[1+\cos\alpha] = \frac{2\times52.36}{115.96^2}(115.96-52.36)(1+\cos 20) = 96.07\%$$

July 06

A Pelton wheel has a mean bucket speed of 10 m/s with a jet of water flowing at the rate of 700 lps under a head of 30 m. The buckets deflect the jet through an angle of 160°. Calculate the power given by water to the runner and the hydraulic efficiency of the turbine. Assume the coefficient of nozzle as 0.98. (08)

Solution:

u = 10 m/s; Q = 0.7 m^3/s; ¤ = 180-160 = 20^o; H = 30 m; C_v = 0.98;

WD/s = ? and ¦$_h$ = *?*

Assume g = $10 m/s^2$

$V = C_v\sqrt{2gH} = 0.98\sqrt{2\times10\times30} = 24$ m/s

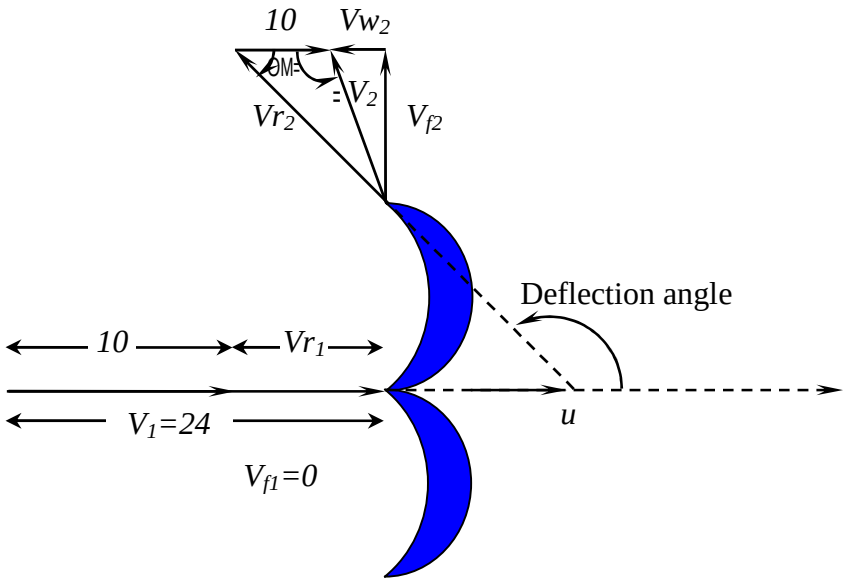

$V_{r1} = V_1 - u = 24 - 10 = 14$ m/s

Assuming no shock and frictional losses we have $V_{r1} = V_{r2} = 14$ m/s

$V_{w2} = V_{r2}\ Cos\ ¤ - u = 14$ x $Cos\ 20 - 10 = 3.16$ m/s

We know that the Work done by the jet on the vane is given by

WD/s $= \rho a V_1[V_{w1} + V_{w2}]u = \rho Qu[V_{w1} + V_{w2}]$ as $Q = aV_1$

$= 1000\times0.7\times10[24 + 3.16] = 190.12$ kN-m/s (Ans)

IP/s = KE/s $= \frac{1}{2}\rho aV_1^3 = \frac{1}{2}\rho QV_1^2 = \frac{1}{2}\times1000\times0.7\times24^2 = 201.6$ kN-m/s

Hydraulic Efficiency = Output/Input = 190.12/201.6 = 94.305%

It can also be directly calculated by the derived equation as

$\eta_h = \frac{2u}{V_1^2}(V_1 - u)[1 + \cos¤] = \frac{2\times10}{24^2}(24 - 10)[1 + \cos 20] = 94.29\%$ (Ans)

Jan 06

A Pelton wheel has to develop 13230 kW under a net head of 800 m while running at a speed of 600 rpm. If the coefficient of Jet C_y = 0.97, speed ratio ϕ = 0.46 and the ratio of the Jet diameter is 1 /16 of wheel diameter. Calculate

i) Pitch circle diameter ii) the diameter of jet

iii) the quantity of water supplied to the wheel

iv) the number of Jets required.

Assume over all efficiency as 85%. (08)

Solution:

P = 13239 kW; H = 800 m; N = 600 rpm; C_v = 0.97; ¤ = 0.46 (Speed ratio)

d/D = 1/16; ¦$_o$ = 0.85; D = ?; d = ?; n = ?;

Assume g = 10 m/s^2 and ° = 1000 kg/m^3

We know that the overall efficiency is given by

$$¦_o = \frac{Output}{Input} = \frac{P}{¥ Q H} = \frac{13239 \times 10^3}{10 \times 1000 \times Q \times 800} = 0.85$$

Hence Q = 1.947 m^3/s (Ans)

Absolute velocity of jet is given by

$$V = C_v \sqrt{2 g H} = 0.97 \sqrt{2 \times 10 \times 800} = 122.696 \text{ m/s}$$

Absolute velocity of vane is given by

$$u = ¤ \sqrt{2 g H} = 0.46 \sqrt{2 \times 10 \times 800} = 58.186 \text{ m/s}$$

The absolute velocity of vane is also given by

$u = \frac{® D N}{60}$ and hence

$$D = \frac{60 u}{® N} = \frac{60 \times 58.186}{® \times 600} = 1.85 m \text{ (Ans)}$$

$$d = \frac{1.85}{16} = 115.625 \text{ mm (Ans)}$$

Discharge per jet = $q = \frac{®}{4} d^2 \times V = \frac{®}{4} \times 0.115625^2 \times 122.696 = 1.288$ m^3/s

No. of jets = $n = \frac{Q}{q} = \frac{1.947}{1.288} \approx 2$ (Ans)

July 05

Design a Pelton wheel for a head of 80m. and speed of 300 RPM. The Pelton wheel develops 110 kW. Take co-eficient of velocity= 0.98, speed ratio= 0.48 and overall efficiency = 80%. (10)

Solution:

H = 80 m; N = 300 rpm; P = 110 kW; C_v = 0.98, K_u=0.48; ¦$_o$ = *0.80*

Assume g = 10 m/s^2 and ° = 1000 kg/m^3

We know that the overall efficiency is given by

$$\eta_o = \frac{Output}{Input} = \frac{P}{\rho g Q H} = \frac{110 \times 10^3}{10 \times 1000 \times Q \times 80} = 0.8$$

Hence Q = 0.171875 m^3/s

Absolute velocity of jet is given by

$$V = C_v \sqrt{2 g H} = 0.98 \sqrt{2 \times 10 \times 80} = 39.2 \text{ m/s}$$

Absolute velocity of vane is given by

$$u = \phi \sqrt{2 g H} = 0.48 \sqrt{2 \times 10 \times 80} = 19.2 \text{ m/s}$$

The absolute velocity of vane is also given by

$u = \frac{\pi D N}{60}$ and hence

$$D = \frac{60u}{\pi N} = \frac{60 \times 19.2}{\pi \times 300} = 1.22 m \text{ (Ans)}$$

Single jet Pelton turbine is assumed

The diameter of jet is given by the discharge continuity equation

$$Q = \frac{\pi}{4} d^2 \times V = \frac{\pi}{4} \times d^2 \times 39.2 \Rightarrow 0.171875$$

Hence d = 74.7 mm

The design parameters are

Single jet

Pitch Diameter = 1.22 m

Jet diameter = 74.7 mm

Jet Ratio = $m = \frac{D}{d} = \frac{1.22}{0.0747} = 16.32$

No. of Buckets = 0.5xm + 15 = 24

Jan 05

It is desired to generate 1000 kW of power and survey reveals that 450 m of static head and a minimum flow of 0.3 m^3/s are available. Comment whether the task can be accomplished by installing a Pelton wheel run at 1000 rpm and having an overall efficiency of 80%.

Further, design the Pelton wheel assuming suitable data for coefficient of velocity and coefficient of drag. (08)

Solution:

P = 1000 kW; H = 450 m; Q = 0.3 m^3/s; N = 1000 rpm; η_o = 0.8

Assume C_v = 0.98; K_u=0.45; ϕ = 1000 kg/m^3; g = 10 m/s^2

$$\eta_o = \frac{Output}{Input} = \frac{P}{\rho g Q H} = \frac{1000 \times 10^3}{10 \times 1000 \times 0.3 \times 450} = 0.74$$

For the given conditions of P, Q and H, it is not possible to achieve the desired efficiency of 80%.

To decide whether the task can be accomplished by a Pelton turbine compute the specific speed N_s

$$N_s = \frac{N\sqrt{P}}{H^{5/4}};$$

where N is the speed of runner, P is the power developed in kW and H is the head available at the inlet.

$$N_s = \frac{1000\sqrt{1000}}{450^{5/4}} = 15.25 < 35$$

Hence the installation of single jet Pelton wheel is justified.

Absolute velocity of jet is given by

$$V = C_v\sqrt{2gH} = 0.98\sqrt{2 \times 10 \times 450} = 92.97 \text{ m/s}$$

Absolute velocity of vane is given by

$$u = \phi\sqrt{2gH} = 0.48\sqrt{2 \times 10 \times 80} = 19.2 \text{ m/s}$$

The absolute velocity of vane is also given by

$u = \frac{\pi DN}{60}$ and hence

$$D = \frac{60u}{\pi N} = \frac{60 \times 19.2}{\pi \times 300} = 1.22m \text{ (Ans)}$$

Single jet Pelton turbine is assumed

The diameter of jet is given by the discharge continuity equation

$$Q = \frac{®}{4} d^2 \times V = \frac{®}{4} \times d^2 \times 39.2 \Rightarrow 0.171875$$

Hence d = 74.7 mm

The design parameters are

Single jet

Pitch Diameter = 1.22 m

Jet diameter = 74.7 mm

Jet Ratio = $m = \frac{D}{d} = \frac{1.22}{0.0747} = 16.32$

No. of Buckets = 0.5xm + 15 = 24

July 04

A double jet Pelton wheel develops 895 MKW with an overall efficiency of 82% under a head of 60m. The speed ratio = 0.46, jet ratio = 12 and the nozzle coefficient = 0.97. Find the jet diameter, wheel diameter and wheel speed in RPM. (12)

Solution:

No. of jets = n = 2; P = 895 kW; ¦$_o$ = 0.82; H = 60 m; K_u = 0.46; m = 12; C_v = 0.97; D = ?; d = ?; N = ?

We know that the absolute velocity of jet is given by

$$V = C_v \sqrt{2gH} = 0.97\sqrt{2 \times 10 \times 60} = 33.6 \text{ m/s}$$

The absolute velocity of vane is given by

$$u = K_u \sqrt{2gH} = 0.46\sqrt{2 \times 10 \times 60} = 15.93 \text{ m/s}$$

Overall efficiency is given by

$$¦_o = \frac{P}{¥ QH} \text{ and hence } Q = \frac{P}{¥ ¦ H} = \frac{895 \times 10^3}{10 \times 10^3 \times 0.82 \times 60} = 1.819 \text{ m}^3/\text{s}$$

Discharge per jet = $q = \frac{Q}{n} = \frac{1.819}{2} = 0.9095 \text{ m}^3/\text{s}$

From discharge continuity equation, discharge per jet is also given by

$$q = \frac{® d^2}{4} V = \frac{® d^2}{4} \times 33.6 \Rightarrow 0.9095$$

$$d = 0.186 m$$

Further, the jet ratio $m = 12 = \frac{D}{d}$

Hence D = 2.232 m

Also $u = \frac{® D N}{60}$ and hence $N = \frac{60u}{® D} = \frac{60 \times 15.93}{® \times 2.232} = 136$ rpm

Note: Design a Pelton wheel: Width of bucket = 5d and depth of bucket is 1.2d

The following data is related to a Pelton wheel:

Head at the base of the nozzle = 80m; Diameter of the jet = 100 mm; Discharge of the nozzle = 0.3m^3/s; Power at the shaft = 206 kW; Power absorbed in mechanical resistance = 4.5 kW. Determine (i) Power lost in the nozzle and (ii) Power lost due to hydraulic resistance in the runner.

Solution:

H = 80 m; d = 0.1m; a = ¼ ®d^2 = 0.007854 m^2; Q = 0.3 m^3/s; SP = 206 kW; Power absorbed in mechanical resistance = 4.5 kW.

From discharge continuity equation, we have,

$Q = a$ x V = 0.007854 x V ⇨0.3

V = 38.197 m/s

Power at the base of the nozzle = ° g Q H

= 1000 x 10 x 0.3 x 80 = 240 kW

Power corresponding to the kinetic energy of the jet = ½ ° a V^3

= 218.85 kW

(i) Power at the base of the nozzle = Power of the jet + Power lost in the nozzle

Power lost in the nozzle = 240 — 218.85 = 21.15 kW (Ans)

(ii) Power at the base of the nozzle = Power at the shaft + Power lost in the (nozzle + runner + due to mechanical resistance)

Power lost in the runner = 240 – (206 + 21.15 + 4.5) = 5.35 kW (Ans)

The water available for a Pelton wheel is 4 m^3/s and the total head from reservoir to the nozzle is 250 m. The turbine has two runners with two jets per runner. All the four jets have the same diameters. The pipeline is 3000 m long. The efficiency if power transmission through the pipeline and the nozzle is 91% and efficiency of each runner is 90%. The velocity coefficient of each nozzle is 0.975 and coefficient of friction *4f* for the pipe is 0.0045. Determine:

(i) The power developed by the turbine; (ii) The diameter of the jet and (iii) The diameter of the pipeline.

Solution:

Q = 4 m^3/s; H_g = 250 m; No. of jets = n = 2 x 2 = 4; Length of pipe = l = 3000 m; Efficiency of the pipeline and the nozzle = 0.91 and Efficiency of the runner = η_h = 0.9; C_v = 0.975; $4f$ = 0.0045

Efficiency of power transmission through pipelines and nozzle =

$$\eta = \frac{H_g - h_f}{H_g} \Rightarrow 0.91 = \frac{250 - h_f}{250}$$

Hence h_f = 22.5 m

Net head on the turbine = $H = H_g - h_f$ = 227.5 m

Velocity of jet = $V_1 = C_v\sqrt{2gH} = 0.975\sqrt{2\times 10\times 227.5} = 65.77$ m/s

(i) Power at inlet of the turbine = WP = Kinetic energy/second = ½ ° a V^3

WP = ½ x 4 x 65.77^2 = 8651.39 kW

$$\eta_h = \frac{\text{Power developed by turbine}}{\text{WP}} = \frac{\text{Power developed by turbine}}{8651.39} \Rightarrow 0.9$$

Hence power developed by turbine = 0.9 x 8651.39 = 7786.25 kW (Ans)

(ii) Discharge per jet = $q = \dfrac{\text{Total discharge}}{\text{No. of jets}} = \dfrac{4.0}{4} = 1.0\,m^3/s$

But $q = \dfrac{\pi}{4}d^2 \times V_1 \Rightarrow 1.0 = \dfrac{\pi}{4}d^2 \times 65.77$

Diameter of jet = d = 0.14 m (Ans)

(iii) If D is the diameter of the pipeline, then the head loss through the pipe is given by = h_f

$$h_f = \frac{4 f L V^2}{2 g D} = \frac{f L Q^2}{3 D^5} \qquad \text{(From } Q = aV\text{)}$$

$$h_f = \frac{0.0045 \times 3000 \times 4^2}{3 D^5} \Rightarrow 22.5$$

Hence D = 0.956 m (Ans)

The three jet Pelton wheel is required to generate 10,000 kW under a net head of 400 m. The blade at outlet is 15° and the reduction in the relative velocity while passing over the blade is 5%. If the overall efficiency of the wheel is 80%, C_v = 0.98 and the speed ratio = 0.46, then find: (i) the diameter of the jet, (ii) total flow (iii) the force exerted by a jet on the buckets (iv) The speed of the runner.

Solution:

No of jets = 3; Total Power P = 10,000 kW; Net head H = 400 m; Blade angle = ¤ = 15°; Vr_2 = 0.95 Vr_1; Overall efficiency = ¦$_o$ = 0.8; C_v = 0.98; Speed ratio = K_u = 0.45; Frequency = f = 50 Hz/s.

We know that ¦$_o = \frac{P}{° g Q H} \Rightarrow 0.8 = \frac{10{,}000 \times 10^3}{1000 \times 10 \times Q \times 400}$

Q = 3.125 m^3/s (Ans)

Discharge through one nozzle = $q = \frac{Q}{n} = \frac{3.125}{3} = 1.042\,\text{m}^3/\text{s}$

Velocity of the jet = $V_1 = C_v\sqrt{2 g H} = 0.98\sqrt{2 \times 10 \times 400} = 87.65\,\text{m}^3/\text{s}$

But $q = \frac{®}{4} d^2 \times V_1 \Rightarrow 1.042 = \frac{®}{4} d^2 \times 87.65$

d = 123 mm (Ans)

Velocity of the Vane = $u = K_u\sqrt{2 g H} = 0.46\sqrt{2 \times 10 \times 400} = 41.14\,\text{m}^3/\text{s}$

Vr_1 = (V_1Ju_1)=87.65J41.14 = 46.51 m/s

Vr_2 = 0.95 Vr_1 = 0.95 x 46.51 = 44.18 m/s

V_{w1} = V_1 = 87.65 m/s

V_{w2} = Vr_2 cos ¤Ju_2 = 44.18 cos 15J41.14 = 1.53 m/s

Force exerted by the jet on the buckets = F_x = ° $q(Vw_1 + Vw_2)$

F_x = 1000 x 1.042 (87.65+1.53) = 92.926 kN (Ans)

Jet ratio = $m = \frac{D}{d} \Rightarrow 10$ (Assumed)

D = 1.23 m

$$u = \frac{® D N}{60}$$

Hence $N = \frac{60u}{® D} = \frac{60 \times 41.14}{® \times 1.23} = 638.8$ rpm (Ans)

Turbines

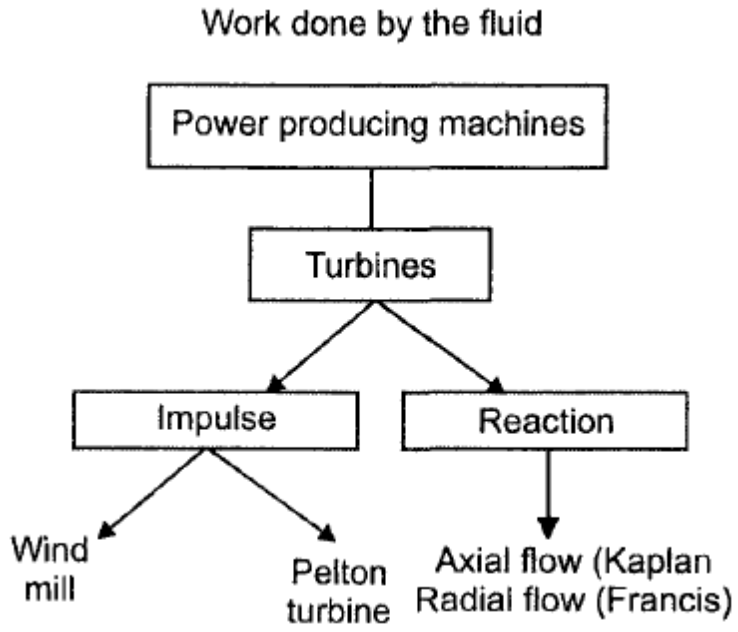

4.5 Turbines

Machines that extract energy from fluid stream are called turbines. They are classified as:

- Hydraulic turbines (Pelton, Francis, Kaplan)
- Steam turbines
- Gas turbines

In hydraulic turbines the working fluid is water and is incompressible. More general classification of hydraulic turbines are:

- impulse
- reaction

Impulse turbines are driven by one or two high velocity jets. Each jet is accelerated in a nozzle external to the turbine wheel known as turbine rotor. If friction and gravity are neglected the fluid pressure and relative velocity do not change as it passes over the blades/buckets.

4.5.1 Pelton Wheel

Pelton wheel is an impulse turbine. It is shown in Fig. 4.9. It is driven by a single jet which lies in the plane of runner. A high velocity jet prossesing kinetic energy strikes the bucket in succession. The water takes nearly 180^0 turn inside the buckets. The water falls into the tail race.

In reaction turbines part of the fluid pressure change takes place externally and part takes place within the runnet. External acceleration occurs in the guide vanes and flow is turned to enter the runner in proper direction. Additional acceleration of fluid relative to rotor occurs within the moving blades. So both relative velocity and pressure change over the runner. Reaction turbines run full of fluid.

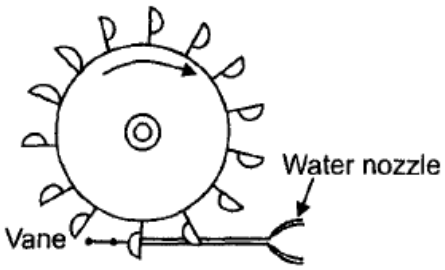

Fig 4.9 Impulse turbine (Pelton wheel).

4.5.2 Francis Turbine

Francis turbine is a reaction turbine shown in Fig. 4.10. Water enters circumferentially through turbine casing. It enters from the outer periphery of guide vanes and flows into runner. It flows down the rotor radially and leaves axially. Water leaving the runner flows through a diffuser known as draft tube before entering the tail race.

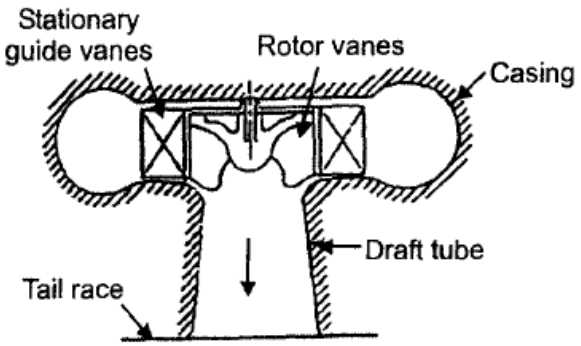

Fig 4.10 Reaction turbine (Francis).

4.5.3 Kaplan Turbine

Kaplan turbine is a reaction turbine shown in Fig. 4.11. The water from the spiral casing enters guide blades similar to Francis. The Kaplan turbine consists of an axial flow runner with 4 to 6 blades of an airfoil section. In this turbine both guide vanes and moving beades are adjustable and therefore high efficiency can be obtained.

4.5.4 Steam Turbines

In steam turbines expansion of high pressure and temperature is expanded in fixed and moving blades of a turbine. Steam is produced in high pressure boiler and after expansion steam condensed in condenser.

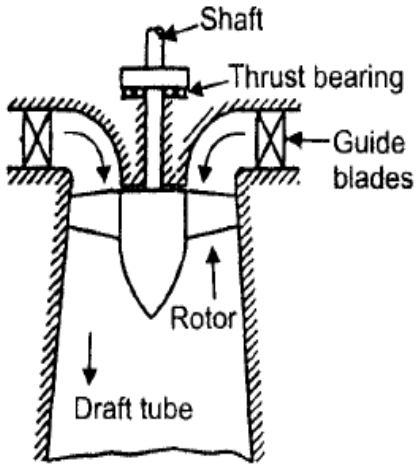

Fig 4.11 Reaction turbine (Kaplan).

4.5.5 Gas Turbine

In gas turbine expansion of high pressure and temperature of gas is expanded in fixed and moving blades of turbine. The exhaust gases after expansion go into the atmosphere.

4.6 Euler's Theory Applied to Turbo Machines

Euler's Theory : The fluid flow through an impeller of a centrifugal pump is shown in F

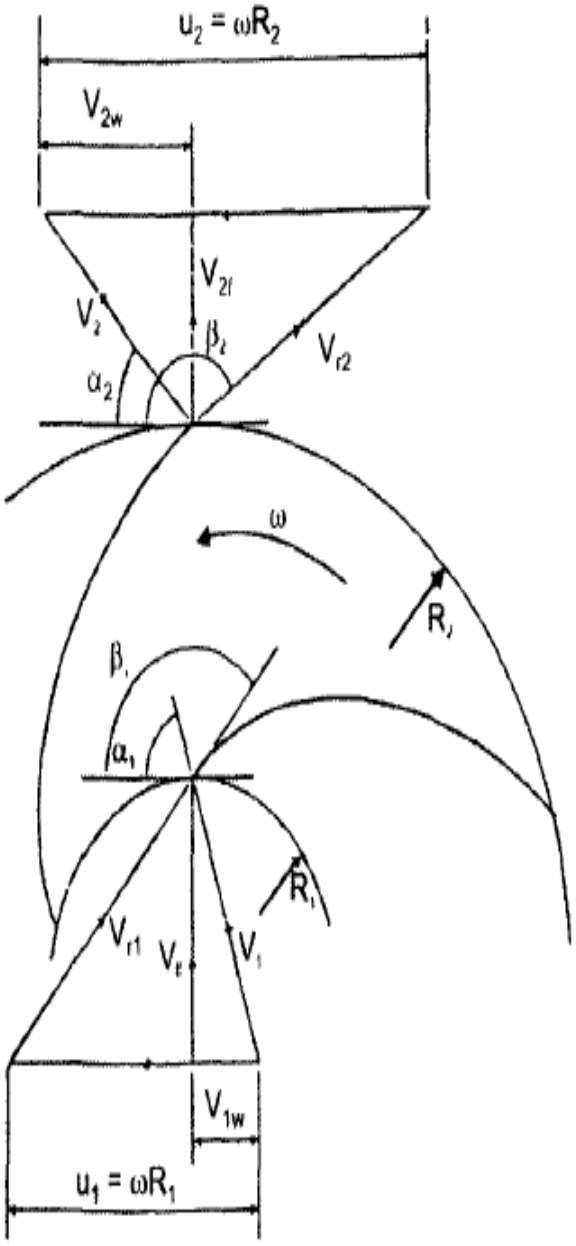

Fig 4.12 Velocity diagrams for pump impeller.

According to Euler's theory torque applied on the impeller is the rate of change of angular momentum of the fluid passing through the impeller. The following assumptions are made.

- The velocity of water is uniform at inlet and exit of the impeller.
- The relative velocities at inlet and exit are tangential to inlet and exit tips of the vanes.

Fig 4.12 shows only two vanes of the impeller, let

V_1 - absolute velocity of the impeller entering the impeller at radius R_1

V_2 - absolute velocity of fluid leaving the impeller at radium R_2

V_{r1} and V_{r2} are relative velocities at inlet and exit, u_1 and u_2 tangential velocities at inlet and exit.

α_1 and α_2 inlet and exit angles of V_1 and V_2

β_1 and β_2 vane tip angles at inlet and exit.

The angles are measured from the forward directed tangents so that both angles β_1 and β_2 are greater than 90^o. The angular velocity ω is connected to tangential velocities u_1 and u_2.

$$u_1 = \omega R_1 \qquad .....(4.1)$$

$$u_2 = \omega R_2 \qquad .....(4.2)$$

According to assumptions made previously V_{r1} and V_{r2} are tangents to the vane tips at inlet and exit.

The velocity V_1 is vector sum of V_{r1} and u_1 at inlet and velocity V_2 is vector sum of V_{r2} and u_2 at exit of vane. Resolve the absolute velocities V_1 and V_2 into tangential and radial components as velocity of whirl and velocity of flow, we have

Velocity of whirl at inlet = $V_{1w} = V_1 \cos\alpha_1$

Velocity of whirl at exit = $V_{2w} = V_2 \cos\alpha_2$

Velocity of flow at inlet = $V_{1f} = V_1 \sin\alpha_1$

Velocity of flow at exit = $V_{2f} = V_2 \sin\alpha_2$

The volume flow rate may be expressed in the form of flow component and flow area A either at inlet or exit given by

$$Q = A_1 V_{1f} = A_2 V_{2f} \quad \text{.....(4.3)}$$

If the width of impeller at inlet and exit is b_1 and b_2 respectively, we have

$$A_1 = \pi D_1 b_1 \quad \text{.....(4.4)}$$

$$A_2 = \pi D_2 b_2 \quad \text{.....(4.5)}$$

where D_1 and D_2 are impeller diameters at inlet and exit

The flow rate Q is then given by

$$Q = \pi D_1 b_1 V_{1f} = \pi D_2 b_2 V_{2f}$$

Also mass flow rate is given by

$$\dot{m} = \rho Q,$$

where ρ is density of fluid

Rate of angular momentum $\overset{o}{M}_1$ of impeller being the product of mean flow rate $\dot{m}$, whirl componant V_{w1} and radius R_1.

$$\overset{o}{M}_1 = \dot{m} V_{1w} R_1 \quad \text{.....(4.7)}$$

$$\overset{o}{M}_2 = \dot{m} V_{2w} R_2$$

Rate of change of angular moment is equal to applied torque

$$T = \dot{m} V_{2w} R_2 - \dot{m} V_{1w} R_1 \quad \text{.....(4.8)}$$

The power input to drive this torque is given by

$$P = T.\omega$$

$$P = \dot{m} \omega (V_{2w} R_2 - V_{1w} R_1)$$

$$P = \dot{m} (u_2 V_{2w} - u_1 V_{1w}) \quad \text{.....(4.9)}$$

4.6.1 Euler's Head

If the whole of mechanical power is converted into hydraulic power then total head H would be given by the relation

$$P = \gamma QH \qquad \text{.....(4.10)}$$

where Q is flow rate and γ sp. weight of the fluid.

Equating eqs. (4.9) (4.10) we get,

$$\boxed{H = \frac{(u_2 V_{2w} - u_1 V_{1w})}{g}}$$

or

$$\boxed{E = \frac{(u_2 V_{2w} - u_1 V_{1w})}{g}} \qquad \text{.....(4.11)}$$

This is called Euler's head of the pump. The head available is actually less than Euler's head. If the water enters the impeller without whirl such that $V_{1w} = 0$ then Euler's equation is written as

$$\boxed{E = \frac{u_2 V_{2w}}{g}} \qquad \text{.....(4.12)}$$

4.6.2 Euler's Equation in the Kinetic Form

It is useful to express Euler's head in terms of their absolute velocities rather than their components. From the velocity triangles of Fig 4.12, we have

$$V_{1w} = V_1 \cos\alpha_1 \text{ and}$$

$$V_{2w} = V_2 \cos\alpha_2$$

Using cosine rule, we have

$$V_{r1}^2 = V_1^2 + u_1^2 - 2u_1 V_1 \cos\alpha_1$$

$$V_{r2}^2 = V_2^2 + u_2^2 - 2u_2 V_2 \cos\alpha_2$$

so that

$$u_1 \cos\alpha_1 = \frac{1}{2}\left(u_1^2 + V_1^2 - V_{r1}^2\right)$$

$$u_2 \cos\alpha_2 = \frac{1}{2}\left(u_2^2 + V_2^2 - V_{r2}^2\right)$$

Substituting in equation (4.11)

$$\boxed{E = \underbrace{\frac{V_2^2 - V_1^2}{2g}}_{\text{I}} + \underbrace{\frac{u_2^2 - u_1^2}{2g}}_{\text{II}} + \underbrace{\frac{V_{r1}^2 - V_{r2}^2}{2g}}_{\text{III}}} \qquad \text{.....(4.13)}$$

From the mode of derivation it is clear that Euler's equation is applicable to a pump and also to a turbine. However, the equation would change its sign. Thus

$$E = \frac{u_1 V_{1w} - u_2 V_2 w}{g} \quad \text{(Turbine)}$$

$$E = \frac{u_2 V_{2w} - u_1 V_{1w}}{g} \quad \text{(Pump)}$$

For axial flow machines $u_1 = u_2 = u$ and

$$E = \frac{u(V_{1w} - V_{2w})}{g} \quad \text{(Turbine)}$$

$$E = \frac{u(V_{2w} - V_{1w})}{g} \quad \text{(Pump)}$$

Pelton Turbine

5.2 Description of Pelton Turbine Installation

Pelton turbine is an impulse turbine as there is no pressure drop across the buckets. The flow is axial, i.e., there is no change in peripheral velocity and water enters and leaves the buckets at the same radius.

Water supplied is from a high head through a long conduit called penstock. The water is accelerated in the nozzle and the head is converted into velocity and discharges at high speed in the form of a jet at atmospheric pressure. The jet strikes deflecting buckets attached to the rim of a rotating wheel (runner) as shown in Fig. 5.1. The kinetic energy of the jet is lost to the buckets and water discharged at relatively low speed falls into lower reservoir or tail race. The tail race is set to avoid submerging the wheel during floded conditions. When large amount of water is available the power can be obtained by connecting two wheels to a single shaft or by arranging two or more jets to a single wheel.

The buckets are double hemispherical in shape. The water strikes the bucket in the centre and flows, out at both sides making a U turn. The surface inside the buckets is polished and smooth to reduce hydraulic losses. A costly material like broonze or stainless steel is generally used for the buckets. The buckets are detachable.

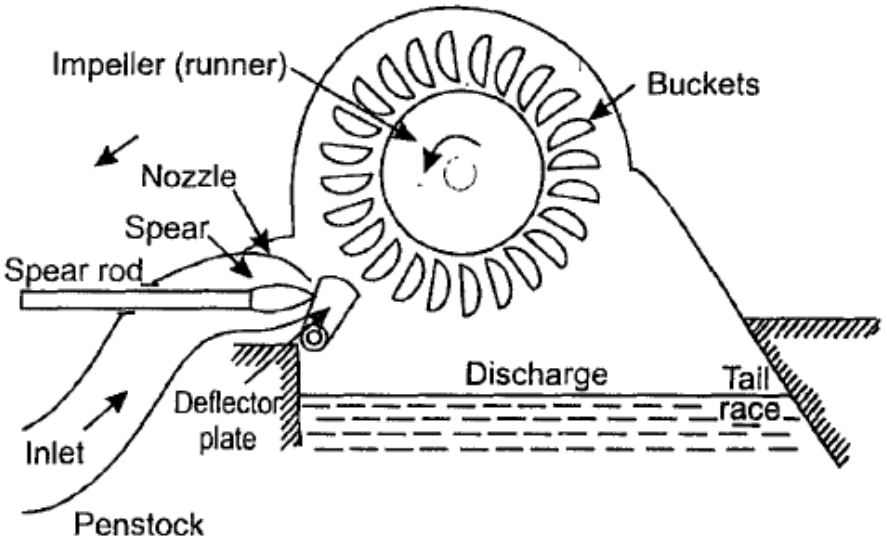

Fig. 5.1 Diagrammatic arrangement of a Pelton wheel.

5.3 Analysis

Pelton wheel installation is shown in Fig 5.4. The water supply is from a constant head reservoir at an elevation H_1 above the centre line of the jet.

A surge tank is installed to dump out any fluctuations of pressure in the penstock. At the end of the penstock is the nozzle which converts head into velocity as jet.

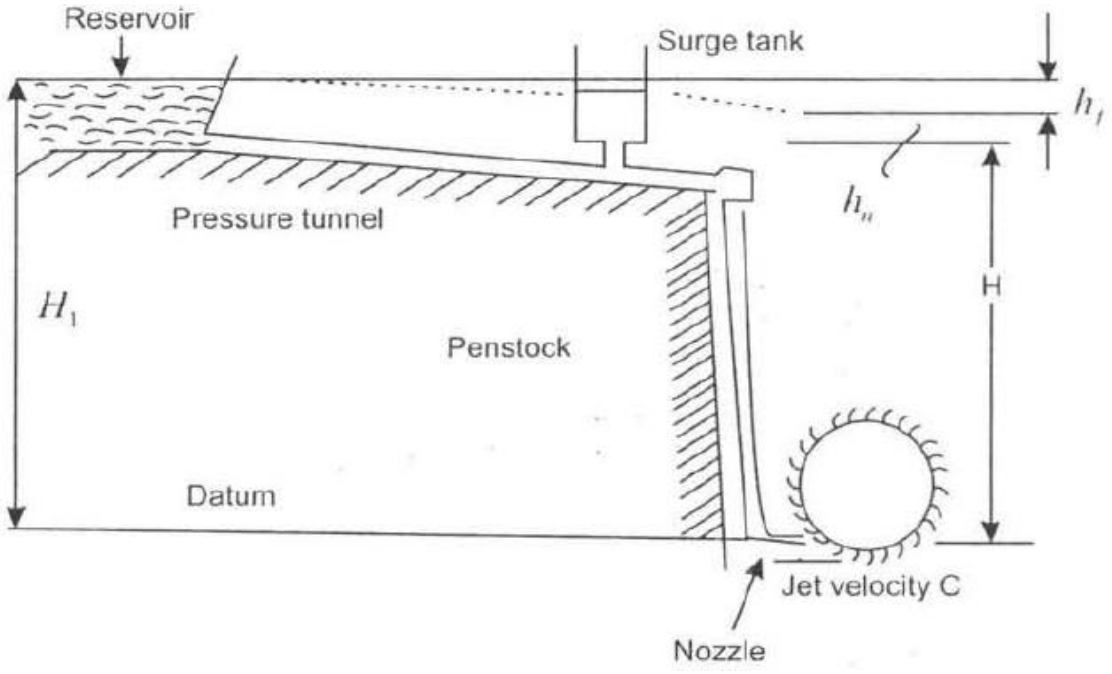

Total head available from the reservoir above nozzle is H_1

Head loss in pressure tunnel and penstock due to friction = h_f

Head loss in the nozzle = h_n

Net head available for power generation at exit of nozzle = H

$$\therefore \quad H = H_1 - h_f - h_n$$

where $$h_f = \frac{flv^2}{2gd}$$

where

l = length of penstock

v = Velocity in penstock

d = diameter of penstock

f = coeff. of friction

In practice the penstock is usually sized so that at rated power the net head is us 85-95% of the total head. The net head is taken to calculate hydraulic efficiency of tur

The jet strikes the bucket at the centre and takes a turn of almost 180° and leav both sides of bucket as shown in Fig, 5.5(a), (b).

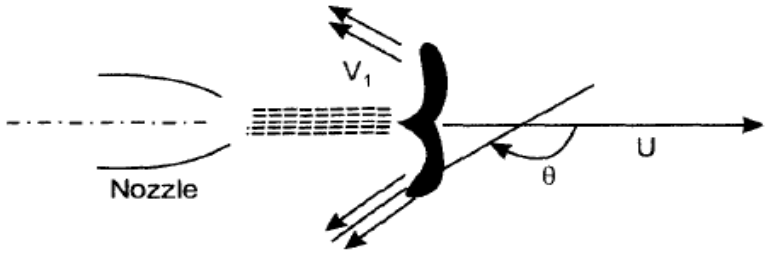

(a)

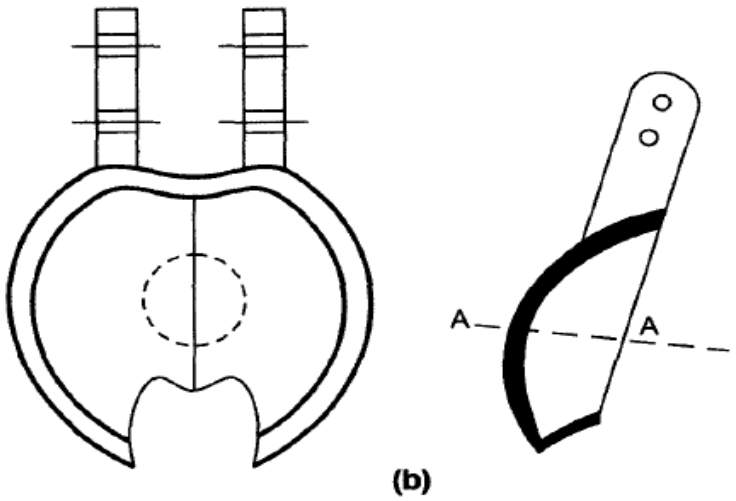

(b)

Fig. 5.5 (a) Jet impuigement **(b)** double hemispherical shape of buckets.

The velocity of the jet is given by

$$V_1 = \sqrt{2gH} \qquad \text{..... (5.1)}$$

The inlet and exit velocity diagrams are shown in Fig 5.3.

The total energy transferred to the wheel is given by Euler's Equation.

$$E = \frac{(u_1 V_{1w} - u_2 V_{2w})}{g} \qquad \text{..... (5.2)}$$

As the turbine is axial the tangential velocity is same at inlet and exit

$u_1 = u_2 = u$ so that eq. 5.2 becomes

$$E = \frac{u(V_{1w} - V_{2w})}{g}$$

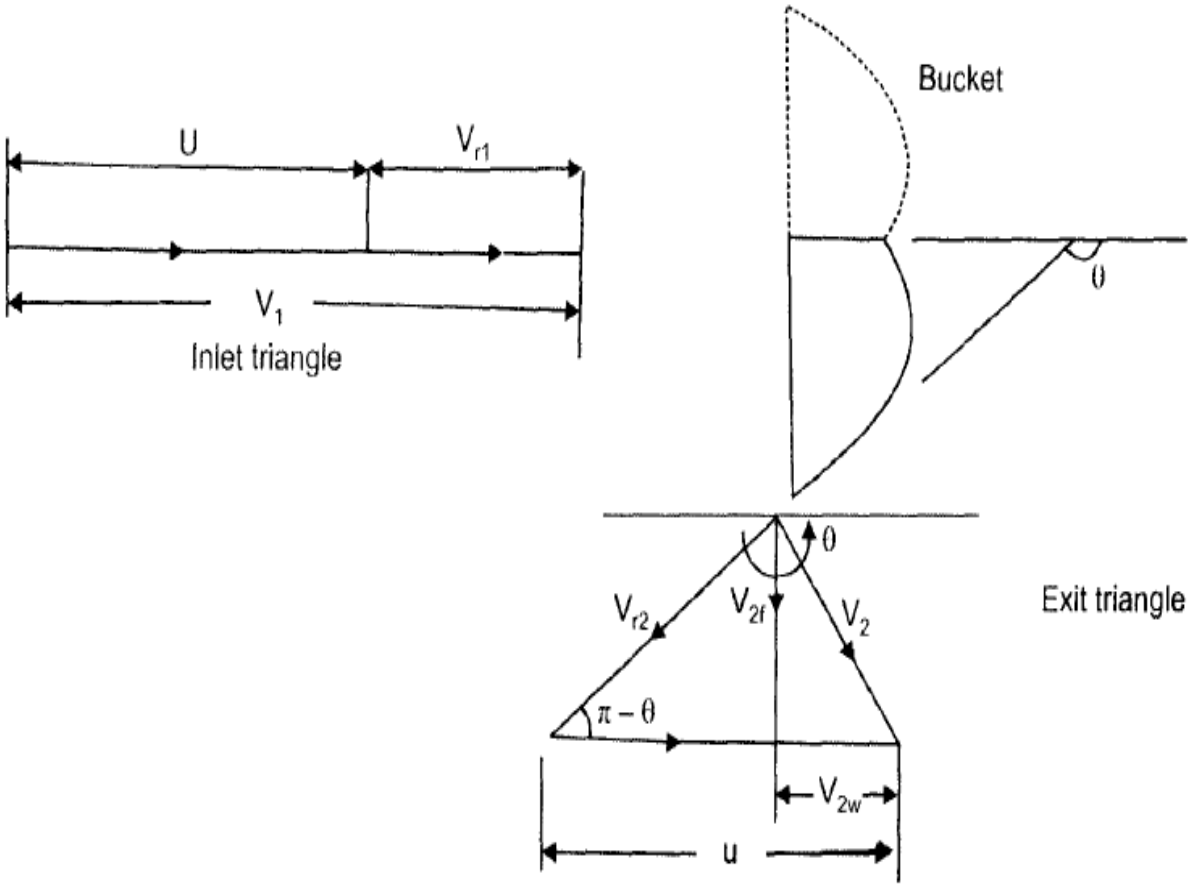

The inlet velocity triangle is a straight line, we have

$$V_{r1} = V_1 - u \text{ and } V_{1w} = V_1$$

Also, $V_{r2} = k\, V_{ri}$, where k is coeff. of velocity due to friction.

The relative velocity vr_2 is tangential to exit tip of the buckets. Superimposing peripheral velocity u we obtain absolute velocity V_2. The velocity Vr_2 makes an angle θ with the centreline of bucket.

$$V_{r2} = k\, V_{r1} = k(V_1 - u) \text{ thus}$$

$$V_{2w} = u - V_{r2} \cos(\pi - \theta)$$

$$V_{r2} = u + V_{r2} \cos\theta$$

$$\therefore \quad V_{2w} = u + k\,(V_1 - u)\cos\theta$$

Writing Euler's equation

$$E = \frac{u\,(V_{1w} - V_{2w})}{g} \qquad \text{.... (5.3)}$$

Substituting $V_{2w} = u + k(V_1 - u)\cos\theta$; as $V_{1w} = V_1$, we have

$$E = \frac{[u\,(V_1 - u - k\,(V_1 - u)\cos\theta]}{g}$$

$$E = \left(\frac{u}{g}\right)[\,V_1 - u - k(V_1 - u)\cos\theta]$$

$$\boxed{E = \frac{u}{g}\,[\,(V_1 - u)\,(1 - k\cos\theta]} \qquad \text{..... (5.4)}$$

The equation shows that there is no energy transfer when the bucket velocity u is either zero or equal to jet velocity V_1. It is reasonable to expect therefore the maximum energy transfer will occur at some intermediate velocity of the bucket velocity.

Thus differentiating E with respect to u and equating to zero for maximum energy transfer

$$\frac{dE}{du} = \frac{(1 - k\cos\theta)(V_1 - 2u)}{g} = 0$$

Hence, $V_1 - 2u = 0$ as $\dfrac{(1 - k\cos\theta)}{g}$ cannot be zero

we have $\boxed{\dfrac{u}{V_1} = \dfrac{1}{2}}$

Thus tangential velocity is half the jet velocity for maximum energy transfer. Substituting this value in eq 5.4

$$E_{max} = \left(\frac{V_1}{2g}\right)\left(V_1 - \frac{V_1}{2}\right)(1 - k\cos\theta)$$

$$E_{max} = \left(\frac{V_1^2}{4g}\right)(1 - k\cos\theta)$$

Inlet kinetic energy to the jet = $V_1^2/2g$

Thus maximum theoretical hydraulic efficiency of Pelton wheel,

$$\eta_{max} = \frac{E}{\text{K.E of jet}}$$

$$\eta_{max} = \frac{\left(\frac{V_1^2}{4g}\right)(1 - k\cos\theta)}{\frac{V_1^2}{2g}}$$

$$\boxed{\eta_{max} = \frac{(1 - k\cos\theta)}{2g}} \qquad \text{..... (5.6)}$$

In an ideal case when $\theta = 180$, $k = 1$; $\eta_{max} = 100\%$. In practice friction exists and K value is in the region of 0.85 - 0.9 and also the value of $\theta = 165^0$ to avoid interference between incoming and outgoing jets. Therefore $\frac{u}{V_1}$ is always less than 0.5. For $\frac{u}{v_1} = 0.46$ and $\theta = 165^o$, the maximum efficiency is around 90% . Rewriting equation 5.4,

$E = \frac{u}{g}(V_1 - u)(1 - k\cos\theta)$ and also K.E of jet = $V_1^2/2g$ and hydraulic efficiency as

$$\eta = \frac{\left(u/g\right)(V_1 - u)(1 - k\cos\theta)}{V_1^2/2g}$$

$$\boxed{\eta_h = (2)\left(\frac{u}{V_1}\right)\left(1 - \frac{u}{V_1}\right)(1 - k\cos\theta)} \qquad \text{..... (5.7)}$$

Hydraulic efficiency $\eta_h = \dfrac{\text{power developed by runner}}{\text{hydraulic power}} = \dfrac{\gamma QE}{\gamma QH}$

Mechanical efficiency $\eta_m = \dfrac{\text{power developed at turbine shaft}}{\text{power developed by runner}} = \dfrac{P}{\gamma QE}$

Overall efficiency $\eta_0 = \dfrac{\text{Power developed at turbine shaft}}{\text{hydraulic power}} = \dfrac{P}{\gamma QH}$

thus $\eta_0 = \eta_h \times \eta_m$

5.4.1 Working Proportions for Design of Pelton Wheel

1. ***Velocity of jet:*** The theoretical velocity of the Jet

$$V_1 = \sqrt{2gH}$$

where H = net head

Actual Velocity of Jet

$$V_a = C_v\sqrt{2gH}$$

where C_v is the coefficient of velocity of the jet which varies from 0.98 to 0.99.

2. ***Power available to the Turbine***

$$P = \gamma QH$$

3. ***Angle*** ϕ is the splitter angle which varies from 10 to 20^0 and relation between ϕ and exit angle θ is

$$\theta = \pi - \phi$$

4. ***Diameter of the Jet (d):*** The diameter of the jet is obtained if flow rate is known.

Flow rate Q = area of the jet × velocity of jet × no. of jets

For a single jet

$$Q = \frac{\pi}{4} d^2 \times V_1$$

$$Q = \frac{\pi}{4} d^2 \times C_v\sqrt{2gH}$$

$$d = \left(\frac{4Q}{\pi C_v\sqrt{2gH}}\right)^{1/2}$$

5. ***Speed ratio*** $\left(\frac{u}{V_1}\right)$: The speed ratio is the ratio of the velocity (u) of the wheel at pitch circle to theoretical velocity of the jet. In practice the value is between 0.44 and 0.46 and average is 0.45.

6. ***Mean Diameter of the Wheel (D):*** It is the diameter between centres of the buckets. The diameter can be obtained from peripherial velocity (u)

$$u = \frac{\pi DN}{60}$$

$$\text{or} \qquad D = \frac{60u}{\pi N}$$

where N = speed of the wheel in revolutions/min.

7. ***Jet ratio (m):*** The ratio of mean diameter of the wheel to diameter of the jet.

$$m = D/d$$

The Jet ratio varies between 10 to 14 and average value of m is 12.

8. ***Size of the buckets:*** The length, width and depth of buckets in terms of diameter of jet 'd' is shown in Fig. 5.10.

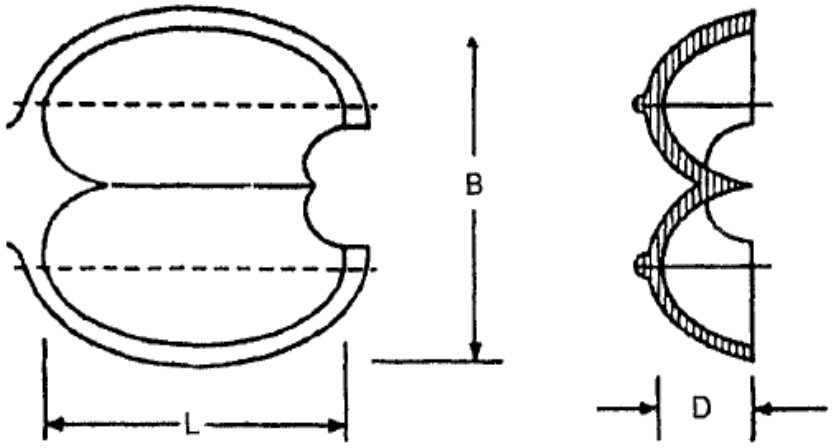

Fig. 5.10 Dimensions of bucket.

- Radial length of bucket L = 2 to 3d
- Axial width of bucket B = 3 to 5d
- Depth of bucket D = 0.8 to 1.2d

E.5.1 A Pelton wheel develops 67.5 kw under a head of 60 m of water. It rotates at 400 rev/min. The diameter of penstock is 200 mm. The ratio of bucket speed of jet velocity is 0.46 and overall efficiency of the installation is 83%. Calculate.

(a) Volumetic flow rate

(b) Diameter of the jet

(c) Wheel diameter

Solution

- Overall efficiency $\eta_0 = \dfrac{P}{\gamma QH}$; $Q = \dfrac{P}{\eta_0 \times \gamma H}$

$$\therefore \quad Q = \frac{67.5 \times 1000}{0.83 \times 9800 \times 60} = 0.138 \text{ m}^3/\text{s}$$

- Velocity of the jet $V_1 = \sqrt{2gH}$

$$= \sqrt{2 \times 9.8 \times 60} = 34.2 \text{ m/s}$$

- Flow rate Q = area of nozzle × velocity of jet

$$Q = \frac{\pi}{4} d^2 \times V_1$$

$$\therefore \quad d^2 = \frac{0.138 \times 4}{\pi \times 34.2} = 5.14 \times 10^{-3}$$

$$d = 0.0716 \text{ m} = 71.7 \text{ mm}$$

$$\frac{u}{V_1} = 0.46, \; u = 0.46 \times 34.2 = 15.7 \text{ m/s}$$

$$u = \frac{\pi DN}{60}$$

$$\therefore \quad D = \frac{60 \times u}{\pi \times N} = \frac{60 \times 15.7}{\pi \times 400} = 0.75 \text{ m}$$

Specific speed of turbine

$$w_T = \frac{\omega \left(P/\rho \right)^{\frac{1}{2}}}{(gH)^{5/4}}$$

where $$\omega = \frac{2N\pi}{60} = \frac{2 \times 400 \times \pi}{60} = 41.8 \text{ rad/s}$$

$$P = 67.5 \times 10^3 \text{ watt}$$

$$\rho = 1000 \text{ kg/m}^3$$

$$H = 60 \text{ m}$$

Substituting,

$$\omega_T = \frac{41.8\left(\frac{67.5\times10^3}{10^3}\right)^{\frac{1}{2}}}{(9.8\times60)^{5/4}}$$

$$\omega_T = 0.11$$

E.5.2 A Pelton wheel works on a head of 400 m. The diameter of the jet is 80 mm. The head loss in penstock and nozzle is 23.6 m. The bucket speed is 40 m/s. The buckets deflect the jet through 165^0. The bucket friction reduces relative velocity at exit by 15% of relative velocity at inlet. The mechanical efficiency of turbine is 90%. Find the flow rate and shaft power developed by the turbine.

Solution

Velocity of the jet $V_1 = \sqrt{2g(H - h_f)}$

$$V_1 = \sqrt{2\times9.8(400-23.6)} = 85.8 \text{ m/s}$$

Euler's head $E = \frac{u}{g}(V_1 - u)(1 - k\cos\theta)$

$$= \frac{40}{9.8}(85.8-40)(1-0.85\times\cos 165^0)$$

$$= \frac{40}{9.8}(85.8-40)(1+0.82)$$

$$E = 340.2 \text{ m}$$

Flow rate Q = area × velocity $= \frac{\pi}{4} d^2 \times V_1$

$$Q = \frac{\pi}{4} \times 80^2 \times 10^{-6} \times 85.8 = 0.43 \text{ m}^3/\text{s}$$

Power developed by the runner = γ QE

$$P_E = \frac{\gamma QE}{1000} = \frac{9800 \times 0.43 \times 340.2}{1000} = 1432 \text{ kw}$$

$$\eta_m = \frac{P}{P_E}; 0.9 = \frac{P}{1432} \quad \therefore P = 1288 \text{ kw}$$

E.5.3 A Pelton wheel is driven by two similar jets transmits 3750 kW to the shaft running at 375 rev/min. The total head available is 200 m and losses is 0.1% of the total head. The diameter of the wheel is 1.45 m, the relative velocity coefficient of the bucket is 0.9, the deflection of the jet is 165^0. Find the hydraulic efficiency, overall efficiency and the diameter of each jet, if the mechanical efficiency is 90%.

Solution

Peripherial velocity $u = \frac{\pi DN}{60} = \frac{\pi \times 1.45 \times 375}{60} = 28.4$ m/s

Total head = 200 m, $h_f = 200 \times 0.1 = 20$ m

Effective head H = total head – losses

$= 200 - 20 = 180$ m

Velocity of the jet $V_1 = \sqrt{2gH} = \sqrt{2 \times 9.8 \times 180} = 59.4$ m/s

Speed ratio $= \frac{u}{V_1} = \frac{28.4}{59.4} = 0.478$

Hydraulic efficiency $\eta_h = 2\frac{u}{V_1}\left(1 - \frac{u}{V_1}\right)(1 - k\cos\theta)$

$= 2 \times 0.478\,(1 - 0.478)\,(1 - 0.9 \times \cos 165^0) = 0.932$

$\eta_h = 93.2\%$

Euler's head $E = \frac{u}{g}(V_1 - u)(1 - k\cos\theta)$

$$E = \frac{28.4}{9.8}(59.4 - 28.4)(1 - 0.9 \times \cos 165^0) = 167.93 \text{ m}$$

Relation between η_0, η_h, η_m is

$\eta_0 = \eta_m \times \eta_h \quad \therefore \eta_0 = 0.9 \times 0.932 = 0.838$

$$\text{hydraulic power} = \frac{P}{\eta_0} = \frac{3750}{0.838} = 4474 \text{ kw}$$

also $$\frac{\gamma QH}{1000} \times 2 = 4474$$

$$Q = \frac{1000 \times 4474}{2 \times 9800 \times 180} = 1.268 \text{ m}^3/\text{s}$$

Flow rate Q = area × velocity of jet

$$Q = \frac{\pi}{4} d^2 \times V_1$$

$$d^2 = \frac{4Q}{\pi \times V_1} = \frac{4 \times 1.268}{\pi \times 59.4} = 0.0272$$

$$d = 164 \text{ mm}$$

Francis Turbine

6.2 Description of Francis Turbine

A sketch of a Francis turbine is shown in Fig. 6.1. The flow is contained in a spiral casing called volute that channel the water into the runner. The volute has decreasing area to maintain uniform velocity, to the row of stationary vanes.

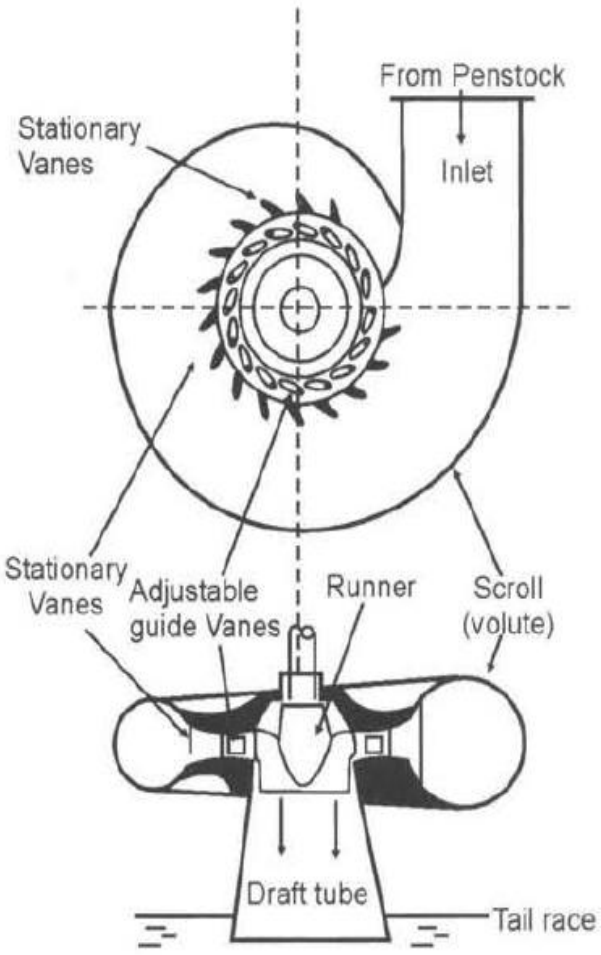

Fig. 6.1 Main components of Francis tubine.

6.3 Analysis

Let

H	-	Total head available to the turbine
V_o	-	Absolute velocity of water at inlet to stationary vanes
V_1	-	Absolute velocity of water at exit to ajustable guide vanes
V_2	-	Absolute velocity of water at exit to runner vanes
V_{r1}	-	Relative velocity at inlet to runner vane
V_{r2}	-	Relative velocity at exit to runner vane
u_1	-	Peripheral velocity at inlet to runner vane
u_2	-	Peripheral velocity at exit to runner vane
V_{1w}, V_{2w}	-	Whirl velocities at inlet and exit of runner vane
V_{1f}, V_{2f}	-	Flow velocities at inlet and exit of runner vane
α_1	-	Guide vane angle
β_1	-	Runner blade inlet angle
β_2	-	Runner blade exit angle

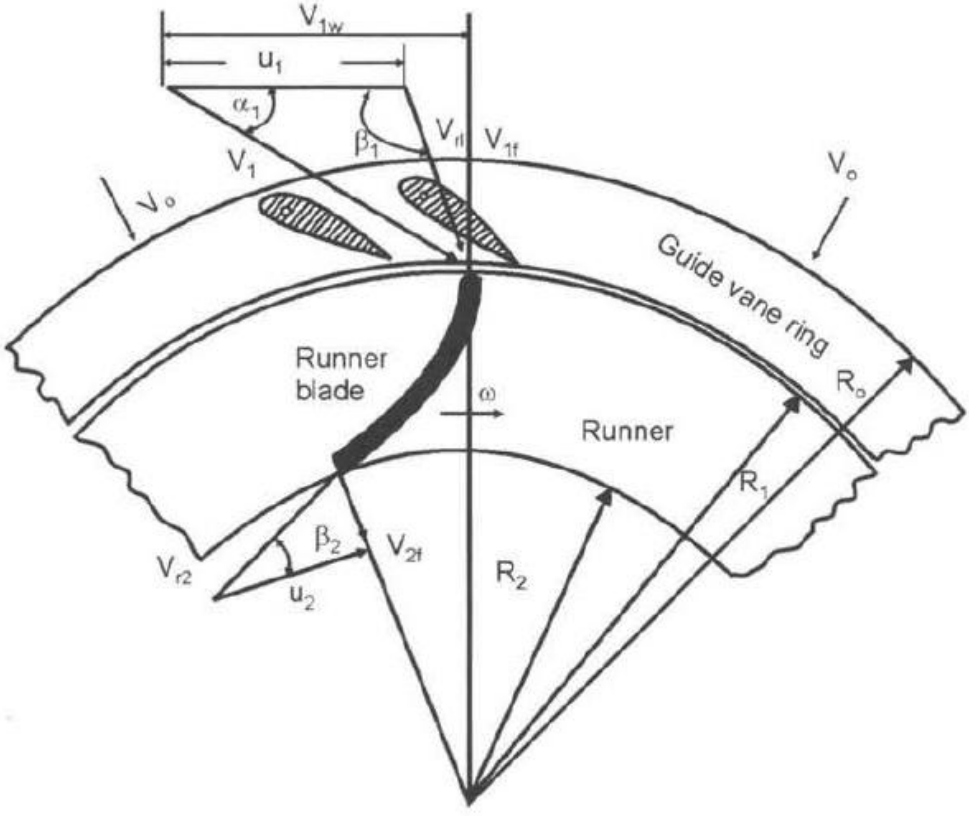

Fig. 6.4 Inlet and exit velocity diagram.

$$u_1 = \omega R_1;\ u_2 = \omega R_2;\ \text{and } \omega = \frac{2N\pi}{60}$$

The water comes out from the guide vanes at absolute velocity V_1 at an angle α_1 to the direction of rotation. The peripheral velocity u_1 is subtracted from V_1 to give relative velocity V_{r1} at angle β_1 to the direction of rotation is obtained.

At exit the water leaves the runner blade at relative velocity V_{r2} which makes an angle β_2 with the direction of rotation. Superimposing u_2 absolute velocity V_2 is obtained.

Euler's head is given by

$$E = \qquad \text{..... (6.1)}$$

If the whirl velocity at exit is zero, $V_{2w} = 0$, which means that velocity V_2 has no horizontal component or $\alpha_2 = 90^\circ$, then Euler's eq. 6.1 for maximum efficiency is given by

$$E = \frac{u_1 V_{1w}}{g} \qquad \text{.....(6.2)}$$

In such a case flow velocity at exit $V_{2f} = V_2$, $\tan\beta_2 = \dfrac{V_2}{u_2} = \dfrac{V_{2f}}{u_2}$ so that β_2 can be determined.

Net head available H across the turbine is the difference in total head between inlet flange (exit of penstock) and tail race water level

- **Total head at inlet** $= \dfrac{P_0}{\gamma} + \dfrac{V^2 o}{2g} + z_0$
- **Total head at exit** $= \dfrac{P_3}{\gamma} + \dfrac{V_3^2}{2g} + z_3$
- **Net head across the turbine**

$$H = \left(\frac{P_o}{\gamma} + \frac{V_0^2}{2g} + z_o\right) - \left(\frac{P_3}{\gamma} + \frac{V_3^2}{2g} + z_3\right) \qquad \text{..... (6.3)}$$

But P_3 = atmospheric pressure = 0; z_3 is tail race taken as datum $z_3 = 0$, thus eq. 6.3 becomes

$$H = \left(\frac{P_o}{g} + \frac{V_o^2}{2g} + z_o\right) - \left(\frac{V_3^2}{2g}\right)$$

$$H = H_1 - h_{fp} - \left(\frac{V_3^2}{2g}\right)$$

where h_{fp} = hydraulic losses in penstock

The hydraulic efficiency is given by,

$$\eta_R = \frac{\text{runneroutput}}{\text{runner input}} = \frac{\gamma QE}{\gamma QH} = \frac{E}{H} = \frac{u_1 V_{1w}}{gH} \quad \text{..... (6.4)}$$

Mechanical efficiency $\eta_m = \dfrac{\text{turbine output}}{\text{runner output}} = \dfrac{P}{\gamma QE}$

Overall efficiency $\eta_o = \dfrac{\text{power output}}{\text{hydraulic input}} = \dfrac{P}{\gamma QH}$

thus $\eta_o = \eta_h \times \eta_m$ ..... (6.5)

Energy developed in the runner in terms of Euler's head

$$E = H - h_{fp} - h_g - h_r - h_d \quad \text{.... (6.6)}$$

where h_{fp} - hydraulic losses in penstock

h_g - hydraulic losses in guide vanes

h_r - hydraulic losses in runner vanes

h_d - hydraulic losses in draft tube

6.4 Draft Tube

A draft tube is connected between runner exit and tail race to obtain continuous stream of water between them. It is diverging tube. The pressure increases and velocity decreases in the tube. The tail race pressure is atmospheric and runner exit pressure is negative (below atmospheric). Then the net head acting on the turbine increases. The turbine works with a

larger head and more power is developed by the turbine. This is the main advantage of installing a draft tube. All Francis turbines will have a draft tube.

Analysis

With references to Fig. 6.5 and applying Bernoulli's equation between point (2) and (3) we get

$$\frac{P_2}{\gamma} + \frac{V_2^2}{2g} + Z_2 = \frac{P_3}{\gamma} + \frac{V_3^2}{2g} + Z_3 + h_d \qquad .....(6.7)$$

where h_d represents losses in the diffuser also P_3 = atmospheric = 0; the tail race is taken as datum and therefore $Z_3 = 0$.

Re-writing eq. 6.7 with the above assumptions, we have

$$\frac{P_2}{\gamma} = \frac{V_3^2 - V_2^2}{2g} - Z_2 + h_d \qquad .....(6.8)$$

Also $V_3 < V_2$, and if hd is neglected, $\frac{P_2}{\gamma}$ in negative.

The draft tube produces negative pressure at exit which increases the pressure head over the turbine.

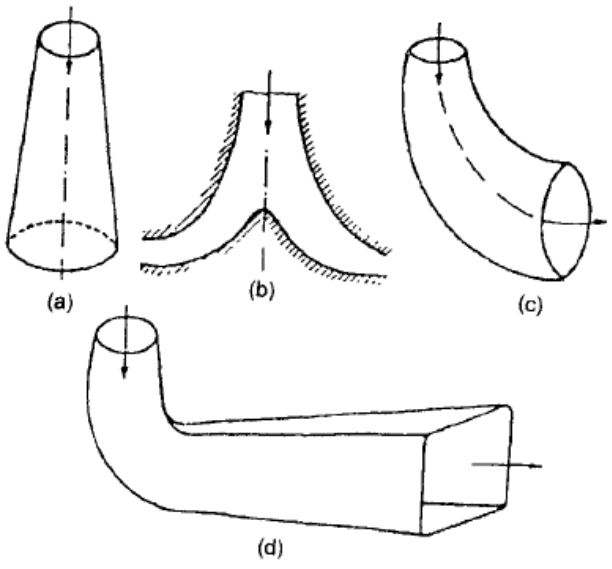

Fig. 6.6 Types of draft tubes.

6.5 Working Proportions of Francis Turbine

Let

B	-	breadth/width of runner vane
D	-	diameter of runner
z	-	number of runner vanes
t	-	thickness of runner vane
n	-	ratio of width to diameter of runner
χ	-	Flow ratio
ϕ	-	speed ratio
V_f	-	flow velocity
$\sqrt{2gH}$	-	Jet velocity

- $n = \frac{B}{D}$ The value of n varies from 0.1 - 0.45

- Flow ratio $\chi = \frac{V_f}{\sqrt{2gH}}$ its value varies from 0.15 - 0.3

- Speed ratio $\phi = \frac{u}{\sqrt{2gH}}$ its value varies from 0.6 - 0.9

- Flow through runner vanes = flow area × velocity of flow

  Area (inlet) = $(\pi D_1 - zt)\, B_1 = \pi D_1\, B_1\, K_1$

  where k_1 is a factor which allows for thickness of runner vanes.

  Area (exit) = $(\pi D_2 - zt)B_2 = \pi D_2\, B_2\, K_2$

  where K_2 is a factor which allows for thickness of runner vanes.

Flow rate

$Q = (\pi D_1 - zt_1)\, B_1\, V_{1f} = (\pi D_2 - zt)\, B_2\, V_{2f}$

$Q = \pi D_1 B_1\, K_1\, V_{1f} = \pi D_2\, K_2\, V_2\, V_{2f}$

$Q = \pi D_1^2\, n_1 K_1 V_{1f} = \pi D_2^2\, n_2\, K_2\, V_{2f}$ ..... (6.9)

if $K_1 = K_2$; $V_{1f} = V_{2f}$; $n_1 = n_2$, then equation becomes

$$B_1\, D_1 = B_2\, D_2$$

Fig. 6.7 shows the runner of Francis turbine. As indicated B is the breadth of runner and D the diameter.

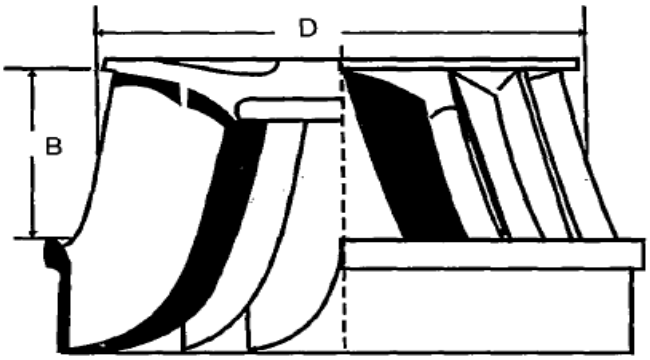

Fig. 6.7 Runner of Francis turbine.

For turbines homologous specific speed N_s is also used, given by the following equation.

$$(Ns)_T = \frac{NP^{\frac{1}{2}}}{H^{\frac{5}{4}}} \qquad \text{..... (6.10)}$$

where H is in meters, P the power output in kw, and speed N in rev/min of runner.

6.7.1 Comparison between Pelton and Francis Turbines

S.No	Pelton turbine	Francis turbine
1	Impulse type	Reaction type
2	Axial flow	Radial flow
3	Jet produced by nozzle - a fixed element	Water suppled by adjustable guide vanes
4	High head	Medium head
5	Low discharge	Medium flow
6	Specifc speed $\omega_T < 0 - 1$	Specific speed ω_T 1 - 3.5
7	Turbine does not run full of water	Turbine runs full of water

E.6.1 An inward flow turbine with radial discharge has an overall efficiency of 80% and develops 150 kw. The head is 8 m and the peripheral velocity at inlet is $0.96\sqrt{2gH}$ and flow velocity is $0.36\sqrt{2gH}$. The runner speed is 150 rev/min; the hydraulic efficiency is 85%.

Determine.

(a) velocity of whirl at inlet

(b) diameter of the wheel at inlet

(c) flow rate

(d) guide vane angle

Solution

- Peripheral velocity $u_1 = 0.96\sqrt{2gH} = 0.96\sqrt{2\times9.8\times8} = 12.02$ m/s

- Flow velocity $v_{1f} = 0.36\sqrt{2gH} = 0.36\sqrt{2\times9.8\times8} = 4.5$ m/s

– Hydraulic efficiency

$$\eta_h = \frac{(u_1 V_{1w} - u_2 V_{2w})}{gH} \text{ as it is radial discharge } V_{2w} = 0$$

$$\eta_h = \frac{u_1 V_{1w}}{gH}, \text{ substituting proper values}$$

$$\therefore \quad 0.85 = \frac{12.02 \times V_{1w}}{9.8 \times 8}$$

$$V_{1w} = 5.54 \text{ m/s}$$

$$\text{inlet angle } \tan \alpha_1 = \frac{V_{1f}}{V_{1w}} = \frac{4.5}{5.54} = 0.812$$

$$\alpha_1 = 39^0$$

$$u_1 = \frac{\pi D_1 N}{60}$$

$$\therefore \quad D_1 = \frac{60 \times u_1}{\pi \times N} = \frac{60 \times 12.02}{\pi \times 150} = 1.53 \text{ m}$$

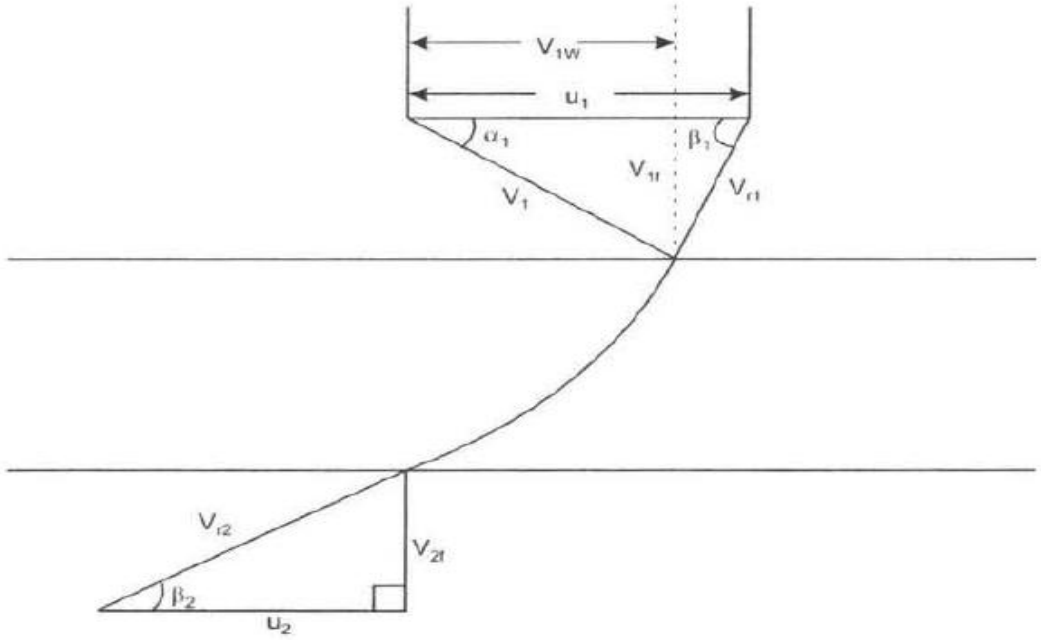

$$\text{overall efficiency } \eta_o = \frac{P}{\gamma Q H}$$

$$\therefore \quad Q = \frac{P}{\gamma H \times \eta_o} = \frac{150 \times 1000}{9800 \times 8 \times 0.8} = 2.4 \text{ m}^3/\text{s}$$

$$Q = 2.4 \text{ m}^3/\text{s}$$

E.6.2 A Francis turbine has the following specifications.

Inlet radius 300 mm, outer radius 150 mm, flow rate 0.05 m^3/s, inlet guide blade 30°, angle the absolute velocity at exit makes an angle of 80° with the axis inlet absolute velocity 6 m/s, exit absolute velocity 3 m/s; overall efficiency 80%, hydraulic efficiency 90%. Determine head and power output if angular velocity is 25 rad/s.

Solution

Refering to velocity diagrams shown in Fig. 6.15, we have

$R_1 = 300$ mm, $R_2 = 150$ mm, $Q = 0.05\ m^3/s$

$\alpha_1 = 30^\circ$, $\alpha_2 = 80^\circ$, $V_1 = 6$ m/s, $V_2 = 3$ m/s

$\eta_o = 80\%$, $\eta_h = 90\%$, $\omega = 25$ rad/s

$$u_1 = \omega R_1 = \frac{300}{1000} \times 25 = 7.5 \text{ m/s}$$

$$u_2 = \omega R_2 = \frac{150}{1000} \times 25 = 3.75 \text{ m/s}$$

$$V_{1w} = V_1 \cos \alpha_1 = 6 \times \cos 30 = 6 \times 0.866 = 5.2 \text{ m/s}$$

$$V_{2w} = V_2 \text{ Cos } \alpha_2 = 3 \times \cos 80 = 3 \times 0.172 = 0.52 \text{ m/s}$$

$$\text{Euler's head } E = \frac{u_1 V_{1w} - u_2 V_{2w}}{g}$$

$$E = \frac{7.5 \times 5.2 - 3.75 \times 0.52}{9.8} = 3.7$$

$$E = 3.7 \text{ m}$$

$$\eta_h = \frac{E}{H}$$

$$H = \frac{3.7}{0.9} = 4.1 \text{ m}$$

Power input $= \gamma QH = \dfrac{9800 \times 0.05 \times 4.1}{1000} = 2$ kw

Power output $= \eta_o \times$ power input $= 2 \times 0.8 = 1.6$ kw

$P = 1.6$ kw

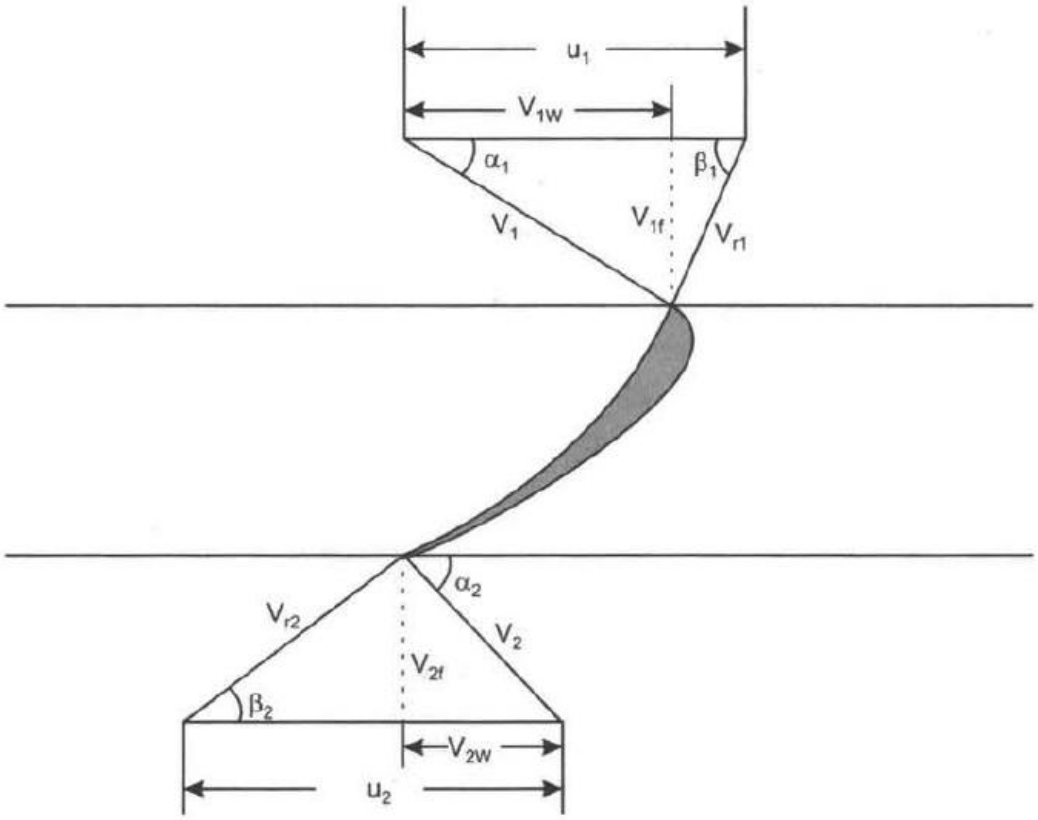

Kaplan Turbine

7.2 Description of Propeller Turbine

The propeller type consists of axial flow runner with 4 to 6 blades of an aerofoil shape as shown in Fig.7.2. The spiral casing and guide vanes are similar to Francis turbine. The flow enters the runner through guide vanes which can be set to any desired angle (within limit) to accommodate changes in power output demand. The runner blades are fixed and cannot change their position. The guide vanes ring is in a plane perpendicular to the shaft so that flow is radial. The runner is situated further downstream so that between guide vanes and the runner the fluid turns through a right angle into axial direction. The runner blades are long in order to accommodate large flow rate and therefore pitch/chord ratio of runner blades is 1 to 1.5 and hence number of blades is small. The propeller type has low head between 5-80 m. Fig. 7.2(a) shows the plan view of guide vanes and Fig.7.2(b) shows profile of the system.

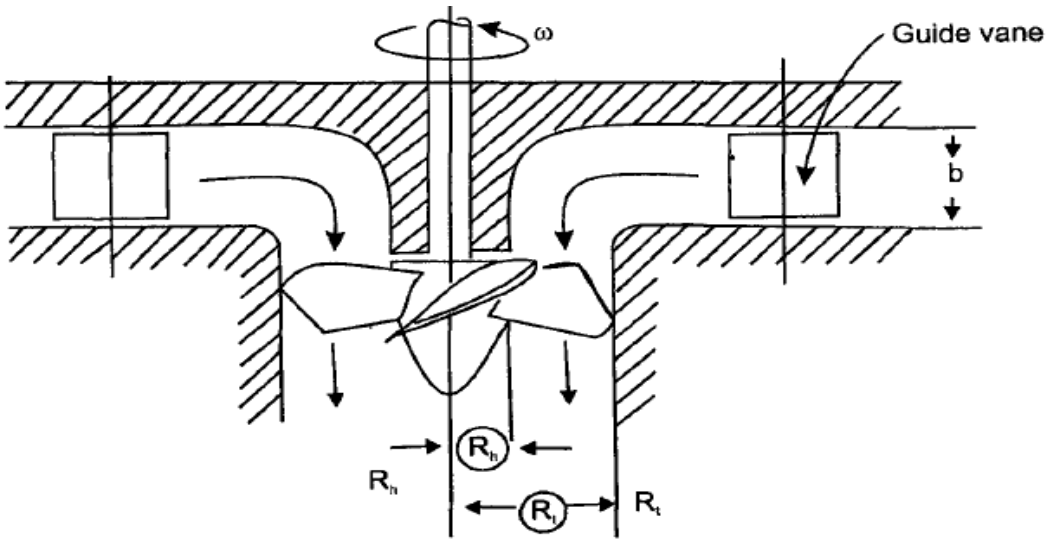

Fig. 7.2(b) Axial-flow propeller type turbine, guide vanes and runner.

7.3 Analysis and Construction of Velocity Diagram

The runner blades are long and there is large difference in radii between the hub and tip of the blades. Therefore velocity diagrams are drawn at the mean radius of the blade. The axial flow velocity is constant as inlet and exit and hence

$$V_{1f} = V_{2f} = V_f$$

The inlet velocity diagram is constructed by substracting blade velocity vector u from absolute velocity vector V_1, which makes an angle α_1 to u to obtain relative velocity V_{r1} as shown in Fig. 7.3.

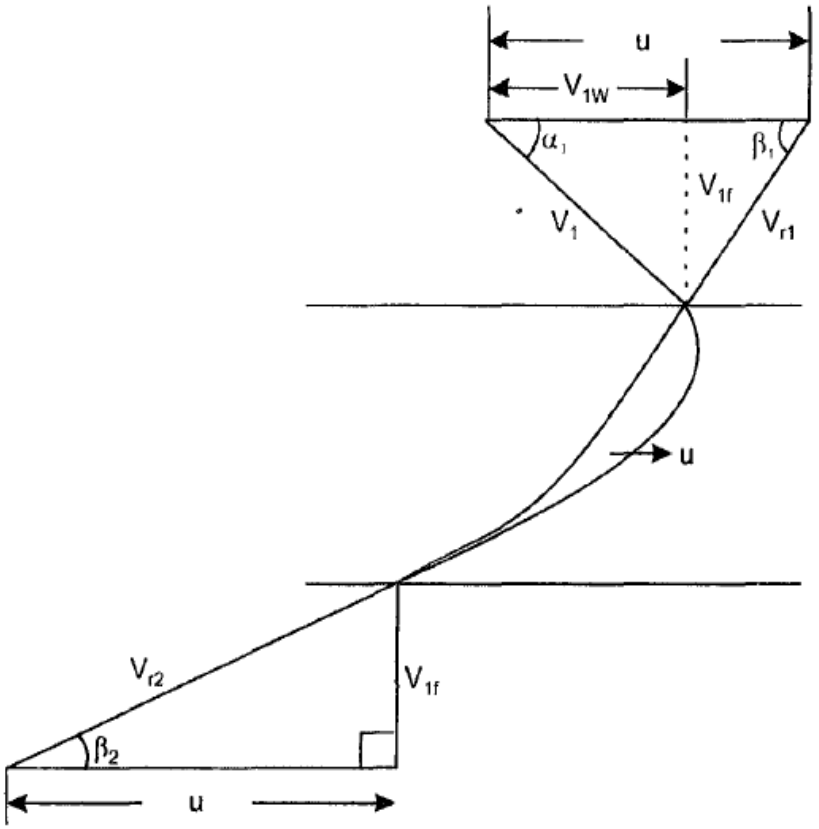

Fig 7.3 Inlet and exit velocity diagrams.

The exit velocity diagram is constructed by drawing relative velocity at exit V_{r2} tangential to exit tip of the blade, superimposing peripheral velocity u, we obtain absolute velocity V_2 which is axial. The velocity diagrams are shown in Fig. 7.4.

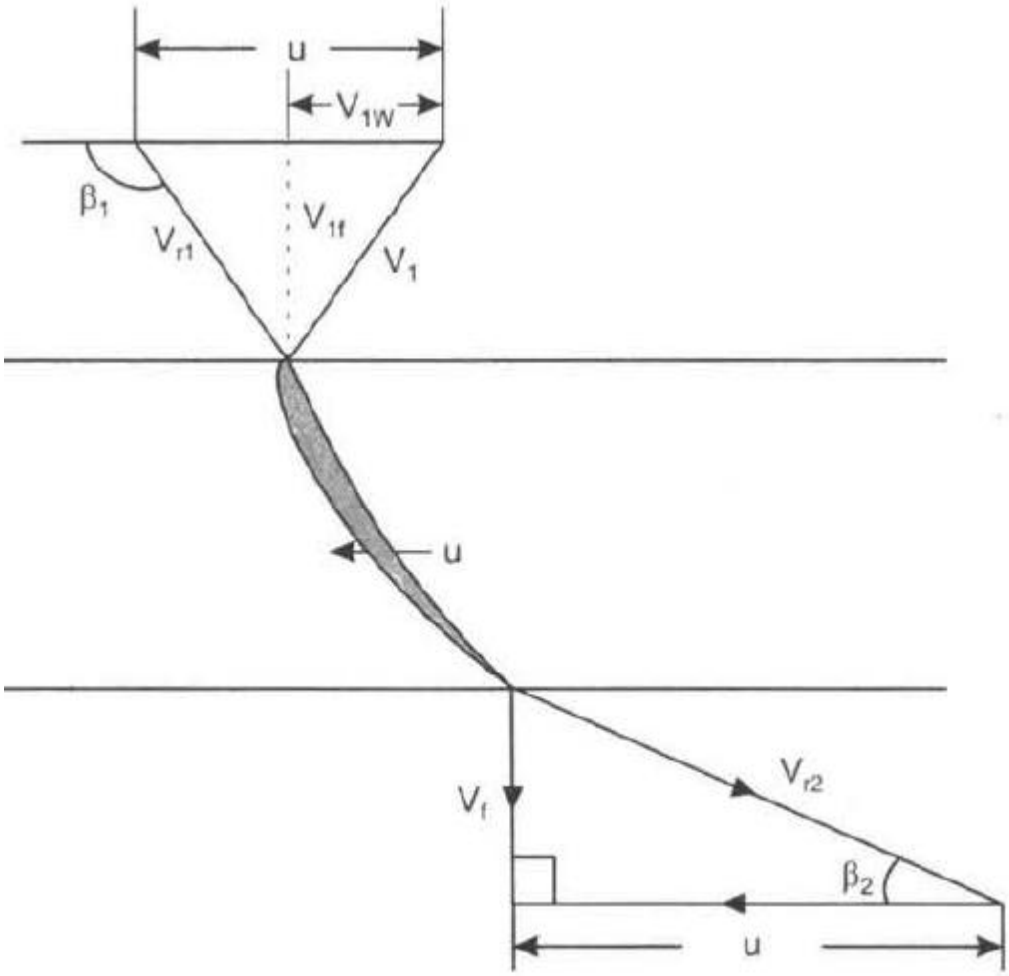

For maximum efficiency the whirl component V_{2w} at exit must be zero because velocity V_2 is axial and also

$$V_2 = V_{2f}$$

Writing Euler's equation as

$$E = \frac{u(V_{1w} - V_{2w})}{g} \qquad \text{as } V_{2w} = 0 \qquad .....(7.1)$$

$$E = \frac{uV_{1w}}{g} \qquad .....(7.2)$$

From inlet diagram, we have

$$V_{1w} = u - V_f \cot(180 - \beta_1) = u + V_f \cot\beta_1$$

Substituting this value of V_{1w} in eq. 7.2

$$E = \frac{u(u + V_f \cot\beta_1)}{g} = \frac{u^2 + uV_f \cot\beta_1}{g}$$

$$E = \frac{u^2 + uV_f \cot\beta_1}{g} \qquad .....(7.3)$$

Flow rate is given by the equation

$$Q = \text{area} \times \text{Velocity of flow}$$

$$Q = \frac{\pi}{4}(D_t^2 - D_h^2)\, V_f \qquad \text{.....(7.4)}$$

where D_t = diameter at the tip

D_h = diameter at the hub

V_f = flow velocity

Hydraulic efficiency is runner power by hydraulic power

$$\eta_h = \frac{E}{H} = \frac{\gamma QE}{\gamma QH} \qquad \text{.....(7.5)}$$

$$\text{Mechanical efficiency } \eta_m = \frac{\text{shaft power}}{\text{runner power}} = \frac{P}{\gamma QE}$$

$$\eta_m = \frac{P}{\gamma QE} \qquad \text{.....(7.6)}$$

$$\text{Overall efficiency} = \frac{\text{shaft power}}{\text{hydraulic power}} = \frac{P}{\gamma QH}$$

$$\eta_o = \frac{P}{\gamma QH} \qquad \text{.....(7.7)}$$

From eqns. 6.6, 6.7 and 6.8 we get,

$$\eta_o = \eta_m \times \eta_h \qquad \text{.....(7.8)}$$

7.6 Comparision between Francis and Kaplan Turbine

Francis	Kaplan
1. Radial flow	Axial flow
2. Number of runner blades 16-20	Number of runner blades 4-6
3. Runner blades constant profile	Twisted blades (profile changes along length of the blade
4. Low efficiences	High efficiences
5. Guide vanes adjustable to change flow rate	Both guides vanes and propeller blades adjustable to control flow rate

7.7 Comparision between Pelton and Kaplan Turbine

Pelton	Kaplan
1. Impulse type	Reaction type
2. Axial flow	Axial flow
3. Nozzle (fixed)	Guide vanes (adjustable)
4. Specific speed ($\omega_s < 1$)	Specific speed ($\omega_T > 2.3$)
5. Buckets have same profile	Blades twisted for higher efficiency

E.7.1 An axial flow turbine operates under a head of 21.8 m and develops 21 MW when running at 140 rpm. The tip diameter is 4.5 m and hub diameter is 2.0 m. The hydraulic efficiency is 94%. Determine inlet and exit angles of blades mean diameter if the overall efficiency is 88%.

Solution

Given H = 21.8 m, P = 21 MW; N = 140 rpm; D_t = 4.5 m, D_h = 2.0m,

$\eta_h = 94\%$, $\eta_n = 88\%$

$$\text{Mean diameter} = \frac{D_t + D_h}{2} = \frac{4.5 + 2.0}{2} = 3.25 \text{ m}$$

$$\omega = \frac{2N\pi}{60}; \quad \omega = \frac{2 \times 140 \times \pi}{60} = 14.65 \text{ rad/s}$$

$$u = \omega r; \quad u = \frac{14.65 \times 3.25}{2} = 23.8 \text{ m/s}$$

$$\eta_h = \frac{uV_{1w}}{gH};$$

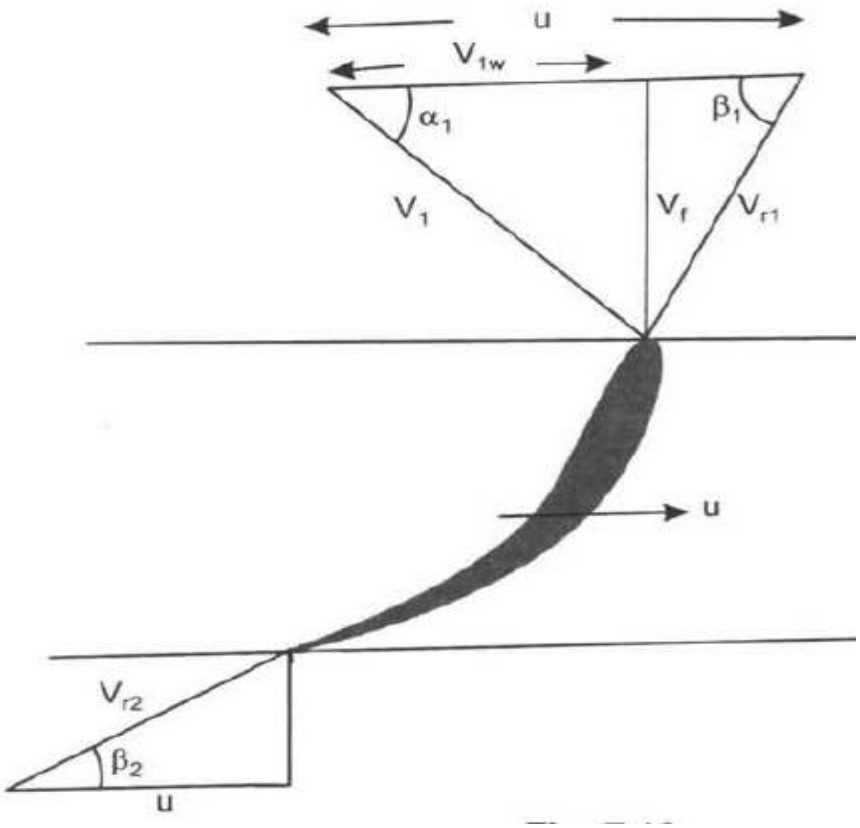

$$V_{1w} = \frac{0.94 \times 9.8 \times 21.8}{23.8} = 8.43 \text{ m/s}$$

$$\eta_0 = \frac{P}{\gamma Q H} \; ; Q = \frac{21 \times 1000 \times 1000}{0.88 \times 9800 \times 21.8} = 111.7 \text{ m}^3/\text{s}$$

$$Q = \frac{\pi}{4}\left(D_t^2 - D_h^2\right) \times V_f$$

$$111.7 = \frac{\pi}{4}\left(4.5^2 - 2^2\right) V_f$$

$$V_f = 8.75 \text{ m/s}$$

$$\tan \beta_1 = \frac{V_f}{u - V_{1w}} = \frac{8.75}{23.8 - 8.43} = \frac{8.75}{15.37} = 0.56$$

$$\beta_1 = 30^o$$

$$\tan \beta_2 = \frac{V_f}{u} = \frac{8.75}{23.8} = 0.36$$

$$\beta_2 = 20^0$$

E.7.2 An axial flow turbine with tip and hub diameters of 2.0 m and 0.8 m, respectively, rotates at 250 rpm. The runner blades are fixed and guide vanes are set at 42^0 to direction of rotation of blade at mean diameter. Also, the blade inlet angle is 148^0 from the direction of velocity of blade. Calculate,

- axial velocity
- flow rate
- exit blade angle
- Euler's power

Solution

Given $D_t = 2.0$ m; $D_h = 0.8$ m; $N = 250$ rpm

$\alpha_1 = 42^0$; $\beta_1 = 148^0$

$$D = = \frac{2+0.8}{2} = 1.4 \text{ m}$$

$$u = \frac{\pi D N}{60} = \frac{\pi \times 1.4 \times 250}{60} = 18.3 \text{ m/s}$$

From inlet triangle of velocities diagram of Fig. 7.11, we have

$$V_f = \tan(\pi - \beta_1)(u - v_{1w}) = \tan \alpha_1 \, V_{1w}$$

$\therefore$ $\tan(\pi - 148)(18.3 - V_{1w}) = \tan 42 \, V_{1w}$

$\therefore$ $V_{1w} = 7.5$ m/s

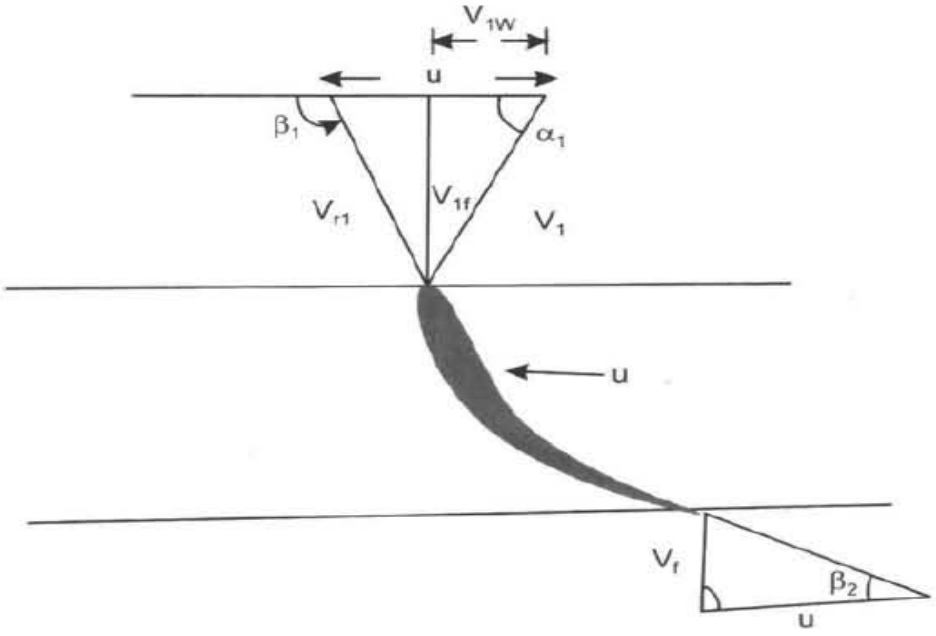

$$\tan \alpha_1 = \frac{V_f}{V_{1w}},$$

$$V_f = 7.5 \times \tan 42 = 6.75 \text{ m/s}$$

$$Q = \frac{\pi}{4}\left(D_t^2 - D_h^2\right) V_f = \frac{\pi}{4}(2^2 - 0.8^2)\, 6.75 = 17.8 \text{ m}^3/\text{s}$$

Euler's head $$E = \frac{u\, V_{1w}}{g} = \frac{18.3 \times 7.5}{9.8} = 14 \text{ m}$$

Euler's power $$\gamma Q E = \frac{9800 \times 17.8 \times 14}{1000} = 2.4 \text{ kW}$$

$$\tan \beta_2 = \frac{V_f}{u} = \frac{6.75}{18.3} = 0.368$$

$$\beta_2 = 20^\circ$$

Geothermal Energy

الطاقة الحرارية الأرضية

الطاقة الحرارية الأرضية هي حرارة الأرض - وهي مورد نظيف ومتجدد يوفر الطاقة حول العالم. تستخدم الولايات المتحدة محطات الطاقة الحرارية الأرضية التجارية على نطاق واسع في درجات حرارة الموارد العميقة (بين 200 درجة فهرنهايت و 700 درجة فهرنهايت) منذ الستينيات. يعد تطوير وإنتاج الطاقة الحرارية الجوفية سوقًا عالميًا مزدهرًا.

1.1. ما هي الطاقة الحرارية الجوفية؟

تنتشر الحرارة من مركز الأرض منذ حوالي 4.5 مليار سنة. عند عمق 6437.4 كم (4000 ميل) ، يحوم مركز الأرض حول نفس درجات الحرارة مثل سطح الشمس ، 9932 درجة فهرنهايت (5500 درجة مئوية) (الشكل 1). يقدر العلماء أن 42 مليون ميجاوات (MW) من تدفق الطاقة من باطن الأرض ، في المقام الأول عن طريق توصيل الطاقة الحرارية الأرضية هي مورد متجدد. واحد من أكبر مزاياها أنها متاحة باستمرار. يضمن التدفق المستمر للحرارة من الأرض إمدادًا لا ينضب من الطاقة بلا حدود لمليارات السنين القادمة.

Figure 1: Temperatures in the Earth

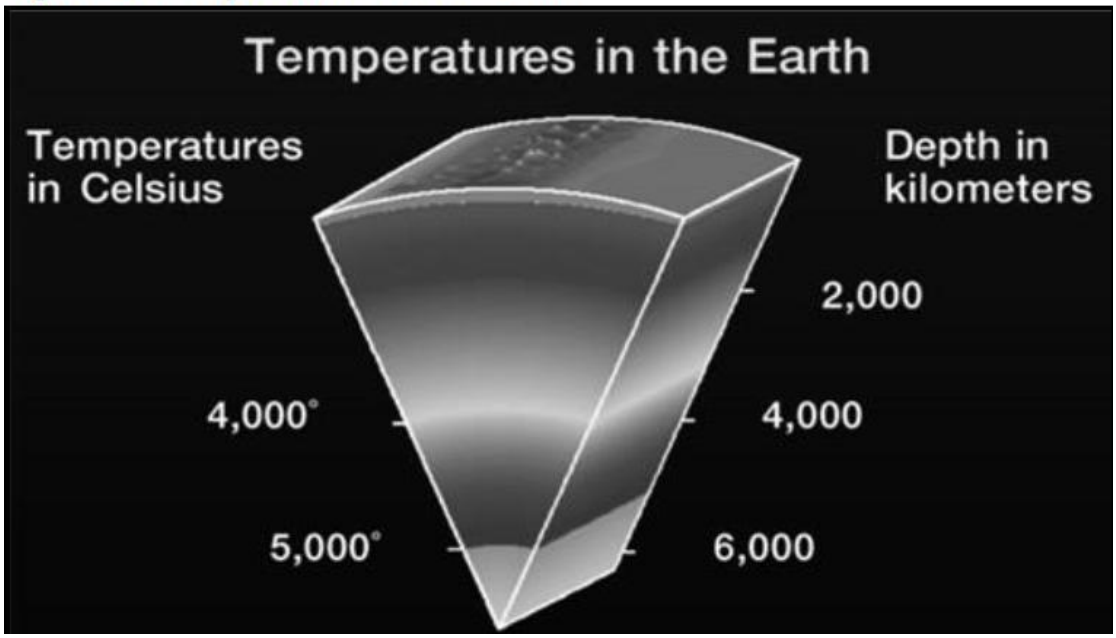

كانت استخدامات الطاقة الحرارية الأرضية لأغراض الحرارة والأغراض الأخرى ممارسات محلية عبر مجموعة متنوعة من ثقافات العالم: "استخدم في نيوزيلندا المياه من الينابيع الساخنة لأغراض الطهي والأغراض الطبية لآلاف السنين. كان لدى الإغريق والرومان القدماء منتجعات حرارية. قام سكان بومبي ، الذين يعيشون بالقرب من جبل فيزوف ، باستغلال الماء الساخن من الأرض لتدفئة مبانيهم. استخدم الرومان المياه الحرارية الأرضية لعلاج أمراض العيون والجلد. يتمتع اليابانيون بمنتجعات حرارية أرضية لقرون.

تغذي مياه الأمطار وذوبان الثلوج طبقات المياه الجوفية الحرارية الجوفية (الشكل 2). عندما يتم حبس الماء الساخن أو البخار في الشقوق والمسام تحت طبقة من الصخور غير المنفتحة ، فإنه يشكل خزانًا حراريًا.

Figure 2: Geothermal Reservoir

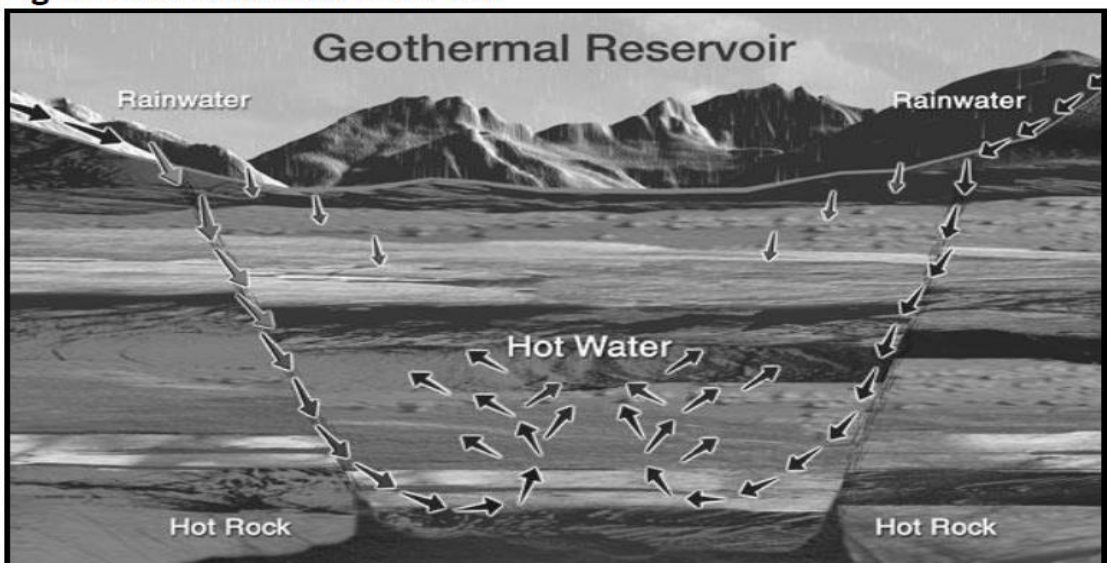

1.2. ما هو مصدر طاقة الأساسي؟

تنتج محطة توليد الطاقة الأساسية الطاقة بمعدل ثابت. نظرًا لأن الطاقة ثابتة ، يمكن أن يظل ناتج الطاقة ثابتًا لمدة 24 ساعة تقريبًا في اليوم ، مما يمنح الطاقة الحرارية الأرضية عامل قدرة أعلى من الطاقة الشمسية أو طاقة الرياح ، والتي يجب أن تنتظر حتى تشرق الشمس أو تهب الرياح ، على التوالي. وهذا يعني أن محطة حرارية أرضية بسعة أقل من محطة تعمل بالطاقة الشمسية أو الرياح يمكن أن توفر كهرباء أكثر توصيلًا.

1.3 كيف تعمل محطة الطاقة الحرارية الأرضية التقليدية؟

بعد الاستكشاف والتحليل الدقيقين ، يتم حفر الآبار لجلب الطاقة الحرارية الأرضية إلى السطح ، حيث يتم تحويلها إلى كهرباء. يوضح الشكل 4 القدرة الحرارية الأرضية المركبة في الولايات المتحدة من 1975 إلى 2012 ، مفصولة حسب نوع التكنولوجيا.

Figure 4: Total U.S. Geothermal Installed Capacity by Technology (MW) 1975–2012

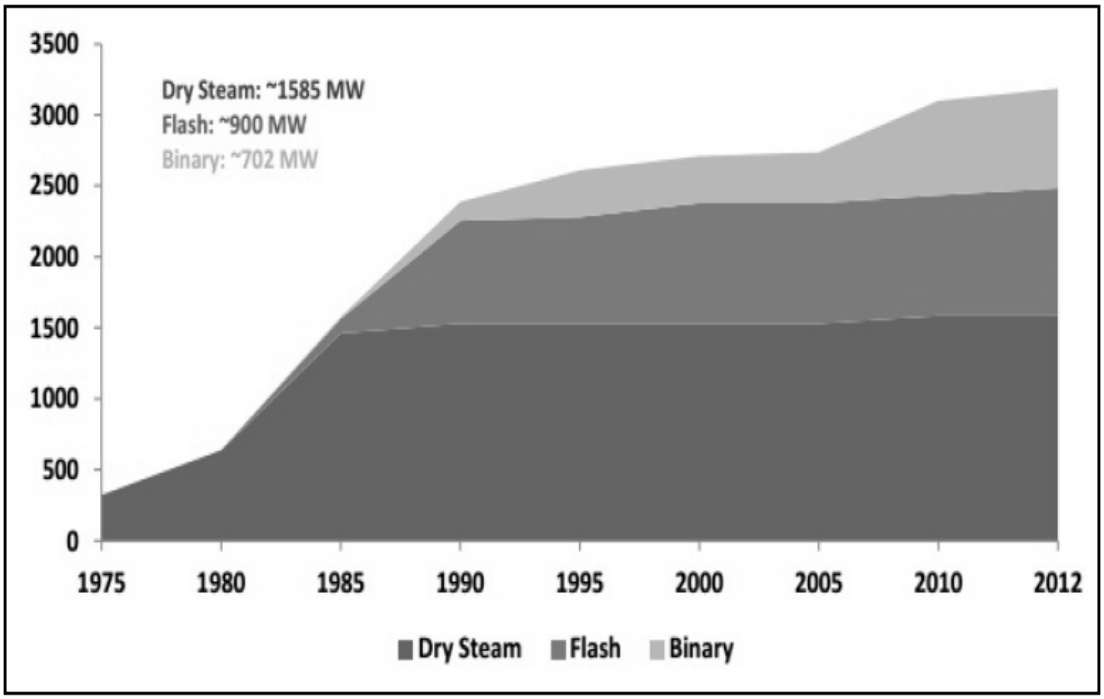

حددت هيئة المسح الجيولوجي الأمريكية مصادر درجة الحرارة المعتدلة بأنها تلك التي تتراوح بين 90 درجة مئوية و 150 درجة مئوية ، وأنظمة الطاقة الحرارية الأرضية عالية الحرارة مثل تلك التي تزيد عن 150 درجة مئوية . الأشكال 5 إلى 7 تصور الأنواع التجارية الثلاثة محطات الطاقة الحرارية الأرضية التقليدية: **وميض ، بخار جاف ، وثنائي.**

في محطة الطاقة الحرارية الأرضية ، يفصل الضغط العالي البخار عن الماء في "فاصل البخار" (الشكل 5) مع ارتفاع الماء وعند انخفاض الضغط. يتم تسليم البخار إلى التوربين ، ثم يقوم التوربين بتشغيل المولد. يتم إعادة حقن السائل في الخزان.

Figure 5: Flash Power Plant

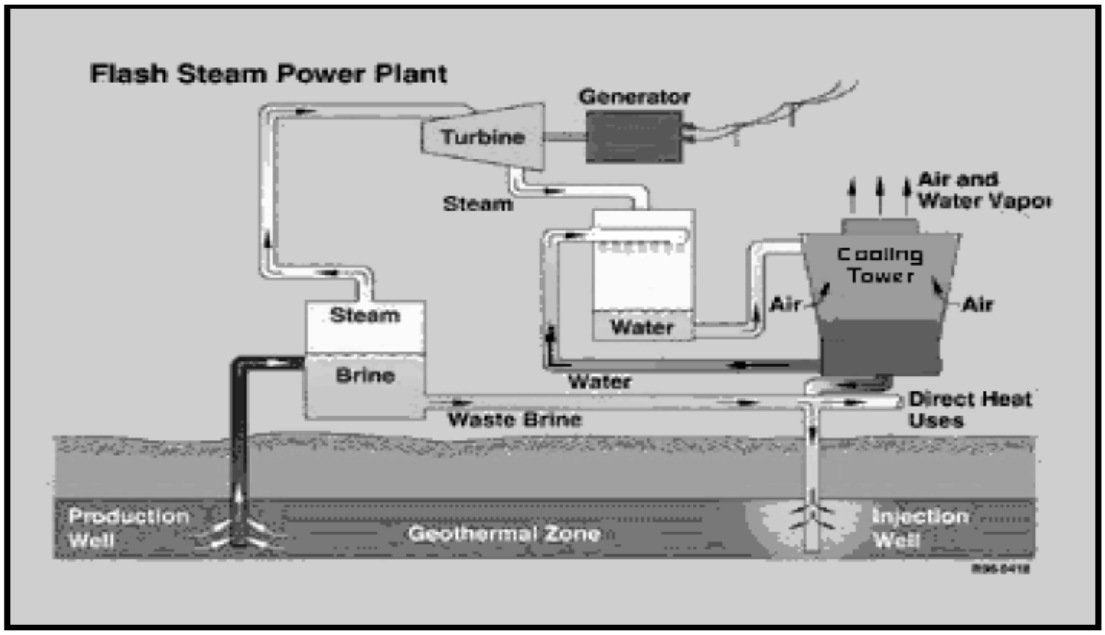

محطة توليد الطاقة البخارية الجافة الحرارية الأرضية ، يتم إنتاج البخار وحده مباشرة من خزان الطاقة الحرارية الأرضية ويستخدم لتشغيل التوربينات التي تعمل على تشغيل المولد (الشكل 6). نظرًا لعدم وجود ماء ، فإن جهاز فصل البخار المستخدم في مصنع الفلاش ليس ضروريًا. تمثل محطات توليد الطاقة بالبخار الجاف حوالي 50٪ من الطاقة الحرارية الأرضية المركبة في الولايات المتحدة وتقع في كاليفورنيا .

Figure 6: Dry Steam Power Plant

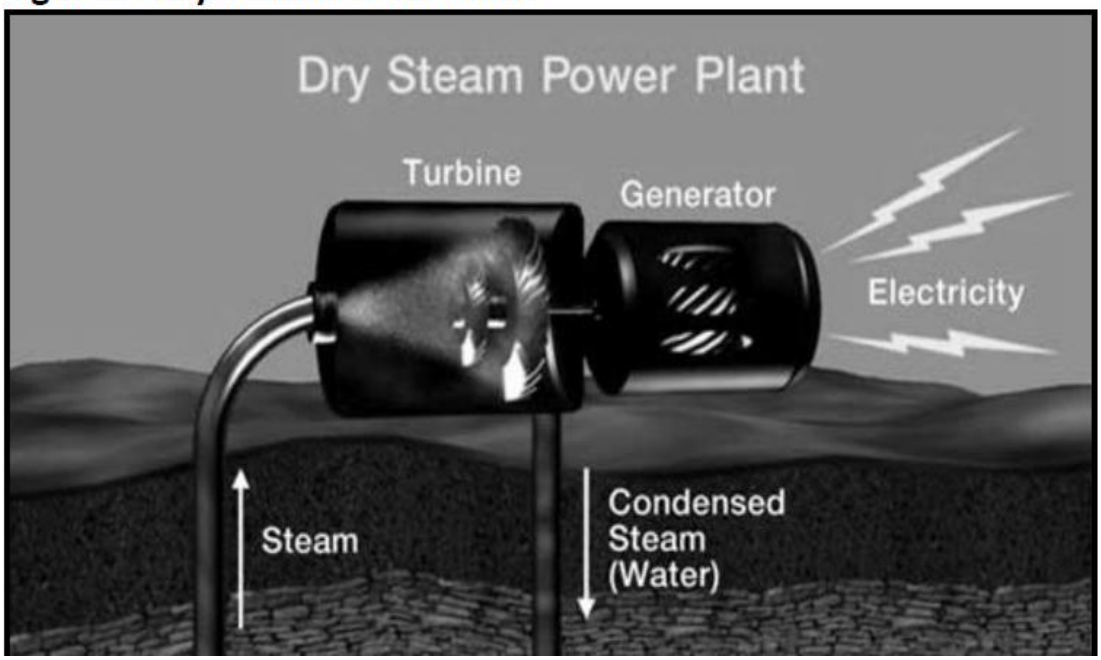

في عام 1981 في مشروع في إمبريال فالي ، كاليفورنيا ، أنشأت التقنيات الجدوى الفنية من النوع التقليدي الثالث لمحطة الطاقة الحرارية الأرضية التجارية على نطاق واسع: ثنائي. كان المشروع ناجحًا للغاية لدرجة أنه سدد قرضه لوزارة الطاقة (DOE) في غضون عام . جعلت محطات الطاقة الحرارية الأرضية الثنائية من الممكن إنتاج الكهرباء من الموارد الحرارية الأرضية أقل من (150 درجة مئوية). وقد أدى ذلك إلى توسيع البصمة الجغرافية للصناعة الأمريكية ، خاصة في العقد الماضي.

تستخدم المحطات الثنائية نظام دورة رانكين, الذي يستخدم المياه الحرارية الأرضية لتسخين سائل ثانٍ يغلي عند درجة حرارة أقل من الماء ، مثل أيزوبيوتان أو خماسي فلورو بروبان. يسمى هذا السائل العامل (أو "السائل الدافع" في الشكل 7). يقوم المبادل الحراري بفصل الماء عن مائع العمل أثناء نقل الطاقة الحرارية. عندما يتبخر مائع العمل ، فإن قوة بخار التمدد ، مثل البخار ، تحول التوربينات الى المولدات. يتم بعد ذلك إعادة ضخ المياه الحرارية الجوفية في حلقة مغلقة ، مع فصلها عن مصادر المياه الجوفية وخفض معدلات الانبعاث بشكل أكبر

(انظر القسم 5). معظم المحطات الحرارية الأرضية الجديدة قيد التطوير في الولايات المتحدة ثنائية

Figure 7: Binary Power Plant

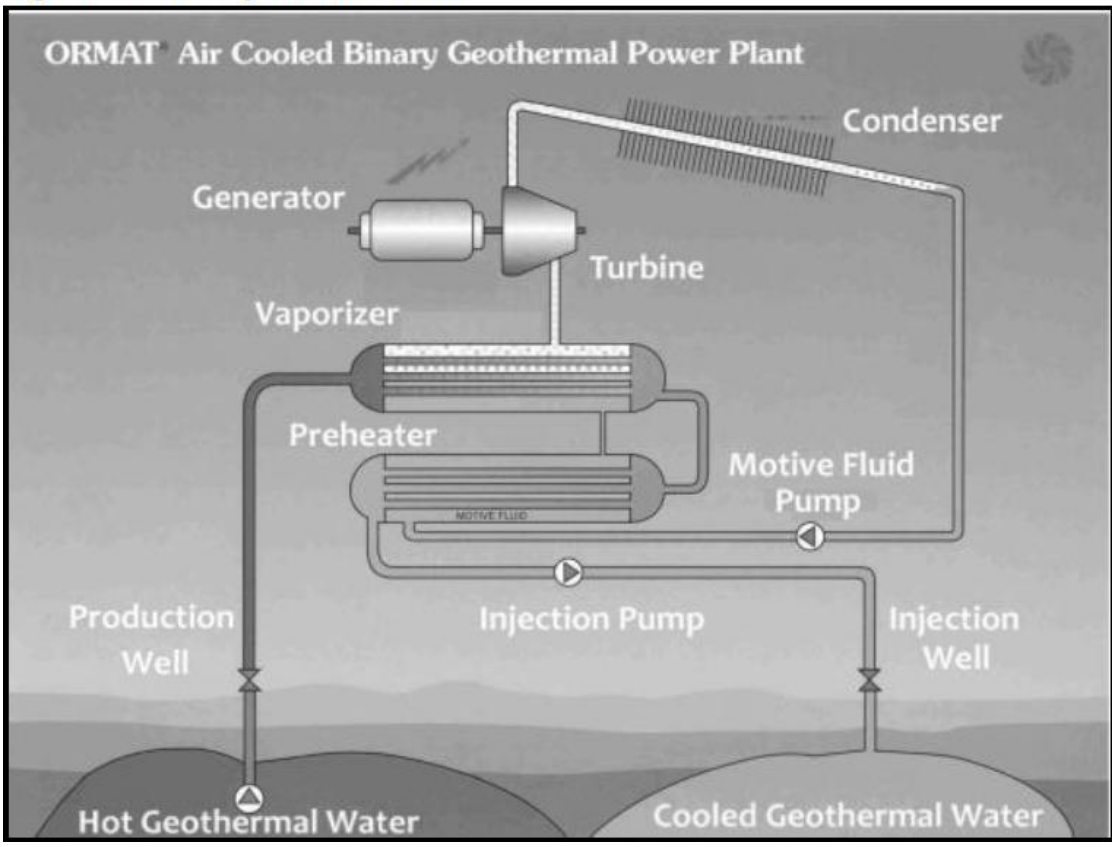

تسمح محطات الطاقة الهجينة بدمج العديد من تقنيات التوليد. في هاواي ، يعمل نظام الدورة المركبة الثنائي فلاش / بونا على تحسين تقنيات الفلاش والحرارة الأرضية الثنائية. تومض سائل الطاقة الحرارية الأرضية إلى خليط من البخار والسائل في الفاصل. يتم تغذية البخار إلى التوربين كما هو الحال في مولد البخار الومضي ويتم تغذية السائل المنفصل إلى مولد دورة ثنائية (الشكل 8).

Figure 8: Flash/Binary Power Plant

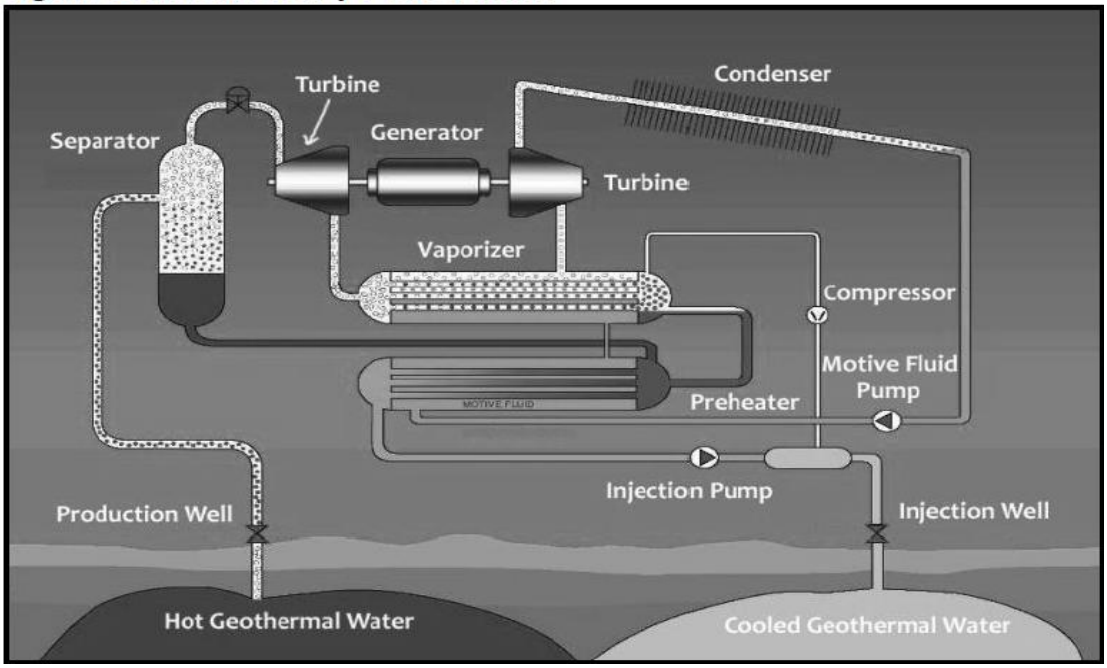

نوع آخر من المحطات الهجينة هو محطة الطاقة الشمسية الحرارية الأرضية لشركة Enel Green Power في ستيلووتر ، نيفادا. يمكن أن يكون هذا النوع من الهجين خيارًا في المناطق الغنية بالموارد ولكنها تتطلب دعمًا اقتصاديًا أو تكنولوجيًا إضافيًا لجعلها قابلة للتطوير في مجال الطاقة.

1.4. كيف تعمل مضخات الحرارة الحرارية الأرضية؟

تختبئ الحيوانات تحت الأرض من أجل الدفء في الشتاء وللهروب من حرارة الصيف. يتم تطبيق نفس المبدأ الأساسي لدرجة الحرارة الثابتة والمعتدلة في باطن الأرض على مضخات الحرارة الحرارية الأرضية (GHPs). تستخدم GHPs متوسط درجات حرارة الأرض بين 40˚ و 70˚ فهرنهايت. في عام 1948 ، طور أستاذ في جامعة ولاية أوهايو أول GHP للاستخدام في مقر إقامته. دخلت مضخة حرارة المياه الجوفية إلى الاستخدام التجاري في ولاية أوريغون في نفس الوقت تقريبًا .

Figure 9: Geothermal Heat Pumps

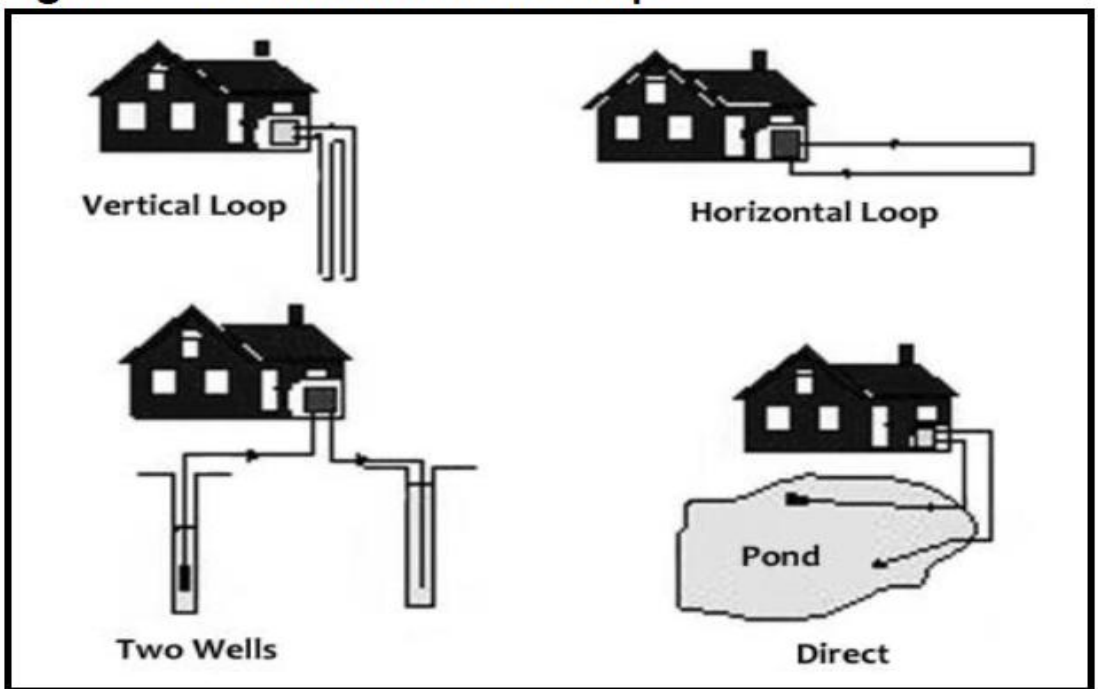

تقوم أنظمة التدفئة والتبريد GHP (Geothermal heat pump) بتدوير الماء أو السوائل الأخرى لسحب الحرارة من الأرض من خلال الأنابيب في حلقة مستمرة من خلال مضخة حرارية ونظام مجاري تقليدي. للتبريد ، يتم عكس العملية ؛ يقوم النظام باستخراج الحرارة من المبنى ويعيدها إلى حلقة الأرض. يمكن استخدام نظام الحلقات في كل مكان تقريبًا في العالم على أعماق أقل من 10 أقدام إلى 300 قدمًا ، ويتم استخدام GHPs في جميع الولايات الخمسين وهي أكثر كفاءة في استهلاك الطاقة بنسبة 45٪ من خيارات أنظمة التدفئة والتبريد القياسية.

1.5. كيف تعمل تطبيقات الاستخدام المباشر؟

يتم استخدام الحرارة الجوفية بشكل مباشر ، بدون محطة للطاقة أو مضخة حرارية ، لتطبيقات مثل التدفئة والتبريد في الأماكن ، وإعداد الطعام ، وحمام الينابيع الساخنة والمنتجعات (العلاج بالمياه المعدنية) ، والزراعة ، وتربية الأحياء المائية ، والبيوت الزجاجية ، وصهر الثلج ، والعمليات الصناعية. يتم تطبيق الاستخدامات الحرارية الأرضية المباشرة عند درجات حرارة الخزان الجوفي ما

بين 90 درجة فهرنهايت و 200 درجة فهرنهايت. ويمكن أيضًا توجيه الحرارة إلى وحدة تسخين المياه لاستخدام المياه الساخنة.

الخلاصة

الطاقة الحرارية الأرضية هي الطاقة الناتجة عن حرارة قلب الأرض. الطاقة الحرارية الأرضية مورد متجدد ، لأن أصله من قلب الأرض. يمكن استخدام الطاقة الحرارية الأرضية لتوليد الكهرباء والاستخدام المباشر للحرارة والذي يشمل الاستخدام المباشر لتدفئة المباني.

بسبب العمليات الجيولوجية المعروفة باسم تكتونية الصفائح ، تم كسر قشرة الأرض 12 طبقًا ضخمًا يتحرك أو ينفصل معًا بمعدل مليمترات في السنة. حيث الطبقتان تصطدم ، يمكن أن تدفع لوحة واحدة تحت الأخرى ، وتنتج ظواهر استثنائية مثل المحيط الخنادق أو الزلازل القوية. في أعماق كبيرة ، وفوق الصفيحة السفلية ، تصبح درجات الحرارة عالية بما يكفي لإذابة الصخور ، وتشكيل الصهارة (Magma). لأن الصهارة أقل كثافة من الصخور المحيطة بها يتحرك نحو قشرة الأرض ويحمل الحرارة من الأسفل. في بعض الأحيان ترتفع الصهارة إلى السطح من خلال قشرة رقيقة أو مكسورة مثل الحمم البركانية.

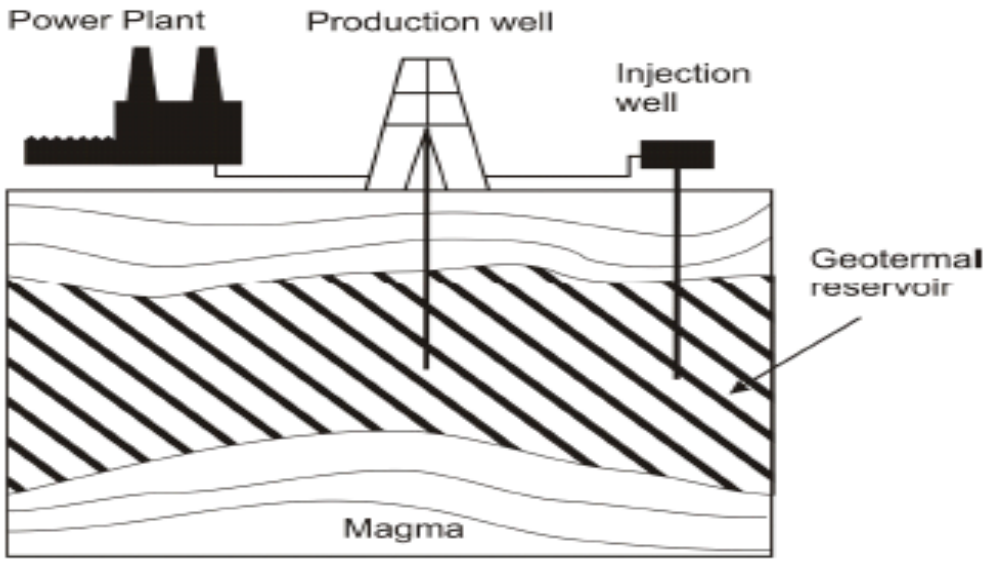

Fig.1. Schematic of geothermal power plant production and injection wells

ومع ذلك ، تظل معظم الصهارة تحت قشرة الأرض وتسخن الصخور المحيطة و المياه الجوفية. يأتي جزء من هذه المياه على طول الطريق إلى السطح من خلال العيوب والشقوق في الأرض مثل الينابيع الساخنة أو السخانات. عندما يكون هذا الماء الساخن المرتفع والبخار محاصرين في نفاذية الصخور تحت طبقة من الصخور غير منفذة ، ويسمى خزان الحرارة الجوفية. هذه الخزانات مصادر الطاقة الحرارية الأرضية التي يمكن استغلالها لتوليد الكهرباء أو الاستخدام المباشر.
الشكل (1) هو رسم تخطيطي لمحطة طاقة حرارية نموذجية توضح موقع الصهارة و خزان الحرارة الجوفية. هنا ، يسحب الإنتاج جيدا السوائل الحرارية الأرضية ، و يعيد بئر الحقن السوائل المبردة إلى الخزان.

يتناول استكشاف الطاقة الحرارية الأرضية سبعة أهداف على الأقل:
1. تحديد الظواهر الحرارية الأرضية
2. التأكد من وجود مجال إنتاج حراري جوفي مفيد
3. تقدير حجم المورد
4. تصنيف مجال الطاقة الحرارية الأرضية
5. موقع المناطق المنتجة
6. تحديد المحتوى الحراري للسوائل التي سيتم تصريفها بواسطة الآبار في مجال الطاقة الحرارية الأرضية
7. تجميع مجموعة من البيانات التي يمكن من خلالها عرض نتائج الرصد المستقبلي

Dry steam
Power plants using dry steam systems were the first type of geothermal power generation plants built. They use steam from the geothermal reservoir as it comes from wells and route it directly through turbine/generator units to produce electricity. An example of a

dry steam generation operation is at the Geysers Region in northern California.

البخار الجاف

كانت محطات الطاقة التي تستخدم أنظمة البخار الجاف النوع الأول من محطات توليد الطاقة الحرارية الأرضية مبني. يستخدمون البخار من خزان الطاقة الحرارية الأرضية لأنه يأتي من الآبار ويوجهها مباشرة من خلال وحدات التوربينات / المولدات لإنتاج الكهرباء. مثال على عملية توليد البخار الجاف في منطقة السخان في شمال كاليفورنيا

Flash steam

Flash steam plants are the most common type of geothermal power generation plants in operation today. They use water at temperatures greater than 360°F (182°C) that is pumped under high pressure to the generation equipment at the surface. Upon reaching the generation equipment, the pressure is suddenly reduced, allowing some of the hot water to convert or “flash” into steam. This steam is then used to power the turbine/generator units to produce electricity. The remaining hot water not flashed into steam, and the water condensed from the steam, is generally pumped back into the reservoir. An example of an area using the flash steam operation is the CalEnergy Navy I flash geothermal power plant at the Coso geothermal field.

وميض البخار

محطات البخار السريعة هي النوع الأكثر شيوعًا لمحطات توليد الطاقة الحرارية الأرضية العاملة اليوم. يستخدمون الماء عند درجات حرارة أكبر من 360 درجة فهرنهايت (182 درجة مئوية) يتم ضخها تحت ضغط عال لمعدات التوليد على السطح. عند الوصول إلى معدات التوليد ، يتم تقليل الضغط فجأة ، مما يسمح بتحويل أو "وميض" بعض الماء الساخن إلى بخار. ثم يستخدم هذا البخار لتشغيل التوربينات / وحدات المولدات لإنتاج الكهرباء. لا يتم وميض الماء الساخن المتبقي

في البخار ، ويتم ضخ الماء المتكثف من البخار بشكل عام إلى الخزان. مثال على منطقة تستخدم عملية البخار الفلاش هي محطة توليد الطاقة الحرارية الأرضية من CalEnergy Navy I في حقل Coso الحرارية الأرضية.

Binary Cycle:

Binary cycle geothermal power generation plants differ from dry steam and flash steam systems because the water or steam from the geothermal reservoir never comes in contact with the turbine/generator units. In the binary system, the water from the geothermal reservoir is used to heat another “working fluid,” which is vaporized and used to turn the turbine/generator units. The geothermal water and the “working fluid” are each confined in separate circulating systems or “closed loops” and never come in contact with each other. The advantage of the binary cycle plant is that they can operate with lower temperature waters (225°F to 360°F) by using working fluids that have an even lower boiling point than water. They also produce no air emissions. An example of an area using a binary cycle power generation system is the Mammoth Pacific binary geothermal power plants at the Casa Diablo geothermal field .

الدورة الثنائية:

تختلف محطات توليد الطاقة الحرارية الأرضية ذات الدورة الثنائية عن أنظمة البخار الجاف والبخار لأن الماء أو البخار من خزان الطاقة الحرارية الأرضية لا يتلامسان مع وحدات التوربينات / المولدات. في النظام الثنائي ، يتم استخدام المياه من الخزان الحراري الجوفي لتسخين "سائل عمل" آخر ، يتم تبخيره واستخدامه لتحويل وحدات التوربينات / المولدات. كل من المياه الحرارية الأرضية و "مائع العمل" محصوران في أنظمة تدوير منفصلة أو "حلقات مغلقة" ولا يتلامسان مع بعضهما البعض. ميزة محطة الدورة الثنائية هي أنها يمكن أن تعمل في مياه ذات درجة حرارة منخفضة (225 درجة فهرنهايت إلى 360 درجة فهرنهايت)

باستخدام سوائل العمل التي لها نقطة غليان أقل من الماء. كما أنها لا تنتج انبعاثات الهواء. مثال على منطقة تستخدم نظام توليد الطاقة بالدورة الثنائية هو محطات الطاقة الحرارية الأرضية الثنائية ماموث باسيفيك في حقل كازا ديابلو الحرارية الأرضية.

Types of geothermal power plants

There are three basic types of geothermal power plants:

- **Dry steam plants** use steam directly from a geothermal reservoir to turn generator turbines. The first geothermal power plant was built in 1904 in Tuscany, Italy, where natural steam erupted from the earth.
- **Flash steam plants** take high-pressure hot water from deep inside the earth and convert it to steam to drive generator turbines. When the steam cools, it condenses to water and is injected back into the ground to be used again. Most geothermal power plants are flash steam plants.
- **Binary cycle power plants** transfer the heat from geothermal hot water to another liquid. The heat causes the second liquid to turn to steam, which is used to drive a generator turbine.

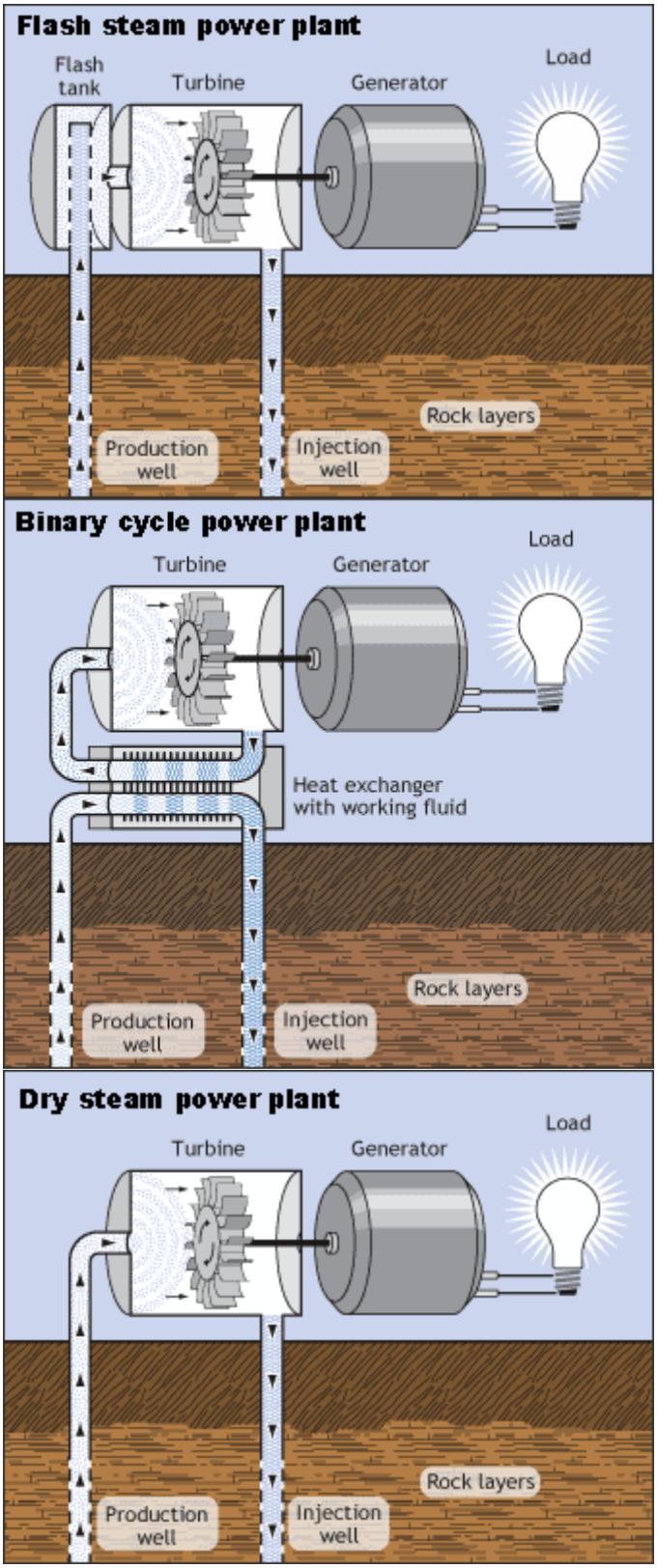
Flash steam power plant
Flash tank
Turbine
Generator
Load
Rock layers
Production well
Injection well
Binary cycle power plant
Turbine
Generator
Load
Heat exchanger with working fluid
Rock layers
Production well
Injection well
Dry steam power plant
Turbine
Generator
Load
Rock layers
Production well
Injection well

CENTRE FOR RENEWABLE &
SUSTAINABLE ENERGY STUDIES

Biomass Energy

UNIVERSITEIT iYUNIVESITHI STELLENBOSCH UNIVERSITY 100 1918 · 2018

science & technology
Department:
Science and Technology
REPUBLIC OF SOUTH AFRICA

NRF National Research Foundation

Eskom

What is Biomass Energy?

- **Biomass** energy is energy derived from **plants** and **animal waste** which are, or were recently, living material.
- Through **photosynthesis**, **light energy** from the sun is converted to **chemical energy** which is stored in plants.
- **Animals** eat plants and **store** the **chemical energy**.
- This stored **chemical energy** in the biomass can be **converted into electricity, fuel and heat**.
- **Evasive species** like seaweed are used as a **source of bioenergy** in recent research.
- Bioenergy plant sources can be divided into **woody, cellulosic and oil rich plants.**

Types of Biomass

Primary Source

Crops

Wood fuel

Sugar cane

Secondary Source

Paper mill sludge

Plant residue

Sewage

Sources

- **Biomass** is **available** almost **everywhere** in the world.
- **Biomass** is divided into **primary** and **secondary** sources.
- **Primary biomass** energy sources are plant materials grown for energy production, such as wood, crops, fruits, maize, sugar cane, and sunflower seeds which get converted to sunflower oil.
- **Secondary biomass** energy sources are **'waste' materials** which can be used for energy production. These include
  - Plant residues: agricultural and forestry residues
  - Fish and animal waste: manure, fish heads and abattoir waste
  - Waste yeast from the beer-brewing industry
  - Paper mill sludge
  - Sewage

Types of Biomass

Primary Source

Crops

Wood fuel

Sugar cane

Secondary Source

Paper mill sludge

Plant residue

Sewage

Sources

- Good primary biomass energy sources have a high yield of **dry material** and **use minimal land**.
- Crops should **generate more energy** than their production consumes.
- Biological power sources are **renewable** and, if harvested sustainably, **CO_2 neutral**.
- This is because the gas emitted during the transfer into useful energy is balanced by the CO_2 absorbed whilst the plants were still growing.
- Unfortunately biomass is **not easily stored** and transport is expensive.

Biomass Conversion Technologies and Products

Harvesting; Pre-Processing

↓

Transport to Bioenergy Plant

↓

- **Combustion** is the process of **burning of material to produce heat**. The heat produced can be used to produce steam to generate electricity.
- **Anaerobic digestion** is a series of biological processes where microorganisms **break down biodegradable material in the absence of oxygen**. The product is biogas (CO_2 and CH_4) and liquid fertilizer. Biogas can be burnt directly for cooking or to produce electricity.
- **Fermentation** is the **conversion of sugar** into acids or alcohol **with the help of bacteria or yeast**.
- **Mechanical processing** can be, for example, **grinding** seeds to extract the oils they contain to produce biofuels.

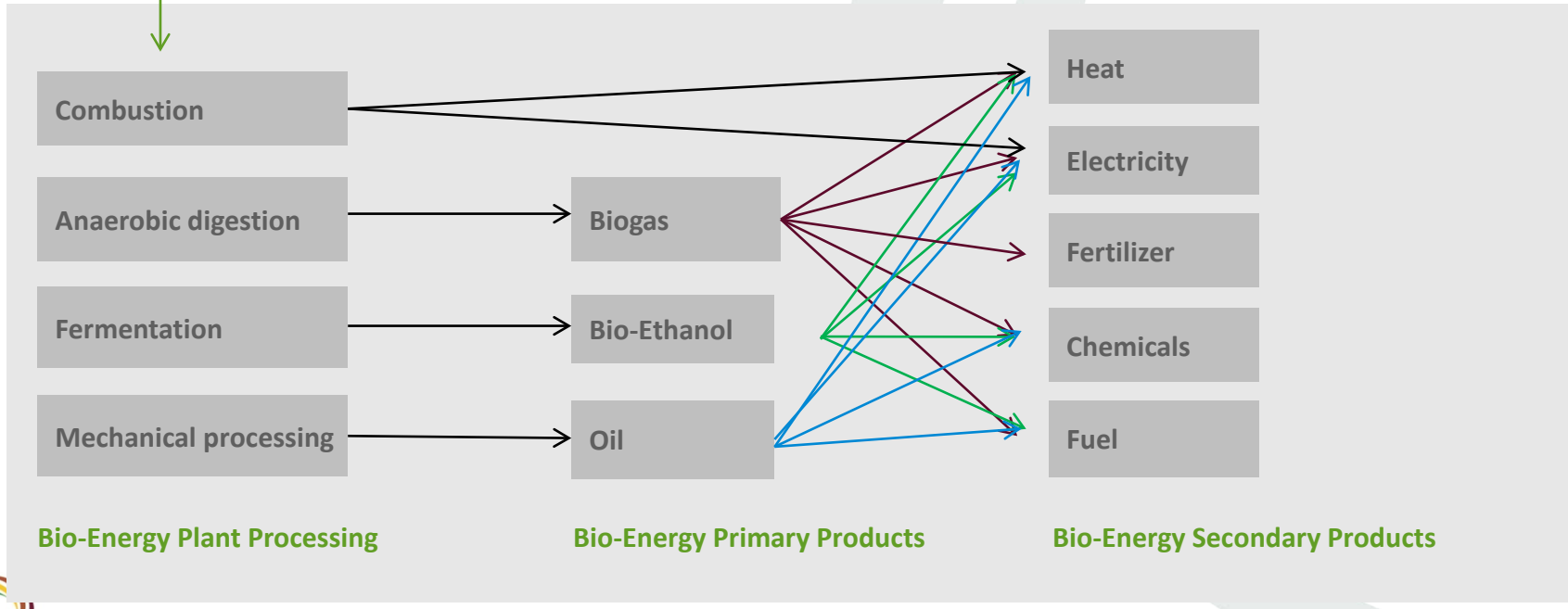

Uses of Biomass: Combustion (Heating & Cooking)

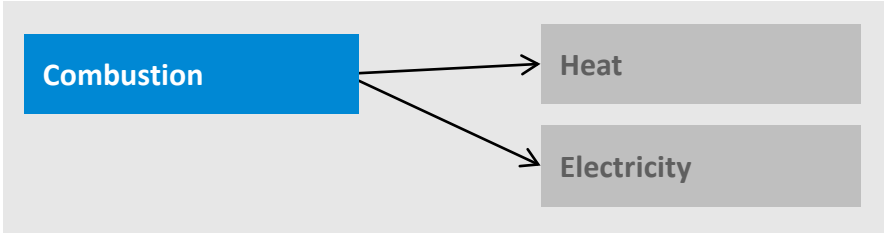

Wood can be burned for heating living spaces or to prepare food.

Uses of Biomass: Combustion (Generating Electricity)

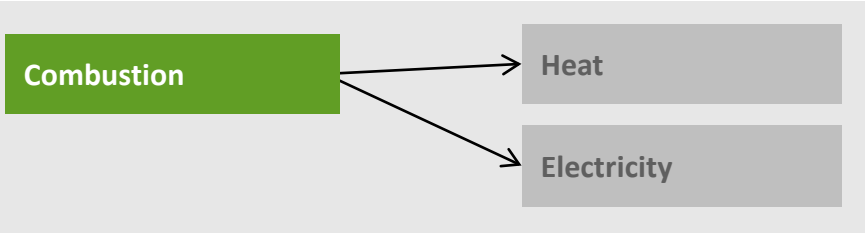

- When wood is burned, the **chemical energy** in biomass is released as **heat and light energy**.
- Biomass power plants work on a **similar principle to natural gas or coal power plants**.
- The heat energy being released **boils water to form steam**, which then turns a generator.
- In combined heat and power systems, the **surplus heat energy** can also be utilized, for example for heating water or nearby homes.
- These power plants are usually **not as large as coal power stations** because their fuel supply has a lower energy content and is not as abundant as coal.

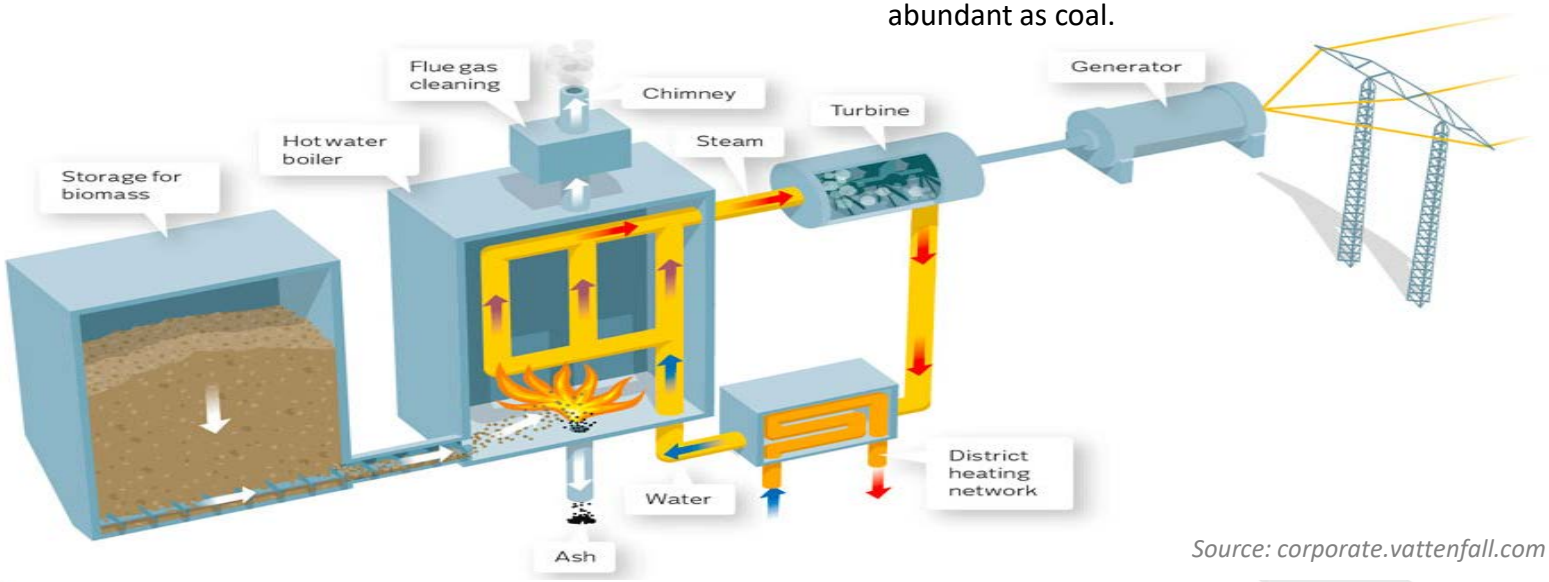

Source: corporate.vattenfall.com

Uses of Biomass: Anaerobic Digestion (Biogas digester)

10m³ Balloon-type digesters installed at Krwakrwa and Melani villages in the Eastern Cape

6m³ Fibreglass fixed-dome digesters installed at Melani, Sompondo, Francis, and Krwakrwa villages

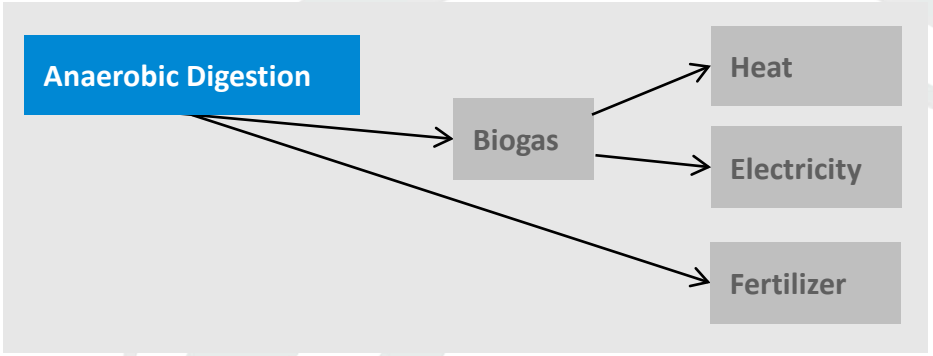

- **Anaerobic digestion** is the process where microorganisms break down organic materials into sugars and then into various acids which are further broken down to produce bio-gas. **Biogas** is a mixture of CO_2 and CH_4. CH_4 (**Methane**) is a combustible gas that can be used directly in biogas stoves for cooking, or in gas engines to produce electricity.
- A **biogas digester** consists of one or more airtight reservoirs into which a suitable feedstock (cow dung, human waste, and abattoir waste or plant material) is placed. The waste should have a high moisture content.
- **Small-scale digesters** for household use are commonly made of concrete, bricks, metal, fibreglass, or plastic.
- **Larger commercial biogas digesters** are made mainly of bricks, mortar, and steel.
- An odourless phosphorus- and nitrogen-laden slurry is produced as waste – an excellent **fertilizer**!
- Depending on the temperature and moisture content, it takes about **6–25 days to fully process a batch**; simpler digesters may take longer.

Uses of Biomass: Anaerobic Digestion (Landfill power plant)

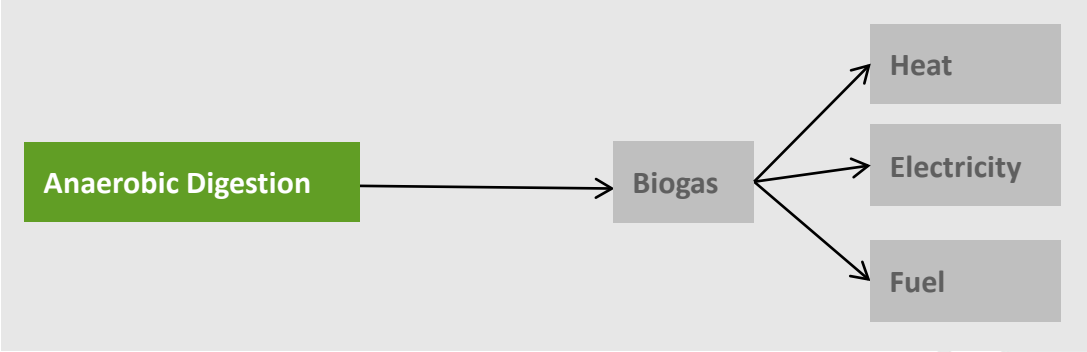

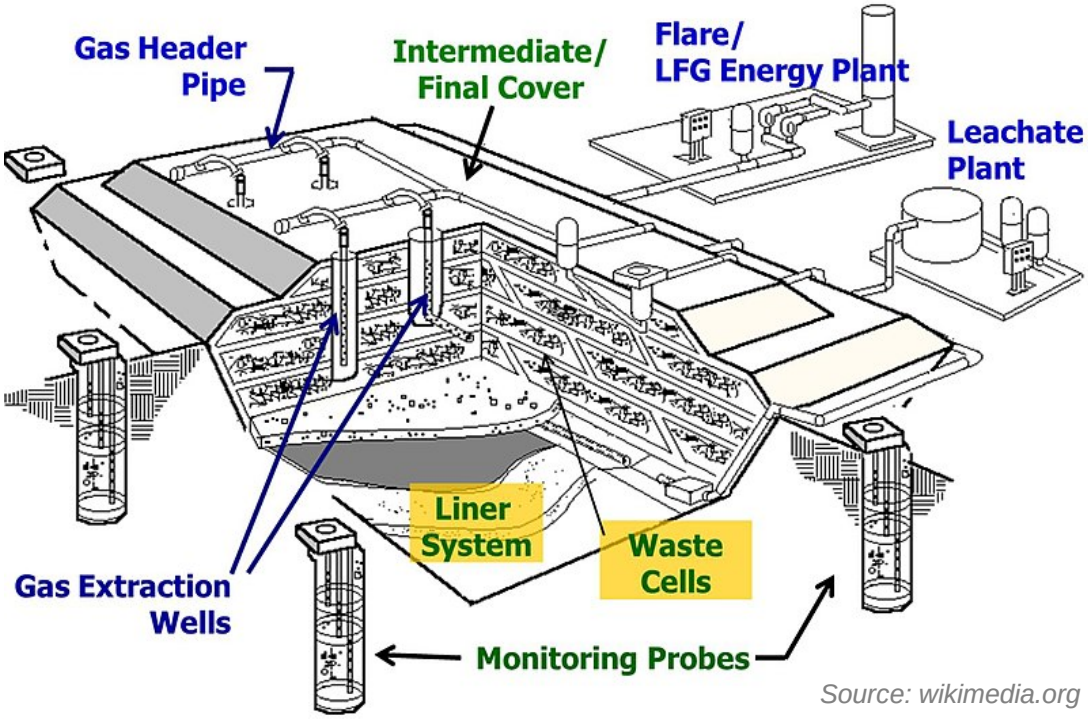

Source: wikimedia.org

- **Landfill power plants** work on the same principle as a bio-digester.
- **Decomposition** is taking place in the absence of oxygen, hence an **anaerobic process** done by micro-organisms.
- A variety of gases are formed of which the most are **methane and carbon dioxide**.
- **Landfill gas utilization** is a process of gathering, processing, and treating the **methane** gas emitted from decomposing garbage to produce **electricity, heat, fuels,** and various **chemical compounds**

Small-scale Biomass Power Plants in South Africa

- The first bidding round of the Renewable Energy Independent Power Producer Procurement Programme (REIPPPP) started in 2011. To date, four bidding rounds have been completed.
- The website: www.eskom.co.za/Whatweredoing/Pages/RE_IPP_Procurement_Programme.aspx
- contains a map which provides details of each REIPPPP project in South Africa

Landfill Johannesburg produces 18 MW

Source: Joburg.org.za

The following details can be viewed on the website:

- Name of the project
- Type of technology being built
- Capacity of the power plant, and the
- Current status of the project

Bidding round	Number of Projects		Capacity allocated (MW)
	Biomass	Landfill	
Window 1	-	-	-
Window 2	-	-	-
Window 3	1 (16 MW)	1 (18 MW)	34
Window 4	1		62
Total	**2**	**1**	**96 MW**

Uses of Biomass: Biofuels

First Generation: Corn

Second Generation: Sugarcane Bagasse

- **Biomass fuel, or biofuel**, is a broad term to describe **material of biological origin that can be used as a source of energy**.
- Biomass can be converted into **liquid biofuels**.
- **First-, second- and third-generation biofuels** can be used in these processes.
- **First-generation biofuels** are made from maize, sugar cane, sunflower oil, soybeans, etc., which are traditionally seen as food crops.
- **Second-generation biofuels** are produced from plant residue, for example maize cobs, sugarcane and sweet sorghum bagasse. The food products are harvested, as well as the residue but the yield in terms of energy is lower.
- **Third-generation biofuels** are cultivated from algae to produce biodiesel from the oil.
- There is **controversy** around first-generation biofuels regarding the ethical question of whether food should be used for fuel.
- Therefore the tendency is that more and more **research is focused on second-generation biofuels**, where one will have the benefit of the food as well as the usefulness of the residue.
- With biofuels we need to ask the following questions:
  1. Can we use food for fuel?
  2. What is the effect of mono crops on nature?

Uses of Biomass: Biofuels

First Generation: Food

Maize

Sugar Cane

Second Generation: Plant and Animal Waste

Sugar Cane Bagasse

Sewage

Third Generation: Algae

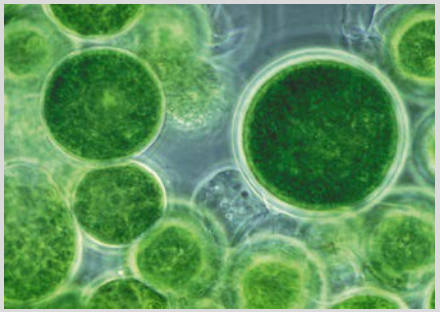

Algae

Algae Photo Bioreactor

Uses of Biomass: Mechanical Processing (Biodiesel)

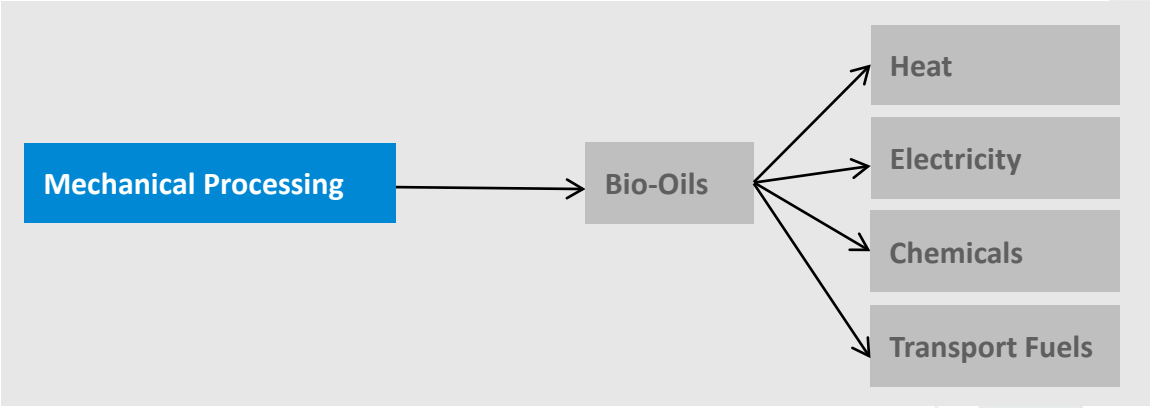

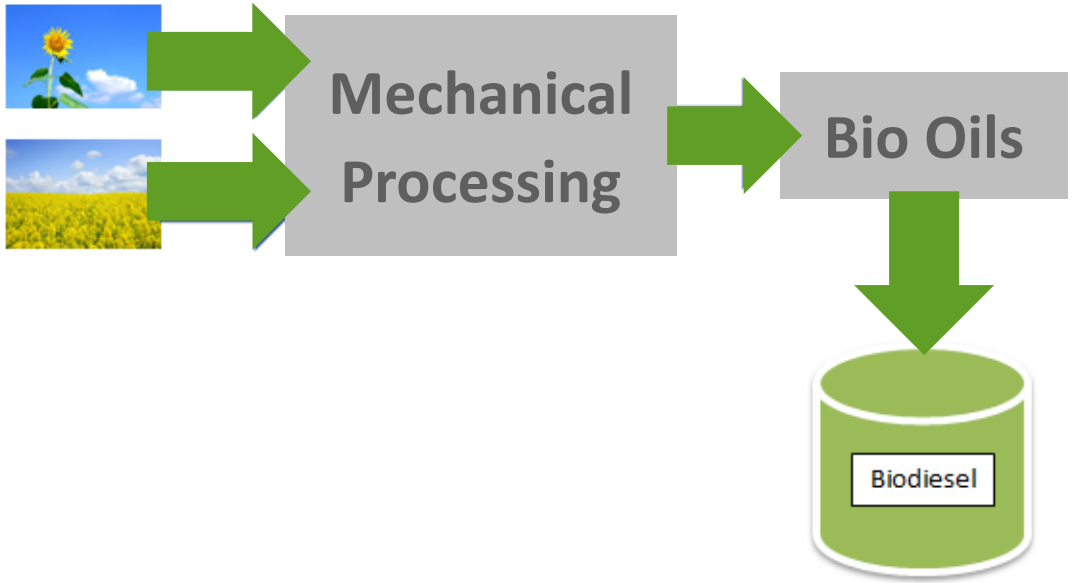

- Biomass fuel, or biofuel, is a broad term to describe material of biological origin that can be used as a source of energy.
- **Biomass can be converted into liquid biofuels through mechanical processing and fermentation**.
- **First-generation food crops** like sunflower seed oil, soybeans and other crops can be converted into biodiesel through mechanical processing.
- **Oil from these fuels are often more effective than wood**, since they represent a more **concentrated energy source**.

Uses of Biomass: Fermentation (Biofuel)

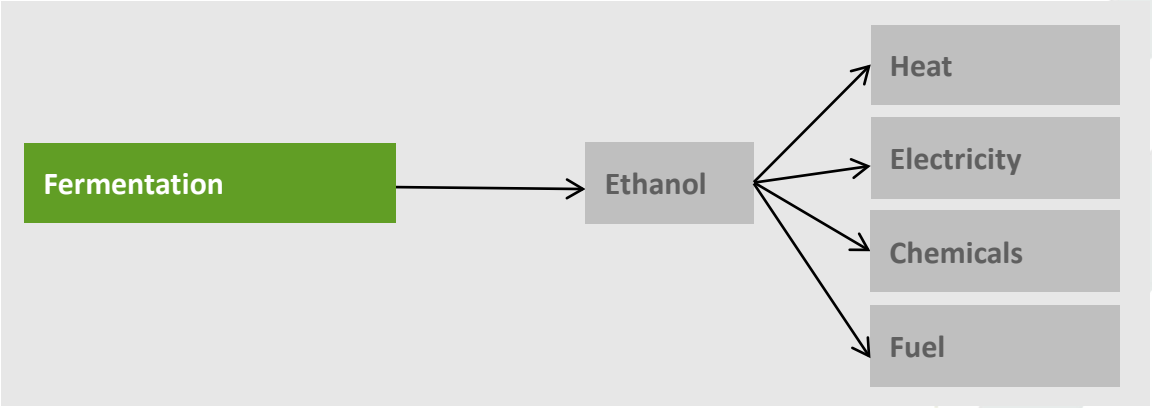

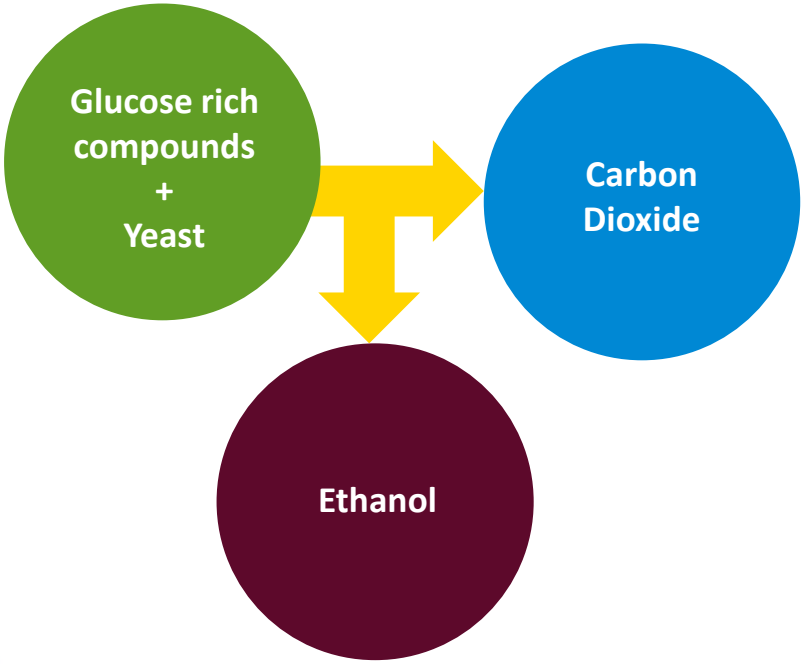

- **First- and second-generation crops** like maize, sugar cane and sweet sorghum bagasse **can be converted into fuel or gas** through a fermentation process.
- Through **fermentation**, maize and sugar cane are converted into:
  - 1. Ethanol – a liquid biomass fuel.
  - 2. Methane – a gas.
- In Brazil, ethanol from sugar cane crops is a major contributor to fuel resources, and is called **gasohol**.
- This **reduces the amount of fossil fuels** needed to power cars.

Uses of Biomass: Algae

Third-generation biomass **(algae) is used to** produce biofuels. The technology is still in the **research phase.**

Benefits

- **Fast growing**
- contains oil; contains no sulphur; non-toxic
- Algae fuel is also known as algal
- **Not** in competition with crops
- **Can be grown** with seawater in the desert and it won't use agricultural space

Concerns

- **Expensive** to develop
- **Cannot** provide **enough oil** to satisfy the **total transport demand**, although it can meet the **aviation** demand which is smaller.

References

Slide 2: Wood,[available online] www.pexels.com/photo/photo-of-woodpile-1787035, Sunflower plantation [available online] www.pexels.com/photo/bed-of-sunflower, Seeds in sacks [available online] www.pexels.com/photo/assortment-batch-colors-cooking-625422 , Cow manure[available online], www.flickr.com ,Seaweed [available online] www.pixnio.com/flora-plants/water-seaweed-and-rock

Slide 3 & 4: Crop [available online] https://www.pexels.com/photo/wheat-field-under-blue-cloudy-sky-701305/, Wood fuel [available online] http://tingatingacapital.com/social-entrepreneurship-success/adonai-foundation-seed-multiplication/, Sugar Cane [available online] https://commons.wikimedia.org/wiki/File:Sugar_Cane_Field_-_En_Route_to_Minas_Viejas_-_Huasteca_Potosina_-_San_Luis_Potosi_-_Mexico_(32550474098).jpg,

Slide 5: Biomass conversion technologies and products [online] http://www.crses.sun.ac.za/technologies-bio-fuel

Slide 6: Flame blaze [online] www.pixabay.com/da/photos

Slide 7: **Biomass Combustion [online]** https://corporate.vattenfall.com/globalassets/corporate/about_energy/illustrations/biomass_becomes_electricity_and_heat3.jpg

Slide 9: Land Fill biogas [online] https://commons.wikimedia.org/wiki/File:Landfill_gas_collection_system.JPG

Slide 11: Corn [Online] https://www.pexels.com/fr-fr/photo/aliments-brouiller-concentrer-cru-603030/, **Sugar cane Bagasse [online]** https://commons.wikimedia.org/wiki/File:Sugarcane_bagasse.jpg

Slide 12: Corn [online] https://www.pexels.com/es-es/foto/agricultura-amarillo-brillante-cereales-547263/, Sewage [online] https://environmentalpol.weebly.com/other-types-of-pollution.html, Algae [online] https://www.greentechmedia.com/articles/read/the-return-of-fed-funded-algae-fuels#gs.riwpt1, Sugarcane bagasse, [online] https://upload.wikimedia.org/wikipedia/commons/f/f6/Sugarcane_bagasse.jpg

Algae Photo Reactor [online] http://userwww.sfsu.edu/art511_h/emerging10/natasha/domef/project1algae.html

Slide 15: Algae [online] https://pixabay.com/en/coast-algae-sea-beach-shore, Bioreactor [online] www.treehugger.com/renewable-energy/algae-biofuel-pioneer-greenfuel-technology

Biofuel Research Journal 22 (2019) 962-979

BRTeam
BIOFUEL RESEARCH TEAM

Biofuel
Research Journal
Journal homepage: www.biofueljournal.com

Review Paper

A review on biomass: importance, chemistry, classification, and conversion

Antonio Tursi*

Department of Chemistry and Chemical Technologies, University of Calabria, Via P. Bucci, Cubo 15D, 87036 Arcavacata di Rende (Cs), Italy.

HIGHLIGHTS

- Overview of biomass sources and related chemical composition are presented.
- Biomass conversion technologies and final products are reviewed and discussed.
- Economic and environmental analysis of biomass-derived energy production was presented.
- Challenges for further expanssion of biomass-derived energy production are presented.

GRAPHICAL ABSTRACT

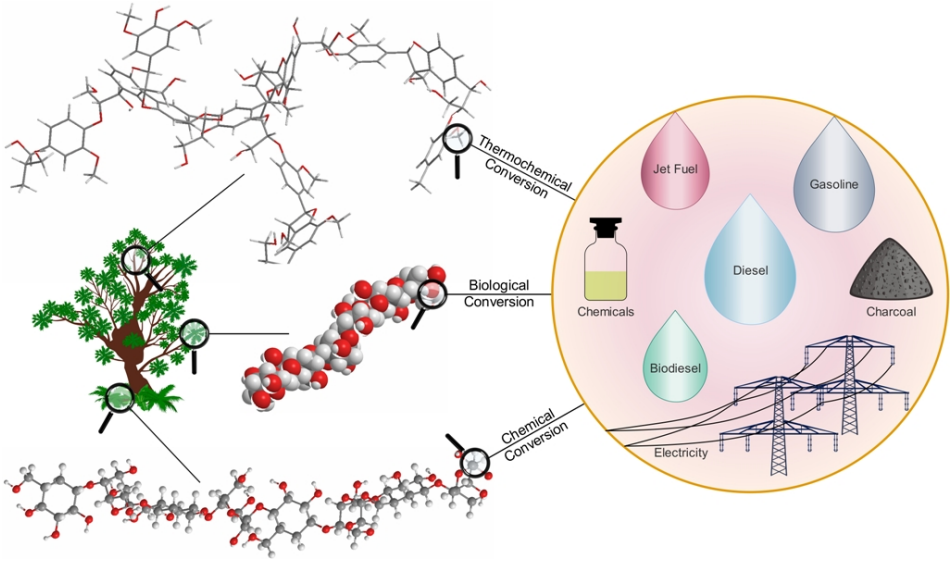

ARTICLE INFO

Article history:
Received 17 February 2019
Received in revised form 29 April 2019
Accepted 5 May 2019
Available online 1 June 2019

Keywords:
Biomass
Lignocelluloses
Pretreatment
Conversion
Biofuels
Sustainability

ABSTRACT

Biomass is currently the most widespread form of renewable energy and its exploitation is further increasing due to the concerns over the devastative impacts of fossil fuel consumption, i.e., climate change, global warming and their negative impacts on human health. In line with that, the present articles reviews the different sources of biomass available, along with their chemical composition and properties. Subsequently, different conversion technologies (i.e., thermo-chemical, biochemical, and physico-chemical conversions) and their corresponding products are reviewed and discussed. In the continuation, the global status of biomass *vs.* the other renewable energies is scrutinized. Moreover, biomass-derived energy production was analyzed from economic and environmental perspectives. Finally, the challenges faced to further expand the share of biomass-derived energy carriers in the global energy market are presented.

* Corresponding author at: Tel.: +39 3401859667
E-mail address: antonio.tursi@unical.it

Please cite this article as: Tursi A. A review on biomass: importance, chemistry, classification, and conversion. Biofuel Research Journal 22 (2019) 962-979.
DOI: 10.18331/BRJ2019.6.2.3

Contents

1. Introduction

The decades we are living are characterized by growth in wealth, but also by higher levels of pollution and the consequent deterioration of public health, mainly due to the increasing usage of fossil fuels for industrial and post-industrial development. As a result, the global society has been striving to find alternative routes for energy production. In line with that, major institutions of several countries have tried to implement a shared regulatory framework to promote renewable energies, thereby diversifying the sources of supply through replacing conventional energy resources.

Considering various alternative energy sources, biomass has been an indispensable part of energy debates within the policy context, strongly desired by the European Union, which has been able to transform saving and environmental protection provisions into strategic execution plans for development.

In fact, biomass could plays a significant role as source of renewable energy (Lauri et al., 2014), with huge potentials in the production of biofuels for transportation, electricity, and heat (Lebaka, 2013). In industrialized countries, the economic and political importance of bioenergy is recognized, as proved by initiatives like "Biomass Action Plan" and the "Multi-Year Plan", prepared by the European Commission and the US Department of Energy, respectively (Chum et al., 2011). The former document underlines the need of reducing carbon dioxide (CO_2) emissions, thereby complying with the commitments signed at the Kyoto Protocol and, especially with respect to the countries not involved in the ratification through increasing their awareness on the issue of global warming; a crucial topic of global importance over the last few years.

The latter document is related to the agricultural and energy policies undertaken by several countries. As part of the agricultural policies, the promotion of bioenergy has increased, leading to a different and more productive use of land and has significantly contributed to the creation of economic opportunities in rural areas, including improvement of farmers' income, containment of the countryside-city migrations, as well as conservation of environment and rural culture.

In addition to these, the problem of climate change has brought countries to higher levels of commitments and new bodies have been created by the scientific community like the International Panel on Climate Change (IPCC) in 1988, in order to limit the production of greenhouse gases (GHGs) released into the atmosphere (Chum et al., 2011; Kaltschmitt, 2013); mainly deriving from the consumption of fossil fuels. This debate has been on going in parallel with the importance of renewable energies, with a closer focus on biomass, as an instrumental element of energy security and sustainable development. With the recent scientific discoveries concerning biomass exploitation, promising techniques have been developed capable of optimized production of electricity, heat, and liquid biofuels from these inexpensive abundant natural materials.

It should be noted that biomass is a completely renewable energy resource, because CO_2 released through its combustion and utilization processes does not lead to an increase in atmospheric carbon dioxide as it is of biogenic origin. In better words, plants use CO_2, released into the environment as a consequence of the degradation processes of the other plants, for their growth and for their metabolic processes (Tkemaladze and Makhashvili, 2016). Therefore, the exploitation of biomass only leads to a

Please cite this article as: Tursi A. A review on biomass: importance, chemistry, classification, and conversion. Biofuel Research Journal 22 (2019) 962-979. DOI: 10.18331/BRJ2019.6.2.3

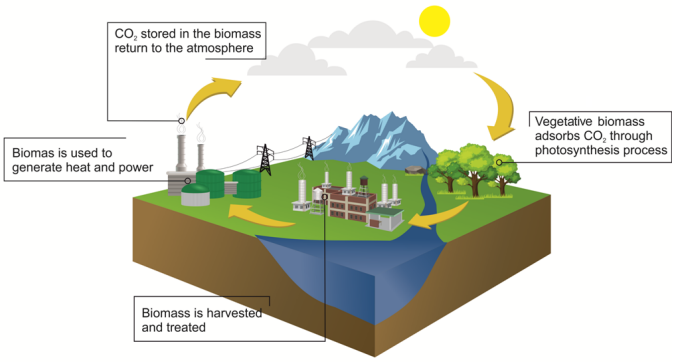

Fig. 1. Carbon cycle throughout the production and utilization of biomass.

faster transfer of CO_2 into the atmosphere that will be used again by plants to produce biomass again (**Fig. 1**) (Kaltschmitt, 2013).

Every organic substance deriving directly or indirectly from the photosynthesis process is considered biomass (Jacobsson and Johnson, 2000). Due to the heterogeneity of the materials, the usage and the origin, the definition of biomass varies. Nevertheless, more generally, biomass is a combination of naturally derived materials, originating from plants such as shrubs, trees, algae, crops as well as all the materials composed of organic matrix except for plastics originating from petrochemical and fossil materials (McKendry, 2002a).

The most important biomass sources (illustrated in **Fig. 2**) are agricultural and forestry residues (wastes from the wood processing industry such as shavings, sawdust, *etc.*), animal residues (livestock farms), sewage, algae, and aquatic crops. Municipal solid waste (MSW) and the waste streams originating from anthropogenic activities also fall in the biomass category; only if they are not reusable in subsequent processing (Kaltschmitt, 2013).

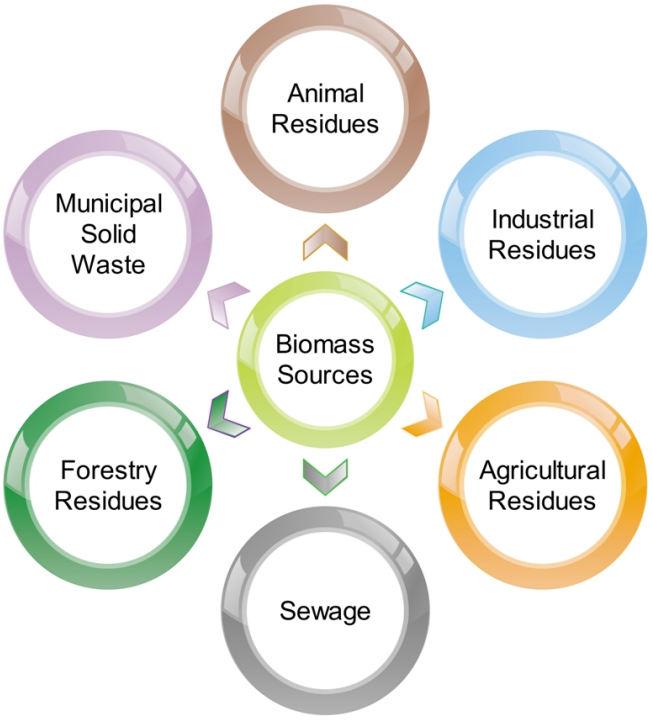

Fig. 2. The most important biomass sources.

Our planet stores a huge amount of biomass available in different areas ranging from forests to oceans. Several reports estimate that the world's total biomass land and aquatic reserves are around 1.8 trillion tons and 4 billion tons, respectively. From an energy point of view, the total biomass in the world has a potential production capacity of 33,000 EJ; corresponding to more than 80 times the annual energy consumption in the world (WBA, 2018). However, currently, biomass is partially exploited, accounting for only 14% of the primary energy in the world, standing at approximately 56 million TJ/yr (1,230 Mtoe/yr). Moreover, the use of this resource does not show a homogenous distribution across the world. More specifically, in some developing countries biomass generates up to 50% of the total energy needs, through the combustion of wood, shrubs, as well as wastes of plant and animal origins while on the other hand, in the developed countries biomass energy production on average stands at approximately 11% of the total energy produced (Chum et al., 2011; WBA, 2018). For instance, the United States meets about 3% of the country`s energy demands by using biomass, corresponding to around 3.2 million TJ/yr (70 Mtoe/yr). The Europe also obtains 3.5% of its energy from biomass (around 40 Mtoe/yr), while some countries like Finland, Sweden, and Austria are well above the average, producing 18%, 17%, and 13% of their total energy from biomass, respectively (Habert et al., 2010).

Overall, considering the huge potentials for the exploitation of biomass as an energy source, some central and northern European countries have set up large plants for heat and power cogeneration using biomass. France, for example, with the largest agricultural lands among the European countries, has implemented a comprehensive tax exemption policy on the production of biodiesel and ethanol, in order to encourage their production. On the other hand, Great Britain has a negligible production of biofuels owing to economic considerations but is focused on the development of huge and effective biogas recovery systems from landfills, both for heat and electricity generation. Other countries like Sweden and Austria traditionally rely on persistent use of firewood for heating and district heating purposes with a tendency towards the coppice plantations (willow, poplar), having higher yields compared with other resources (Habert et al., 2010).

2. Chemical characterization of biomass

The composition of biomass is largely diverse. For example, residues of plant origin are mainly composed of cellulose, hemicellulose, and lignin with varying percentages (**Fig. 3** and **Table 1**), while cattle manure is rich in proteins and cereals are mainly composed of starch. Different chemical structures obviously result in different chemical properties (Yokoyama, 2008).

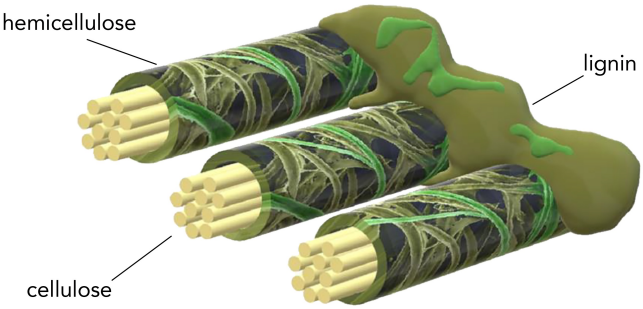

Fig. 3. Structure of lignocellulosic biomass.

2.1. Cellulose

Cellulose, a linear polymer, is a complex carbohydrate (or polysaccharide) with a high molecular weight and a maximum of 10,000 monomeric units of D-glucose, linked by β-1,4-glycosidic bonds. Cellulose

Please cite this article as: Tursi A. A review on biomass: importance, chemistry, classification, and conversion. Biofuel Research Journal 22 (2019) 962-979. DOI: 10.18331/BRJ2019.6.2.3

Table 1.
Structure and chemical composition of cellulose, hemicellulose, and lignin in plant cell walls (Xu et al., 2005; Chen, 2014).

Compositional element	Subunits	Subunits bonds	Composition	Polymer
Cellulose	D-Pyranglucose units	β-1,4-Glycosidic bonds	β-Glucan	Several hundred to tens of thousands
Hemicellulose	D-Xylose, mannose, L-arabinose, galactose, glucuronic acid	β-1,4-Glycosidic bonds in main chains; β-1.2-, β-1.3-, β-1.6-glycosidic bonds in side chains	Polyxylose Galactoglucomannan (Gal-Glu-Man) Glucomannan (Glu-Man)	Less than 200
Lignin	Guaiacylpropane (G), syringylpropane (S), p-hydroxyphenylpropane (H)	Various ether bonds (mainly β-O-4); carbon-carbon bond	G lignin, GS lignin, GSH lignin	4,000

molecular formula is $(C_6H_{12}O_6)_n$ (n indicates the degree of polymerization) and its structural base is cellobiose (i.e., 4-o-β-D-glucopyranosyl-D-glucopyranose) (**Fig. 4**).

Cellulose is the most abundant organic compound that can be found in nature (e.g., 90% and 50% of cotton and wood structure are contributed by cellulose, respectively) possessing a structural function in plant cell walls (Bonechi et al., 2017).

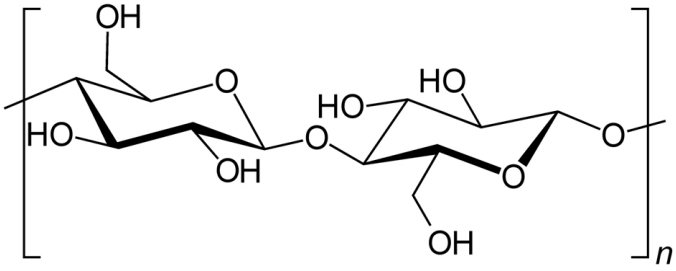

Fig. 4. The structural formula of cellulose.

The reactivity and morphology of cellulose chains are substantially influenced by the intermolecular hydrogen bond between the hydroxyl group on C-3 carbon and the oxygen of the nearby glycosidic ring. The formation of these bonds makes the molecules more stable and rigid. In some cases, the presence of many intermolecular bonds can generate an orderly crystalline region due to the considerable proximity between the different monomers (**Fig. 5**) (Chen, 2014).

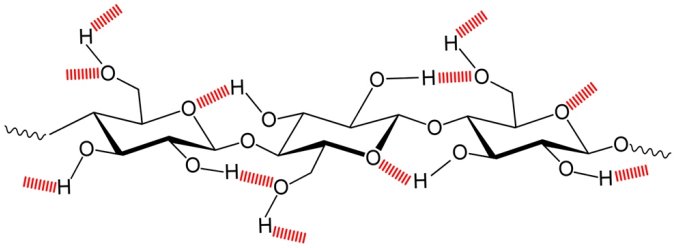

Fig. 5. Inter and intra-molecular hydrogen bonding in cellulose.

Alternation of the crystalline and amorphous regions of cellulose could affect the accessibility of its functional groups, which are involved in reactions. In fact, the reactivity of cellulose depends on the reactive capacity of its primary and the secondary hydroxyl groups, emerging from the glycosidic rings. In particular, the primary hydroxyl groups have a higher reactivity than the secondary ones due to lower steric impediment (Chen, 2017).

X-ray diffraction studies have shown that cellulose macromolecules in their crystalline structure have a regular and orderly arrangement, leading to a density of 1.588 g/cm^3. Conversely, in the amorphous regions, there are greater distances among the molecular chains because of the wide and irregular disposition of the macromolecules and as a result, the density of the cellulose in the amorphous regions is lower, i.e., 1.5 g/cm^3. Generally, the percentage of crystalline structure in cellulose ranges between 30 to 80% (Chen, 2014; Bonechi et al., 2017).

The amorphous region of the cellulose is the most exposed part of the molecule, and is first to be attacked by cellulase enzyme leading to the hydrolysis of the molecule. When cellulose is completely hydrolyzed, D-glucose (a monosaccharide) is produced, whereas through partial hydrolysis, a disaccharide (cellobiose) and smaller polysaccharides are formed (with n values ranging between 3 and 10) (Bonechi et al., 2017). On the contrary, the crystalline part is hydrophobic in nature, i.e., does not absorb water and therefore, it needs to be subjected to a set of treatments called mercerization (from the name of the English dye and fabric chemist John Mercer who conceived the process in 1844) in order to obtain a hydrophilic cellulose.

Overall, in the last two centuries, due to its important properties and applications, cellulose has become an important raw material for the pulp and paper as well as chemical fiber industries. Furthermore, it currently plays an important role in various fields related to environmental protection, such as the application of cellulose water remediation to remove dangerous pollutants such as hydrocarbons and heavy metals (Arias et al., 2017; Tursi et al., 2018a and b; Tursi et al., 2019).

2.2. Hemicellulose

Hemicellulose is one of the major constituents of plant cell walls and consists of heterogeneous branched polysaccharides. It is strongly linked to the surface of cellulose microfibrils. The content and structure of hemicellulose are different depending on the type of plant (Bala et al., 2016). The various sugar units are arranged with different substituents and in different proportions. Hemicellulose decomposes thermally between 180 °C and 350 °C, thereby producing non-condensable gas, coal, and a variety of ketones, aldehydes, acids, and furans (Carpenter et al., 2014).

In nature, hemicellulose is amorphous and has adhesive properties, with a high tendency to toughen when it is dehydrated. While cellulose is composed by glucose units linked by β-1,4-glycosidic bonds, hemicellulose almost entirely consists of sugars with five carbon atoms (xylose and arabinose) (**Fig. 6**) and six carbon atoms (glucose, galactose, mannose, and rhamnose) with an average molecular weight of <30,000 (McKendry, 2002a; Jindal and Jha, 2016; Bonechi et al., 2017). The different groups of molecules making up hemicellulose include xylans, mannans, galactans, and arabinogalactans.

2.2.1. Xylans

Xylans are polysaccharides possessing a structural function in plant cell

Please cite this article as: Tursi A. A review on biomass: importance, chemistry, classification, and conversion. Biofuel Research Journal 22 (2019) 962-979. DOI: 10.18331/BRJ2019.6.2.3

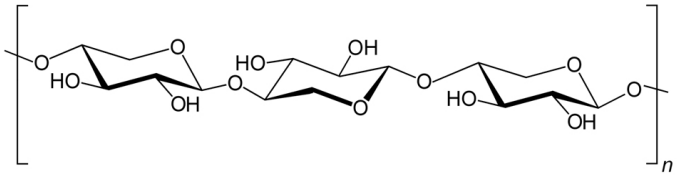

Fig. 6. The structural formula of hemicellulose.

walls. The main chain of xylan is similar to that of cellulose, however, it is composed of D-xylose (instead of D-glucose) as monomeric unit with traces of L-arabinose (Bajpai, 2009). Xylans are characterized by a main backbone formed by β-1.4 linkages between d-xylose units and related branches (**Fig. 7**) (Madeira et al., 2017).

The nature of the ramification of the main chain is variable: branches consisting of L-arabinofuranose linked to the 0–3 positions of D-xylose residues and of D-glucuronic acid, acetyl esters or 4-O-methyl-D-glucuronic acid linked to the 0–2 positions. Other groups could be linked to other substituents such as ferulate groups (Schaechter, 2009). Their abundance and composition within plant cells depend on the origin of the plant. A relationship between the chemical structure of xylans and their botanical origins has already been established (Bajpai, 2009; Chen, 2014).

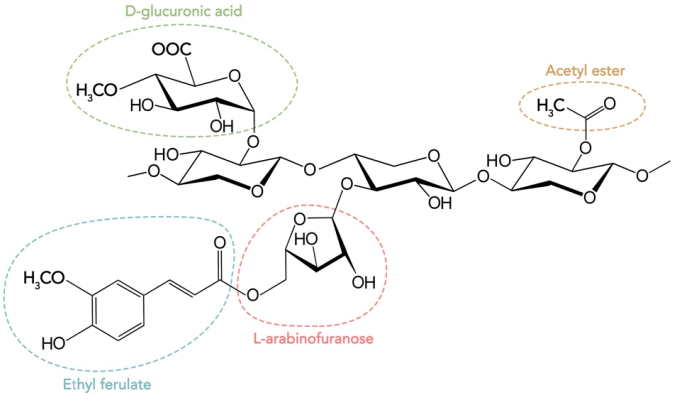

Fig. 7. The structural formula of xylans and derivates.

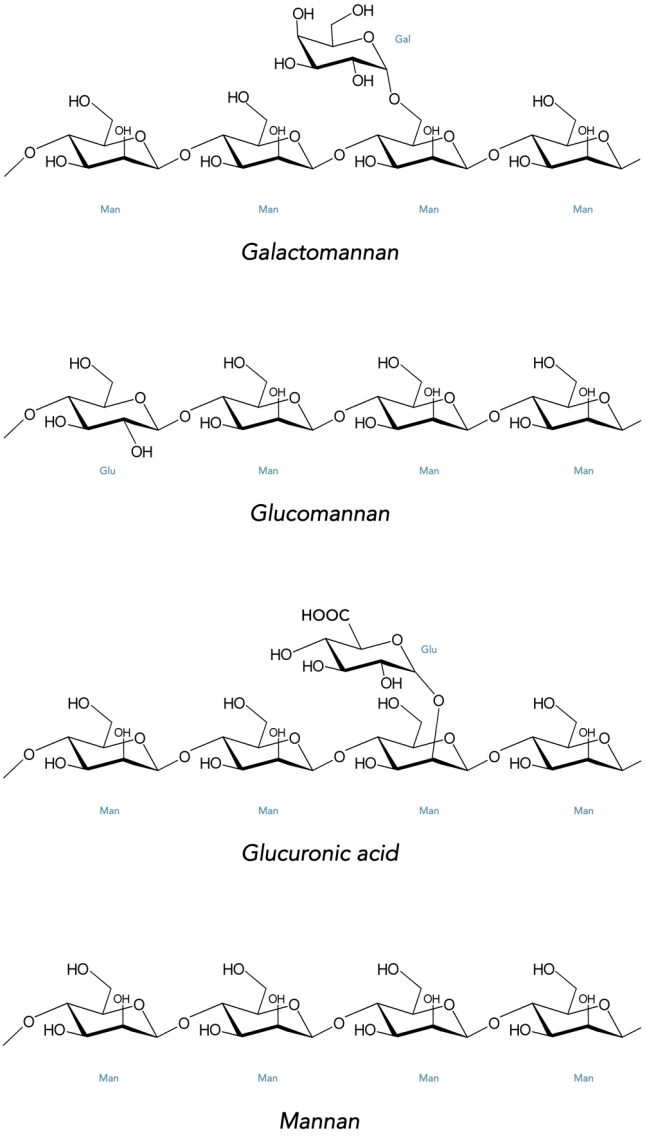

Fig. 8. The structural formula of mannans and derivates.

2.2.2. Mannans

Hemicellulose is mainly made up of mannans. The mannan compounds include mannan, galactomannan, glucomannan, glucuronic acid mannan, *etc.* (**Fig. 8**). Mannans are composed of mannose residues connected by β-(1→4) bonds while the galactomannans consist of galactose units bound with a β-(1→6) bonds (Amidon et al., 2008). The main chain of glucomannan is composed of glucose and mannose units (the hydroxyl group of mannose can also be acetylated), linked by β-(1→4) bonds, with a ratio of 1: 3, and a galactose residue as branched chain. The glucuronic acid, which is predominant in the cell wall, is made up of mannose and glucoronic acid residues linked by β-(1→4) and β-(1→2) bonds in the main chain, respectively (Chen, 2014).

2.2.3. Galactans and arabinogalactans

The backbone of galactans is composed of galactose residues connected by β-(1→4) bonds while galactose residues, as side chain, are attached to the O-6. Arabinogalactan is a polysaccharide, particularly abundant in larch bark (*Larix occidentalis*). It has a skeleton consisting of galactan with lateral chains made of glucose and arabinose. Galactose and arabinose coexist in a molar ratio of 6:1. Furthermore, ferulic acid may be linked to some arabinose and galactose residues (Amidon et al., 2008). The most common arabinogalactan include galactose residues (which may also be terminal) linked to O-3 or O-6 positions of the main chain and arabinofuranose residues linked to O-3 or O-5 positions. On the other hand, other types of arabinogalactan have galactose residues bound to O-4 or O-3 positions and arabinofuranose residues linked by an O-5 bond (Chen, 2014).

2.3. Lignin

Lignin is also contained in plant cell walls, with the function of binding, cementing, and putting the fibers together in order to enhance the compactness and resistance of the plant structure. Lignin is also recognized for its encrusting effect, as it covers the fibers. Therefore, in order to extract cellulosic fibers from plant materials, lignin degradation is essential.

The lignin content varies according to plant species (25-30% up to values around 50% for very hard woods such as ebony) and age; annual

Please cite this article as: Tursi A. A review on biomass: importance, chemistry, classification, and conversion. Biofuel Research Journal 22 (2019) 962-979. DOI: 10.18331/BRJ2019.6.2.3

plants containing about 10-12%. Its elemental composition is approximately 61-65% carbon, 5-6% hydrogen, and the remaining is oxygen (Fromm et al., 2003).

The term lignin denotes a complex amorphous aromatic polymer with a three-dimensional network, composed of phenylpropane units linked together. The monomeric units are held together by different ways: through oxygen bridges between two propyl and phenyl groups, between a phenyl and a propyl group, or through carbon-carbon bonds between the same groups. In particular, this macromolecule is formed through the radical oxidative polymerization of three hydroxycinnamyl alcohols representing the basic structural monomers: p-phenyl monomer (type H), guaiacyl monomer (type G) and siringyl monomer (type S), deriving from coumarinic, coniferyl and synapyl alcohol, respectively (**Fig. 9**). These compounds differ from each other due to the different degrees of methoxylation (Xu et al., 2005).

Furthermore, in the lignin structure, there are many polar groups and hydroxyl groups allowing the establishment of strong intramolecular and intermolecular hydrogen bonds. These in turn make lignin insoluble in any solvents except alkaline solutions. Through condensation reactions, lignin is split into soluble and insoluble lignin, with the latter forming a precipitate.

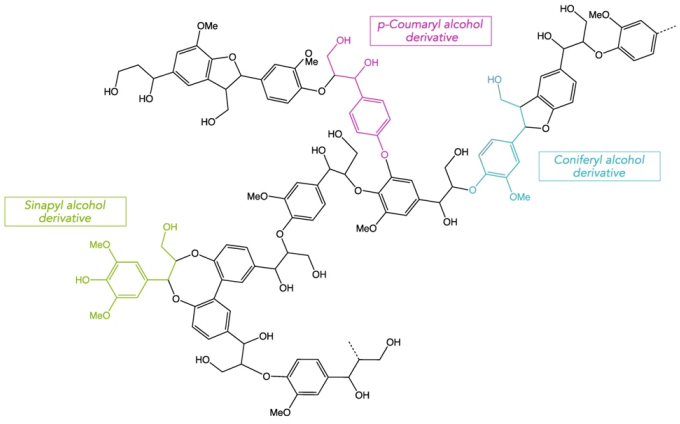

Fig. 9. The structural formula of lignin and its precursors.

The softening temperature of dry lignin ranges from 127 to 129 °C, however as the molecular weight of lignin grows, the softening temperature increases as well. Furthermore, the water contained inside the molecules acts as plasticizer, leading the softening temperature to decrease with an increase in the water content (Chen, 2014).

The modification of the cell wall by lignin infiltration is called lignification, a phenomenon leading to high mechanical resistance to the structure. Other than possessing greater mechanical resistance, lignified membranes become less swollen than cellulosic membranes, because the dipole -OH- cellulose groups are largely saturated by lignin. Overall, given the considerably high global availability of lignin, i.e., around 300 billion tons, with an annual increase of about 20 billion tons (Hodásová et al., 2015), development of innovative technologies for lignin valorization is essential.

In the last decade, the pulp and paper industry alone has produced approximately 50 million tons of extracted lignin (Wells and Ragauskas, 2016). Nevertheless, only 1 million tons of lignin from this sector has been used for the production of various value-added products, while the remaining has been burnt as low value fuel; lignin has a greater calorific value compared to lignocellulose biomass (Xie et al., 2016).

2.3.1. Lignin valorization: value-added products

Recently, scientific research has focused on improving lignin conversion processes, in order to use it as raw material for the production of high value-added products, rather than burning it, such as dispersants (for building sector, enhanced oil recovery, production of printing ink, *etc.*), emulsifiers (as bitumen additives), precursors (for the production of vanillin, benzene, toluene and xylene, *etc.*), and finally for the production of various types of bio-based polymers, such as biocomposites, bioplastics, binders, additives, *etc.* (Rana et al., 2018).

The efficiency of separating polymers, including lignin, from the cell walls of lignocellulosic biomass is a crucial parameter, since it drives the biomass conversion rate in the final product (Hodásová et al., 2015). Yields and costs vary according to the type of biomass, the separation process, and the treatment times. Different methods are used to separate lignin from lignocellulosic biomass and are classified according to the applied process, i.e., steam explosion, kraft, organosolv, soda, lignosulfonates, and pyrolytic lignin (Wang et al., 2013). Alkaline and acidic procedures are the most efficient methods for lignin extraction. Furthermore, the organosolv process, which uses mixtures of alcohol and water at a temperature of about 200 °C, represents another very effective method for this purpose (Welker et al., 2015). The extracted or separated lignin can be used as an unchanged macromolecule or it can be further modified, through processes of depolymerization (or fragmentation), into simpler and more usable forms. In some cases, after depolymerization, other methods such as reductive and oxidative conversion, functionalization of hydroxyl groups, and introduction of other functional groups are used for the production of several high value-added bio-based products (Laurichesse and Avérous, 2014; Welker et al., 2015; Abejón et al., 2018).

Nevertheless, depolymerization is the most challenging step in the conversion of lignin into valuable products (Kosa and Ragauskas, 2012; Xie et al., 2016). It can be performed by biological, chemical, and, thermochemical treatments, as well as by using homogeneous and heterogeneous catalysis, leading to the fractionation of aromatic compounds into simpler structures at the end of treatment (Xie et al., 2016).

Chemical depolymerization/fragmentation occurs could be conducted different processes: (1) pyrolysis, (2) hydrogenation, (3) hydrolysis, (4) oxidation, and (5) gasification. The choice of process and the fragmentation efficiency depend mainly on the type of lignin used (Pandey and Kim, 2011; Welker et al., 2015). Biological methods have also been considered for the depolymerization of lignin through (1) enzymatic oxidation or (2) microbial conversion with the use of microbes, bacteria, fungi, and termites capable of decomposing biomass to perform their metabolic functions (Sanchez, 2009; Welker et al., 2015).

In general, the value-added products derived from lignin, can be split into three main groups: biofuels, macromolecules, and aromatics (Smolarski, 2012), which could be used by different sectors as illustrated in **Table 2**.

Table 2.
Lignin-derived value-added products (Hodásová et al., 2015; Rana et al., 2018).

Sector	Products	Type of lignin
Biofuels	(I) Bio-oil from pyrolysis and liquefaction (II) Biodiesel *via* Fischer-Tropsch process (III) Syngas from gasification	(I) Lignosulfonates (II) Kraft (III) Organosolv (IV) Pyrolytic
Chemicals	(I) Phenolic/aromatics compounds (II) Dispersants (III) Emulsifiers (IV) Flocculants	(I) Lignosulfonates (II) Kraft (III) Organosolv (IV) Soda (V) Steam explosion
Materials/polymers	(I) Biocomposites and bioplastics (II) Carbon fibers (III) Activated carbons (IV) Adsorbents (V) Binders (VI) Additives for cement/paints	(I) Lignosulfonates (II) Kraft (III) Organosolv (IV) Soda
Environmental	(I) Pesticides (II) Herbicides (III) Water treatment agents (IV) Soil and dust agents	(I) Kraft (II) Organosolv
Pharmaceuticals	(I) Antioxidants (II) Cosmetics (III) Prebiotics	(I) High grade (derived from Kraft lignin)

Please cite this article as: Tursi A. A review on biomass: importance, chemistry, classification, and conversion. Biofuel Research Journal 22 (2019) 962-979. DOI: 10.18331/BRJ2019.6.2.3

2.4. Starch

Starch represents the main reserve of carbohydrates in vegetable tubers and seeds. It is found in the form of granules (of different morphological appearances depending on plant species), each containing several million of amylopectin molecules and a large number of amylose molecules.

In nature, starch can be found in two forms: approximately 25-27% as amylose, which is soluble in hot water and approximately 73-75% as amylopectin, which is water-insoluble. Amylopectin (without amylose) can be isolated from "waxy" corn starch, while amylose (without amylopectin) is isolated by hydrolysis of amylopectin with pullulanase (Vorwerg et al., 2002).

The empirical formula of starch is $(C_6H_{10}O_5)_n$, where *n* is a variable number ranging from a hundred to a few thousand; indicating the residues of α-D-glucose units (in the $^4C_1$ conformation) that are linked together to create the polymers (Edwards et al., 2003).

2.4.1. Amylose

Amylose molecules are single non-branched chains with 500-20,000 α-(1-4) D-glucose units, adopting a helical structure (**Fig. 10**). Amylose occurs in different forms of A, B, and V. The A and B forms both show stiff left-handed helices with six glucose units per turn. The only characteristic that differentiates the two forms from each other has to do with the different packing of the starch helices. Single helical amylose has hydrogen boding betweem O-2 and O-6 atoms on the external surface of the helix with only the ring oxygen pointing inward.

The V form of amylose is generated by co-crystallization processes with compounds including iodine, alcohols, fatty acids and dimethyl sulfoxide (Winger et al., 2009). The hydrogen bonds among aligned chains causes retrogradation and release of the water (syneresis), allowing the aligned chains to form a double-stranded hydrophobic structure resistant to amylases. This is the reason why amylose gives resistance to starch.

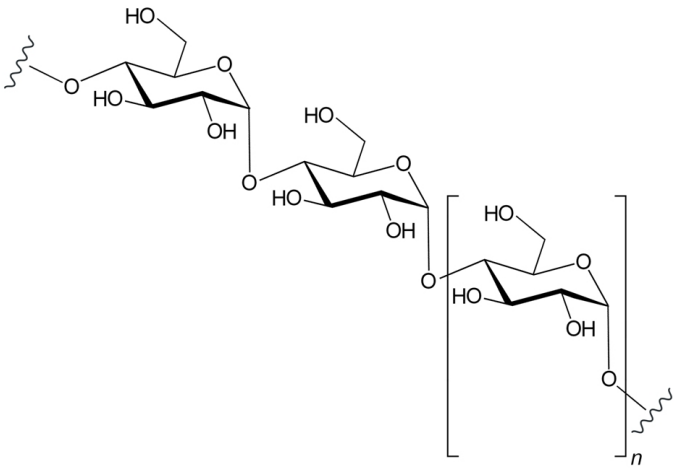

Fig. 10. The structural formula of amylose.

2.4.2. Amylopectin

As the main component of starch, amylopectin is one of the largest molecules found in nature. It is composed of linear chains of α-D-glucopyranosyl units bound by (1→4) bonds, while the branching point is connected by α- (1→6) bonds (**Fig. 11**) (Winger et al., 2009).

Amylopectin is composed of three different types of chains: a larger number of “external” non-branched chains (called A-chains) than internal branched chains (called B-chains). The third chain (called C-chains) is the only one including a single reduction group. The average length of the A-chains is in the range of 13-23 residues, while the B-chains have a higher average length of about 23-25 residuals.

Several studies demonstrate that depending on the sources, the relative molecular weight of amylopectin, is between 10^7 and 10^8 daltons (Singh et al., 2003; Waniska et al., 2016), in particular, Buléon et al. (1998) estimated that the number of amylopectin chains in a single starch granule stands at 5.4×10^7.

The most important reaction that amylopectine can undergo is certainly the hydrolysis, which occurs in the process of seed germination, involving the dissolution of the α(1→4) bonds by the α- and β-amylase enzymes and the consequent production of dextrins (small segments containing (1→6) bonds). Dextrins will subsequently be cleaved by other enzymes known as dextrinase completing the digestion of starch to glucose (Winger et al., 2009).

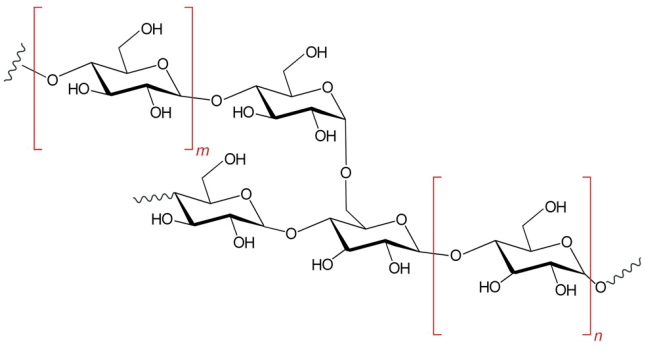

Fig. 11. The structural formula of amylopectine.

2.5. Minor organic components

Several studies have shown that different biomass substrates can contain important quantities of minor organic components, which may influence the treatment processes. These are listed below as follows (Vassilev et al., 2012):

- 2-40% of lipids, 6-71% of proteins, and up to 6% of nucleic acid in algae (Demibars, 2010).
- 2-4% of acetyls in some straws and flax (Tamaki, 2010).
- 1-4% of uronic acids in pine, eucalyptus, and sorghum grass.
- Up to 10% of proteins in pine, reeds, spruce, birch, and maize (Huber et al., 2006; Tamaki and Mazza, 2010).

2.6. Inorganic matter

In general, biomass also contains inorganic substances (ash) in traces, whose quantity varies according to the type of raw material (Alaswada et al., 2015). Among these, the common elements are metals such as calcium, sodium, potassium, magnesium, phosphorus, silicon, aluminum, and iron (Werkelin et al., 2005).

In addition to various species of crystallized minerals, the inorganic matter (on average around 7%, DW) also contains different amorphous phases of natural origin. Normally, the most common solid residues that exist in biomass are water-soluble residues such as chlorides, sulphates, oxalates, nitrates, carbonates, and both organic and inorganic amorphous materials.

During some pretreatment processes, biomass is dried at 105 °C and further heated in furnaces at temperatures reaching 750 °C. Under such circumstances, elements such as carbon, hydrogen, oxygen, nitrogen, and sulfur evaporate as gaseous compounds due to their chemical characteristics, while the ash residue remains, containing mineral elements in their oxide forms (Chen, 2014).

2.7. Other elements in biomass

In lignocellulosic materials and in plants (except for carbon, hydrogen, oxygen, and other basic elements), there are other minority components in

Please cite this article as: Tursi A. A review on biomass: importance, chemistry, classification, and conversion. Biofuel Research Journal 22 (2019) 962-979. DOI: 10.18331/BRJ2019.6.2.3

small quantities, i.e., pigments, waxes, alkaloids, and terpenes.

2.8. Fluid matter

The fluid material is an aqueous solution contained in biomass. It contains various cation and anion species. The moisture content of biomass is normally in the range of 10-60% but in some types of raw biomass, it can even reach as high as 80-90%. The fluid matter content depends on the starting composition of biomass and observed percentage values can be related to high water content in living cells. Fast-growing crops, for example, possess high water contents and typical elements related to vegetal physiology, such as Na, Ca, K, Mg, N, P, Cl, and S (Vassilev et al., 2012).

3. Biomass classification

Due to the substantial differences in term of variety and quantity of biomass, and their different compositional characteristics, there is no univocal way of classification of biomass, so they can be grouped differently, depending on purpose and scope.

According to origin, function and final products, generally biomass is classified in two ways:

I. Categorization based on types of biomass existing in nature (according to ecology or type of vegetation);
II. Categorization based on the use and application of biomass as feedstock.

The former is the most used classification splitting biomass into different groups (**Table 3**):

I. Wood and woody biomass
II. Herbaceous biomass
III. Aquatic biomass
IV. Animal and human waste biomass
V. Biomass mixtures

Typical chemical composition of different biomass groups are tabulated in **Table 4**.

3.1. Wood and woody biomass

The woody biomass includes different components, mainly consisting of carbohydrates and lignin. Generally, this category consists of materials such as trees and roots residues, bark and leaves of woody shrubs both above and below ground, which can be converted into energy by direct combustion (or gasification) or through numerous conversion processes (Vassilev et al., 2012).

Typically, the biomass used for the production of energy and fuel comes from four primary sources:

I. Production residues;
II. Residues of non-merchant timber;
III. Post-consumption wood wastes;
IV. Urban and agricultural wastes.

Table 3.
Biomass classification: groups, varieties, and species (Vassilev et al., 2012).

Biomass group	Varieties and species
Wood and woody biomass	Coniferous or deciduous; Angiospermous or gymnospermous; Stems, branches, foliage, bark, chips, lumps, pellets, briquettes, sawdust, sawmill and others from various wood species.
Herbaceous biomass	Grasses and flowers (alfalfa, arundo, bamboo, bana, brassica, cane, cynara, miscanthus, switchgrass, timothy, others); straws (barley, bean, flax, corn, mint, oat, rape, rice, rye, sesame, sunflower, wheat, others); other residues (fruits, shells, husks, hulls, pits, pips, grains, seeds, coir, stalks, cobs, kernels, bagasse, food, fodder, pulps, cakes, *etc*.).
Aquatic biomass	Marine or freshwater algae; macroalgae (blue, green, blue-green, brown, red) or microalgae; seaweed, kelp, lake weed, water hyacinth, *etc*.
Animal and human waste biomass	Bones, meat-bone meal; various manures, *etc*.

Woody biomass is currently the most important renewable energy source in the world. In 2010, the global use of woody biomass led to an energy production of approximately 30 EJ while 16 EJ was related to household fuelwood and 14 EJ to industrial use of woody biomass (Lauri et al., 2014).

3.2. Herbaceous biomass

The European standard EN 14961-1, which classifies solid biofuels, suggests the following definition for herbaceous biomass (Chum et al., 2011):

"Herbaceous biomass is from plants that have a non-woody stem and which die back at the end of the growing season. It includes grains or seeds crops from food processing industry and their by-products such as cereal straw".

Generally, herbaceous biomass resources belong to one of the following two main groups, i.e., agricultural residues and energy crops.

I. Agricultural residues are by-products of food, fibers, or food industries. Some of these by-products are collected for different end-uses, such as animal feed. In any cases, these residues are not fully monitored and their availability across different regions and their potential applications as bioenergy are not fully clear.
II. Energy crops, on the other hand are exploited only in the bioenergy sector.

Efficient exploitation of this biomass can lead to positive impacts at regional level, by replacing fossil fuels and creating new jobs and revenues.

Table 4.
Typical chemical composition of different biomass groups (wt.%) (Vassilev et al., 2010).

Biomass group	C* (%)	O (%)	H (%)	S (%)	N (%)	VM (%)	FC (%)	M (%)	A (%)
Wood and woody biomass	49-57	32-45	5-10	<1-1	<1-1	30-80	6-25	5-63	1-8
Herbaceous biomass	42-58	34-49	3-9	<1-1	<1-3	41-77	9-35	4-48	1-19
Aquatic biomass	27-43	34-46	4-6	1-3	1-3	42-53	22-33	8-14	11-38
Animal and human waste biomass	57-61	21-25	7-8	1-2	6-12	43-62	12-13	3-9	23-34
Biomass mixtures	45-71	16-46	6-11	<1-2	1-6	41-79	1-15	3-38	3-43

* Abbreviations: Carbon (C), Oxygen (O), Hydrogen (H), Sulfur (S), Nitrogen (N), Volatile matter (VM), Fixed carbon (FC), moisture (M), and ash (A) content.

Please cite this article as: Tursi A. A review on biomass: importance, chemistry, classification, and conversion. Biofuel Research Journal 22 (2019) 962-979. DOI: 10.18331/BRJ2019.6.2.3

3.3. Aquatic biomass

The term aquatic biomass includes macroalgae, microalgae, and emerging plants (Di benedetto, 2011):

I. Macroalgae are multicellular organisms that can quickly reach up to 60 m in length. They are mainly used for food production and hydrocolloids extraction.
II. Microalgae are microscopic organisms, which can be subdivided into the following subgroups: diatoms, green and golden algae. Diatoms are unicellular and brown algae, generally only a few μm in size; they represent one of the main components of aquatic microflora and one of the largest source of biomass on earth. Green algae are particularly abundant in freshwater resources. The main product obtained from these algae is starch, although oils can also be produced. Golden algae are similar to diatoms and produce oils and carbohydrates.
III. Emerging plants grow partially submerged in marshes and swamps.

In nature, there are about 55,000 species and over 100,000 strains of brackish water, freshwater, and terrestrial algae. The great advantage of using these simple organisms is their ability to convert sunlight, water, and CO_2 into a wide variety of metabolites and chemicals that end up in algal biomass (Vassilev and Vassileva, 2016).

Currently, aquatic biomass is considered as an ideal raw material for the production of third-generation biodiesel, as it is not in competition with food crops, along with the advantage of producing considerably larger amounts of biomass per hectare compared to land crops. However, there are still considerable economic and technological challenges to be overcome before such biofuels could be effectively commercialized. Moreover, it should be noted that there are many parameters influencing the performance of aquatic biomass such as levels of irradiation, CO_2 and O_2 concentrations, temperature, pH, salinity, and nutrients (Strezov and Evans, 2014).

3.4. Animal and human waste biomass

The most common sources are bones, meat meal, various types of animal manures, and human dung (Vassilev et al., 2012) (**Table 3**). In the past, these wastes were recovered and sold as fertilizers or simply used on agricultural land, but the introduction of more stringent environmental regulations on pollution, health, and odor concerns, has led to proper waste management. Anaerobic digestion is the most convenient method to convert this waste into useful products. For instance, biogas, as a bioenergy product of the process, could be used to generate electricity in turbines and internal combustion engines or could be burned directly for cooking or to heat rooms and water (Horan, 2018).

3.5. Biomass mixtures

In some cases, when several substrates belonging to different classes, mentioned above, are in mixed form, they are classified in this category.

4. Energy from biomass

As mentioned earlier, biomass could be a source of renewable energy and by replacing fossil fuels could substantially limit their environment impacts. Biomass, through treatment and conversion processes, can be converted into different types of energy carriers. The parameters that determine the choice of the production process are diverse but the most important ones include the renewable end-product required, the quality and quantity of biomass, and the cost of the process (Dalena et al., 2017).

Biomass can be converted into two main types of energy carriers (McKendry, 2002a):

I. Electrical/heat energy;
II. Transportation fuels;

The following physicochemical characteristics of biomass play a crucial role in directing the available feedstock into both or either of these domains:

- Moisture content (intrinsic and extrinsic);
- Caloric value;
- Proportions of fixed carbon and volatile substances;
- Ash content;
- Alkali metal content;
- Cellulose/lignin ratio.

The first five properties largely influence the conversion processes of dry biomass, while the first and the last one are essential for the conversion processes of wet biomass (McKendry, 2002b).

With regard to lignocellulosic biomass, it should undergo pretreatment processes in order to become suitable for conversion into transportation fuels and value-added co-products (Agbor et al., 2011; Dalena et al., 2017). In fact, pretreatment is aimed at simultaneously decreasing the crystallinity index of cellulose and increasing its available surface area by removing the layers of lignin and hemicellulose, leading to a more efficient cellulose hydrolysis (Mosier et al., 2005; García et al., 2011; Zhao et al., 2012).

Pretreatment methods used for lignocellulosic materials are classified into mechanical, chemical, chemical/mechanical, and biological methods (**Table 5**).

5. Conversion technologies

The processes involved in biomass conversion into energy are commonly classified as follows (**Table 6**):

I. Thermo-chemical conversions;
II. Biochemical conversions;
III. Physico-chemical conversions.

5.1. Thermo-chemical conversion of biomass

In thermo-chemical conversion processes, energy is produced by applying heat and chemical processes. There are four thermo-chemical conversion processes, i.e., combustion, pyrolysis, gasification, and liquefaction.

5.1.1. Combustion

The combustion processes produce approximately 90% of the total renewable energy obtained from biomass. Combustion plants can operate on different types of biomass, i.e., wood, dry leaves, hard vegetable shells, rice husk, dried animal dung, *etc.* (Lebaka, 2013).

In the combustion process, biomass and oxygen are combined in a high temperature environment to form carbon dioxide, water vapour, and heat (**Eqs. 1** and **2**).

$$\text{Biomass} + \text{Oxygen} \rightarrow \text{Carbon Dioxide} + \text{Water} + \text{Heat} \quad \text{Eq. 1}$$

The approximate chemical equation for biomass combustion is:

$$CH_{1.44}O_{0.66} + 1.03\ O_2 \rightarrow CO_2 + 0.72\ H_2O + \text{Heat} \quad \text{Eq. 2}$$

The amount of generated heat depends on many factors but mainly on the type of biomass used in the process, although the average thermal energy produced is 20 MJ/kg of biomass (Nussbaumer, 2003).

As showed by the **Equations 1** and **2**, the combustion process is an exothermic chemical reaction, i.e., the biomass is burnt in the presence of air with the subsequent release of chemical energy that could be converted into mechanical and electrical energy (Lebaka, 2013; Kaushika et al., 2016).

Combustion process is carried out inside combustion chambers at the temperatures ranging between 800 to 1000 °C. An essential requirement of the dry biomass used is its moisture content, which should be less than 50%. Typically, biomass combustion plants (which use wood and forest residues as fuel) generate between 20 to 50 MWe, with related electrical efficiencies of 25-30%. Further developments of these systems and the application of fluidized bed systems and advanced gas cleaning have resulted in increased

Please cite this article as: Tursi A. A review on biomass: importance, chemistry, classification, and conversion. Biofuel Research Journal 22 (2019) 962-979. DOI: 10.18331/BRJ2019.6.2.3

Table 5.
Main pretreatment methods used for lignocellulosic materials.

Pretreatment category	Type	Short description
Mechanical	Milling	Use of techniques and mechanical devices to reduce the biomass in size.
	Ultrasonic	Use of ultrasonic techniques and apparatus to break down biomass into smaller molecules.
Chemical	Liquid hot water	Pretreatment performed with water at elevated temperatures in the range of 150–230 °C and high pressures for lignin, hemicellulose, and cellulose hydrolysis (Harmsen et al., 2010).
	Weak acid	Dilute acid is sprayed onto the raw material and the mixture is held at 160-220 °C for short periods to achieve lignin, hemicellulose, and cellulose hydrolysis (Chen et al., 2017).
	Strong acid hydrolysis	Strong concentrated acids (such as H_2SO_4 and HCl) are used for lignin, hemicellulose, and cellulose hydrolysis (Sun and Cheng, 2002).
	Alkaline hydrolysis	Calcium (or sodium) hydroxide and ammonia are used to reduce lignin content and remove some hemicellulose.
	Organosolv	Organic solvent or organic solvent mixtures with water are used to remove lignin before cellulose enzymatic hydrolysis.
	Oxidative	Oxidising agents such as H_2O_2, ozone, oxygen or air, are used for the delignification of cellulose.
	Room Temperature Ionic Liquids (RTIL)	Inorganic anions and organic cations are used for the separation of lignin and to increase the accessibility of cellulose under environmental conditions and without the use of acidic or alkaline solutions (Imai et al., 2004).
Chemical/Mechanical	Steam explosion	High pressure saturated steam is injected into a reactor filled with biomass and subsequently, with a sudden reduction in pressure, the biomass undergoes an explosive decompression breaking lignin and degrading hemicellulose (Harmsen et al., 2010).
	AFEX	Liquid ammonia is used at high temperature and pressure in a reactor. Subsequently, a drastic reduction of the pressure is applied leading to reduced lignin and hemicellulose contents while cellulose is de-crystallized (Teymouri et al., 2005; Harmsen et al., 2010).
	CO_2	High pressure CO_2 is injected into the batch reactor containing biomass. The pressure reduction generates an explosive decompression improving the subsequent hydrolysis (Sun and Cheng, 2002).
	Mechanical/alkaline pretreatment	The process consists of a continuous mechanical pretreatment of lignocellulosic biomass with the addition of an alkali. The result is a soluble fraction of lignin, hemicellulose, and other compounds in addition to the insoluble part of cellulose (Harmsen et al., 2010).
Biological	Biological hydrolysis	In a reaction batch, microorganisms (such as white and brown fungi) are used to degrade hemicellulose and lignin (Harmsen et al., 2010).

Table 6.
Main conversion technologies and their corresponding products (Mesa et al., 2010; Lebaka, 2013; Portha et al., 2017).

Process/Technology		Feedstock	Usable end product
Thermo-chemical conversion	*Combustion*	(I) Agricultural residues (II) Woody residues (II) Animal wastes	(I) Heat (II) Electricity
	Pyrolysis	(I) Agricultural residues (II) Woody residues	(I) Pyrolysis oil (II) Producer gas (III) Char
	Gasification	(I) Agricultural residues (II) Woody residues	(I) Producer gas (II) Liquid fuels (III) Char
	Liquefaction	(I) Agricultural residues (II) Algal biomass	(I) Fertilizer/biofuel (II) Syngas (III) Liquid fuels
Biochemical conversion	*Anaerobic digestion*	(I) Animal wastes (II) Sewage sludge	(I) Liquid fuels (II) Biogas (II) Electricity
	Fermentation	(I) Agricultural residues (II) Sugars (III) Starch	(I) Liquid fuels (bioethanol)
Physico-chemical conversion	*Esterification/Transesterification*	(I) Vegetable oils (II) Animal fats (II) Waste oils	(I) Liquid fuels (II) Glycerol

Please cite this article as: Tursi A. A review on biomass: importance, chemistry, classification, and conversion. Biofuel Research Journal 22 (2019) 962-979. DOI: 10.18331/BRJ2019.6.2.3

electricity production from biomass, on a scale of 50-80 MWe, with electrical efficiencies of up to 30-40% (McKendry, 2002b). A typical scheme of the biomass combustion process is shown in **Figure 12**.

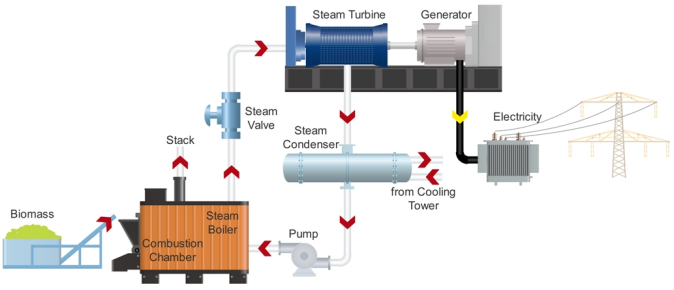

Fig. 12. Biomass combustion scheme.

5.1.2. Pyrolysis

Pyrolysis is the conversion process of specific biomass into liquid (bio-oil), solid (charcoal), and gaseous (combustible gas) products through partial combustion at temperatures around 500 °C and in the absence of oxygen (Lebaka, 2013). High temperatures allow the vaporization of the volatile components of the biomass producing gases, whose vapours are condensed into liquids by liquefaction. The liquid fuel resulting from this process can be stored and subsequently used for various heating and electricity generation applications. In addition to liquid fuels, the pyrolysis process also produces other combustible products such as charcoal, gas, and many other value-added chemicals (Kaushika et al., 2016).

The typical scheme of the biomass pyrolysis process is shown in **Figure 13**.

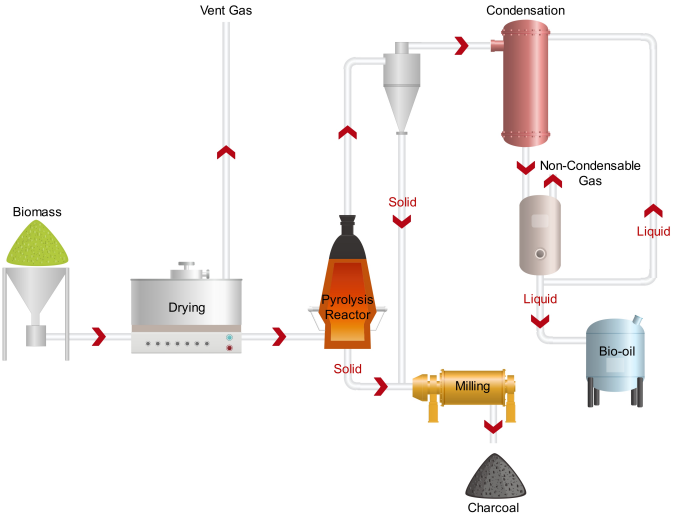

Fig. 13. Biomass pyrolysis scheme.

As mentioned earlier, simple pyrolysis systems are performed at temperatures below 600 °C, while in industrial plants, where temperatures higher than 600-1000 °C are arched, the gas produced contains higher quantities of hydrogen. Obviously, these processes require more sophisticated systems and management as well (Di Blasi, 2008).

The pyrolysis process consists of four main steps taking place at different temperatures following the order presented below (Portha et al., 2017):

a. Drying of the incoming biomass at temperatures ranging between 100-120 °C;
b. Distillation of the outlet gases, mainly N_2, CO, and CO_2, acetic acid and methanol at 275 °C;
c. Exothermic reactions occurring at temperatures between 280 °C and 350 °C, thereby removing complex mixtures of chemical substances (i.e., ketones, aldehydes, phenols, esters), CO_2, carbon monoxide (CO), methane (CH_4), C_2H_6, and H_2 by breaking the weakest chemical bonds;
d. Removal of all volatile compounds by evaporation at 350 °C, with formation of higher proportions of H_2, CO, and carbon; the last one remains in the form of charcoal as residues.

Condensed liquids (tar, pyroleptic acid and derivatives) from the pyrolysis process can be separated. The approximate yield of the products from 100 kg of dry wood is: 30 kg of charcoal, 14 m^3 of gas (calorific value of 10.4 MJ/m^3), 7.6 L of wood oil and light tar, 1.4 L of methyl alcohol, 3 kg of pitch, 5.3 L of acetic acid, 0.8 L of esters, *etc.* (Damartzis and Zabaniotou, 2011).

There are different ways of carrying out the pyrolytic process affecting the production of bio-oil, syngas and carbonaceous residues:

I. Carbonization, the most ancient and known pyrolysis process, occuring at temperatures between 300 and 500 °C (Kaltschmitt, 2013). From this process, only a solid fraction (vegetable coal) is recovered.
II. Slow or conventional pyrolysis occurs at moderate temperatures around 500 °C, through which approximately three fractions are obtained in equal proportions. Slow pyrolysis requires longer reaction and transformation times than fast pyrolysis due to low temperature and heating values.
III. Fast pyrolysis takes place at medium-low temperatures (from 500 to 650 °C), in which the gasification reactions take place quickly and with short contact times, so that the intermediate compounds are reformed, bringing the production of the liquid fraction up to 70-80 wt.% of the incoming biomass. Generally, this type of pyrolysis produces 60% of bio-oil, 20% of bio-coal, and 20% of gas.
IV. Flash pyrolysis is performed at temperatures higher than 650 °C with contact times of less than one second and favours the production of the gaseous fraction (efficiency reaching 80%).

Currently, the pyrolysis process is mainly used for the production of the liquid fraction, i.e., the bio-oil, which can be used as fuel for energy production through co-generators. The use of bio-oil has considerable advantages including more competitive production cost compared to other biofuels, a balance of neutral CO_2 emissions, and a high energy density if refined well (Kaltschmitt, 2013).

5.1.3. Gasification

The gasification process converts solid carbon materials (solid biomass) into a gas, called synthesis gas or syngas, mainly composed of CO, hydrogen (H_2), and nitrogen (N_2). Syngas can be used as fuel to generate electricity, or as a basis for a large number of products in the petrochemical and refinery industries, such as methanol, ammonia, synthetic gasoline, *etc.* (Rahimpour et al., 2012)

The first gasification technologies were developed in the early decades of the twentieth century. There are different types of treatment and processes, but they all share some common characteristics. Of course, the dominant technology is the partial oxidation of the solid matrix at high temperatures, which produces a syngas consisting of CO and H_2 in various ratios, whose combination accounts for more than 85% of the total volume, while the remaining gas includes CO_2 and CH_4 (Molino et al., 2016).

This treatment is a rather complex thermochemical process that can be carried out in a closed air-tight chamber under air suction or low air pressure relative to the atmospheric pressure. The gas produced by gasification is subsequently 'cleaned', to remove impurities and recover trace elements at once. This makes gasification a very interesting process thanks to the ability to remove all the pollutants from the syngas, in particular with regard to the materials with high contents of heteroatoms or impurities that cannot be treated with other procedures. For instance, through this technology, sulfur could generally be recovered in elementary form, while the purified gas

Please cite this article as: Tursi A. A review on biomass: importance, chemistry, classification, and conversion. Biofuel Research Journal 22 (2019) 962-979. DOI: 10.18331/BRJ2019.6.2.3

could be used for chemicals production and/or electricity generation (Fig. 14).

The produced gas consists of several combustible and non-combustible fractions; depending on both the type of biomass and the operational conditions of the process. In general, the produced gas has a calorific value of between 4.5 and 6 MJ/m^3, corresponding to 10 to 50% of the calorific value of natural gas (Akia et al., 2014).

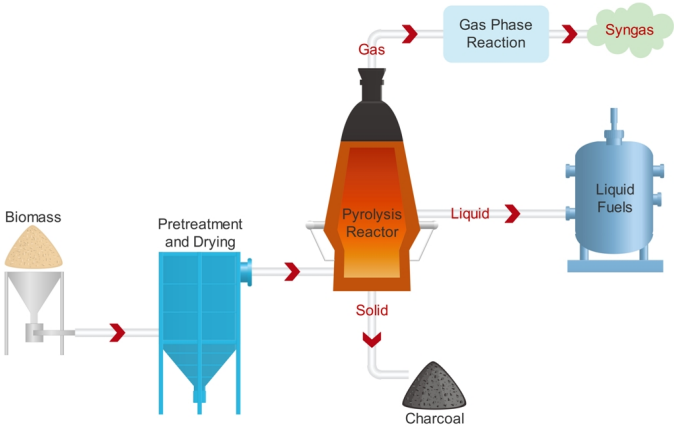

Fig. 14. Biomass gasification scheme.

The biomass gasification process essentially involves four different processes (Portha et al., 2017) (Fig. 14):

I. Oxidation (exothermic stage)

The oxidation phase of biomass gasification is performed to reach the necessary operating temperature to implement the endothermic processes. Oxidation is carried out in the absence of oxygen (Molino et al., 2016).

The reactions occurring during the oxidation phase are as follows (Eqs. 3, 4, and 5) (Kaltschmitt, 2013):

Combustion of coal	$C + O_2 \rightarrow CO_2$	ΔH = -394 kJ/mol	Eq. 3
Partial oxidation	$C + ½\ O_2 \rightarrow CO$	ΔH = -111 kJ/mol	Eq. 4
Hydrogen combustion	$H_2 + ½\ O_2 \rightarrow H_2O$	ΔH = -242 kJ/mol	Eq. 5

Therefore, the main purpose of this step is to obtain the thermal energy that allows the entire process to be performed. The resulting combustion product is a mix of CO, CO_2, and water.

II. Drying (endothermic stage)

In the drying step, the moisture in the biomass is removed at over 100 °C by converting it into steam followed by elevating the temperature to 150 °C to complete the process. The heat input necessary for this phase is proportional to the moisture content of the raw material and generally derives from the previous oxidation phase (Molino et al., 2016).

III. Pyrolysis (endothermic stage)

Pyrolysis is the anaerobic thermal decomposition of the carbonaceous material deriving from the biomass, which generates a solid fraction (represented by a fraction of high carbon content, called "char" and by inert residues in the form of ash), a liquid fraction (called "tars" that consists of complex and condensable organic substances at relatively low temperatures), and a gaseous fraction (a mixture of incondensable gases such as H_2, CO_2, and CO and light hydrocarbons at room temperature, called pyrolysis gas) (Roos, 2010). In this step, the breakage of the chemical bonds of the molecules (with higher molecular weights), leads to the formation of lighter molecules. The pyrolysis stage is endothermic and takes place at temperatures ranging between 250 and 700 °C (Eq. 6):

$$\text{Biomass} \leftrightarrow H_2 + CO + CO_2 + CH_4 + H_2O\ (g) + \text{Tar} + \text{Char} \qquad \text{Eq. 6}$$

In Equation 6, since biomass is already treated, the term biomass can be replaced by the formula of cellulose $C_6H_{10}O_6$, which is the main component of the biomass contributing around 50-55% of the total weight of the matrix (Molino et al., 2016). Regarding cellulose, pyrolysis reactions occur between 600 and 700 °C.

Within this process step, on average 12.01 kg of carbon is completely oxidized with 22.39 m^3 of oxygen supplied by the air to produce 22.26 m^3 of CO and about 0.04 GJ of heat (Molino et al., 2016).

IV. Reduction (endothermic stage)

In the reduction phase (gas phase reactions), the mixture of gas and coal, derived from the previous phases of pyrolysis and oxidation, are transformed. The products of the previous phases react with each other, leading to the formation of the final syngas. The main reactions occurring in the reduction phase are shown in Equations 7, 8, 9, and 10) (Zhang et al., 2013):

Boudouard reaction:

$$C + CO_2 \leftrightarrow 2CO \qquad \Delta H = 172\ \text{kJ/mole} \qquad \text{Eq. 7}$$

Character reform:

$$C + H_2O \leftrightarrow CO + H_2 \qquad \Delta H = 131\ \text{kJ/mole} \qquad \text{Eq. 8}$$

Water gas displacement reaction:

$$CO + H_2O \leftrightarrow CO_2 + H_2 \qquad \Delta H = -41\ \text{kJ / mole} \qquad \text{Eq. 9}$$

Methanation:

$$C + 2H_2 \leftrightarrow CH_4 \qquad \Delta H = -75\ \text{kJ / mole} \qquad \text{Eq. 10}$$

Equations 7 and 8 are endothermic and are favoured by increases in temperature, while Equations 9 and 10 are exothermic and are positively fostered by low temperatures; ultimately the global endothermic contribution is greater than the exothermic one, making the contribution of the reactions globally endothermic, so that the whole step requires energy.

The reduction temperature represents a fundamental parameter in determining the composition and characteristics (such as tar pre-stress and lower heating capacity) of the syngas and of the final solid residue. In fact, the higher the temperature of the process is, the higher the degree of oxidation of the coal will be; resulting in low levels of solid residues and tar at the end of the process.

The gasification processes are carried out at temperatures ranging between 800 and 1100 °C, while this range could be between 500 and 1600 °C, when the process requires the use of oxygen for the gasification phase (Shen et al., 2012).

In conclusion, gasification technology can be a proper solution for the production of energy from biomass, despite the high concentrations of pollutants potentially generated by the process as by-products (i.e., tar, ammonia, hydrogen sulphide, and hydrochloric acid).

5.1.4. Liquefaction

Liquefaction is a biomass conversion process conducted in water at moderate temperatures ranging between 280 to 370 °C and high pressures (10-25 MPa). A liquid biogranulate, similar to crude oil, as well as other gaseous, aqueous, and solid by-products are also generated (López Barreiro et al., 2013).

Please cite this article as: Tursi A. A review on biomass: importance, chemistry, classification, and conversion. Biofuel Research Journal 22 (2019) 962-979. DOI: 10.18331/BRJ2019.6.2.3

The obtained products has a high heating and a low oxygen content making it a chemically stable fuel. The main purpose of liquefaction is to obtain high H/C ratio oil. For this type of conversion, two processes, based on the raw materials used, are distinguished: lignocellulosic biomass (dry raw material) liquefaction and algal biomass (wet raw material) liquefaction. In both cases, the raw material requires a preliminary treatment, which consists in the removal of woody biomass contaminants along with obtaining a stable suspension, thereby reducing the size of the particles (through alkaline treatments) for easy pumping into reactors (Gollakota et al., 2018).

Principally, the most used process includes the use of lignocellulosic biomass processed at a temperature of about 350 °C and a pressure of 150 bar for about 15 min. Under these process conditions, a spontaneous phase separation takes place, generating a gaseous phase of CO_2, solid residues, bio-crude, and a minor aqueous phase (Rowbotham et al., 2012). The obtained solid phase material could be used directly as biofuel or fertilizer (**Fig. 15**). The aqueous phase could be used inside the plant for processes requiring water or in anaerobic digestion. The bio-crude produced, which has a low oxygen content, requires further refining to be commercially exploited (Yu et al., 2011).

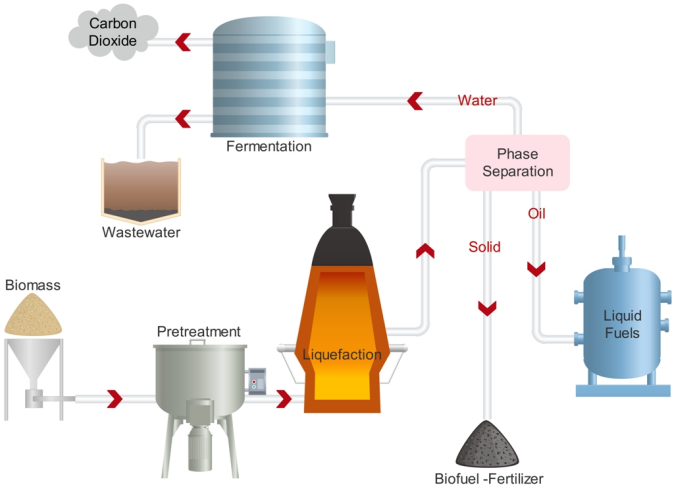

Fig. 15. Biomass liquefaction scheme.

5.2. Biochemical conversion of biomass

Biochemical conversion processes allow the decomposition of biomass to available carbohydrates, which could be converted into liquid fuels and biogas, as well as different types of bio-products, using biological agents such as bacteria, enzymes, *etc.* (Mahalaxmi and Williford, 2014). The most used biochemical technologies include anaerobic digestion and fermentation (Brethauer and Studer, 2015).

5.2.1. Anaerobic digestion

Anaerobic digestion is a multi-step biological process that is useful not only for proper waste management but also for generating renewable energy (Zamani, 2015). It consists of four basic stages, i.e., hydrolysis, acidogenesis, acetogenesis, and methanogenesis. During the whole process, there are series of chemical reactions occuring through natural metabolic pathways, enabled by microorganisms in an oxygen-free environment. These reactions break down the organic macromolecules into simpler molecules leading to the generation of biogas (a mix of methane and carbon dioxide as well as traces of other gases) and digestate. The feedstocks commonly used in this type of process, include sewage sludge, agricultural residues, MSW, and animal manure (Sharma, 2015). A schematic presentation of anaerobic digestion process is shown in **Figure 16**.

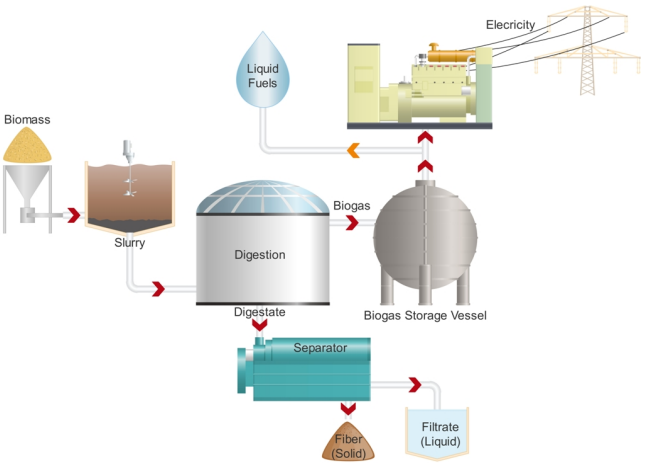

Fig. 16. Biomass anaerobic digestion scheme.

The biogas produced possesses an energy content 20-40% lower than the heating value of the raw material. The process is ideal for organic wastes with a moisture content ranging between 80 to 90%. One of the advantages of the process lies in the potential of the final biogas to be used directly in ignition gas engines and gas turbines. The overall conversion efficiency of this process is 21%. Residual heat from the engines and turbines can be recovered through an exchanger (Yadvika et al., 2004).

The basic stages of the anaerobic digestion process are explained below (Zamani, 2015):

I. Hydrolysis

Hydrolysis represents the initial phase of the process: biomass (consisting of very large organic polymers such as fats, carbohydrates, and proteins) is converted into smaller molecules such as fatty acids, simple sugars, and amino acids, respectively (Horan, 2018). It should be noted that most of the large molecules are further decomposed in the acidogenesis stage. On the other hand, other by-products resulting from the hydrolysis stage, including hydrogen and acetate, are used in the final stage of the process, i.e., methanogenesis.

II. Acidogenesis

Acidogenesis is the second stage of anaerobic digestion, through which acidogenic microorganisms (fermentative bacteria) further decompose the products of the hydrolysis stage, producing NH_3, CO_2, H_2, H_2S, alcohols, lighter volatile fatty acids, carbonic acids, and alcohols. Acidogenesis process only partially decomposes the biomass; therefore, for the final production of methane, the acetogenesis process is required.

III. Acetogenesis

This step employs acetogenic microorganisms catabolising the products created in the acidogenesis phase into acetic acid (CH_3COOH), CO_2, and H_2. Acetogens finalize the break down process of the biomass facilitating the action of the methanogenic archaea to produce methane as biofuel.

IV. Methanogenesis

Methanogenesis is the final stage of anaerobic digestion during which, as mentioned earlier, methane is generated from the main products of acetogenesis (i.e., CH_3COOH and CO_2) through hydrogenotrophic methanogenesis and/or acetoclastic methanogenesis as shown in **Equations 11** and **12**, respectively.

Please cite this article as: Tursi A. A review on biomass: importance, chemistry, classification, and conversion. Biofuel Research Journal 22 (2019) 962-979. DOI: 10.18331/BRJ2019.6.2.3

Hydrogenotrophic methanogenesis $CO_2 + 4H_2 \rightarrow CH_4 + 2H_2O$ Eq. 11

Acetoclastic methanogenesis $CH_3COOH \rightarrow CH_4 + CO_2$ Eq. 12

5.2.2. Fermentation

The fermentation process of organic materials consists of a series of biochemical reactions, converting simple sugars (hexoses and pentoses) into ethanol and CO_2, under anaerobic conditions by microorganisms mainly yeasts (**Eq. 13**). The microorganisms commonly used to carry out the process are the *Saccharomyces Cerevisiae*, while the feedstock used for this type of process are categorized into three different classes: sugars, starch, and lignocellulosic substrates. In detail, the theoretical yield of the process is 51.14 g of ethanol and 48.86 g of CO_2, from 100 g of hexoses or pentoses (**Eqs. 14** and **15**). In addition to ethanol and CO_2, glycerol and carboxylic acids are also produced as by-products. The quality and yields of the process depend on various factors such as feedstock, temperature, pH, inoculum, and fermentation time (Strezov et al., 2014).

Sugars $\rightarrow$ Ethanol + CO_2 + by-products Eq. 13

$C_6H_{12}O_6$ (hexoses) $\rightarrow 2\ C_2H_5OH + 2\ CO_2$ Eq. 14

$3\ C_5H_{10}O_5$ (pentoses) $\rightarrow 5\ C_2H_5OH + 5\ CO_2$ Eq. 15

The conversion of sugars into ethanol could take place through different metabolic pathways depending on the starting substrate. More specifically, (a) from hexoses such as glucose, through glycolysis or Embden-Meyerhof pathway (EMP) (Taherzadeh and Karimi, 2008) and (b) from pentoses, through a pentose phosphate pathway (PPP). The conversion reactions of the hexoses are faster than those of the pentoses.

At the end of the conversion process, ethanol is distilled and dehydrated, in order to obtain concentrated alcohol, while the solid residues can be used as fuel in boilers for the production of gas or can be used as feed for livestock (Mariod, 2016). A schematic presentation of biomass fermentation process is shown in **Figure 17**.

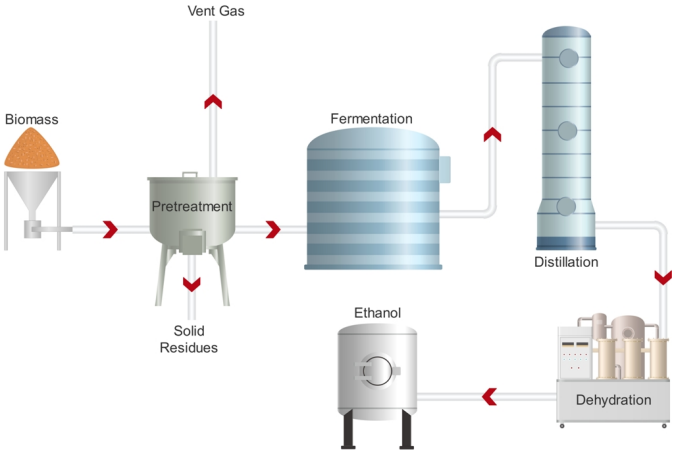

Fig. 17. Biomass fermentation scheme.

5.3. Physico-chemical conversion of biomass

The physico-chemical conversion processes of biomass leads to the production of high-density biofuels (**Fig. 18**). More specifically, various types of vegetable oil ad animal fats are converted into biodiesel through esterification and/or transesterification processes. Major vegetable oils used to produce first generation biodiesel include rapeseed oil and sunflower oil accounting for 80-85% and 10-15% of the total biodiesel production worldwide, respectively (Fukuda et al., 2001). Waste oils including waste cooking oil (WCO) and microbial oil including algal oil could also be used to produce second and third generation biofiesel, respectively.

It should be noted that oils are mainly composed of triglycerides, which do not represent a usable fuel. In fact, the transformation of the crude vegetable oil is necessary as otherwise, problems such as incomplete combustion and consequent accumulation of residues in engines are expected. Therefore, the raw material must undergo further processing, i.e., mainly transesterification, to break apart the triglyceride molecules into their constituents, i.e., fatty acids and glycerol. The latter is in fact the source of high viscosity of vegetable oils.

Through the transesterification reaction, the triglycerides are converted into methyl or ethyl esters (biodiesel) through the use of methyl or ethyl alcohol (in excess), respectively, in the presence of mostly an alkaline catalyst (i.e., NaOH or KOH) (**Eq. 16**):

Oil + Short chain alcohol $\rightarrow$ Biodiesel + glycerol Eq. 16

The transesterification process of triglycerides occurs at low temperatures (50-70 °C) and at atmospheric pressure. The obtained product is neutralized and purified, especially for the presence of glycerol (Leung et al., 2010).

The glycerol fraction is much denser than the biodiesel fraction, so it can be separated from biodiesel using a phase separator. Once the glycerol and biodiesel phases have been separated, the excess alcohol could be removed by distillation or partial evaporation. Once separated from glycerol, biodiesel is usually purified by water-washing (liquid-liquid extraction) in order to remove residual catalysts and soaps. The product is finally dried and stored.

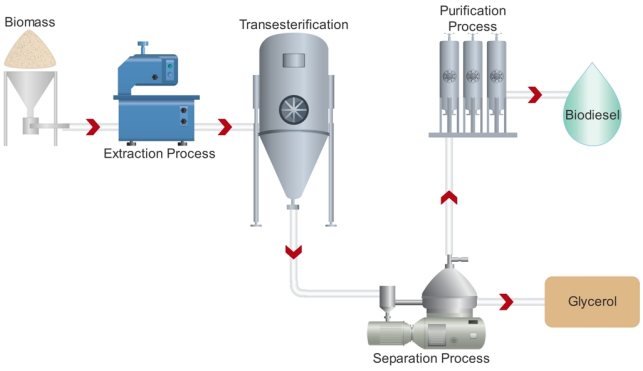

Fig. 18. Biomass physico-chemical conversion scheme.

Biodiesel is a renewable, biodegradable, and non-toxic fuel and its physicochemical parameters are very close to those of diesel. Some unique features, such as high oxygen content and high lubrication properties, ensure efficient combustion of biodiesel in diesel engines.

Regarding the glycerol (or glycerine), rather than considering it as waste, it could be valorized into various value-added compounds with applications in various industries such food and pharmaceutical ones (Canakci and Van Gerpen, 1999).

6. Biomass *vs.* other renewable energies

According to the latest estimates provided by the International Energy Agency (IEA, 2018), global energy consumption has grown by 37% over the last 15 years, standing at 368 EJ in 2016 against 269 EJ in 2000. Currently, renewable energy resources account for 66 EJ, accounting for approximately 18% of the total global energy consumption out of which 72.3% is contributed by biomass (WBA, 2018) (**Fig. 19**).

Please cite this article as: Tursi A. A review on biomass: importance, chemistry, classification, and conversion. Biofuel Research Journal 22 (2019) 962-979. DOI: 10.18331/BRJ2019.6.2.3

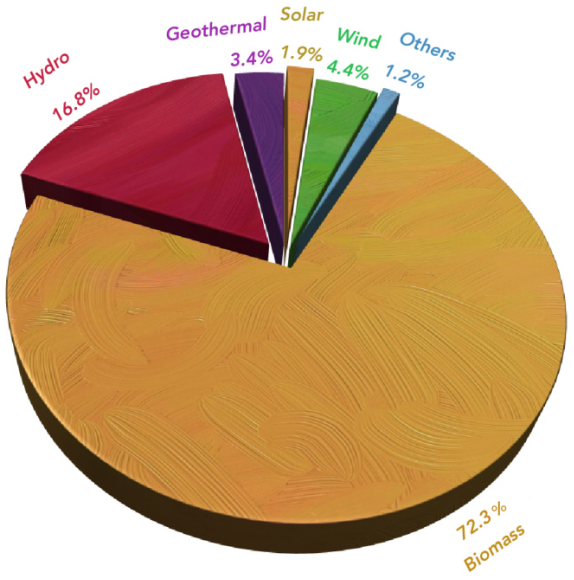

Fig. 19. Global renewable energy resources.

Biomass-derived energy production has increased from 42.8 EJ in 2000 to 56.5 EJ in 2016 (+32%), largely matching the increase in demand over the last two decades (WBA, 2018) (**Table 7**). As shown, in 2016, biomass-derived energy production is mainly contributed by solid biomass and liquid biofuel, collectively contributing 93% of the whole value. Moreover, according to the production trend across 2000-2016, liquid biofuel showed an outstanding growth in utilization, accounting for 6% of the total bioenergy supply in 2016, compared to 1% in 2000.

Table 7.
Bioenergy supply of biomass in 2000-2016 (WBA, 2018).

Year	Bioenergy supply through biomass (EJ)					
	Total	Municipal solid waste	Industrial waste	Solid biomass	Biogas	Liquid biofuels
2000	42.8	0.74	0.47	40.9	0.28	0.42
2016	56.5	1.43	1.03	49.1	1.31	3.59

Taking into consideration the end-products derived from biomass, in all cases, an enormous increase in global production has recorded over the last 15 years (**Table 8**), confirming a trend towards a renewable approach to production and consumption. Specifically and as mentioned earlier, global biofuels production has registered a growth trend from approximately 16 billion L in the year 2000 to 143 billion L in the year 2016 (of which 65% was bioethanol, 25% was biodiesel, and 10% was other biofuels). In addition, electricity, heat, and biogas have recorded outstanding growths in production (WBA, 2018).

Furthermore, the renewable energy sector has recorded a growing trend in recruitment with the latest estimates showing that employment by this sector has risen from 2.4 million in 2012 to 3.1 million in 2017. This further highlights the important role of the biomass sector in driving and boosting the world economy (WBA, 2018).

6.1. Economic and environmental analysis of biomass-derived energy production

Among the various resources and renewable technologies, biomass could represent the most promising economic lever for developing countries, providing benefits to the level of employment and, at the same time, environmental protection.

Table 8.
Global production of the main energy products derived from biomass in 2000 and 2016 (WBA, 2018).

End product	Year	Global production	Unit
Electricity	2000	164	Terawatt h (TWh)
	2015	528	
Heat	2000	414,081	Terajoule (TJ)
	2015	940,492	
Liquid biofuels	2000	15.9	Billion L
	2017	143	
Biogas	2000	13.2	m^3
	2016	60.8	

In order to provide an economic analysis of the different production technologies generating the main products from biomass (i.e., electricity and biofuels), an assessment of the production cost, conversion efficiency, and size of the processing is presented. The parameters taken into consideration include the levelized cost of energy (LCOE, USD/kWh) and the cost of the final biofuel (USD/L), for the production of electrical energy and biofuels, respectively. **Table 9** shows the comparison between the most commonly used technologies and the related evaluation parameters.

As presented, manufacturing cost and conversion efficiency of the processes taken into consideration can vary significantly, based on the raw material used and the type of conversion performed. In general, the cost of electricity production is between 0.03 USD and 0.24 USD/kWh, while for the biofuel, the production cost ranges between 0.13 and 0.99 USD/L. Nevertheless, the prices of conventional electricity and fuels are still competitive compared to their bio-based counterparts. Despite this, unlike the use of fossil fuels, the environmental advantages are huge for several reasons:

I. Biomass is a renewable energy source and therefore, it will not exhaust;
II. Biomass energy is generated mainly from constantly increasing wastes disposed of by various sectors, which would otherwise be released into the environment;
III. The use of biomass could significantly reduce the amount of GHG emissions, contributing to the mitigation of environmental crises such as climate change and global warming.

Regarding the last item, several studies have shown a clear decrease in GHGs emissions, in specific cases even greater than 90% in response to the replacement of fossil fuels with biomass-derived energy. **Figure 20** shows a comparison of CO_2 emissions (expressed as Mt CO_2-eq/Mtoe) of conventional energy sources and biomass-derived energy sources, with their respective savings in GHGs emissions.

7. Concluding remarks and future prospects

Replacement of fossil energy carriers with biomass-derived energy carriers could bring about positive impacts from multiple perspectives, i.e., economic, environmental, and health. Moreover, production of biomass-derived energy could be achieved under any geographical conditions owing the large availability of biomass all over the world while it could simultaneously contribute to efficient management of various waste streams. Technological innovations to increase productivity and reduce costs are the main challenges to further expand the share of such renewable energy carriers. Efforts should be directed toward the development of more user-friendly cost-efficient technologies at various scales to attract more investment in the field.

Creating further awareness towards the advantages of biomass exploitation for renewable energy production is also necessary. It should be

Please cite this article as: Tursi A. A review on biomass: importance, chemistry, classification, and conversion. Biofuel Research Journal 22 (2019) 962-979. DOI: 10.18331/BRJ2019.6.2.3

Table 9.
Economic evaluation of several biomass technologies for electricity and biofuels production (De Wit et al., 2010; Dutta et al., 2011; Chen et al., 2012; IRENA, 2012).

Electricity			
Technology	**Plant size (dry ton/yr)**	**LCOE* (USD/kWh)**	**Conversion efficiency (kWh/ton)**
Gasification	175,000	0.06 – 0.24	30 – 40 %
Anaerobic digestion	770,000	0.06 – 0.19	25 – 40 %
Combustion	350,000	0.03 – 0.22	25 – 35 %
Pyrolysis	175,000	0.07 – 0.24	33 – 50 %
Biofuels			
Technology	**Plant size (million L/yr)**	**USD/L**	**Conversion efficiency (L of ethanol or biodiesel/ton)**
Enzymatic hydrolysis	231	0.37 – 0.66	29 – 33 %
Thermochemical process	245	0.35 – 0.88	24 – 32 %
Gasification	111 – 143	0.46 – 0.47	18 – 23 %
Fast pyrolysis	134 – 220	0.13 – 0.16	20 – 33 %
Fisher-Tropsch	45 – 360	0.35 – 0.94	14 %
Transesterification	30 – 284	0.68 – 0.99	97 – 99 %

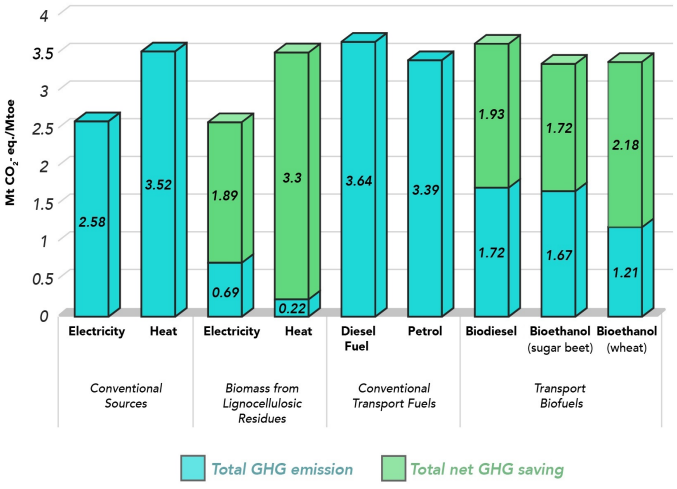

Fig. 20. Comparison of CO_2 emissions from conventional energy sources biomass-derived energy sources along with their respective savings in GHGs emissions

highlighted that production of biomass-derived energy carriers, i.e., bio-electricity and biofuels could be regarded as an efficient means of meeting some of the main Sustainable Development Goals (SDGs) set by the United Nations General Assembly in 2015 for the year 2030 in particular Affordable and Clean Energy.

References

[1] Abejón, R., Pérez-Acebo, H., Clavijo, L., 2018. Alternatives for chemical and biochemical lignin valorization: hot topics from a bibliometric analysis of the research published during the 2000-2016 period. Processes. 6(8), 98.

[2] Agbor, V.B., Cicek, N., Sparling, R., Berlin, A., Levin, D.B., 2011. Biomass pretreatment: fundamentals toward application. Biotechnol. Adv. 29(6), 675-685.

[3] Akia, M., Yazdani, F., Motaee, E., Han, D., Arandiyan, H., 2014. A review on conversion of biomass to biofuel by nanocatalysts. Biofuel Res. J. 1(1), 16-25.

[4] Alaswada, A., Dassisti, M., Prescotta, T., Olabia, A.G., 2015. Technologies and developments of third generation biofuel production. Renew. Sust. Energy Rev. 51, 1446-1460.

[5] Amidon, T.E., Wood, C.D., Shupe, A.M., Wang, Y., Graves, M., Liu, S., 2008. Biorefinery: conversion of woody biomass to chemicals, energy and materials. J. Biobased Mater. Bioenergy. 2(2), 100-120.

[6] Anex, R.P., Aden, A., Kazi, F.K., Fortman, J., Swanson, R.M., Wright, M., Satrio, J.A., Brown, R.C., Daugaard, D.E., Platon, A., Kothandaraman, G., Hsu, D.D., Dutta, A., 2010. Techno economic comparison of biomass-to-transportation fuels via pyrolysis, gasification, and biochemical pathways. Fuel. 89, 529-535.

[7] Arias, F.E.A., Beneduci, A., Chidichimo, F., Furia, E., Straface, S., 2017. Study of the adsorption of mercury (II) on lignocellulosic materials under static and dynamic conditions. Chemosphere. 180, 11-23.

[8] Bajpai, P., 2009. Xylanases, in: Schaechter, M., Lederberg, J. (Eds.), Encyclopedia of Microbiology. Academic Press, San Diego, pp. 600-612.

[9] Bala, J.D., Lalung, J., Al-Gheethi, A.A.S., Norli, I., 2016. A Review on Biofuel and Bioresources for Environmental Applications, in: Ahmad, M., Ismail, M., Riffat, S. (Eds.), Renewable Energy and Sustainable Technologies for Building and Environmental Applications. Springer, Cham, pp. 205-225

[10] Biochemical Conversion: Using Hydrolysis, Fermentation, and Catalysis to Make Fuels and Chemicals.

[11] Bonechi, C., Consumi, M., Donati, A., Leone, G., Magnani, A., Tamasi, G., Rossi, C., 2017. Biomass: An overview, in: Dalena, F., Basile, A., Rossi, C. (Eds.), Bioenergy Systems for the Future: Prospects for Biofuels and Biohydrogen. Elsevier Publishing, London, pp. 3-42.

[12] Brethauer, S., Studer, M.H., 2015. Biochemical conversion processes of lignocellulosic biomass to fuels and chemicals-a review. Chimia. 69(10), 572-581.

Please cite this article as: Tursi A. A review on biomass: importance, chemistry, classification, and conversion. Biofuel Research Journal 22 (2019) 962-979. DOI: 10.18331/BRJ2019.6.2.3

[13] Buléon, A., Colonna, P., Planchot, V., Ball, S., 1998. Starch granules: structure and biosynthesis. Int. J. Biol. Macromol. 23(2), 85-112.
[14] Canakci, M., Van Gerpen, J.H., 1999. Biodiesel production via acid catalysis. Transactions of the ASAE. 42(5), 1203-1210.
[15] Carpenter, D., Westover, T.L., Czernik, S., Jablonski, W., 2014. Biomass feedstocks for renewable fuel production: a review of the impacts of feedstock and pretreatment on the yield and product distribution of fast pyrolysis bio-oils and vapors. Green Chem. 16(2), 384-406.
[16] Chen, H., 2014. Chemical composition and structure of natural lignocellulose, in: Chen, H. (Ed.), Biotechnology of Lignocellulose. Springer, Dordrecht, pp. 25-71.
[17] Chen, J., Li, C., Ristovski, Z., Milic, A., Gu, Y., Islam, M.S., Wang, S., Hao, J., Zhang, H., He, C., Guo, H., Fu, H., Miljevic, B., Morawsk, L., Thai, P., 2017. A review of biomass burning: Emissions and impacts on air quality, health and climate in China. Sci. Total Environ. 579, 1000-1034.
[18] Chen, X., Khanna, M., Yeh, S., 2012. Stimulating learning-by-doing in advanced biofuels: effectiveness of alternative policies. Environ. Res. Lett. 7(4), 045907.
[19] Chum, H., Faaij, A., Moreira, J., Berndes, G., Dhamija, P., Dong, H., Gabrielle, B., Goss Eng, A., Lucht, W., Mapako, M., Masera Cerutti, O., McIntyre, T., Minowa, T., Pingoud, K., 2011. Bioenergy, in: Edenhofer, O., Pichs-Madruga, R., Sokona, Y., Seyboth, K., Matschoss, P., Kadner, S., Zwickel, T., Eickemeier, P., Hansen, G., Schlömer, S., von Stechow, C. (Eds.), IPCC Special Report on Renewable Energy Sources and Climate Change Mitigation. Cambridge University Press, Cambridge
[20] Dalena, F., Senatore, A., Tursi, A., Basile, A., 2017. Bioenergy production from second- and third-generation feedstocks, in: Dalena, F., Basile, A., Rossi, C. (Eds.). Bioenergy Systems for the Future: Prospects for Biofuels and Biohydrogen. Elsevier Publishing, London, pp. 559-599.
[21] Damartzis, T., Zabaniotou, A., 2011. Thermochemical conversion of biomass to second generation biofuels through integrated process design-a review. Renew. Sust. Energy Rev. 15(1), 366-378.
[22] Demirbas, A., 2010. Use of algae as biofuel sources. Energy Convers. Manage. 51(12), 2738-2749.
[23] de Wit, M., Junginger, M., Lensink, S., Londo, M., Faaij, A., 2010. Competition between biofuels: modelling technological learning and cost reductions over time. Biomass Bioenergy. 34(2), 203-217.
[24] Di benedetto, A., 2011. The potential of aquatic biomass for CO_2-enhanced fixation and energy production. Greenhouse Gases Sci. Technol. 1(1), 58-71.
[25] Di Blasi, C., 2008. Modeling chemical and physical processes of wood and biomass pyrolysis. Prog. Energy Combust. Sci. 34(1), 47-90.
[26] Edwards, S., Chaplin, M.F., Blackwood, A.D., Dettmar, P.W., 2003. Primary structure of arabinoxylans of ispaghula husk and wheat bran. Proc. Nutr. Soc. 62(1), 217-222.
[27] Fromm, J., Rockel, B., Lautner, S., Windeisen, E., Wanner, G., 2003. Lignin distribution in wood cell walls determined by TEM and backscattered SEM techniques. J. Struct. Biol. 143(1), 77-84.
[28] Fukuda, H., Kondo, A., Noda, H., 2001. Biodiesel fuel production by transesterification of oils. J. Biosci. Bioeng. 92(5), 405-416.
[29] García, V., Päkkilä, J., Ojamo, H., Muurinen, E., Keiski, R.L., 2011. Challenges in biobutanol production: how to improve the efficiency?. Renew. Sust. Energy Rev. 15(2), 964-980.
[30] Gollakota, A.R.K., Kishore, N., Gu, S., 2018. A review on hydrothermal liquefaction of biomass. Renew. Sust. Energy Rev. 81, 1378-1392.
[31] Habert, G., Bouzidi, Y., Chen, C., Jullien, A., 2010. Development of a depletion indicator for natural resources used in concrete. Resour. Conserv. Recycl. 54(6), 364-376.
[32] Harmsen, P.F.H., Hujigen, W., Bermudez, L., Bakker, R., 2010. Literature review of physical and chemical pretreatment processes for lignocellulosic biomass. Wageningen UR Food & Biobased Research.
[33] Hodásová, L., Jablonský, M., Škulcová, A., Ház, A., 2015. Lignin, potential products and their market value. Wood Res. 60(6), 973-986.
[34] Horan, N.J., 2018. Introduction, in: Horan, N., Yaser, A., Wid, N. (Eds.), Anaerobic Digestion Processes. Green Energy and Technology. Springer, Singapore, pp 1-7.
[35] Huber, G.W., Iborra, S., Corma, A., 2006. Synthesis of transportation fuels from biomass: chemistry, catalysts, and engineering. Chem. Rev. 106(9), 4044-4098.
[36] IEA, 2018. World energy balances, IEA World Energy Statistics and Balances (database). Int. Energy Agency.
[37] Imai, M., Ikari, K., Suzuki, I., 2004. High-performance hydrolysis of cellulose using mixed cellulase species and ultrasonication pretreatment. Biochem. Eng. J. 17(2), 79-83.
[38] IRENA, 2012. Biomass for power generation, renewable energy technologies: Cost Analysis Series, Irena Working Paper, International Renewable Energy Agency.
[39] Jacobsson, S., Johnson, A., 2000. The diffusion of renewable energy technology: an analytical framework and key issues for research. Energy Policy. 28(9), 625-640.
[40] Jiang, T.D., 2001. Lignin, Chemical Ind. Press, Beijing, pp. 1-17.
[41] Jindal, M.K., Jha, M.K., 2016. Hydrothermal liquefaction of wood: a critical review. Rev. Chem. Eng. 32(4), 459-488.
[42] Kaltschmitt, M., 2013. Renewable energy from biomass, Introduction, in: Kaltschmitt, M., Themelis, N.J., Bronicki, L.Y., Söder, L., Vega, L.A. (Eds.), Renewable Energy Systems. Springer, New York.
[43] Kaushika, N.D., Reddy, K.S., Kaushik, K., 2016. Biomass Energy and Power Systems, in: Kaushika, N.D., Reddy, K.S., Kaushik, K. (Eds.). Sustainable Energy and the Environment: A Clean Technology Approach. Springer, Cham, pp. 123-137.
[44] Kosa, M., Ragauskas, A.J., 2012. Bioconversion of lignin model compounds with oleaginous *Rhodococci*. Appl. Microbiol. Biotechnol. 93(2), 891-900.
[45] Lauri, P., Havlík, P., Kindermann, G., Forsell, N., Böttcher, H., Obersteiner, M., 2014. Woody biomass energy potential in 2050. Energy Policy. 66, 19-31.
[46] Laurichesse, L., Avérous, S., 2014. Chemical modification of lignins: towards biobased polymers. Prog. Polym. Sci. 39(7), 1266-1290.
[47] Lebaka, V., 2013. Potential bioresources as future sources of biofuels production: An Overview, in: Gupta, V., Tuohy, M.G. (Eds.), Biofuel Technol. Springer, Berlin, pp. 223-258.
[48] Leung, D.Y.C., Wu, X., Leung, M.K.H., 2010. A review on biodiesel production using catalyzed transesterification. Appl. Energy. 87(4),1083-1095.
[49] López Barreiro, D., Prins, W., Ronsse, F., Brilman, W., 2013. Hydrothermal liquefaction (HTL) of microalgae for biofuel production: state of the art review and future prospects. Biomass Bioenergy. 53, 113-127.
[50] Madeira Jr, J.V., Contesini, F.J., Calzado, F., Rubio, M.V., Zubieta, P., Lopes, D.B., de Melo, R.R., 2017. Agro-industrial residues and microbial enzymes: an overview on the eco-friendly bioconversion into high value-added products, in: Brahmachari, G., Demian, A.L., Adrio, J. (Eds.), Biotechnology of microbial enzymes- Production, biocatalysis and industrial applications. Academic Press, pp. 475 -511.
[51] Mahalaxmi, S., Williford, C., 2014. Biochemical conversion of biomass to fuels, in: Chen, W., Suzuki, T., Lackner, M. (Eds.), Handbook of climate change mitigation and adaptation. Springer, New York, pp. 1-28.
[52] Mariod, A.A., 2016. Extraction, Purification, and Modification of Natural Polymers, in: Olatunji, O. (Ed.), Natural Polymers. Springer, Cham, pp. 63-91.
[53] McKendry, P., 2002. Energy production from biomass (part 2): conversion technologies. Bioresour. Technol. 83(1), 47-54.
[54] McKendry, P., 2002. Energy production from biomass (part 1): overview of biomass. Bioresour. Technol. 83(1), 37-46.
[55] Mesa, L., González, E., Ruiz, E., Romero, I., Cara, C., Felissia, F., Castro, E., 2010. Preliminary evaluation of organosolv pre-treatment of sugar cane bagasse for glucose production: application of 2^3 experimental design. Appl. Energy. 87(1), 109-114.

Please cite this article as: Tursi A. A review on biomass: importance, chemistry, classification, and conversion. Biofuel Research Journal 22 (2019) 962-979. DOI: 10.18331/BRJ2019.6.2.3

[56] Molino, A., Chianese, S., Musmarra, D., 2016. Biomass gasification technology: the state of the art overview. J. Energy Chem. 25(1), 10-25.
[57] Mosier, N., Wyman, C., Dale, B., Elander, R., Lee, Y.Y., Holtzapple, M., Ladisch, M., 2005. Features of promising technologies for pretreatment of lignocellulosic biomass. Bioresour. Technol. 96(6), 673-686.
[58] Nussbaumer, T., 2003. Combustion and co-combustion of biomass: fundamentals, technologies, and primary measure for emission reduction. Energy Fuels. 17(6), 1510-1521.
[59] Pandey, M.P., Kim, C.S., 2011. Lignin depolymerization and conversion: a review of thermochemical methods. Chem. Eng. Technol. 34, 29-41.
[60] Portha, J.F., Parkhomenko, K., Kobl, K., Roger, A.C., Arab, S., Commenge, J.M., Falk, L., 2017. Kinetics of Methanol Synthesis from Carbon Dioxide Hydrogenation over Copper-Zinc Oxide Catalysts. Ind. Eng. Chem. Res. 56(45), 13133-13145.
[61] Rana, R., Nanda, S., Meda, V., Dalai, A.K., Kozinski, J.A., 2018. A review of lignin chemistry and its biorefining conversion technologies. J. Biochem. Eng. Bioprocess. Technol. 1(2).
[62] Rahimpour, M.R., Arab Aboosadi, Z., Jahanmiri, A.H., 2012. Synthesis gas production in a novel hydrogen and oxygen perm-selective membranes tri-reformer for methanol production. J. Nat. Gas Sci. Eng. 9, 149-159.
[63] Roos, C.J., 2010. Clean Heat and Power Using Biomass Gasification for Industrial and Agricultural Projects, U.S. Department of Energy.
[64] Rowbotham, J., Dyer, P., Greenwell, H., Theodorou, M., 2012. Thermochemical processing of macroalgae: a late bloomer in the development of third-generation biofuels?. Biofuel. 3(4), 441-461.
[65] Sanchez, C., 2009. Lignocellulosic residues: biodegradation and bioconversion by fungi. Biotechnol. Adv. 27(2), 185-194.
[66] Schaechter, M., 2009. Encyclopedia of Microbiology, in: Nanninga, N. (Ed.), Cell Structure, Organization, Bacteria and Archaea, third ed. Academic Press, New York, pp. 357-374.
[67] Sharma, V.K., 2015. Technology development and innovation for production of next-ge neration biofuel from lignocellulosic wastes, in: Sharma, A., Kar, S. (Eds.), Energy sustainability through green energy. Green Energy Technology. Springer, New Delhi, pp. 315-350.
[68] Shen, D.K., Xiao, R., Gu, S., Luo, K.H., 2011. The pyrolytic behavior of cellulose in lignocellulosic biomass: a review. RSC Adv. 1(9), 1641-1660.
[69] Singh, N., Singh, J., Kaur, L., Sodhi, N.S., Singh, B.G., 2003. Morphological, thermal and rheological properties of starches from different botanical sources. Food Chem. 81(2), 219-231.
[70] Smolarski, N., 2012. High-value opportunities for lignin: unlocking its potential. Frost & Sullivan, Paris.
[71] Strezov, V., 2014. Properties of biomass fuels, in: Strezov, V., Evans, T.J. (Eds.), Biomass processing technologies. CRC Press, Boca Raton, pp. 1-32.
[72] Sun, Y., Cheng, J., 2002. Hydrolysis of lignocellulosic materials for ethanol production: a review. Bioresour. Technol. 83(1), 1-11.
[73] Sun, J., Wang, W., Yue, Q., Ma, C., Zhang, J., Zhao, X., Song, Z., 2016. Review on microwavemetal discharges and their applications in energy and industrial processes. Appl. Energy. 175, 141-157.
[74] Taherzadeh, M.J., Karimi, K., 2008. Pretreatment of lignocellulosic wastes to improve ethanol and biogas production: a review. Int. J. Mol. Sci. 9(9), 1621-1651.
[75] Tamaki, Y., Mazza, G., 2010. Measurement of structural carbohydrates, lignins, and micro-components of straw and shives: effects of extractives, particle size and crop species. Ind. Crops Prod. 31(3), 534-541.
[76] Teymouri, F., Laureano-Perez, L., Alizadeh, H., Dale, B.E., 2005. Optimization of the ammonia fiber explosion (AFEX) treatment parameters for enzymatic hydrolysis of corn stover. Bioresour. Technol. 96(18), 2014-2018.
[77] Tkemaladze, G.S., Makhashvili, K.A., 2016. Climate changes and photosynthesis. Ann. Agrar. Sci. 14(2), 119-126.
[78] Tursi, A., Beneduci, A., Chidichimo, F., De Vietro, N., Chidichimo, G., 2018. Remediation of hydrocarbons polluted water by hydrophobic functionalized cellulose. Chemosphere. 201, 530-539.
[79] Tursi, A., Chatzisymeon, E., Chidichimo, F., Beneduci, A., Chidichimo, G., 2018. Removal of endocrine disrupting chemicals from water: adsorption of bisphenol-a by biobased hydrophobic functionalized cellulose. Int. J. Environ. Res. Public Health. 15(11), 2419.
[80] Tursi, A., De Vietro, N., Beneduci, A., Milella, A., Chidichimo, F., Fracassi, F., Chidichimo, G., 2019. Low pressure plasma functionalized cellulose fiber for the remediation of petroleum hydrocarbons polluted water. J. Hazard. Mater. 373, 773-782.
[81] Vassilev, S.D., Andersen, L., Vassileva, C., Morgan, T., 2012. An overview of the organic and inorganic phase composition of biomass. Fuel, 94, 1-33.
[82] Vassilev, S.V., Baxter, D., Andersen, L.K., Vassileva, C.G., 2010. An overview of the chemical composition of biomass. Fuel. 89(5), 913-933.
[83] Vassilev, S.V., Vassileva C.G., 2016. Composition, properties and challenges of algae biomass for biofuel application: an overview. Fuel. 181, 1-33.
[84] Vorwerg, W., Radosta, S., Leibnitz, E., 2002. Study of a preparative-scale process for the production of amylose. Carbohydr. Polym. 47(2), 181-189.
[85] Wang, H., Tucker, M., Ji, Y., 2013. Recent development in chemical depolymerization of lignin: a review. J. Appl. Chem. Article ID 838645.
[86] Waniska, R.D., Rooney, L.W., McDonough, C.M., 2016. Sorghum: Utilization, in: Wrigley, C.W., Corke, H., Seetharaman, K., Faubion, J. (Eds.), Encyclopedia of Food Grains, second ed. Academic Press, San Diego, pp. 116-123.
[87] WBA, 2018. WBA Global bioenergy statistics 2018, Summary Report. World Bioenergy Association, www.worldenergy.org.
[88] Wells, T., Ragauskas, A.J., 2016. On the future of lignin-derived materials, chemicals and energy. Innov. Ener. Res. 5(2), 117.
[89] Welker, C.M., Balasubramanian, V.K., Petti, C., Rai, K.M., DeBolt, S., Mendu, V., 2015. Engineering plant biomass lignin content and composition for biofuels and bioproducts. Energies. 8(8), 7654-7676.
[90] Werkelin, J., Skrifvars, B.J., Hupa, M., 2005. Ash-forming elements in four Scandinavian wood species. Part 1: summer harvest. Biomass Bioenergy. 29(6), 451-466.
[91] Winger, M., Christen, M., Van Gunsteren, W.F., 2009. On the Conformational Properties of Amylose and Cellulose Oligomers in Solution. Int. J. Carbohydr. Chem. 2009, Article ID 307695.
[92] Xie, S., Ragauskas, A.J., Yaun, J., 2016. Lignin conversion: opportunities and challenges for the integrated biorefinery. Ind. Biotechnol. 12(3), 161-167.
[93] Xu, F., Zhong, X.C., Sun, R.C., Jones, G.L.L., 2005. Lignin distribution and ultrastructure of Salix psammophila. Trans Chin. Pul Pap. 20(1), 6-9.
[94] Sreekrishnan, T.R., Kohli, S., Rana, V., 2004. Enhancement of biogas production from solid substrates using different techniques-a review. Bioresour. Technol. 95(1), 1-10.
[95] Yokoyama, S., 2008. The Asian Biomass Handbook. A guide for biomass production & utilization, The Japan Institute of Energy, Tokio.
[96] Yu, G., Zhang, Y., Schideman, L., Funk, T., Wang, Z., 2011. Distributions of carbon and nitrogen in the products from hydrothermal liquefaction of low-lipid microalgae. Energy Environ. Sci. 4(11), 4587-4595.
[97] Zamani, A., 2015. Introduction to lignocellulose-based products, in: Karimi, K. (ed.), Lignocellulose-Based Bioproducts. Springer, Cham, pp. 1-36.
[98] Zhang, J., Weng, X., Han, Y., Li, W., Gan, Z., Gu, J., 2013. Effect of supercritical water on the stability and activity of alkaline carbonate catalysts in coal gasification. J. Energy Chem. 22(3), 459-467.
[99] Zhao, X., Zhang, L., Liu, D., 2012. Biomass recalcitrance. Part I: the chemical compositions and physical structures affecting the enzymatic hydrolysis of lignocellulose. Biofuel Bioprod. Biorefin. 6(4), 465-482.

Please cite this article as: Tursi A. A review on biomass: importance, chemistry, classification, and conversion. Biofuel Research Journal 22 (2019) 962-979. DOI: 10.18331/BRJ2019.6.2.3